FILM COOLING FROM INCLINED CYLINDRICAL HOLES USING LARGE EDDY SIMULATIONS

A DISSERTATION

SUBMITTED TO THE DEPARTMENT OF AERONAUTICS AND ASTRONAUTICS

AND THE COMMITTEE ON GRADUATE STUDIES

OF STANFORD UNIVERSITY

IN PARTIAL FULFILLMENT OF THE REQUIREMENTS

FOR THE DEGREE OF

DOCTOR OF PHILOSOPHY

Yulia V. Peet

September 2006

I certify that I have read this dissertation and that, in my opinion, it is fully adequate in scope and quality as a dissertation for the degree of Doctor of Philosophy.

_____

Sanjiva K. Lele
(Principal Advisor)

I certify that I have read this dissertation and that, in my opinion, it is fully adequate in scope and quality as a dissertation for the degree of Doctor of Philosophy.

_____

Juan J. Alonso

I certify that I have read this dissertation and that, in my opinion, it is fully adequate in scope and quality as a dissertation for the degree of Doctor of Philosophy.

_____

John K. Eaton

Approved for the University Committee on Graduate Studies.

Abstract

The blades in the first stage of the high pressure turbine experience a harsh thermal environment. The flows exiting the combustion chamber are at high temperatures exceeding the melting point of the turbine blade material. In order to avoid the detrimental effect of contact between hot gases and the blade surface, cooling measures are employed. Film cooling is a strategy which consists of taking some bleed air from the compressor and supplying it through discrete holes on the blade surface to form a protective layer. However, due to the complex three-dimensional interactions between the coolant and the mainstream, it is difficult to achieve desired cooling performance. Understanding of these mechanisms will be useful in designing cooling schemes.

The goal of the present study is to investigate numerically the physics of the flow, which occurs during the film cooling from inclined cylindrical holes. Large Eddy Simulation (LES) is performed modeling a realistic film cooling configuration, which consists of a large stagnation-type reservoir, feeding an array of film holes flowing into a flat plate turbulent boundary layer. Special computational methodology is developed for this problem, involving coupled simulations using multiple computational codes. A fully compressible LES code is used in the area above the flat plate, while a low Mach number LES code is employed in the plenum and film holes. The motivation for using different codes comes from the essential difference in the nature of the flow in these different regions.

Flowfield is analyzed inside the plenum, film hole and a crossflow region. Flow inside the plenum is mostly stagnating, except for the region close to the exit, where it accelerates rapidly to turn into the hole. The sharp radius of turning at the trailing edge of the plenum–pipe connection causes the flow to separate from the downstream wall of the film hole. To conserve the total mass flux, an acceleration occurs upstream of the separation bubble, causing the so-called "jetting effect". The influence of these effects persists all the way through the hole exit, creating exit velocity distribution with a gap in the center due to the in-hole separation, contrary to the velocity profile of a developed pipe flow. By changing

effective angle of inclination, the separation inside the film hole leads to decrease in cooling effectiveness.

After coolant injection occurs, the complex flowfield is formed consisting of coherent vortical structures. These are horseshoe vortices upstream of the jet, downstream spiral separation node (DSSN) right after the jet injection and counter-rotating vortex pair (CRVP) occupying the wake of the jet. All these strong coherent structures are responsible for bringing hot crossflow fluid in contact with the walls of either the film hole or the blade, thus reducing cooling protection.

Mean velocity and turbulent statistics are compared to experimental measurements and good agreement is obtained. LES results are used to assess the applicability of basic assumptions of conventional eddy viscosity turbulence models used with Reynolds-averaged (RANS) approach. These models relate Reynolds stress tensor to the mean rate of strain through a single coefficient, the eddy viscosity. It is shown here by calculating the ratio between the shear stresses and the corresponding components of the rate of strain tensor, that the distribution of eddy viscosities for different shear stress components is different: xy component is the smallest, almost three times smaller than the other two components, especially in the near-wall region. Different values for the thermal diffusivity as deduced from the three components of the turbulent heat fluxes are also found, thermal diffusivity in streamwise direction is about five times larger than in the other directions. Modeling the Reynolds stresses with a single coefficient leads to erroneous RANS predictions: underprediction of the magnitude of spanwise shear stresses ($u'w'$), underestimation of the lateral growth and overestimation of the vertical penetration. In the current LES, $u'w'$ shear stress is in a good agreement with experiments.

Film cooling performance is analyzed by looking at the distribution of mean temperature. Comparison of adiabatic film cooling effectiveness with experiments shows fair agreement for the centerline and laterally-averaged effectiveness. Lateral distribution of effectiveness is in especially good agreement, showing the correct prediction of the lateral growth of the jet.

Acknowledgements

This work would not have been possible without many people who contributed in its development. First, I would like to thank my advisor, Professor Sanjiva Lele, who has always been understanding and supportive, and whose knowledge and useful suggestions helped enormously. I would also like to thank the members of my reading committee, Professors Juan Alonso and John Eaton, for providing insightful comments and helping to acquire the "big picture". Two people who developed the computational codes used in the present work and allowed me two borrow them deserve special thanks: late Dr. Charles Pierce and Dr. Andy Xiong. I would also like to acknowledge the contribution of Dr. Bogard who provided me with the detailed database of his experimental data. I was fortunate to be a member of ASC integration group and greatly benefited from collaboration with its members, Professors Parviz Moin and Heinz Pitsch, research associates and post docs George Kalitzin, Gorazd Medic, Franc Ham, Ken Mattson and others. I would also like to thank all past and present members of Dr. Lele's research group for valuable discussions and motivating ideas and many Aero&Astro students for friendship and moral support. I am extremely grateful for all the help and support, both physical and intellectual, of my husband Matthew, who took care of our two-month old daughter during the preparation of this manuscript.

Contents

List of Tables

List of Figures

xiv

Nomenclature

Acronyms

CRVP	Counter Rotating Vortex Pair
DES	Detached Eddy Simulation
DNS	Direct Numerical Simulation
DSSN	Downstream Spiral Separation Node
HSV	Horseshoe Vortices
JCF	Jet in Crossflow
LES	Large Eddy Simulation
RANS	Reynolds Averaged Navier-Stokes Equations
RLV	Ring Like Vortices
RMS	Root Mean Square
RSTM	Reynolds Stress Transport Model
TBL	Turbulent Boundary Layer
TKE	Turbulent Kinetic Energy
TL	Turbulence Levels

Notation

$()_\infty$	Free-stream quantity
$()_j$	Jet quantity
$()^\star$	Dimensional quantity
$\overline{()}$	Reynolds averaged or filtered quantity
$\tilde{()}$	Favre averaged or filtered quantity
$()_{rms}$	Root mean square value of a quantity
$()'$	Fluctuation of a quantity

$()_{nc}$	Quantity corresponding to no-cooling
$()_c$	Quantity in the compressible code
$()_{lm}$	Quantity in the low Mach number code
$()_i$	Quantity at the inflow
$()_r$	Quantity at the recycling station
$()_{aw}$	Adiabatic wall quantity
$()_w$	Quantity at the wall
$()^+$	Quantity non-dimensionalized with wall units

Roman Symbols

B	Blowing ratio
C_μ, C_k	SGS model coefficients
c	Speed of sound
c_p	Specific heat at constant pressure
c_v	Specific heat at constant volume
d	Jet diameter
DR	Density ratio
e	Internal energy
$E(k)$	Energy spectrum
h	Enthalpy
k, k_t	Thermal diffusivity and turbulent thermal diffusivity
k	Turbulent kinetic energy
k	Wavenumber
H	Boundary layer shape factor
I	Momentum ratio
L	Length of the film hole
M	Mach number
N	Number of grid points
n	Coordinate in wall-normal direction
p	Pressure
q	Heat flux
R	Gas constant
$R_1\,R_2$	Riemann invariants

Re	Reynolds number
Re_x	Reynolds number based on streamwise distance x
Re_θ	Reynolds number based on θ
s	Entropy
T	Temperature
t	Time
U	Nonconservative flow variables
U_∞	Magnitude of freestream velocity
U_j	Magnitude of mean axial coolant velocity
u, v, w	Velocities in cartesian coordinates
u_x, u_r, u_θ	Velocities in cylindrical coordinates
VR	Velocity ratio
$x,\ y,\ z$	Cartesian coordinates
$x,\ r,\ \theta$	Cylindrical coordinates

Greek Symbols

Δt	Time step size
$\Delta x, \Delta y, \Delta z$	Grid size
α	Injection angle
β	Skew angle
γ	Ratio of specific heats
$\delta, \delta^\star$	Boundary layer 99% and displacement thickness
ϵ	Dissipation rate
η	Adiabatic film cooling effectiveness
η	Blasius similarity variable
ρ	Density
θ	Momentum boundary layer thickness
Θ	Normalized temperature
μ, μ_t	Molecular and turbulent dynamic viscosity
ν	Kinematic viscosity
τ_w	Shear stress at wall

Chapter 1

Introduction

1.1 Film Cooling Methodology

Gas turbine engine thermal efficiency and a power output are directly proportional to the combustor exit temperature, as follows from the analysis of an idealized thermodynamic cycle. Therefore, drive for increasing engine performance leads to pushing turbine inlet temperatures up. As a consequence, these temperatures usually exceed the melting point of a turbine blade material. To allow for such temperatures, cooling measures for the turbine airfoils are necessary. Since 1960, the cooling methods have played an important role in gas turbine engine design. Early on, simple convective cooling schemes were employed, which used high-pressure bleed air from the compressor to circulate through internal convection channels. In the 1970s, a new cooling strategy was introduced, where the bleed compressor air is supplied from the internal convective passages onto the surface of the airfoil through the film holes drilled in the surface material. This technology was given a name "film cooling", and nowadays it is used at all regions of the airfoils, particularly in the first and second stages of the blade.

One of the major difficulties arising with the introduction of film-cooling is a potential drop in jet engine efficiency due to the reduced amount of air available for generating thrust. Therefore, the goal of a cooling scheme designer is to achieve the most effective thermal protection for a given component with the minimum negative influence on the overall engine performance. Thus, careful decisions should be made about the shape and the location of cooling holes throughout the airfoil and amount of flow supplied through each hole. Ideally, the basis for these decisions would be a certain knowledge of "cause-and-effect" relations with respect to film cooling, i.e. a set of rules telling how the system is going to react

to a change in one of its inputs. However, difficulty in obtaining such information arises due to an extreme sensitivity of the problem to all the details of the exact geometrical and physical conditions. Bogard & Thole (2006), in their recent review of film cooling, try to classify numerous parameters affecting the film cooling performance in terms of the significance of their effect. The result of their classification is shown in Table 1.1. In a natural environment, all these factors act together determining the final performance. Even in laboratory conditions, it is not easy to isolate an effect of each individual factor, since changing one of them often leads to a change in another (for example, changing density ratio will also change momentum flux ratio provided mass flux ratio stays the same etc.). Moreover, even if one could determine an influence of each of the parameters individually, the problem is not necessarily additive, that is several factors acting together might have a different effect than a direct sum of individual effects. In other words, every combination of the factors can potentially change the film cooling performance.

In a situation when it is yet impossible to obtain straightforward "directions" in designing cooling schemes, a good understanding of the mechanisms involved in film cooling process is desirable. When the cooling jet is injected into a crossflow, a highly complex three-dimensional flow arises as a result of the jet-crossflow interaction. Coherent vortical structures created during this interaction tend to lift the cooling jet from the surface, reducing film cooling coverage. Understanding the physics of the cooling flow will help to estimate a performance of a given cooling strategy based on the flow analysis and compare different schemes with each other, even if exact answers are not yet possible to obtain. The knowledge of the flow dynamics can also facilitate an invention of more efficient cooling configurations. The goal of the present study is to obtain such a knowledge through an accurate simulation of film cooling flowfield and detailed analysis of the flow structure.

A review of experimental and numerical investigations of film cooling problem published in open literature is presented next.

1.2 Evaluation of Film Cooling Performance

An ultimate goal in gas turbine film cooling is to reduce the surface heat transfer, since it is the excessive heat flux which is detrimental for the blade material. Heat flux is evaluated as

$$q = h \left(T_{ref} - T_w \right), \tag{1.1}$$

Coolant/mainstream conditions	Hole geometry and configuration	Airfoil geometry
Mass flux ratio* Momentum flux ratio*	Shape of the hole* Injection angle and compound angle of the coolant hole*	Hole location Leading edge Main body Blade tip Endwall
Mainstream turbulence*	Spacing between holes, P/d	Surface curvature*
Coolant density ratio Approach boundary layer	Length of the hole, L/d Spacing between row of holes and number of rows	Surface roughness
Mainstream Mach number Unsteady mainstream flow Rotation		

Table 1.1: Factors affecting film-cooling performance (from Bogard & Thole (2006)). Asterisk denotes the factors that have significant effect on film cooling performance

where h is the heat transfer coefficient, T_w is the wall temperature, and T_{ref} is the reference temperature. For estimating heat flux in the presence of film cooling, T_{ref} should be the local fluid temperature next to the airfoil surface. Since for an adiabatic surface, adiabatic wall temperature T_{aw} is the fluid temperature right above the surface, it is considered to be an appropriate reference temperature for an evaluation of film cooling heat transfer. Consequently, the heat flux with film cooling is written as

$$q_{fc} = h_{fc}\left(T_{aw} - T_w\right), \tag{1.2}$$

where the subscript "fc" refers to film cooling. Hence, one of the most important variables in predicting film cooling heat transfer is the adiabatic wall temperature, which is representative of the fluid temperature just above the surface. Adiabatic wall temperature is usually reported in experiments trough a non-dimensional parameter called film cooling effectiveness defined as

$$\eta = \frac{T_{aw} - T_\infty}{T_j - T_\infty}, \tag{1.3}$$

where T_∞ is the free-stream temperature and T_j is the temperature of a cooling jet. It is necessary to evaluate adiabatic wall temperature in a non-dimensional form, so that the laboratory results could be projected onto the real engine conditions.

Generally, when a cooling jet is injected into a crossflow, high levels of turbulence are

generated in the shear layers and in the wake behind the jet. These high levels of turbulence result in a higher mixing between the coolant jet and a crossflow, which, in turns, increase the heat transfer coefficient. Therefore, heat transfer coefficient h_{fc} in the presence of film-cooling would be higher than the heat transfer coefficient h_0 in the free boundary layer. This effect should be taken into account while predicting surface heat flux in the presence of film cooling.

To evaluate the ultimate benefit of a cooling scheme, the net reduction in heat flux Δq_{fc} to the airfoil surface should be estimated as

$$\Delta q_{fc} = 1 - \frac{q_{fc}}{q_0} = 1 - \frac{h_{fc}(T_w - T_{aw})}{h_0(T_w - T_\infty)} = 1 - \frac{h_{fc}}{h_0} \frac{\eta}{\Theta}. \tag{1.4}$$

The net heat flux reduction relates the heat transfer that would have occurred on the airfoil with no film cooling, q_0, to that with film cooling, q_{fc}. Θ is the nondimensional temperature defined as

$$\Theta = \frac{T_w - T_\infty}{T_j - T_\infty}. \tag{1.5}$$

Therefore, both film cooling effectiveness, η, and heat transfer coefficient with film-cooling, h_{fc}, are important for the estimation of an ultimate film cooling performance.

1.3 Experimental Studies

Since the bulk of experimental investigations of film cooling have been done with flat surface test plates, this configuration will be implied by default, unless otherwise specified.

Velocity/blowing/momentum ratio is perhaps the most important parameter in film cooling problem, since it determines the regime under which the cooling jet operates. These three factors are combined together, since they are inherently interconnected. With increasing blowing ratio the jet tends to separate from the surface, completely changing the cooling pattern. Ramsey & Goldstein (1971) observed that as the blowing ratio increases, the CRVP (counter-rotating vortex pair) begins to lift away from the wall, causing a gradual reduction in film cooling effectiveness. Kruse (1984) demonstrated that, depending on the flow conditions, the jet may reattach, leading to an increase in effectiveness downstream. Thole *et al.* (1992), who studied an influence of blowing ratio on a cooling from a row of inclined holes, identified three distinct regimes: fully attached coolant jets ($I < 0.4$); coolant jets that detached then reattached($0.4 < I < 0.8$); and coolant jets that are fully detached ($I > 0.8$). The effect of coolant separation on film effectiveness is presented in Sinha *et al.*

(1991) by analyzing the distributions of centerline effectiveness η_c versus streamwise co-ordinate x/d for different momentum ratios. For low momentum ratios ($I < 0.3$), when the jet stays fully attached, η_c monotonically decreases with x/d. For detached–reattached jets ($0.3 < I < 0.7$), η_c first decreases due to the lift-off of the core of the jet and then increases again after the reattachment occurs. For completely detached jets ($I > 0.7$), fast initial decay of η_c is accompanied by the low levels of effectiveness for an entire downstream region. Baldauf *et al.* (2002) documents an effect of blowing ratio on the laterally-averaged film-effectiveness $\bar{\eta}$. For the attached jets, overall level of $\bar{\eta}$ increases with B. However, when B is increased beyond 0.6, indicating the start of detachment-reattachment regime, the peak level of $\bar{\eta}$, which occurs in the near field, decreases as a consequence of a jet lift-off. However, $\bar{\eta}$ values in the far field, beyond $x/d = 20$, continues to increase with B, since the tendency of coolant jet separation to reduce $\bar{\eta}$ is offset by the increase in $\bar{\eta}$ caused by raising coolant mass flow. Eventually the separation effects dominate, and for $B > 1$, the level of $\bar{\eta}$ decreases over the full length measured. This implies that optimal blowing ratio exists, providing maximum cooling performance. In the configuration investigated by Baldauf *et al.* (2002), this optimum occurs at about $B = 0.6$,

An issue of scaling of film cooling performance is of significant importance. Particularly, the question is: does the blowing or momentum ratio provides the better scaling? Abramovich (1963), compiling the results of numerous early studies, argues that the behavior of three-dimensional film cooling jet is correlated better using the momentum ratio, I, rather than the blowing ratio, B. Thole *et al.* (1992) clarifies that it is the coolant jet separation characteristics that scale with the momentum ratio, I, explaining it by the fact that the dynamics of the force of the mainstream impacting on the coolant jet and causing it to turn toward the wall is primarily a function of the momentum of the coolant jet relative to the momentum of the mainstream. This is the same reason, why the jet trajectories correlate with the momentum ratio, as studied by Margason (1968), Hasselbrink & Mungal (2001), Muppidi & Mahesh (2005) and others. Sinha *et al.* (1991) and Ethridge *et al.* (2001) report that film cooling performance is correlated with the blowing ratio when the jet remains attached to the surface. This is because the blowing ratio scales the thermal capacity of the coolant, since the convective transport of temperature is proportional to ρU_j. Once the jet detaches, the data are better correlated by the momentum ratio. This is further confirmed by Baldauf *et al.* (2002), who finds that the $\bar{\eta}$ curves collapse for different regimes if plotted versus x/Bs_e for $B \leq 1$ ($I \leq 0.57$), when the jets do not significantly separate from the surface. Here $s_e = A_{hole}/P$ is a characteristic width of the hole. As

the blowing ratio is raised to $B > 1$ ($I > 0.57$), resulting in the jet detachment, there is a continual decrease in $\bar{\eta}$ with increasing B when plotted versus x/Bs_e, showing that the scaling with the blowing ratio is no longer valid.

Another important parameter effecting film cooling performance, as seen in table 1.1, is an injection angle. An intuitive argument would suggest that the smaller an injection angle α, the more effective the cooling scheme, since shallower angles provide lower jet trajectories. However, this intuitive argument is not valid. Ramsey & Goldstein (1971) compared the performance of inclined at 35° and normal injection holes and reported that under the same coolant/mainstream conditions the inclined jet exhibited less penetration and less spreading in vertical and lateral directions. This indicates that shallower angles provide less lateral mixing than steeper injection angles. Foster & Lampard (1980) also tested hole injection angles of 35° and 90° and observed slightly decreased film effectiveness for the 90° holes at $B = 0.5$. However, improved performance was found for the 90° holes for a high blowing ratio $B = 1.4$, when the jet lifts off the cooled surface. These authors argue that although holes with normal injection produce higher trajectory, they also generate a higher degree of spanwise mixing, allowing the jets to coalesce and reattach to the surface sooner than shallower injection holes. This effect becomes more apparent at higher blowing ratios when the film cooling jet completely lifts off the surface. Baldauf *et al.* (2002) found similar results comparing 30°, 60° and 90° injection holes. Goldstein & Stone (1997) investigated an effect of hole inclination on concave and convex surfaces, and looked at 15°, 25° and 45° angles. They concluded that for very low blowing ratios, $B < 0.3$, the resulting film effectiveness is primarily determined by mainstream parameters and is not sensitive to the hole inclination. For intermediate blowing ratios, jets with shallower angles perform better, since they possess lower trajectories and therefore delay the jet lift-off. For high blowing ratios, steeper injection holes result in better effectiveness due to increased mixing, confirming the results of Foster & Lampard (1980).

Hole length to diameter ratio (L/d) has an effect on the flow development inside the film hole. Burd & Simon (1997) measured film effectiveness and mean centerline velocity for an injection with $L/2 = 2.3$ and $L/d = 7$ inclined holes. This work was supplemented by an additional measurements of discharge coefficients by Burd & Simon (1999). Their data suggest that the separation bubble is formed at the film hole walls close to the entrance to the film hole. With the short holes, this leads to an increase of the effective angle of the inclination (α). This was attributed to jetting of coolant flow on the upstream edge of the film cooling hole. Longer holes alleviate this effect, resulting in more developed exit flow.

This effect is strengthened with the blowing ratio. As a result, longer holes generally lead to better cooling effectiveness than the shorter holes. Lutum & Johnson (1999) refined this study, examining hole lengths that ranged from $L/d = 1.75$ to $L/d = 18.0$. Data from this repost also indicated an improvement in film cooling performance as the hole is lengthened, given the flow conditions used. The rise in effectiveness is particularly sensitive to hole lengths in the range $0 \leq L/d \leq 5.0$.

Although not listed in Table 1.1, supply plenum conditions play an important role in the overall development of the coolant flow. Wittig *et al.* (1996) and Hale *et al.* (2000) investigated an effect of the flow direction in a narrow plenum ($H/d \sim 2$), combined with an injection from short holes ($0.66 < L/d < 3$), both perpendicular and inclined at 35°, on film cooling effectiveness. They compared the co-flowing and counter-flowing plenum with the short hole injection ($0.66 < L/d < 3$) for both perpendicular and inclined at 35° holes. They found that effect of plenum conditions is larger for the shorter holes. The behavior with respect to the flow direction was different for the perpendicular and inclined holes. Counter-flowing plenum was superior for perpendicular holes; however, co-flowing plenum showed better cooling effectiveness for inclined holes.

Peterson & Plesniak (2002, 2004) furthered this study, trying to explain why the counter-flowing plenum produces better results than the co-flowing plenum for the perpendicular holes. They performed hydrodynamic measurements and looked on the flow inside the plenum, g=film hole and above the test surface for the perpendicular injection with $L/d = 0.66$. They discovered that the in-plenum and in-hole vortices with the different sign of rotation are produced depending on the flow direction. For the co-flowing plenum, the vortices rotated in the same direction as CRVP above the test surface, which led to CRVP enhancement and higher jet trajectory with less lateral spreading, leading to decrease in cooling effectiveness. For the counter-flowing plenum, the sense of the rotation for in-hole and in-plenum vortices was the opposite, resulting in large cooling effectiveness. For the inclined holes, the worse performance of co-flowing plenum is attributed to a larger amount of separation in the hole entrance resulting in larger effective inclination angle, as previously discussed. Complimentary measurements of discharge coefficients presented by Gritsch *et al.* (2001), Bunker & Bailey (2001), Hay *et al.* (1985) combined the effects of cooling hole inlet crossflow and hole inclination. Data from these studies confirm the conclusion than interaction of inlet crossflow and hole inclinations has a significant effect on coolant flow.

An important issue in the supply plenum conditions is an existence of the sharp corner

between the plenum and the film hole. Johnston *et al.* (2002) compared the turbulence field produced by pitched ($\alpha = 30°$) and skewed ($\beta = 60°$) jets originating from the plenum having both sharp and smooth corner. They found that the turbulence levels (TL) were almost three times larger in the near filed ($x/d \leq 5$) for the sharp corner; however, this turbulence decayed fast, showing identical TL levels for both cases in the far field ($x/d > 10$). It was argued that increased levels of turbulence in the near field come from the film hole, where the flow separation and the shearing between the slow-moving flow and the "jetting" region produced high levels of turbulence. In terms of film cooling, an elevated levels of turbulence are non-desirable, since they increase the mixing between jet and crossflow and heat transfer coefficient.

1.3.1 Computational Studies

Integral Models

The first detailed calculation procedures applied to predict the behavior of jets in cross-flow were integral models. In these models, integral equations are derived either by considering a balance of forces acting over an elementary control volume of the jet or by integrating three-dimensional Navier-Stokes equations in two spatial dimensions. The effect of pressure drag, entrainment of cross-stream fluid and spreading rates are taken into account by way of empirical relations. As a result, a set of ordinary differential equations is obtained, which is solved either numerically or analytically involving simplifying ad-hoc assumptions. Abramovich (1963) developed analytical model for predicting the trajectory of a jet in a crossflow by assuming that the momentum of the jet in the direction normal to the crossflow was preserved and that the pressure difference across the jet was balanced by the centrifugal force due to its curvature. The model involved approximating the kidney-shaped cross-section of the jet with an ellipse in order to derive an equation for the trajectory of the jet. Fan (1967) developed an integral model incorporating the effects of drag forces and entrainment for a buoyant jet in crossflow. Ziegler & Wooler (1973) and Grivés (1978) proposed a set of closed form equations for the CRVP spacing and strength based on the theoretical assumptions about the jet trajectory and mixing. Subramanya & Porey (1984) suggested a similar model, but for blowing ratios closer to film cooling operating conditions. Kim *et al.* (1985) reported an analytical mixing model for a buoyant jet injected into the pipe based on fitting experimental data. Accomplishments of this model are an inclusion of injection angle and use of the applicable range of blowing ratios. In addition, a switch was implemented changing the physics of the model from the turbulent-diffusion dominated

mixing processes for weak jets to inviscid dynamics mechanisms for strong jets. Karagozian (1986) proposed an analytical model for the vorticity in a transverse jet, approximating CRVP by locally two-dimensional Rankine vortex and using viscosity to account for the vortex separation. Clearly, all these models involve some simplifying assumptions, which suffer from lack of generality. The next step towards more accurate numerical prediction is to turn to full three-dimensional Navier-Stokes equations.

Algebraic Turbulence Models

The most popular approach in simulating turbulent flows of engineering interest is to solve Reynolds Averaged Navier Stokes (RANS) equations, employing the closure models for un-closed Reynolds stresses. RANS simulations capture only the time-averaged flow variables and thus use relatively coarse meshes, allowing short turnaround time for obtaining numerical solution. The simplest form of the turbulence model is based on the Boussinesq eddy viscosity assumption, where the turbulent stresses are represented as

$$-\overline{\rho\, u_i'\, u_j'} = -\frac{2}{3}\rho\, k\, \delta_{ij} + 2\mu_t(\bar{S}_{ij} - \frac{1}{3}\delta_{ij}\bar{S}_{kk}), \tag{1.6}$$

where k is the turbulent kinetic energy, $\bar{S}_{ij}$ is the mean rate of strain and μ_t is the eddy viscosity. First attempt to use RANS equations with a closure model to predict the jet-in-crossflow behavior was that of Chien & Schetz (1975) with a constant eddy viscocity assumption. The most commonly used algebraic model for an eddy viscosity, however, is that of Baldwin & Lomax (1978), where eddy diffusivity is expressed in terms of mixing length in both the inner and outer layers. In a series of papers, Garg & Gaugler (1995), Garg & Gaugler (1997*b*),Garg & Gaugler (1997*a*) used the Baldwin-Lomax model to obtain predictions of flow and heat transfer over a film-cooled C3X vane. They obtained qualitatively good agreement with experimental data, but significant differences were noted in the vicinity of the film cooling injection rows and in the leading edge regions. Apparently, due to strong pressure gradients and separation in the immediate vicinity of injection, algebraic models provide bad approximation for film cooling flows. Also, in the leading edge region, there is a stagnation point anomaly, which is hard to predict with algebraic turbulence models.

Two-Equation Turbulence Models

Two-equation turbulence models have been widely used for numerical simulation of film cooling flows. However, following these simulations, a general conclusion is that while two equation models provide improved predictions with respect to algebraic models, they are unable to represent the near field accurately. The lateral spreading and mixing of film-cooling jet is under-predicted by two-equation turbulence models, while the vertical penetration is over-predicted (Berhe & Patankar (1996), Lakehal *et al.* (1998), York & Leylek (1999), Hoda & Acharya (2000), Acharya *et al.* (2001)). Acharya *et al.* (2001) compared seven different turbulent models for a case study of a jet injected from the square hole corresponding to the experimental setup of Ajersch *et al.* (1995). The authors found that all the models significantly underpredicted the spanwise shear stress $u'w'$ responsible for spanwise mixing and a lateral growth; representative $u'w'$ profiles together with the spanwise velocity w/U_j and turbulent kinetic energy obtained with different two-equation models at several downstream locations documented in the paper of Acharya *et al.* (2001), are reproduced here in figure 1.1. The reason for this disagreement lies in intrinsic assumption of two-equation turbulence models. As in algebraic models, the same equation (1.6) is used to model turbulent stresses. The only difference between two-equation and algebraic models is that the eddy viscosity is not approximated with an ad-hoc formula, but obtained from a kinetic energy and a dissipation rate (or some other related quantities depending on the model), for which additional equations are derived and solved. In equation (1.6), a single coefficient (eddy viscosity) relates the Reynolds stress tensor and a mean rate of strain tensor, essentially assuming that the principal axes of these two tensors are aligned. Such an assumption has been experimentally and numerically shown to be inaccurate for film cooling flows. Wang *et al.* (1996) and Kaszeta & Simon (2000) estimated different components of eddy viscosity in their experiments (dividing shear stresses by the corresponding components of the strain rate) and verified the anisotropy of the eddy viscosity downstream of the hole. In fact, the lateral eddy viscosity (xz component) was found to be significantly larger near the wall than the vertical eddy viscosity (xy component). Since turbulence models are specifically tuned to correctly predict xy shear stress, they are expected to model xy eddy viscosity correctly. However, because of the isotropy of the model, xz eddy viscosity and therefore lateral stress $u'w'$ will be underestimated. Anisotropy corrections have been proposed, for example, by Bergeles *et al.* (1978), who suggested a linear relationship to model an anisotropy of the eddy viscosity for very low blowing ratios $B < 0.1$. However, these corrections are much simpler than the actual flow anisotropies and do not lead to an
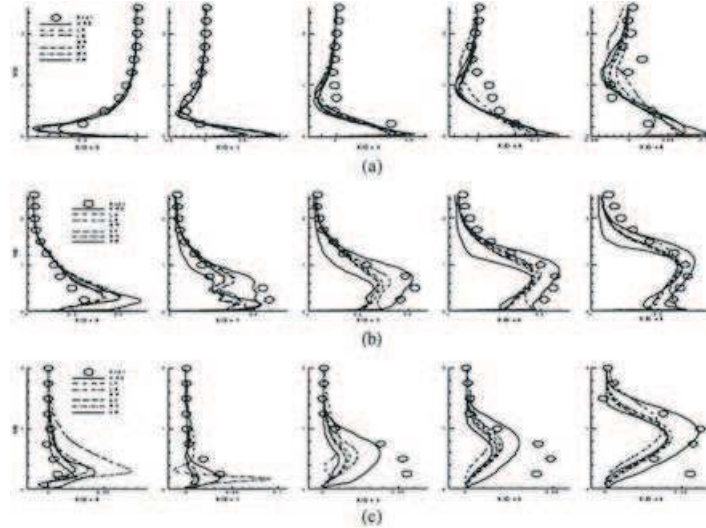
Figure 1.1: (a) Spanwise velocity, w/U_j (top figure) (b) turbulence kinetic energy, (middle figure) and (c) transverse shear stress $(u'w')$ along $z/d = -0.5$. Lines, RANS simulations with different two-equation models; symbols, experiments of Ajersch *et al.* (1995). Adopted from the paper of Acharya *et al.* (2001).

improved prediction in the hole vicinity (the prediction does improve further downstream, as the flow recovers to a standard turbulent boundary layer, see Ajersch *et al.* (1995)). With the intent of improving the results, Acharya *et al.* (2001) implemented Reynolds-Stress Transport Model (RSTM), where each component of Reynolds stresses is solved for, and, therefore, turbulence anisitropy can be represented. However, RSTM results did not show any significant improvement over two-equation models and, in fact, demonstrated poorer agreement for the kinetic energy. Perhaps, not only anisotropy, but also inability of RANS simulations to capture the effects of large scale unsteadiness in the near field contributes to the lack of agreement. In terms of film cooling performance, the described deficiencies of two-equation turbulence models lead to an overpediction of a centerline cooling effectiveness due to inability to resolve the jet separation and narrower lateral distribution of effectiveness due to an underestimation of spanwise mixing (Leylek & Zerkle (1994); Walters & Leylek (1997)). These two trends cancel each other leading to a good agreement in laterally-averaged effectivness for the wrong reasons.

DES, LES and DNS Studies

Further improvement beyond RANS simulations in terms of accurate representation of turbulence is Detached Eddy Simulations (DES) technique. DES is a hybrid technique first proposed by Spalart *et al.* (1997) as a numerically feasible and plausibly accurate approach for predicting massively separated flows (see also Spalart (2000)). In DES, the aim is to combine the most favorable aspects of RANS and LES, namely, application of RANS models for predicting the attached boundary layers and LES for resolution of time-dependent, three dimensional large eddies. In natural applications of the method, an entire boundary layer is treated by RANS and with an LES treatment of separated regions. This is accomplished by employing one-equation Spalart-Allmaras model (Spalart & Allmaras (1994)) and modifying a lengthscale in eddy viscosity destruction term to be the minimum of the distance to the closest wall and a lengthscale proportional to the local grid spacing, i.e. $\tilde{d} = \min(d, C_{DES}\,\Delta)$. This ensures that RANS treatment is retained near the solid walls, where $d << \Delta$; while away from the walls, where $\Delta << d$, the subgrid model is obtained (see Squires (2005), Strelets (2001) for more detailed description). Kapadia & Roy (2003) performed DES of a film cooling flow from inclined cylindrical hole supplied by a large plenum, simulating experimental setup of Sinha *et al.* (1991), with 2.1×10^6 cells. No turbulence statistics were presented. However, the authors reported higher centerline and lower spanwise averaged effectiveness in the far field than experimental data of Sinha *et al.* (1991). To the contrary, centerline effectiveness was underpredicted in the near field. In addition, the problem with too little spanwise diffusion still persisted in DES. These findings probably suggest the necessity of treating all regions of the flow, and not just the immediate vicinity of the hole trailing edge, with LES, since large scale unsteady three-dimensional structures persist beyond the separated region just downstream of the jet injection.

Direct Numerical Simulations (DNS) resolve all the relevant flow scales, so that no modeling is required. DNS studies of jets in crossflow start with the simulations of Hahn & Choi (1997) for a slot injection into a laminar crossflow and normal circular jet injection into a turbulent crossflow. For the circular jet injection case, 14.6×10^6 grid points were used. Due to limitations of computational resources, jet Reynolds number was 1750, much lower than in comparable experiments. A parabolic profile was imposed at the injection location with a blowing ratio of $B = 0.5$. Muldoon & Acharya (1999) presented direct numerical simulations of a rectangular coolant jet injected normally into crossflow on a $128 \times 128 \times 64$ grid that mirrored an experimental setup of Ajersch *et al.* (1995). Tyagi & Acharya (1999*c*,*a*,*b*, 2000) repeated the same calculations using LES, studying the influence

of various parameters on the flow physics. Much better prediction of transverse shear stress was obtained with LES and DNS than with RANS turbulence models (see Acharya *et al.* (2001)). Yuan *et al.* (1999) examined the trajectory and entrainment characteristics of a round jet in a laminar crossflow for Reynolds numbers of 1,050 and 2,100 using LES with 1.34×10^6 grid points. Their comparison with experimental data for the mean velocity magnitude and r.m.s. fluctuations showed good agreement in the immediate vicinity of the jet injection, degradation in the jet wake and improvement further downstream. Tyagi & Acharya (2003) performed LES of film cooling flow from an inclined cylindrical hole using an incompressible flow solver with the passive scalar tracking and obtained fairly good comparison with experiments for the mean flowfield. A link between surface adiabatic effectiveness and a dynamics of unsteady coherent hairpin structures has been proposed. Liu & Pletcher (2005) performed LES of a similar configuration, but using a compressible code and studying high density ratios. Good comparison of centerline adiabatic effectiveness with the measurements of Schmidt *et al.* (1996) was documented, except for the lower value of effectivness right after the jet injection. Rozati & Tafti (2006) recently presented preliminary results on LES of leading edge film cooling from an inclined cylindrical holes.

1.4 Overview and Accomplishments

The primary goal of the present study is to perform accurate numerical simulation of a realistic film cooling configuration to achieve better understanding of the physics of the problem and to highlight important features of the flow, which might be useful in subsequent numerical studies and cooling schemes design. The following is the list of accomplishments of the present study:

- Special computational methodology is developed coupling compressible and low Mach number codes into a single time-accurate solver through an exchange of unsteady interface conditions using an overlapping grid technique.

- The coupling methodology is thoroughly tested on steady and unsteady laminar problems. Stability of the proposed interface conditions is verified and accuracy of the coupled solution is confirmed.

- The problem of laminar jet in a laminar crossflow is simulated as a model problem for film cooling type interactions. Good agreement with DNS studies (Muppidi & Mahesh (2005)) is obtained.

- A new insight on the coherent vortical systems for low velocity ratio jet in crossflow (JCF) is developed. Existence of two layers of hairpin vortical structures is documented and the mechanism of its formation is proposed.

- Auxiliary LES of turbulent boundary layer using the recycling-rescaling technique of Lund *et al.* (1998) is performed. A new compressibility correction suited for weekly-compressible flows is proposed. The problem of a drift in boundary layer thickness during long time integration is identified and a fix is suggested by applying the rescaling and recycling procedure only within the boundary layer, and not above its edge. Good agreement with other simulations and experiments is obtained for mean velocity and turbulent stresses. These calculations serve the purpose to provide inflow boundary conditions for film cooling simulations.

- Large Eddy Simulations of realistic film cooling configuration matching experiments of Pietrzyk *et al.* (1989) is performed. It includes large stagnation-type plenum, array of inclined film holes and a flat test surface. To the authors' knowledge, it is the first LES of film cooling published in the open literature which incorporates the plenum into the model.

- The flowfield inside the plenum, film hole and above the test surface is analyzed. The separation inside the film hole is revealed and the way it influences jet exit velocity distribution is documented. It confirms the importance of including the plenum into the simulations.

- Flow above the test surface is visualized by looking at three-dimensional streamline pattern. Coherent structures are revealed, such as horseshoe vortices, DSSN vortex and CRVP.

- Velocity field above the surface is related to the three-dimensional vortical systems and compared with experiments. Agreement with experimental data is very good.

- Turbulence normal and shear stresses above the surface are compared with experimental data. Reasonable agreement is obtained.

- Different components of eddy viscosity are calculated by dividing the shear stresses by the corresponding components of the rate of strain tensor. xy component is generally the smallest, almost three times smaller than the other two components, especially in the near-wall region. Different components of thermal diffusivity are also assessed.

Diffusivity in streamwise direction is five times larger than in vertical and spanwise directions.

- Superiority of LES versus RANS approach is confirmed for JCF flows, since an assumption of isotropic eddy viscosity and thermal diffusivity used in RANS turbulence models is not justified. This assumption leads to under-prediction of spanwise shear stress component and lateral spreading of the jet by RANS, which is not observed in the current LES.

- Film cooling performance is analyzed by looking at mean normalized temperature and adiabatic cooling effectiveness. The negative influence of JCF coherent structures on film cooling performance is demonstrated, showing the mechanism by which they bring hot crossflow fluid towards the wall. Comparison of the centerline and laterally-averaged effectiveness with experiments is fair. Lateral distribution shows very good agreement.

Chapter 2

Numerical Methodology

2.1 Introduction

A simplified schematic representation of film cooling geometry is shown in figure 2.1. It consists of the turbine blade, plenum and an array of film cooling holes. In real engine components film cooling holes are supplied by serpentine passage that winds through the blade. However, in most of film cooling experiments plenum is approximated by a very large reservoir feeding the film holes. Figure 2.1 assumes such a reservoir; note that the relative scale between cooling holes and a plenum is not accurately reproduced in this schematic representation.

For numerical simulations of film cooling flow one can pursue three different strategies. As a simplest approximation, no-slip boundary conditions on the surface of the turbine blade can be modified to account for the supply of the cooling flux. However, due to the large number of parameters which influence the exit conditions for the film cooling flow, it is impossible to obtain a reasonable degree of accuracy with such an approach. The next step is to extend the numerical domain a little further to include the film cooling hole. Then the cooling flow naturally develops as it exits the hole and the necessity for ad-hoc boundary conditions at the turbine blade surface is removed. However, the question then arises about the boundary conditions to use at the inflow of the cooling hole. Usually fully developed turbulent pipe profile is specified at the entrance to the hole and unrealistically long delivery tubes are modeled. Example of such an approach is LES of discrete-hole film cooling by Liu & Pletcher (2005) who used $L/d \sim 8$. Typical film cooling hole length in real turbine engines is $L/d \sim 3.5$ or even smaller. Measurements of the cooling flow inside short film holes reveal that it is very far from the fully-developed pipe flow. In fact, the flow

inside the hole exhibits rather complex behavior, featuring boundary layer separation at the downstream wall and the non-symmetric distribution of momentum across the cross-section. The details of the flowfield inside the hole and, in turn, resulting film cooling effectiveness distribution depend greatly on the geometry and flow conditions inside the supply plenum. Therefore, it is necessary to incorporate the effect of the plenum on the film cooling flow for an accurate numerical prediction of the overall flowfield. Tyagi & Acharya (2003) in their LES of film cooling flow from an inclined jet try to account for the presence of the plenum. They do it in two different ways. For the short delivery tube $L/d = 1.75$ they assume large stagnation-type plenum fed by air streams flowing parallel to the main crossflow. To simulate long tube $L/d = 6$ they maintain $L/d = 1.75$ in LES and provide mean velocities at the tube inlet obtained from a separate RANS calculation where a $6\,d$ long delivery tube fed by a large cylindrical plenum is modeled. Turbulent velocity fluctuations are added generated with a Gaussian random number generator. As for the first approach, it was shown in experimental studies that the flow in the plenum is rather complex when it approaches the cooling hole inlet. The strong coupling between the flow in the plenum and the hole exists, making it difficult to assume some exit plenum boundary conditions without the knowledge of the overall plenum-hole flowfield. With respect to the second approach, RANS simulations of Leylek & Zerkle (1994) show that due to the separation and jetting effect turbulence inside the hole is quite anisotropic and it is not accurate to approximate it by specifying random fluctuations. The conclusion follows that due to the strong coupling between the flow in the plenum, film cooling hole and the flow above the blade surface it is desirable to include all these regions into the numerical simulation. This is the approach we are going to follow. There were many RANS and one DES study that used exact film cooling geometry with different degrees of success. However, the current effort is the first LES known to the authors which attempts an accurate representation of all these three regions in the simulations.

The choice of numerical method is dictated by the essence of the flow physics in each of these three different regions. One of the important parameters to consider is the effect of compressibility. Typical distribution of Mach number for the flow above the realistic turbine blade is shown in figure 2.2 for the inlet Mach number of 0.340 (courtesy of Kodzwa (2005)). It is seen that Mach number varies along the blade reaching the value as high as 1.4. The most harsh thermal conditions for the turbine blade exists, however, at the leading edge, since it is the leading edge which is in the immediate contact with gases just exiting the combustion chamber. And although the overall surface of the blade needs to be cooled,
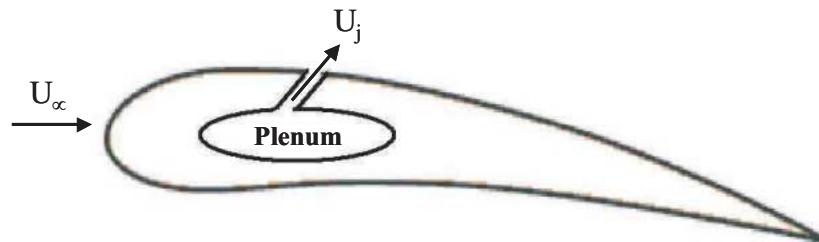
Figure 2.1: Simplified schematic representation of film cooling geometry.
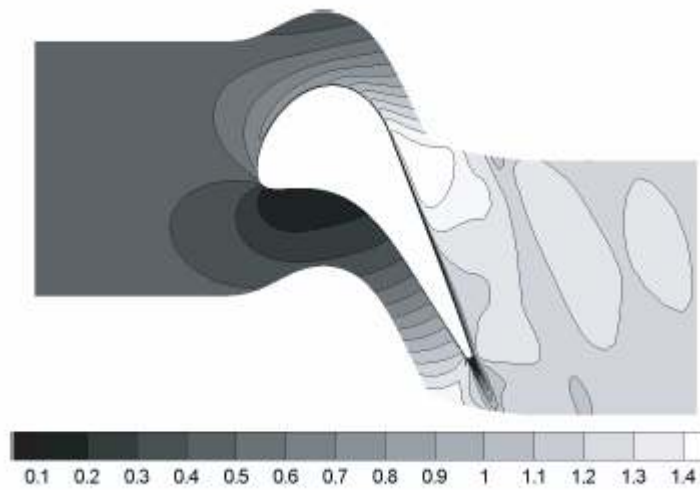
Figure 2.2: Typical Mach number distribution for the flow around the turbine blade, inlet Mach number $M \approx 0.340$ (courtesy of Kodzwa (2005)).

the leading edge region requires the most intensive cooling measures and most inventive cooling design strategies. The present computational approach has been developed with the ultimate goal of studying the leading edge film cooling. In the vicinity of the leading edge the flow is usually in a subsonic regime, with Mach numbers reaching the value of 0.5 or so. So, compressible effects are important in the region above the turbine blade, and the use of fully compressible Navier-Stokes equations is necessary. For LES of the flow in the vicinity of the leading edge shock-capturing capabilities are not necessary and high-order central-difference method can be employed, like the one used by Xiong (2004) to study effects of free-stream turbulence on the leading edge heat transfer.

Intuitively, compressible effects should not be important inside the film cooling hole. Given the Mach number M_∞ for the approaching mainstream, it is possible to estimate the Mach number M_j for the coolant jet knowing the two basic parameters defining the film cooling regime:

i) density ratio $DR = \frac{\rho_j}{\rho_\infty}$, and

ii) blowing ratio $B = \frac{\rho_j U_j}{\rho_\infty U_\infty}$.

Since

$$M = \frac{U}{c} = \frac{U}{\sqrt{\gamma R T}}, \tag{2.1}$$

it follows that

$$\frac{M_j}{M_\infty} = \frac{U_j}{U_\infty}/\sqrt{\frac{T_j}{T_\infty}} = \frac{U_j}{U_\infty}\sqrt{\frac{\rho_j}{\rho_\infty}} = \frac{\rho_j U_j}{\rho_\infty U_\infty}/\sqrt{\frac{\rho_j}{\rho_\infty}} = B/\sqrt{DR}. \tag{2.2}$$

Values for blowing ratio B in real gas turbine engines range from 0 to 5 depending on the geometry and flow conditions (Kodzwa (2005)). Although the typical value of B is about 1 (Eaton (2006)), in the present work we are looking at the low range of the blowing ratios, $B \sim 0.5$. Density ratio DR depends on the temperatures of the coolant and the mainstream. The mainstream has an absolute total temperature in excess of $1500\,K$, usually in $1500 \div 1800\,K$ range. The coolant flow has an absolute temperature of about $800\,K$ (Kodzwa (2005)). It gives the minimum value for $DR_{min} \sim 2$. However, with the modern tendency to increase jet engine performance and drive turbine inlet temperatures as high as possible, the density ratio is only expected to rise. Using $B = 0.5$ and $DR > 2$ gives the Mach number ratio $M_j/M_\infty < 0.4$. For $M_\infty \sim 0.1 \div 0.5$, the Mach number for the coolant jet is $M_j \sim 0.04 \div 0.2$. Clearly, for these particular flow conditions, compressibility effects

Mainstream	Film hole	Plenum
$0.1 \div 0.5$	$0.04 \div 0.2$	10^{-4}

Table 2.1: Mach number estimations for film cooling geometry components.

are not important in the film cooling hole. And therefore there is no need to solve fully-compressible Naiver-Stokes equations inside the hole. If we consider the delivery plenum and try to estimate Mach number for the flow inside the plenum, we should take into account that supply plenum is usually approximated by a very large reservoir in film cooling experiments, and therefore in numerical simulations which try to match these experiments. Typical width of such a reservoir W_{plenum} is about 20 film hole diameters. Since the temperature of the coolant in the plenum and the film hole is the same, Mach number ratio M_{plenum}/M_j is equal to the velocity ratio U_{plenum}/U_j (equation (2.1)), which is in turn inversely proportional to the area ratio A_{plenum}/A_j:

$$\frac{M_{plenum}}{M_j} = \frac{U_{plenum}}{U_j} = \frac{A_j}{A_{plenum}} \sim \frac{1}{(W_{plenum}/d)^2} \sim \frac{1}{400}. \tag{2.3}$$

In other words, due to the stagnating nature of the flow inside the plenum, Mach number in the plenum is 400 times smaller than Mach number inside the film hole (giving the value of $M_{plenum} \sim 10^{-4}$) except for the regions very close to the plenum exit, where the flow accelerates rapidly due to the sharp change in cross-sectional area. Mach number estimations for all three components of film cooling geometry are summarized in Table 2.1.

The very low value of Mach number inside the plenum has certain numerical implications, which can be explained in terms of the wave speed disparity (Müller (1999)). If compressible equations are used in the regions with vanishing Mach number, the ratio of the acoustic wave speed $u + c$ to the entropy wave speed u is

$$\frac{u + c}{u} = 1 + \frac{1}{M} \to \infty \quad for \quad M \to 0, \tag{2.4}$$

For an explicit time integration the time step Δt is limited by a stability condition

$$\Delta t \leq \sigma \frac{\Delta x}{|u| + c} \to 0 \quad for \quad M \to 0, \tag{2.5}$$

where $\sigma = O(1)$ is CFL number. For implicit time-advancement the ratio of the largest and

smallest moduli of the eigenvalues of the Jacobian matrix corresponding to the wave speed ratio (equation (2.4)) is infinite, and so the matrix becomes ill-conditioned for $M \to 0$. It results in large factorization errors and lack of correct asymptotic behavior as the Mach number approaches zero (Turkel *et al.* (1994)). To remedy the situation, preconditioning can be used which changes the eigenvalues of the system of compressible flow equations in order to remove the large disparity of wave speeds. A large class of time-derivative preconditioners, when time derivatives are multiplied by a matrix that slows the speed of the acoustic waves toward the fluid speed, have been developed. The steady problems were considered by Turkel (1987), Strelets (2001), Van Leer *et al.* (1991), time-derivative preconditioners for steady-state problems is given by Turkel (1999). Several investigators have also used preconditioning for time-accurate flows (Guerra & Gustaffson (1986), Gustaffson (1987), Gustaffson & Stoor (1991), Pletcher & Chen (1993), Dailery & Pletcher (1996), Weiss & Smith (1994), Venkateswaran & Merkle (1995)). However, efficient preconditioners for unsteady Navier-Stokes equations, especially with an application to high-Reynolds number turbulent flows are still a subject of on-going research.

An alternative approach to using a single code is to develop a hybrid multi-code capability. With such an approach, each component of geometry, i.e. plenum, film cooling holes and the region exterior to the blade surface in figure 2.1, is treated with its own numerical code best suited for simulating this component individually. Different numerical codes are combined together by unsteady coupling procedure allowing for an exchange of time-dependent state information through the interfaces. As follows from the previous analysis, the use of fully-compressible code is necessary for the region above the blade surface. The best numerical code to implement in the plenum region is low Mach number code. It discretely solves low Mach number approximation to Navier-Stokes equations, where terms with the same Mach number scaling are grouped together and, so that the issue of wave speed disparity is thus avoided. Values of Mach number inside the film hole (table 2.1) are small enough for compressibility effects not to be important. Due to the similarity of geometry of film cooling hole and a plenum (both have cylindrical shape and contain internal flow) it is convenient to use the same code for approximating the flow inside the film hole as inside the plenum, i.e. low Mach number code. The use of different numerical codes for simulating different geometry components is summarized in Table 2.2.

The idea of multi-domain approach, or domain decomposition method, with an exchange of flow information through the interfaces is not new. Often complexity of geometry and difficulty in creating a single computational grid with high resolution in all the critical

Mainstream	Film hole	Plenum
Compressible code	Low Mach number code	Low Mach number code

Table 2.2: Numerical codes used for simulating different geometry components.

places leads to the splitting of a computational domain into different blocks and combining them together through the interface conditions. There are two different approaches to the domain decomposition method. In the first approach the overlapping or overset grids are used and some kind of interpolation scheme is implemented to transform the boundary values from one grid to another. Much work has been devoted to studying conservative interpolation schemes for overlapping grids (Berger (1985), Berger & Oliger (1984), Berger (1987), Chesshire & Henshaw (1994), Cali & Couaillier (2000)). Another approach uses non-overlapping computational grids, where the location of grid points is exactly matched at the interfaces (Carpenter *et al.* (1999), Manna *et al.* (2004), Abide & Viazzo (2005)). All of these studies considered the case when the set of equations solved in each sub-domain is exactly the same. Berger & Oliger (1984), Chesshire & Henshaw (1994), Carpenter *et al.* (1999) looked at hyperbolic partial differential equations; Parter (1999), Pfeiffer *et al.* (2003), Chang & Chien (2003) studied elliptic problems. Domain decomposition methods have been applied to the computation of compressible flows by Kopriva (1991), Kopriva (1994), Kopriva & Kolias (1996), Hesthaven (1997), Hesthaven (1998), Tidriri (1995), Renaud & Gauthier (1997), Nördstrom & Carpenter (1999). Incompressible flows were treated by Strikwerda & Scarbnick (1993), Manna *et al.* (2004), Manna *et al.* (2005), Abide & Viazzo (2005), Houzeaux & Codina (2004), Vereecke *et al.* (2003).

In the present methodology, however, set of partial differential equations being solved is different in different sub-domains. Coupling between numerical solutions of compressible and low Mach number equations is necessary. Due to the difference of equations in each sub-domain and, as a consequence, numerical methods used, analytical studies of the accuracy and convergence of the global solution are extremely complicated. However, the necessity for such a multi-physics multi-code approach in engineering community is emerging. With the advance in performance and capabilities of modern computers, the drive towards large-scale integrated simulations of highly complex flow systems is growing. Examples of such integrated multi-component simulations include aero-thermal flow through an entire gas turbine engine (Schlüter *et al.* (2002, 2003*a*,*b*, 2005)), hybrid unsteady simulations for helicopters etc (see, for example, McCroskey (1995) for a review of computational challenges in helicopter simulations). The different flow physics in each individual component of such

systems (compressor and turbine versus combustor in the jet engine, flow right next to the helicopter blade versus far-field flow) calls for the coupling of solvers different in nature, such as compressible/low-Mach number codes, LES/RANS and LES/URANS solvers. This area of multi-code multi-physics coupling is emerging, and not many papers have been published on this subject. In our methodology, a stable coupling procedure between compressible and low Mach number LES codes with overlapping grid technique is proposed, and can be considered as breaking new ground in this area.

This chapter is organized as follows. First, governing equations and numerical method for the compressible code are presented in section 2.2. In section 2.3 low Mach number approximation to Navier-Stokes equations is described together with the numerical implementation. LES methodology and subgrid turbulence model used in both codes is documented in section 5.5. The procedure for coupling the codes is presented in section 2.5, and numerical tests validating the accuracy and stability of the coupling procedure are shown in section 2.6.

2.2 Compressible Code

The governing equations and numerical method for the compressible code used in the current simulations are presented in this section. For all the missing details, the reader is referred to Ph.D. Thesis of Dr. Zhongmin Xiong (2004).

2.2.1 Governing Equations

System of equations governing the motion of a compressible fluid consists of continuity, momentum and energy equations. These equations can be written in the following form using Cartesian tensor notation and dimensional primitive variables (dimensional quantities are denoted with the superscript "*" throughout this manuscript)

$$\rho^*_{,t} + (\rho^* u_i^*)_{,i} = 0, \tag{2.6}$$

$$\rho^* u_{i,t}^* + \rho^* u_j^* u_{i,j}^* = -p_{,i}^* + \tau_{ij,j}^*, \quad i = 1, 2, 3, \tag{2.7}$$

$$\rho^* h_{,t}^* + \rho^* u_j^* h_{,j}^* = (p_{,t}^* + u_j^* p_{,j}^*) + q_{j,j}^* + \tau_{ij}^* u_{i,j}^*, \tag{2.8}$$

where ρ^* is the density, u_i^* is the velocity vector, p^* is the thermodynamics pressure, τ_{ij}^* is the viscous stress tensor, q_i^* is the heat flux vector and h^* is the fluid enthalpy defined by

$$h^* = e^* + p^*/\rho^*, \tag{2.9}$$

where e^* is the internal energy per unit mass. In the above equations, subscripts following by a comma denote partial differentiation with respect to the subscript, and the Einstein summation convention is used.

Newtonian fluid is assumed, so that the viscous stress tensor and the heat flux vector are given by

$$\tau_{ij}^* = 2\,\mu^*\,S_{ij}^* + \lambda^* u_{k,\,k}^*\,\delta_{ij}, \tag{2.10}$$

$$q_j^* = -k^*\,T_{,j}^*, \tag{2.11}$$

where μ^* and λ^* are the first and second coefficients of viscosity respectively, k^* is the thermal conductivity, $S_{ij}^* = \frac{1}{2}\left(u_{i,\,j}^* + u_{j,\,i}^*\right)$ is the rate-of-strain tensor, T^* is the absolute temperature and δ_{ij} is the Kronecker delta symbol.

To close the system of equations (2.6) – (2.8), an equation of state is needed which relates the thermodynamics variables

$$p^* = \rho^* R^* T^*, \tag{2.12}$$

where $R^* = c_p^* - c_v^*$ is the gas constant, c_p^* is the specific heat capacity at constant pressure and c_v^* is the specific heat capacity at constant volume. Temperatures considered in the current application are well below the oxygen vibrational temperature $\Theta_v|_{O_2} \sim 2230K$, at which vibrational degrees of freedom become excited. Therefore an approximation of a calorically perfect gas can be used, for which both c_p^* and c_v^* are constant, as is their ratio $\gamma = c_p^*/c_v^*$. Under these assumptions, the internal energy and the enthalpy are related to the absolute temperature by

$$e^* = c_v^* T^*, \tag{2.13}$$

$$h^* = c_p^* T^*. \tag{2.14}$$

To cast equations (2.6)–(A.7) into non-dimensional form, the following relations are used

$$
\begin{aligned}
\rho &= \frac{\rho^*}{\rho_r^*}, & u_i &= \frac{u_i^*}{u_r^*}, & T &= \frac{T^*}{T_r^*}, \\
p &= \frac{p^*}{\rho_r^* u_r^{*2}}, & \mu &= \frac{\mu^*}{\mu_r^*}, & \lambda &= \frac{\lambda^*}{\mu_r^*}, \\
k &= \frac{k^*}{k_r^*}, & x_i &= \frac{x_i^*}{L_r^*}, & t &= \frac{t^*}{L_r^*/u_r^*},
\end{aligned}
\tag{2.15}
$$

where the subscript r denotes the reference variables, whose particular values are defined for each given problem. Substituting relations (2.15) in (2.6)–(A.7) yields the following nondimensional form for the governing equations

$$
\rho_{,t} + (\rho\, u_i)_{,i} = 0,
\tag{2.16}
$$

$$
\rho\, u_{i,t} + \rho\, u_j\, u_{i,j} = -p_{,i} + \frac{1}{Re}[(2\,\mu\, S_{ij})_{,j} + (\lambda\, u_{j,j})_{,i}],
\tag{2.17}
$$

$$
\rho T_{,t} + \rho u_j T_{,j} + (\gamma-1)\rho T u_{j,j} = \frac{\gamma}{Pr\, Re}[kT_{,i}]_{,i} + \frac{\gamma\,(\gamma-1)\,M^2}{Re}[2\,\mu\, S_{ij}\, S_{ij} + \lambda\, S_{ii}\, S_{jj}],
\tag{2.18}
$$

$$
p = \frac{\rho\, T}{\gamma\, M^2},
\tag{2.19}
$$

where

$$
M = \frac{u_r^*}{c_r^*}, \qquad Re = \frac{\rho_r^*\, u_r^*\, L_r^*}{\mu_r^*}, \qquad Pr = \frac{\mu_r^*\, c_{pr}^*}{k_r^*},
\tag{2.20}
$$

are Mach number, Reynolds number and Prandtl number, respectively. At the derivation of the nondimensional energy equation (2.18), equation (A.7) is used to eliminate enthalpy. The continuity equation (2.6) along with the equation of state (2.12) allows to remove the explicit pressure dependence. Viscosity μ is related to the temperature through the Sutherland law

$$
\mu = T^{\frac{3}{2}}\frac{1 + S_0}{T + S_0},
\tag{2.21}
$$

where $S_0 = S_0^*/T_r^*$ and $S_0^* = 111K$ for air. The second coefficient of viscosity λ is computed using Stokes hypothesis of zero bulk viscosity, so that $\lambda = -\frac{2}{3}\mu$. The thermal conductivity k is determined assuming constant Prandtl number, so that $k = \mu$ in nondimensional variables. Fluid is assumed to be air with a Prandtl number of 0.71 and the ratio of specific heat capacities γ of 1.4.

2.2.2 Numerical Method

Time Advancement Scheme

Fully implicit, approximately-factorized second-order accurate time marching scheme is used to advance the governing equations (2.16)–(2.18) in time. A linearized dual sub-iteration scheme is employed to accelerate the convergence of sub-iterations.

To introduce an implicit time marching scheme, the governing equations (2.16)–(2.18) are first recast into a form

$$U_{,t} + F(U) = 0, \tag{2.22}$$

where $U = \{\rho, u, v, w, T\}^T$ is the vector of flow variables, $F(U)$ represents convective and viscous terms.

The second-order backward implicit Euler scheme is used for the approximation of the time derivative, so that equation (2.22) becomes

$$\frac{3U^{n+1} - 4U^n + U^{n-1}}{2\Delta t} + F(U^{n+1}) = 0. \tag{2.23}$$

To solve equation (2.23), $F(U^{n+1})$ is linearized with respect to U^n:

$$F(U^{n+1}) = F(U^n) + G(U^n)\Delta U^n + O(\Delta U^2), \tag{2.24}$$

where $G(U^n) = \partial F/\partial U^n$ is the Jacobian of $F(U^n)$ and $\Delta U^n = U^{n+1} - U^n$. Substituting (2.24) together with the expression $U^{n+1} = U^n + \Delta U^n$ into (2.23) and neglecting the second-order terms $O(\Delta U^2)$, we obtain the following equation for the unknown vector ΔU^n:

$$M(U^n)\Delta U^n = \frac{1}{3}[U^n - U^{n-1} - 2\Delta t\, F(U^n)], \tag{2.25}$$

where

$$M(U^n) = I + \frac{2\,\Delta t}{3}G(U^n). \tag{2.26}$$

Approximate Factorization

To investigate the structure of the discrete matrix $M(U^n)$, let's start with its continuous counterpart,

$$M(U) = I + \frac{2\,\Delta t}{3}G(U), \tag{2.27}$$

where $G(U) = \partial F/\partial U$ is the Jacobian of $F(U)$.

To this purpose, write the vector of convective and viscous terms $F(U)$ in a general form

$$
\begin{aligned}
F(U) \;=\;& AU_{,x} + BU_{,y} + CU_{,z} \\
-\;& V_{xx}U_{,xx} - V_{xy}U_{,xy} - V_{xz}U_{,xz} \\
-\;& V_{yy}U_{,yy} - V_{yz}U_{,yz} - V_{zz}U_{,zz},
\end{aligned}
\tag{2.28}
$$

where matrices (A, B, C, V_{ij}) are functions of U and its gradients. Then the Jacobian

$$
G(U) = \frac{\partial F}{\partial U} = \left[\frac{\partial F}{\partial U_1} \cdots \frac{\partial F}{\partial U_5} \right]
\tag{2.29}
$$

has the form

$$
\begin{aligned}
G(U) \;=\;& D + A\Delta_x + B\Delta_y + C\Delta_z \\
-\;& V_{xx}\Delta_{xx} - V_{xy}\Delta_{xy} - V_{xz}\Delta_{xz} \\
-\;& V_{yy}\Delta_{yy} - V_{yz}\Delta_{yz} - V_{zz}\Delta_{zz},
\end{aligned}
\tag{2.30}
$$

and, consequently, the matrix $M(U)$ given by expression (2.27), can be written as

$$
\begin{aligned}
M(U) = \quad I \;+\; \tfrac{2\Delta t}{3} \quad & (D + A\Delta_x + B\Delta_y + C\Delta_z \\
& -V_{xx}\Delta_{xx} - V_{xy}\Delta_{xy} - V_{xz}\Delta_{xz} \\
& -\, V_{yy}\Delta_{yy} - V_{yz}\Delta_{yz} - V_{zz}\Delta_{zz}).
\end{aligned}
\tag{2.31}
$$

Here $(\Delta_x,\ \Delta_y,\ \Delta_{xy}\ldots)$ are continuous differential operators

$$
\Delta_x = \frac{\partial}{\partial x}, \quad \Delta_y = \frac{\partial}{\partial y}, \quad \Delta_{xy} = \frac{\partial}{\partial x \partial y} \ldots,
\tag{2.32}
$$

and the matrix D is calculated as

$$
\begin{aligned}
D^k \;=\;& \partial A/\partial U_k \cdot U_{,x} + \partial B/\partial U_k \cdot U_{,y} + \partial C/\partial U_k \cdot U_{,z} \\
-\;& \partial V_{xx}/\partial U_k \cdot U_{,xx} - \partial V_{xy}/\partial U_k \cdot U_{,xy} - \partial V_{xz}/\partial U_k \cdot U_{,xz} \\
-\;& \partial V_{yy}/\partial U_k \cdot U_{,yy} - \partial V_{yz}/\partial U_k \cdot U_{,yz} - \partial V_{zz}/\partial U_k \cdot U_{,zz},
\end{aligned}
\tag{2.33}
$$

where D^k stands for the kth column of D. For an analytic expression of matrices (A, B, C, D, V_{ij}) through the flow variables for the non-dimensional equations (2.16)–(2.18) the reader is referred to Collis (1997).

When equations (2.16)–(2.18) are discretized in space, the 5×5 continuous matrix $M(U)$ becomes a discrete matrix with the size proportional to the size of the computational grid. For three-dimensional problems, discrete matrix $M(U^n)$ is a sparse matrix of the size $(N_x\, N_y\, N_z)^2$, where N_x, N_y, N_z are the number of grid points in x, y, z directions,

respectively. An exact pattern of sparsity depends on the numerical scheme used for the discretization of the first and the second spatial derivatives. Direct inversion of the matrix $M(U^n)$ in the time-advancement scheme (2.25) is, therefore, prohibitively expensive. A number of different techniques is proposed to reduce the computational cost of the inversion of this matrix. One of them is an approximate factorization technique employed in the present numerical method. Approximate factorization is used to reduce a multi-dimensional problem to a sequence of one dimensional problems in terms of the matrix inversion.

The idea of an approximate factorization is to group the differential operators which act in the same direction and to substitute the exact matrix $M(U^n)$ by its approximation, expressed as a product of an easily invertible one-dimensional matrices (Briley & McDonald (1975); Beam & Warming (1978)):

$$
\begin{aligned}
M(U^n) &\approx [I + \tfrac{2\Delta t}{3}(A\Delta_x + D - V_{xx}\Delta_{xx})] \\
&\times [I + \tfrac{2\Delta t}{3}(B\Delta_y - V_{yy}\Delta_{yy})] \\
&\times [I + \tfrac{2\Delta t}{3}(C\Delta_z - V_{zz}\Delta_{zz})] + O(\Delta t^2).
\end{aligned}
\tag{2.34}
$$

This approximation is valid to an order of Δt^2. Note that the differential operators $(\Delta_x,\ \Delta_y,\ \Delta_{xy}\ldots)$ now correspond to the discrete operators. To ensure that the factorization error $O(\Delta t^2)$ is negligible and does not corrupt the solution, a time step far smaller than that required by the time accuracy has to be used in unsteady computations.

Dual Time Stepping

To alleviate this problem, the dual time formulation is developed, where an inner iteration called sub-iteration is introduced at each physical time step of an unsteady computation (Rai (1987); Pulliam (1993)). If the sub-iteration converges, the factorization error is eliminated. To achieve that, the new pseudo time-derivative $U_{,\tau}$, where τ is the pseudo time variable, is added to the equation (2.23)

$$
U_{,\tau} + \frac{3U^{n+1} - 4U^n + U^{n-1}}{2\Delta t} + F(U^{n+1}) = 0.
\tag{2.35}
$$

When (2.35) reaches the steady-state, $U_{,\tau} = 0$, equation (2.23) is recovered. Introducing a sub-iteration index k and approximating $U_{,\tau}$ by the first-order backward Euler scheme

$$
U_{,\tau} = \frac{U^{k+1} - U^k}{\Delta \tau},
\tag{2.36}
$$

equation (2.35) becomes

$$\Delta U^k + \frac{\Delta\tau}{2\Delta t}(3U^{n+1} - 4U^n + U^{n-1}) + \\ \Delta\tau G\left(U^n\right)\Delta U^n = -\Delta\tau F(U^n),$$

(2.37)

where $\Delta\tau$ is an appropriately chosen pseudo time step for sub-iteration and $\Delta U^k = U^{k+1} - U^k$. Replacing $n+1$ by $k+1$ and performing some reorganization, which can be found in Xiong (2004), the following equation is obtained

$$[I + \frac{3\Delta\tau}{2\Delta t}I + \Delta\tau G\left(U^n\right)]\Delta U^k = -\Delta\tau \mathcal{R}^{\,k},$$

(2.38)

where

$$\mathcal{R}^{\,k} = \frac{3U^k - 4U^n + U^{n-1}}{2\Delta t} + F(U^k).$$

(2.39)

For each physical time step , U^n is taken to be the initial value for U^k with $k = 0$ to start the sub-iteration. When sub-iteration converges, $\Delta U^k \to 0$, and hence $U^{k+1} = U^k$. The final value of U^{k+1} can then be taken as U^{n+1} and $\mathcal{R}^{n+1} = 0$ recovers the second-order fully implicit scheme in (2.23). Using approximate factorization technique for the equation (2.38), the following factorized iteration scheme is obtained

$$[S + \Delta\tau(A\Delta_x + D - V_{xx}\Delta_{xx})]\mathcal{P} = -\Delta\tau\mathcal{R}^k,$$

(2.40)

$$[S + \Delta\tau(B\Delta_y - V_{yy}\Delta_{yy})]\mathcal{Q} = S\mathcal{P},$$

(2.41)

$$[S + \Delta\tau(C\Delta_z - V_{zz}\Delta_{zz})]\Delta U^k = S\mathcal{Q},$$

(2.42)

where

$$S \equiv I + \frac{3\Delta\tau}{2\Delta t}I.$$

(2.43)

Since the left hand side operator in (2.38) is only a function of U^n, it is possible to perform an LU decomposition of the coefficient matrices in (2.40)–(2.42) at the first sub-iteration step, store the factored matrices and use them throughout until the sub-iteration converges. It significantly improves the sub-iteration efficiency.

Spatial Discretization

Although a flat surface is used in the current simulations, the present compressible code has a capability of calculating flows around curvilinear surfaces using body-fitted meshes.

This capability also allows to cluster points in the regions of high spatial gradients. To achieve that, the physical domain (x, y, z) is transformed into a computational domain (ξ, η, z) using a two dimensional mapping $(x, y) \mapsto (\xi, \eta)$, where ξ and η belong to $[0, 1]$. The grid in spanwise direction, z, is assumed to be homogeneous with uniform node spacing. Distribution of grid points in the computational domain is also uniform: $\xi_i = \Delta\xi(i-1)$ for $1 \leq i \leq N_\xi$ and $\eta_j = \Delta\eta(j-1)$ for $1 \leq j \leq N_\eta$. The following derivative operators are used for approximating first and second derivatives $\frac{\partial f}{\partial \xi}$ and $\frac{\partial^2 f}{\partial \xi^2}$ (only ξ direction is presented since the differencing schemes are analogous in η and z directions). An interior points, the fourth-order accurate central difference scheme is employed

$$\left(\frac{\partial f}{\partial \xi}\right)_i = \frac{1}{12\Delta\xi}[(f_{i-2} - f_{i+2}) - 8(f_{i-1} - f_{i+1})], \tag{2.44}$$

$$\left(\frac{\partial^2 f}{\partial \xi^2}\right)_i = \frac{1}{12(\Delta\xi)^2}[-(f_{i-2} - 2f_i + f_{i+2}) + 16(f_{i-1} - 2f_i + f_{i+1})]. \tag{2.45}$$

Near the computational boundaries, the finite difference stencil needs to be biased towards the interior. Although different boundary closures can generally be proposed, including the stencils which satisfy summation by parts (SBP) property (Carpenter *et al.* (1999); Nördstrom & Carpenter (1999); Mattson *et al.* (2005)), in implicit methods it is important to keep the coefficient matrices (2.40)–(2.42) easy to invert, which influences the choice of the boundary scheme. As in the interior points, a five point stencil is used in the present numerical method at the boundary grid point ξ_1 and at the second grid point ξ_2. The resulting difference schemes are fourth and third order accurate for the first and second derivatives respectively. For the first grid point ξ_1 they are

$$\left(\frac{\partial f}{\partial \xi}\right)_1 = \frac{1}{12\Delta\xi}[-25f_1 + 48f_2 - 36f_3 + 16f_4 - 3f_5], \tag{2.46}$$

$$\left(\frac{\partial^2 f}{\partial \xi^2}\right)_1 = \frac{1}{12(\Delta\xi)^2}[11f_1 - 20f_2 + 6f_3 + 4f_4 - f_5], \tag{2.47}$$

and for the second grid point ξ_2 they become

$$\left(\frac{\partial f}{\partial \xi}\right)_2 = \frac{1}{12\Delta\xi}[-3f_1 - 10f_2 + 18f_3 - 6f_4 + f_5], \tag{2.48}$$

$$\left(\frac{\partial^2 f}{\partial \xi^2}\right)_2 = \frac{1}{12(\Delta\xi)^2}[35f_1 - 104f_2 + 11f_3 - 56f_4 + 11f_5]. \tag{2.49}$$

Similar expressions hold for the derivatives at nodes $N_\xi - 1$ and N_ξ but with the stencils reversed and the signs switched on the coefficients for the first derivative.

After the derivatives are obtained in the computational space, they are transformed to the physical space through the metrics of the mapping function. For the first derivatives the transformation is

$$\left\{ \begin{array}{c} \frac{\partial}{\partial x} \\ \frac{\partial}{\partial y} \end{array} \right\} = \left[\begin{array}{cc} \xi,_x & \eta,_x \\ \xi,_y & \eta,_y \end{array} \right] \left\{ \begin{array}{c} \frac{\partial}{\partial \xi} \\ \frac{\partial}{\partial \eta} \end{array} \right\}, \tag{2.50}$$

and for the second derivatives

$$\left\{ \begin{array}{c} \frac{\partial^2}{\partial x^2} \\ \frac{\partial^2}{\partial x \partial y} \\ \frac{\partial^2}{\partial y^2} \end{array} \right\} = \left[\begin{array}{ccc} (\xi,_x)^2 & 2\,\xi,_x\,\eta,_x & (\eta,_x)^2 \\ \xi,_x\,\xi,_y & \xi,_x\,\eta,_y + \xi,_y\,\eta,_x & \eta,_x\,\eta,_y \\ (\xi,_y)^2 & 2\,\xi,_y\,\eta,_y & (\eta,_y)^2 \end{array} \right] \left\{ \begin{array}{c} \frac{\partial^2}{\partial \xi^2} \\ \frac{\partial^2}{\partial \xi \partial \eta} \\ \frac{\partial^2}{\partial \eta^2} \end{array} \right\} + \left[\begin{array}{cc} \xi,_{xx} & \eta,_{xx} \\ \xi,_{xy} & \eta,_{xy} \\ \xi,_{yy} & \eta,_{yy} \end{array} \right] \left\{ \begin{array}{c} \frac{\partial}{\partial \xi} \\ \frac{\partial}{\partial \eta} \end{array} \right\}, \tag{2.51}$$

where $(\xi,_x, \eta,_x, \ldots)$ are metrics of the mapping transformation. Implicit iterative scheme (2.40)–(2.42) in computational space will take the following form

$$[S + \Delta\tau(\check{A}\Delta_\xi + \check{D} - \check{V}_{\xi\xi}\Delta_{\xi\xi})]\mathcal{P} = -\Delta\tau\mathcal{R}^k, \tag{2.52}$$

$$[S + \Delta\tau(\check{B}\Delta_\eta - \check{V}_{\eta\eta}\Delta_{\eta\eta})]\mathcal{Q} = S\mathcal{P}, \tag{2.53}$$

$$[S + \Delta\tau(\check{C}\Delta_z - \check{V}_{zz}\Delta_{zz})]\Delta U^k = S\mathcal{Q}, \tag{2.54}$$

where matrices $(\check{A}, \check{B}, \check{C}, \check{D}, \check{V}_{ij})$ are obtained from matrices (A, B, C, D, V_{ij}) as

$$\check{A} = \xi,_x A + \xi,_y B + \xi,_{xx} V_{xx} + \xi,_{xy} V_{xy} + \xi,_{yy} V_{yy} \tag{2.55}$$

and so on. $(\Delta_\xi, \Delta_\eta, \Delta_{\xi\eta} \ldots)$ are differential operators in the computational space. With the above forth-order discretization scheme, the left hand side in each of the equations (2.52)–(2.54) is a block penta-diagonal matrix (see the structure in figure 2.3) with additional blocks at the boundary nodes to account for the high order boundary treatment. Each block is a 5×5 matrix for the five flow variables. The resulting coefficient matrix can be inverted efficiently using direct Gaussian elimination method.

Since subiteration is a steady-state problem, the pseudo time step $\Delta\tau$ can be allowed to vary spatially in order to accelerate the subiteration convergence. Taking into account the physical domain of dependence within a computational cell, $\Delta\tau$, in a general curvilinear coordinates, is chosen by

$$\Delta\tau = CFL\frac{\Delta\xi\Delta\eta}{\Lambda}, \tag{2.56}$$
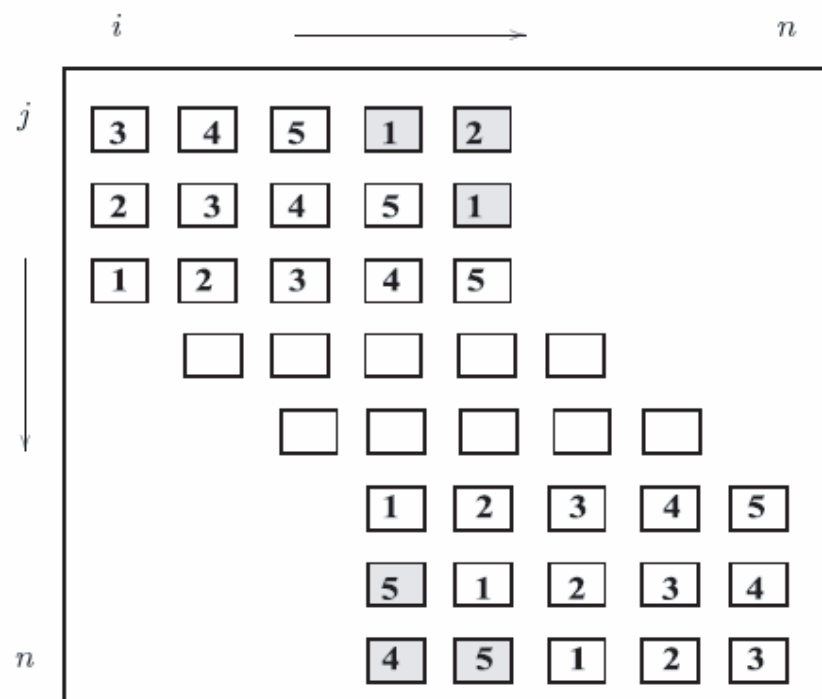
Figure 2.3: The structure of block penta-diagonal coefficient matrix resulting from implicit fourth-order finite difference scheme. Each block is a 5×5 matrix.

where

$$\Lambda = |J_{1i}\bar{u}_i|\Delta\eta + |J_{2i}\bar{u}_i|\Delta\xi + \\ \bar{c}\,[(J_{11}^2 + J_{12}^2)\Delta\eta^2 + (J_{21}^2 + J_{22}^2)\Delta\xi^2]^{1/2}. \tag{2.57}$$

In this expression J is the Jacobian of the mapping and $\bar{c}$ is the local speed of sound. This definition of Λ includes the convective and acoustic phenomena but ignores the viscous diffusion. A similar expression can be derived to include viscous effects, but the equation (C.12) was found to be adequate for accelerating convergence to the steady state. The CFL number in (2.56) is specified using a uniform physical time step Δt for unsteady computations which is independent of $\Delta\tau$ and reflects the time resolution requirement for the physical process of interest.

Boundary Conditions

Boundary conditions are needed to provide the solution at the boundary points, which corresponds to the inflow, outflow, top and bottom boundaries of the computational domain.

In the implicit solver, boundary conditions are required in terms of δU. Consider an arbitrary flow constraint, at time level $n+1$, on the flow variable $U_k,\ k=1,5$

$$g_k(U^{n+1}) = 0, \tag{2.58}$$

which is some function, possibly nonlinear, of the primitive variables at time step $n+1$. Linearizing the equation (2.58) with respect to U^n, we get

$$\left(\frac{\partial g_k}{\partial U_i}\right)^n \delta U_i = -g_k(U_i^n), \tag{2.59}$$

where $\delta U_i = U_i^{n+1} - U_i^n$. Equation (2.59) is used at the boundary point in place of discretized equations of motions for the constraint quantity Therefore, to specify implicit boundary conditions for the flow variable U_k, we need to define a constraint, g_k, and the variation of the constraint, δg_k

$$\delta g_k \equiv \left(\frac{\partial g_k}{\partial U}\right)_i \delta U_i \tag{2.60}$$

For example, consider the application of the boundary condition on the streamwise velocity component, $u = u_s$, where u_s is some specified value for the time $n+1$. Then the flow constraint (2.58) looks like

$$g_u(U^{n+1}) = u - u_s = 0, \tag{2.61}$$

the variation of the constraint (2.60)

$$\delta g_u = \delta u \qquad (2.62)$$

and the equation (2.59) representing the boundary condition for δu becomes

$$\delta u = -g_u = -(u - u_s) = 0. \qquad (2.63)$$

We now describe boundary conditions applied at the different boundaries of the computational domain.

At the wall, the no-slip boundary conditions $u_i = 0$, $i = 1, 3$ are used for the three velocity components. Either isothermal, $T = T_w$, or adiabatic, $\partial T/\partial n = 0$, boundary conditions are formulated for the temperature depending on the problem. For the body orthogonal meshes used here, an adiabatic condition can be written in computational space as $(\partial T/\partial \eta)|_{\eta=0} = 0$ and the derivative is approximated by a fourth-order one-sided difference (2.46). Density at the wall is determined using continuity equation.

At the inflow, boundary conditions are based on the locally one-dimensional Riemann invariants. According to characteristics analysis, for a subsonic inflow, four incoming quantities must be specified along with one outgoing quantity computed from the interior domain. The specific choice of these quantities depend on the formulation of particular problem. In the current method, we constraint the entropy, spanwise and tangential velocities, and the incoming Riemann invariant. The outgoing Riemann invariant is computed by first-order extrapolation from points in the interior, adjacent to the boundary. The locally one-dimensional Reimann invariants are defined in the direction normal to the inflow boundary as

$$R_1 = v_n - \frac{2c}{\gamma - 1}, \quad R_2 = v_n + \frac{2c}{\gamma - 1}, \qquad (2.64)$$

where c is the local speed of sound and v_n is the velocity normal to the boundary. Hence, at the inflow boundary

$$s = s_{in}, \ w = w_{in}, \ v_t = v_{in},$$
$$R_1 = R_{1\,in}, \ R_2 = R_{2\,out}, \qquad (2.65)$$

where v_t is the velocity tangential to the boundary. Here the subscript "*in*" refers to the incoming quantities, which, for the turbulent inflow, are the sum of the mean and fluctuating components. The subscript "*out*" refers to the outgoing quantities extrapolated from the interior, thus $R_{2\,out}$ is computed from the interior domain by linear extrapolation. Numerical

experiments show that higher order extrapolations are unstable (see Collis (1997)). Once the Riemann invariants are computed, the values of v_n and c at the boundary are obtained

$$v_n = \frac{1}{2}(R_{1\,in} + R_{2\,out}), \quad c = \frac{\gamma - 1}{4}(R_{2\,out} - R_{1\,in}). \tag{2.66}$$

If we define entropy as $s^* = T^*/(\rho^*)^{\gamma-1}$ and non-dimensional entropy as

$$s = \frac{s^*}{T_r^*/(\rho_r^*)^{\gamma-1}}, \tag{2.67}$$

then density and temperature can be computed as

$$T = (M\,c)^2, \quad \rho = \left(\frac{T}{s_{in}}\right)^{\frac{1}{\gamma-1}}. \tag{2.68}$$

The non-dimensional expressions $s = T/\rho^{\gamma-1}$ and $c = \sqrt{T}/M$ are used while deriving (2.68).

Riemann invariant formulation is also used at the top boundary for boundary layer and film cooling simulations with box-type domain. However, since positive vertical velocity exists at the top boundary, this will correspond to the subsonic outflow. Only one quantity, the first Riemann invariant $R_1 = v_n - 2\,c/(\gamma-1)$, is specified as incoming. Entropy, spanwise and tangential velocities, as well as the second Riemann invariant $R_2 = v_n + 2\,c/(\gamma-1)$ are extrapolated from the interior. At the outflow, the parabolized Navier-Stokes equations are solved (see Collis (1997)), i.e. the streamwise second-order derivatives in the equations are neglected. The streamwise pressure gradient is estimated a priori and treated as a source term in the equations. This treatment is found to yield an adequate and stable outflow boundary conditions for the laminar mean flow and turbulent calculations. In spanwise direction, periodic boundary conditions are imposed in the present study. Boundary conditions used at the interfaces with low-Mach number code when coupling is employed are discussed in section 2.3. Present numerical method is validated for steady computations using self-similar analytic solutions for compressible laminar boundary layer over a flat plate with and without heat transfer. The details of the numerical tests are described in appendix A.

Artificial Dissipation

Numerical method described above uses fourth-order central difference discretization for spatial terms. Because of its symmetric stencil, central-difference scheme is non-dissipative,

unlike numerical schemes with biased stencils, such as upwind schemes. The lack of numerical dissipation can result in numerical instability due to the generation of unresolved high wave number components by nonlinear flow interactions, especially when simulating turbulent flows. In order to damp these unresolved components, a fourth-order artificial dissipation is introduced by adding the following term to the right-hand side of Navier-Stokes equations

$$D = -\sigma_d\left(\xi, \eta,\, z,\, t\right)\left(\Delta\,\xi^4\frac{\partial^4 U}{\partial\,\xi^4} + \Delta\,\eta^4\frac{\partial^4 U}{\partial\,\eta^4} + \Delta\,z^4\frac{\partial^4 U}{\partial\,z^4}\right), \tag{2.69}$$

where $U = \{\rho, u, v, w, T\}^T$ is the vector of flow variables and $\sigma_d\left(\xi, \eta,\, z,\, t\right)$ is the coefficient, which controls the amount of the added dissipation. The regions, where high wave number components are generated and artificial dissipation is required, are not fixed in space and time, but depend on the local state of the flow. To make sure that the model removes the energy from wave numbers close to the Nyquist wavenumber without corrupting the remaining flow, a special form for the coefficient $\sigma_d\left(\xi, \eta,\, z,\, t\right)$ is proposed, proportional to the high-order derivatives of the local strain rate. It imparts spectral-like behavior to the model, thus eliminating the need for *ad hoc* limiters to reduce the value of the coefficient σ_d in smooth regions. In multiple dimensions it can be written as

$$\sigma_d\left(\xi, \eta,\, z,\, t\right) = \epsilon_d\,\Delta^{r+1}\,\overline{|\nabla^r\,|S|\,|}, \tag{2.70}$$

where ϵ_d is the model constant, $\Delta = (\Delta\,\xi\,\Delta\,\eta\,\Delta\,z)^{1/3}$ is the local grid spacing, $|S| = (S_{ij}\,S_{ij})^{1/2}$ is the magnitude of the rate of strain tensor and ∇^r is the polyharmonic operator which defines a sequence of Laplacians. For example, $r = 2$ corresponds to a single Laplacian $\nabla^2\,|S|$, $r = 4$ leads to the biharmonic operator $\nabla^4\,|S| = \nabla^2(\nabla^2|S|)$ and so on. The overbar $(\overline{f})$ denotes a truncated-Gaussian filter, defined as

$$\overline{f}(\mathbf{x}) = \int_{-L}^{L} G\left(|\mathbf{x} - \mathbf{x}'|; L\right) f(\mathbf{x}')\,d^3\mathbf{x}', \tag{2.71}$$

where

$$G(\mathbf{x}'; L) = \frac{e^{-6\,\mathbf{x}'^2/L^2}}{\int_{-L}^{L} e^{-6\,\mathbf{x}'^2/L^2}d^3\mathbf{x}'}, \quad L = 4\,\Delta. \tag{2.72}$$

This filter eliminates cusps introduced by the absolute value operator in (2.70), which, in turn, ensures that the value of σ_d is positive, and the added terms (2.69) perform stabilizing

function. In the present work, equation (2.72) is approximated along each grid line as

$$
\begin{aligned}
\overline{f}_j = {} & \tfrac{3565}{10,368} f_j + \tfrac{3091}{12,960}(f_{j-1} + f_{j+1}) + \tfrac{1997}{25,920}(f_{j-2} + f_{j+2}) + \tfrac{149}{12,960}(f_{j-3} + f_{j+3}) \\
& + \tfrac{107}{103,680}(f_{j-4} + f_{j+4})
\end{aligned}
\tag{2.73}
$$

with modified stencil at the boundaries and periodicity in z-direction. The transfer function associated with this filter closely matches a Gaussian. The value $r = 2$ is used in the present simulations, $\epsilon_d = 0.025$ is set for the model coefficient.

The formulation (2.70) for the artificial dissipation coefficient σ_d in equation (2.69) is inspired by the hyperviscosity model proposed by Cook & Cabot (2004, 2005) for simulating turbulent flows with shocks and extended by Fiorina & Lele (2005) to account for high temperature and species gradients. However, in spite of the seeming similarity, the model proposed here and the models described in Cook & Cabot (2004, 2005) and Fiorina & Lele (2005) are inherently different. Hyperviscosity model of Cook & Cabot (2004, 2005) introduces a correction to molecular viscosity and thus modifies the viscous stresses, entering momentum and energy equations. Adding artificial viscosity to the molecular viscosity is similar in nature to an idea of introducing turbulent viscosity to account for increased mixing in turbulent flows, although the details of the modeling and the meaning of these two viscosities is different. Artificial diffusivity based on the high-order derivatives of entropy proposed by Fiorina & Lele (2005) also takes the form of the gradient diffusion terms added to the mass and species transport equation. Artificial dissipation (2.69) introduced in the present method is proportional to the fourth order derivatives, rather than the second order derivatives in diffusion-type terms, and assumes the same form and the same value of the coefficient σ_d for each of the governing equations.

2.3 Low Mach Number Code

The governing equations and numerical method for the low Mach number code used in the current simulations are presented in this section. For all the missing details, the reader is referred to Ph.D. Thesis of Dr. Charles D. Pierce (2001).

2.3.1 Governing Equations

The conservation laws of mass, momentum and energy in a general case of a compressible viscous fluid are stated in section 2.2.1 (equations (2.6)–(A.7)). When normalized with the relations (2.15), these equations take the non-dimensional form (2.16)–(2.19). If Mach

number M becomes very low, the non-dimensional pressure given by equation (2.19), $p = \rho\, T/\gamma\, M^2$, grows infinitely large. Therefore, this normalization fails in a very low Mach number limit. To remedy the situation, we can employ different normalization for pressure, simply

$$p = \frac{p^*}{p_r^*}, \tag{2.74}$$

where p_r^* is some reference pressure. With the relation (2.74) for non-dimensional pressure and relations (2.15) for all other variables, equations (2.16)–(2.19) transform into

$$\rho_{,t} + (\rho\, u_i)_{,i} = 0, \tag{2.75}$$

$$\rho\, u_{i,t} + \rho\, u_j\, u_{i,j} = -\frac{1}{\tilde{M}^2} p_{,i} + \frac{1}{Re}[(2\,\mu\, S_{ij})_{,j} + (\lambda\, u_{j,j})_{,i}], \tag{2.76}$$

$$\rho T_{,t} + \rho u_j T_{,j} + (\gamma-1)\rho T u_{j,j} = \frac{\gamma}{Pr\, Re}[k\, T_{,i}]_{,i} + \frac{(\gamma-1)\,\tilde{M}^2}{Re}[2\,\mu\, S_{ij}\, S_{ij} + \lambda\, S_{ii}\, S_{jj}], \tag{2.77}$$

$$p = \rho\, T, \tag{2.78}$$

where $\tilde{M} = \sqrt{\gamma}\, M$ is introduced to avoid the dependence on γ. All nondimensional flow quantities now remain of order $O(1)$ for any low reference Mach number.

To arrive at low Mach number approximation of the equations (2.75)–(2.78), an asymptotic analysis is used, where all flow variables are expanded in the power series of $\tilde{M}$, as for example the pressure

$$p\,(\mathbf{x}, t, \tilde{M}) = p^{(0)}\,(\mathbf{x}, t) + \tilde{M}\, p^{(1)}\,(\mathbf{x}, t) + \tilde{M}^2\, p^{(2)}\,(\mathbf{x}, t) + O\,(\tilde{M}^3), \tag{2.79}$$

where $p^{(0)}$, $p^{(1)}$, $p^{(2)}$ are zeroth, first and second order pressure, respectively. These expansions are then substituted back into the governing equations (2.75)–(2.78). The terms are reordered according to the powers of $\tilde{M}$, and coefficients of the monomials $\tilde{M}^l$, $l = 0, 1, 2, ...$ are set to zero. Skipping all further details of the derivation, which are given, for example, in Lele (1998), Müller (1999), we state zeroth-order Navier-Stokes equations, $l = 0$, in the low Mach number limit

$$\rho_{,t}^{(0)} + (\rho^{(0)}\, u_i^{(0)})_{,i} = 0, \tag{2.80}$$

$$\rho^{(0)}\, u_{i,t}^{(0)} + \rho^{(0)}\, u_j^{(0)}\, u_{i,j}^{(0)} = -p_{,i}^{(2)} + \frac{1}{Re}[(2\,\mu^{(0)}\, S_{ij}^{(0)})_{,j} + (\lambda^{(0)}\, u_{j,j}^{(0)})_{,i}], \tag{2.81}$$

$$\rho^{(0)}\, T_{,t}^{(0)} + \rho^{(0)}\, u_j^{(0)}\, T_{,j}^{(0)} = \frac{1}{Pr\, Re}[k^{(0)}\, T_{,i}^{(0)}]_{,i} + \frac{\gamma-1}{\gamma}\frac{d\,p^{(0)}}{d\,t}. \tag{2.82}$$

$$p^{(0)}(t) = \rho^{(0)}(\mathbf{x}, t) \, T^{(0)}(\mathbf{x}, t). \tag{2.83}$$

where the following relation was used to eliminate the divergence of velocity in the energy equation (2.82)

$$u_{j,j}^{(0)} = \frac{1}{\gamma \, \rho^{(0)} \, T^{(0)}} \left[\frac{\gamma}{Pr \, Re} [k^{(0)} \, T_{,i}^{(0)}]_{,i} - \frac{d \, p^{(0)}}{d \, t} \right]. \tag{2.84}$$

It is worth noting that the second order pressure $p^{(2)}$ appears in the equations of motion (2.80)–(2.83), while the first order pressure $p^{(1)}$ drops out. Another observation is that the zeroth order pressure $p^{(0)}$ is only a function of time, but it is constant in space. Therefore, the overall pressure $p(\mathbf{x}, t)$ has an asymptotic expansion

$$p(\mathbf{x}, t, \tilde{M}) = p^{(0)}(t) + \tilde{M}^2 \, p^{(2)}(\mathbf{x}, t) + O(\tilde{M}^3). \tag{2.85}$$

Zeroth-order pressure $p^{(0)}(t)$ plays the role of a thermodynamic pressure, whereas second-order pressure $p^{(2)}(\mathbf{x}, t)$ is decoupled from the density and temperature. Its role is similar to the pressure in incompressible flow: the divergence of the momentum equation (2.81) yields a Poisson equation for the second-order pressure $p^{(2)}$. However, as opposed to incompressible equations, the momentum and energy equations are coupled in the low Mach number approximation (2.80)–(2.83) through the density $\rho^{(0)}$ and the equation of state. This coupling is more involved than the coupling via buoyancy term in the Boussinesq equations, which are only valid for small density and temperature variations (Rehm & Baum (1978)). To the contrary, low Mach number equations admit large density and temperature variations.

Finally, casting the equations (2.80)–(2.83) into a conservation form and restricting our attention to the flows, where the thermodynamic pressure $p^{(0)}$ is constant in time, as well as in space (this is valid, when the total heat conduction and heat release rate $\int_V Q^{(0)} \, dV$, $Q^{(0)} = [k^{(0)} \, T_{,i}^{(0)}]_i + \rho^{(0)} \, q^{(0)}$, $q^{(0)}$ is the nondimensional heat release rate, and the volume flow $\int_{\partial V} \mathbf{u}^{(0)} \cdot \mathbf{n} \, dA$ are zero in the computational domain, see Müller (1999)), we get the working set of equations for the present low Mach number code:

$$\rho_{,t} + (\rho \, u_i)_{,i} = 0, \tag{2.86}$$

$$(\rho \, u_i)_{,t} + (\rho \, u_j \, u_i)_{,j} = -p_{,i}^{(2)} + \frac{1}{Re} [(2 \, \mu \, S_{ij})_{,j} + (\lambda \, u_{j,j})_{,i}], \tag{2.87}$$

$$(\rho \, T)_{,t} + (\rho \, u_i \, T)_{,i} = \frac{1}{Pr \, Re} [k \, T_{,i}]_{,i}, \tag{2.88}$$
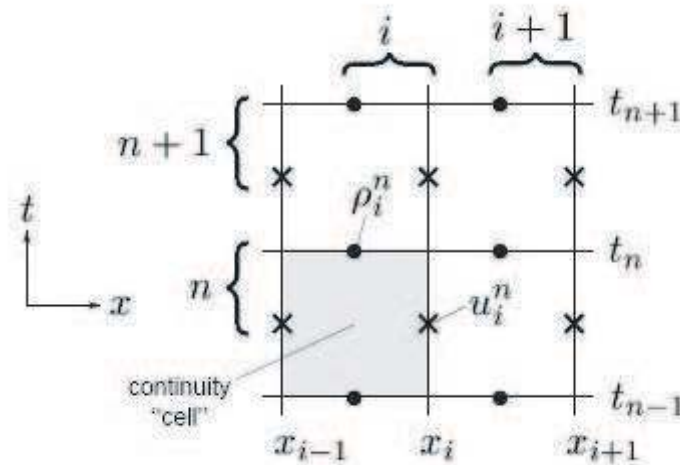
Figure 2.4: Schematics of a staggered space-time mesh.

$$p^{(0)} = \rho \, T. \tag{2.89}$$

Superscript denoting the order of the variable is dropped here for all the quantities, except for the pressure. So, all the variables without a superscript in the equations (2.86)–(2.89) are zeroth order by default.

2.3.2 Numerical Method

Spatial Discretization

In the present numerical method, velocity components are staggered with respect to the density and other scalars in both space and time (Harlow & Welch (1965)). Density and velocities are placed at the space-time mesh around the "continuity cells", in their natural positions based on their respective roles in the continuity equation (see figure 2.4). Temperature and pressure are collocated with the density. By convention, variables defined on the cell faces oriented in a positive coordinate direction are assigned the same indices as the cell (see figure 2.4).

Second-order central-difference discretization is used in the present method. To keep the notation compact, let us introduce the interpolation operators

$$\bar{u}^x|_{i,j} = \frac{u_{i+1/2,j} + u_{i-1/2,j}}{2}, \quad \bar{u}^y|_{i,j} = \frac{u_{i,j+1/2} + u_{i,j-1/2}}{2} \tag{2.90}$$

and the second-order differencing operators

$$\delta_x\left(u\right)|_{i,j} = \frac{u_{i+1/2,j} - u_{i-1/2,j}}{\Delta x}, \quad \delta_y\left(u\right)|_{i,j} = \frac{u_{i,j+1/2} - u_{i,j-1/2}}{\Delta y}. \tag{2.91}$$

In order to discretize governing equations (2.86)–(2.88), it is convenient to work with the mass flux g_i (or momentum per unit volume), given by

$$g_i = \overline{\overline{\rho}^{\,x_i}}^{\,t} u_i, \tag{2.92}$$

and, conversely,

$$u_i = g_i / \overline{\overline{\rho}^{\,x_i}}^{\,t}. \tag{2.93}$$

Then, equations (2.86)–(2.88) take the following discrete form (note that interpolation operators do not follow the summation convention)

$$\delta_t\left(\rho\right) + \delta_{x_i}\left(g_i\right) = 0, \tag{2.94}$$

$$\delta_t\left(g_i\right) + \delta_{x_j}\left(\overline{\overline{g_j}^{\,x_i}}^{\,t}\,\overline{\overline{u_i}^{\,x_j}}^{\,t}\right) = -\delta_{x_i}(p^{(2)}) + \delta_{x_j}(\tau_{ij}), \tag{2.95}$$

$$\delta_t\left(\rho\,T\right) + \delta_{x_i}\left(g_i\,\overline{\overline{T}^{\,x_i}}^{\,t}\right) = \delta_{x_i}\left[\overline{\overline{k}^{\,x_i}}^{\,t}\delta_{x_i}(\overline{T}^{\,t})\right], \tag{2.96}$$

where

$$\tau_{ij} = \begin{cases} \overline{\overline{\mu}^{\,x_i}}^{\,x_j}\left[\delta_{x_j}(\overline{u_i}^{\,t}) + \delta_{x_i}(\overline{u_j}^{\,t})\right], & i \neq j \\ 2\,\mu\left[\delta_{x_j}(\overline{u_i}^{\,t}) - \frac{1}{3}\,\delta_{x_k}(\overline{u_k}^{\,t})\right], & i = j \end{cases} \tag{2.97}$$

for $\lambda = -2/3\,\mu$.

Central-difference discretization described above is known to be vulnerable to the formation of spatial oscillations or "wiggles" due to dispersion errors. This can be especially problematic when the advection of scalar is considered, since the central-difference scheme can cause a scalar to disperse in unphysical ways, including the propagation of oscillations into the regions where the scalar is supposed to be uniform. To alleviate this problem, an upwind biased scheme was adopted in the present method for the scalar advection only. While upwind schemes are detrimental when used for the computation of turbulent velocity fields due to their damping effect on the turbulence spectra (Mittal & Moin (1997)), their deleterious effects on scalar advection are relatively minor, because scalar transport is linear (no scale interaction), and thus, the damping of small scales does not effect the dynamics of the large scales. The present method uses the QUICK scheme (Leonard (1979)), which replaces the two-point interpolation (2.90) with an upwinded, three-point interpolation to
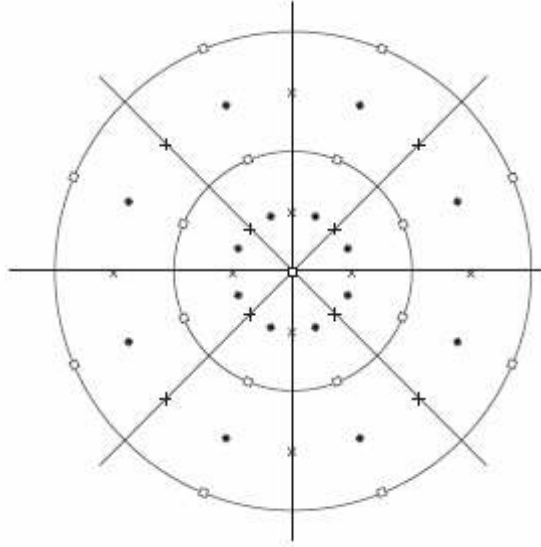
Figure 2.5: Staggered grid in cylindrical coordinates. $\bullet$: ρ, P, T, u_x; $\times$: u_θ; $\square$: u_r.

the cell face when computing scalar advective fluxes, resulting in a five-point stencil overall.

Cylindrical Coordinates

In the present study, the governing equations are solved in cylindrical coordinates to simulate the cylindrical geometry of the film-cooling supply hole. The coordinates x, r and θ correspond to the axial, radial and azimuthal directions, respectively. A schematic of the grid is shown in figure 2.5. The reader is referred to Pierce (2001) for the exact form of discrete equations (2.94)–(2.97) in cylindrical coordinates.

The centerline treatment used in this work is described below. It is clear from the figure 2.5 that all quantities except for u_r are staggered in the radial direction with respect to the centerline (i.e., they are located at $\Delta r/2$ from the centerline), while u_r itself is collocated with the centerline. Therefore, centerline conditions are only needed for u_r and $f_{\theta r}$ (the flux in radial direction entering the momentum equation for u_θ, see (Pierce (2001)). Derivatives of quantities that are staggered with respect to the centerline can be obtained by differencing opposing values across the centerline, accounting for reversals in the directions of the radial and azimuthal unit vectors through the centerline (Mohseni & Colonius (2000)). Centerline boundary conditions for u_r and $f_{\theta r}$ are obtained by averaging correspoding values across

the centerline (Akselvoll & Moin (1995)):

$$u_r\left(r=0,\,\theta\right) = \frac{1}{2}\left[u_r\left(\Delta r,\,\theta\right) + u_r\left(\Delta r,\,\theta + \pi\right)\right]. \tag{2.98}$$

Time Advancement Scheme

The semi-implicit, iterative solution procedure is used to advance discrete equations (2.94)–(2.97) in time. The time-advancement scheme is similar to the Crank-Nicolson or trapezoidal scheme, but the right-hand sides are evaluated using variables that have been interpolated in time to the midpoints between the solution at times t^n and t^{n+1}. In terms of a single ordinary differential equation,

$$\frac{d\,u}{d\,t} = f\left(u\right), \tag{2.99}$$

the time discretization may be written as

$$\frac{u^{n+1} - u^n}{\Delta t} = f\left[\frac{1}{2}(u^n + u^{n+1})\right]. \tag{2.100}$$

For linear $f\left(u\right)$, this is identical to the trapezoidal scheme. For nonlinear $f\left(u\right)$, implicit equation (2.100) can be solved using Newton-Raphson iterations. Let u_k^{n+1} be the kth iterative approximation to u^{n+1}. Then, applying Newton-Raphson iteration method to (2.100), one obtains

$$u_{k+1}^{n+1} = u^n + \Delta t\, f\left[\frac{1}{2}(u^n + u_k^{n+1})\right] + \frac{1}{2}\Delta t\left[\frac{\partial f}{\partial u}\right](u_{k+1}^{n+1} - u_k^{n+1}), \tag{2.101}$$

with initial guess

$$u_0^{n+1} = u^n. \tag{2.102}$$

This can also be expressed in "delta" or residual form,

$$\left[1 - \frac{1}{2}\Delta t\frac{\partial f}{\partial u}\right](u_{k+1}^{n+1} - u_k^{n+1}) = u^n + \Delta t\, f\left[\frac{1}{2}(u^n + u_k^{n+1})\right] - u_k^{n+1}. \tag{2.103}$$

If the Jacobian $\partial f/\partial u$ in (2.103) is set to zero, the iterative scheme becomes explicit. This scheme has stability properties that depend on the number of iterations performed each time step. The linear stability properties of the explicit scheme are documented in Pierce (2001) using the linear model problem, $d u/d t = \lambda u$. A minimum of two iterations are required for second-order accuracy. Additional iterations may improve stability but do not

increase the order of accuracy. It was found that linear stability limits are not significantly increased beyond three iterations (see Pierce (2001)).

If the Jacobian in (2.103) is not set to zero, but simplified with the approximate factorization technique (discussed in section 2.2.2), semi-implicit schemes result. The economy of the semi-implicit scheme derives from a judicious choice of which terms to treat implicitly and which to treat explicitly. Usually only the stiffest terms in each equation are treated implicitly, such as derivatives in a coordinate direction that has a much greater variation in grid spacing than the other directions. For example, where grid refinement occurs near the wall, only derivatives in the wall-normal direction would be treated implicitly. In the present study, the following terms are treated implicitly: advection and diffusion in the radial and azimuthal directions and the pressure in all directions via Poisson equation.

The step-by-step iterative solution procedure employed in the present study to advance the governing equations (2.94)–(2.97) in time is summarized below. In the following, the superscript "n" refers to the solution values that are known from the previous time level, the superscript "k" refers to the iteration cycle between the solutions at time step "n" and "$n + 1$", the superscript "0" indicates the initial guess for the first iteration when $k = 0$, and a hat placed above a symbol is used for a provisional value of some quantity.

Step 1: Choose predictors (initial guesses) for the values of the variables at the next time level:

$$u_i^0 = u_i^n, \quad T^0 = T^n, \quad ... \tag{2.104}$$

This choice corresponds to using explicit Euler (or first-order Runge-Kutta) for the first iteration. For the density predictor, experience has shown that it is best to ensure that the predictors for the density and velocity satisfy the continuity equation (Pierce (2001)). That is, the predicted rate-of-change of density should correspond to the predicted mass flux divergence:

$$\rho^0 = \rho^n - \Delta t \, \delta_{x_i} (g_i^0) \tag{2.105}$$

Step 2: The temperature transport equation (2.96) is first advanced, so that a better estimate for the density can be obtained early in the iteration process. Semi-implicit penta-diagonal equations resulting from the QUICK discretization are solved for the advection and diffusion in the radial and azimuthal directions using approximate factorization, as discussed above. Time-advancing (2.96) yields $(\rho T)^{k+1}$, from which a provisional estimate

for T^{k+1} is obtained using the current density predictor:

$$\hat{T} = (\rho T)^{k+1}/\rho^k. \tag{2.106}$$

Boundary conditions are enforced on $\hat{T}$.

Step 3: The density is updated from the equation of state (2.89):

$$\rho^{k+1} = p^{(0)}/\hat{T}. \tag{2.107}$$

Step 4: Temperature is re-updated based on the new density:

$$T^{k+1} = (\rho T)^{k+1}/\rho^{k+1}. \tag{2.108}$$

Boundary conditions are applied to T^{k+1}.

Step 5: To advance the momentum equations (2.95), the fractional-step method is used (Kim *et al.* (1985)), which is, perhaps, the most popular method to satisfy the velocity divergence constraint in the incompressible-type simulations. In a fractional step method, the mass flux g_i^{k+1} and the pressure $\left(p^{(2)}\right)^{k+1}$ are split into their provisional part and an additive correction:

$$g_i^{k+1} = \widehat{g}_i + \delta\, g_i, \quad \left(p^{(2)}\right)^{k+1} = \widehat{p^{(2)}} + \delta\, p^{(2)}. \tag{2.109}$$

Expressions (2.109) are then substituted into the momentum equations (2.95)

$$\frac{\widehat{g}_i + \delta\, g_i - g_i^n}{\Delta\, t} = -\delta_{x_i}\left(\widehat{p^{(2)}} + \delta\, p^{(2)}\right) + R_i, \tag{2.110}$$

where all terms in the right-hand side, except for the pressure, are grouped into a generic term R_i for convenience. Equation (2.110) is then split into a predictor part and a corrector part as follows:

$$\frac{\widehat{g}_i - g_i^n}{\Delta\, t} = -\delta_{x_i}\left(\widehat{p^{(2)}}\right) + R_i, \tag{2.111}$$

$$\delta\, g_i = -\Delta\, t\, \delta_{x_i}\left(\delta\, p^{(2)}\right). \tag{2.112}$$

In a predictor part of the fractional-step method, equation (2.111) is advanced in time to

yield provisional estimates for the mass flux components $\hat{g}_i$. In the present work, semi-implicit tri-diagonal equations resulting from the central-difference discretization are solved separately for each velocity component for advection and diffusion in the radial and azimuthal directions using approximate factorization. The pressure from the previous iteration $\left(p^{(2)}\right)^k$ is used for the provisional value $\widehat{(p^{(2)})}$, i.e. $\widehat{(p^{(2)})} = \left(p^{(2)}\right)^k$. Provisional velocity components are then computed using

$$\widehat{u_i} = \widehat{g}_i / (\overline{\rho}^{\,x_i\,t})^{k+1}. \tag{2.113}$$

Boundary conditions are applied to $\widehat{u}_i$.

Step 6: In general, provisional mass fluxes $\widehat{g}_i$ do not satisfy the continuity equation (2.94). Corrector part of the fractional-step method ensures that the final velocity field do satisfy the continuity. Taking the divergence of (2.112) leads to the Poisson equation for the pressure correction $\delta\, p^{(2)}$:

$$
\begin{aligned}
\delta_{x_i}[\delta_{x_i}(\delta\, p^{(2)})] &= -\delta_{x_i}(\delta\, g_i)/\Delta t \\
&= -\delta_{x_i}(g_i^{k+1} - \widehat{g}_i)/\Delta t \\
&= \frac{1}{\Delta t}\left[\delta_{x_i}(\widehat{g}_i) + \frac{\rho^{k+1} - \rho^n}{\Delta t}\right],
\end{aligned}
\tag{2.114}
$$

where the continuity equation (2.94) was used to substitute for $\delta_{x_i}(g_i^{k+1})$.

Step 7: The velocities and pressure are updated:

$$g_i^{k+1} = \widehat{g}_i - \Delta t\, \delta_{x_i}(\delta\, p^{(2)}), \tag{2.115}$$

$$u_i^{k+1} = g_i^{k+1} / (\overline{\rho}^{\,x_i\,t})^{k+1}, \tag{2.116}$$

$$\left(p^{(2)}\right)^{k+1} = \left(p^{(2)}\right)^k + \delta\, p^{(2)}. \tag{2.117}$$

The continuity equation based on the density determined in Step 3 is now satisfied exactly. This completes one full cycle of the iterative process. If more iterations are desired the process would continue with Step 2. While only two iterations are required to ensure the second-order accuracy in time, in practice more iterations might be needed to ensure stability (Pierce (2001)); usually, three to five iterations is sufficient. The computational

time step is selected by computing a generalized CFL number

$$\text{CFL} = \frac{u\,\Delta t}{\Delta x} + \frac{\nu\,\Delta t}{\Delta x^2} \tag{2.118}$$

based only on axial convection and diffusion (since these are the only terms treated explicitly). CFL number limit is taken from the linear stability analysis and corresponds to $\text{CFL}_{lim} = 2$.

2.4 Turbulence Modeling

2.4.1 Filtering and LES Equations

Turbulence modeling is achieved in both codes by employing Large Eddy Simulation (LES) technique. In LES, all of the field variable are decomposed into resolved and subgrid-scale parts. The resolved, or large-scale field, is obtained from the instantaneous field by the filtering operation

$$\overline{f}(\mathbf{x}) = \int_V G(\mathbf{x}, \mathbf{x}')\, f(\mathbf{x}')\, d^3\mathbf{x}'. \tag{2.119}$$

In general, $G(\mathbf{x}, \mathbf{x}')$ can be any spatial filter. Integration is performed over the flow domain V. In both of the present numerical methods, however, filtering is implicitly defined by the computational grid, as opposed to explicit filtering (Ghosal & Moin (1995), Vasilyev *et al.* (1998)). Implicit filtering leads to the box-type function $G(\mathbf{x}, \mathbf{x}')$ in (2.119), which is defined for each computational cell as

$$G(\mathbf{x}, \mathbf{x}') = \begin{cases} 1/V_{cell}(\mathbf{x}), & \mathbf{x} \text{ and } \mathbf{x}' \text{ are in the same computational cell} \\ 0, & \mathbf{x} \text{ and } \mathbf{x}' \text{ are in different computational cells} \end{cases} \tag{2.120}$$

$V_{cell}(\mathbf{x})$ is the volume of the computational cell containing $\mathbf{x}$. Quantities per unit volume (density and pressure) are treated using a Reynolds decomposition,

$$f = \overline{f} + f', \tag{2.121}$$

while quantities per unit mass (velocity, temperature, viscosity, thermal conductivity) are best described by a Favre (density-weighted) decomposition,

$$f = \widetilde{f} + f'', \tag{2.122}$$

where

$$\widetilde{f} = \overline{\rho\, f}/\bar{\rho}. \tag{2.123}$$

The LES equations for the resolved field are formally derived by substituting the above decompositions into the governing equations and then subjecting the equations to the filtering operation (2.119). LES equations for the large-scale field for both the compressible solver and the low Mach number solver are listed in Xiong (2004) and Pierce (2001), respectively, and not repeated here. Favre decomposition is beneficial in comparison to Reynolds decomposition for two reasons. First, it significantly simplifies the filtered governing equations in both the compressible and low Mach number formulation. Second, it ensures that the filtering process does not alter the form of the conservation laws, which is important for the low Mach number code written in the conservation form.

2.4.2 Subgrid-Scale Closure Model

When filtering is applied to the governing equations, the filtered nonlinear terms, such as the stress tensor $\overline{\rho}\,\widetilde{u_i u_j}$, the heat flux $\overline{\rho}\,\widetilde{u_i T}$ etc. are decomposed into the resolved and subgrid scale (SGS) components as follows:

$$\overline{\rho}\,\widetilde{u_i u_j} = \overline{\rho}\,\widetilde{u}_i\,\widetilde{u}_j + \underbrace{\overline{\rho}\left(\widetilde{u_i u_j} - \widetilde{u}_i\,\widetilde{u}_j\right)}_{t_{ij}} \tag{2.124}$$

$$\overline{\rho}\,\widetilde{u_i T} = \overline{\rho}\,\widetilde{u}_i\,\widetilde{T} + \underbrace{\overline{\rho}\left(\widetilde{u_i T} - \widetilde{u}_i\,\widetilde{T}\right)}_{q_i} \tag{2.125}$$

The subgrid-scale terms t_{ij} and q_i represent the statistical effects of the instantaneous small-scale fluctuations on the resolved scales. Their derivatives $t_{ij,j}$ and $q_{i,i}$ appear with the negative sign at the right-hand side of the filtered momentum and energy equations, respectively (Xiong (2004); Pierce (2001)). These terms are unclosed and require modeling.

In both of the numerical codes described above, the anisotropic part of SGS stress tensor t_{ij} is modeled using an eddy viscosity assumption

$$t_{ij} - \frac{1}{3}\,t_{kk}\,\delta_{ij} = -2\,\mu_t\,\left(\widetilde{S}_{ij} - \frac{1}{3}\widetilde{S}_{kk}\,\delta_{ij}\right) \tag{2.126}$$

where $\widetilde{S}_{ij} = \frac{1}{2}\left(\widetilde{u}_{i,j} + \widetilde{u}_{j,i}\right)$.

The eddy viscosity μ_t is given by the Smagorinsky model (Smagorinsky (1963))

$$\mu_t = C_\mu \,\overline{\rho}\, \Delta^2 \, |\widetilde{S}|, \tag{2.127}$$

where

$$|\widetilde{S}| = \left(\widetilde{S}_{ij}\,\widetilde{S}_{ij}\right)^{1/2} \tag{2.128}$$

and Δ is the length scale associated with the width of the filter (2.119). The isotropic part, or the trace of the SGS stress tensor, t_{kk}, is related to the subgrid kinetic energy $\frac{1}{2}\,q^2$ as

$$t_{kk} = \overline{\rho}\,\left(\widetilde{u_k u_k} - \widetilde{u}_k \widetilde{u}_k\right) = q^2. \tag{2.129}$$

The subgrid kinetic energy is often parameterized using Yoshizawa's expression

$$\frac{1}{2}\,q^2 = C_q\,\overline{\rho}\,\Delta^2\,|\widetilde{S}|^2. \tag{2.130}$$

The residual heat flux q_i is modeled as a subgrid turbulent flux with a gradient-diffusion assumption

$$q_i = -k_t\,\widetilde{T},_i, \tag{2.131}$$

where the coefficient k_t is given by the eddy diffusivity model

$$k_t = C_k\,\overline{\rho}\,\Delta^2\,|\widetilde{S}|. \tag{2.132}$$

The eddy diffusivity model (2.132) has the same algebraic form as the eddy viscosity model (2.127), but the model coefficient is different. The ratio of the two coefficients gives the subgrid turbulent Prandtl number, $Pr_t = C_\mu/C_k$.

2.4.3 The Dynamic Procedure

The dynamic procedure is used in the present method to compute the eddy coefficients C_μ, C_q, C_k and the turbulent Prandtl number, Pr_t. The dynamic procedure (Germano *et al.* (1991); Moin *et al.* (1991)) is a method for calculating dimensionless scaling coefficients in subgrid-scale models for filtered nonlinear terms and is briefly outlined here in general form.

For an arbitrary non-linear term $f(u)$, which is a function of the field variables u, the filtered term $\overline{f(u)}$ can be decomposed into a resolved part $f(\overline{u})$ and a modeled part $m(\overline{u})$, which depends on the field variables but in general can also depend explicitly on space and

time and on the other parameters, such as the grid filter width, Δ:

$$\overline{f(u)} = f(\overline{u}) + m(\overline{u}). \tag{2.133}$$

The basic idea behind the dynamics procedure is to consider how $f(u)$ and $m(u)$ vary with the filter width. To this purpose, an expression similar to (2.133) can be written for the filtered term at a larger filter width, $\widehat{\Delta}$, referred to as the test filter:

$$\widehat{\overline{f(u)}} = f(\widehat{\overline{u}}) + m(\widehat{\overline{u}}). \tag{2.134}$$

Filtering to the test level is indicated by the hat symbol. Test filter width $\widehat{\Delta}$ is usually taken to be twice the width of the grid filter, $\widehat{\Delta} = 2\Delta$. If (2.133) is test filtered and subtracted from (2.134), the following identity results:

$$\widehat{f(\overline{u})} - f(\widehat{\overline{u}}) = m(\widehat{\overline{u}}) - \widehat{m(\overline{u})}. \tag{2.135}$$

All terms in this equation are computable from the known resolved field. It represents the "band-passed" contribution to the nonlinear term in the scale range between the grid and the test filter levels. A consistent subgrid model should contribute the same amount as the resolved field in this band. The key of the dynamic procedure is to use this identity as a constraint for calibration of subgrid-scale models.

For the dynamic procedure to be applicable, the quantity to be modeled must vary substantially between the grid and the test filter scales; otherwise, the difference in (2.135) will not be significant and cannot be used for modeling subgrid-scale quantities. Examples of quantities that can not be modeled dynamically are dissipation and chemical reaction rates (Pierce (2001)), because these phenomena occur almost exclusively at the smallest scales, which are always unresolved in LES.

The dynamic procedure is usually applied to the situations in which the subgrid model can be written as

$$m(\widehat{u}) = C \, s(\widehat{u}, \Delta), \tag{2.136}$$

where $s(\widehat{u}, \Delta)$ is a dimensionally consistent algebraic scaling law and C is an unknown dimensionless coefficient, which in dynamic procedure is allowed to vary in space and time. Substituting this form into (2.135) one obtains

$$\widehat{f(\overline{u})} - f(\widehat{\overline{u}}) = C^{\star} s(\widehat{\overline{u}}, \widehat{\Delta}) - C \, \widehat{s(\overline{u}, \Delta)}, \tag{2.137}$$

where $C^\star$ is the model coefficient at the test filter level.

At this point, the various forms of the dynamic procedure differ as how to use this equation to calculate the model coefficient, C. In the present study, C is assumed to be statistical quantity, which varies slowly in space and time and is scale invariant. Therefore, we set $C^\star = C$ and allow C to pass through the test filtering operator in the right most term of equation (2.137). To simplify the notation, the following definitions are introduced:

$$\mathcal{L} = \widehat{f(\overline{u})} - f(\widehat{\overline{u}}), \quad \mathcal{M} = s(\widehat{\overline{u}}, \widehat{\Delta}) - \widehat{s(\overline{u}, \Delta)}, \tag{2.138}$$

where $\mathcal{L}$ is called the Leonard term and $\mathcal{M}$ is the model term. The equation for model coefficient C now can be written as

$$\mathcal{L} = C \, \mathcal{M}. \tag{2.139}$$

Although equation (2.135), leading to an expression (2.139) is an exact identity when $m(u)$ is the exact subgrid residual, it should only be expected to hold in a statistical sense (and should not be applied locally and instantaneously) when $m(u)$ is modeled. The reason for this is the following. In filtering the governing equations, we have replaced the instantaneous variations that occur within each subgrid volume with a statistical description of a subgrid state. However, the band-passed filtered fields in (2.135) are based on instantaneous data, and the test filtering process itself does not provide sufficient averaging to produce converged statistics in the band-pass filtered scale range. This may explain why LES practitioners have found that some form of averaging is required in order to compute stable model coefficients with the dynamic procedure. Related discussions are given by Ghosal *et al.* (1995), Carati & Eijnden (1997).

In the compressible code, an averaging (indicated by the angle brackets) is applied in the spanwise direction and C is calculated from an equation(2.139) as

$$C = \frac{\langle \mathcal{L} \rangle}{\langle \mathcal{M} \rangle}. \tag{2.140}$$

In a low Mach number code, a least-squares procedure (Lilly (1992)) is employed to compute C, with an averaging in the azimuthal direction,

$$C = \frac{\langle \mathcal{L} \cdot \mathcal{M} \rangle}{\langle \mathcal{M} \cdot \mathcal{M} \rangle}. \tag{2.141}$$

Model coefficients in equations (2.127), (2.130) and (2.132) are evaluated using the dynamic procedure. To simplify the expressions for the coefficients, the following notation

for the Favre (density-weighted) averaging at the test filter level is introduced:

$$\check{\widetilde{u}} = \widehat{\overline{\rho}\,\widetilde{u}}/\widehat{\overline{\rho}}. \tag{2.142}$$

Applying the dynamic procedure (2.141) to the SGS Reynolds stress model (2.126) gives

$$C_\mu = \frac{\langle \mathcal{L}_{ij} \rangle}{2\,\langle \mathcal{M}_{ij} \rangle} \quad \text{or} \quad C_\mu = \frac{\langle \mathcal{L}_{ij} \cdot \mathcal{M}_{ij} \rangle}{2\,\langle \mathcal{M}_{ij} \cdot \mathcal{M}_{ij} \rangle}, \tag{2.143}$$

where

$$\mathcal{L}_{ij} = \left(\widehat{\overline{\rho}\,\widetilde{u}_i\,\widetilde{u}_j} - \widehat{\overline{\rho}}\,\check{\widetilde{u}}_i\,\check{\widetilde{u}}_j \right) - \frac{1}{3}\left(\widehat{\overline{\rho}\,\widetilde{u}_k\,\widetilde{u}_k} - \widehat{\overline{\rho}}\,\check{\widetilde{u}}_k\,\check{\widetilde{u}}_k \right)\delta_{ij}, \tag{2.144}$$

$$\mathcal{M}_{ij} = -\left[\widehat{\overline{\rho}}\,\widehat{\Delta}^2\,|\check{\widetilde{S}}|\,(\check{\widetilde{S}}_{ij} - \frac{1}{3}\check{\widetilde{S}}_{kk}\delta_{ij}) - \overline{\rho}\,\Delta^2\,|\widetilde{S}|\,\widehat{(\widetilde{S}_{ij} - \frac{1}{3}\widetilde{S}_{kk}\delta_{ij})} \right]. \tag{2.145}$$

The same procedure used for the kinetic energy model (2.130) would result in the coefficient

$$C_q = \frac{\langle \mathcal{L} \rangle}{2\,\langle \mathcal{M} \rangle} \quad \text{or} \quad C_q = \frac{\langle \mathcal{L} \cdot \mathcal{M} \rangle}{2\,\langle \mathcal{M}^2 \rangle}, \tag{2.146}$$

$$\mathcal{L} = \widehat{\overline{\rho}\,\widetilde{u}_k\,\widetilde{u}_k} - \widehat{\overline{\rho}}\,\check{\widetilde{u}}_k\,\check{\widetilde{u}}_k, \quad \mathcal{M} = \widehat{\overline{\rho}}\,\widehat{\Delta}^2\,|\check{\widetilde{S}}|^2 - \overline{\rho}\,\widehat{\Delta^2\,|\widetilde{S}|^2}. \tag{2.147}$$

Isotropic part of the SGS stress tensor $t_{kk} = q^2$ is often included into the pressure term by defining

$$p_T = \overline{p} + \frac{1}{3}\,t_{kk} = \overline{p} + \frac{2}{3}C_q\,\overline{\rho}\,\Delta^2\,|\widetilde{S}|^2. \tag{2.148}$$

However, in the compressible code, the coefficient C_q is set to zero to ensure numerical stability (Xiong (2004)) following most of the previous studies. In the low Mach number code the isotropic part of the residual stress is also not computed, with the justification that acoustic interactions and compressibility effects are negligible (Pierce (2001)).

For the subgrid turbulent heat flux model (2.131), the coefficient C_k is calculated from

$$C_k = \frac{\langle \mathcal{L}_i \rangle}{\langle \mathcal{M}_i \rangle} \quad \text{or} \quad C_k = \frac{\langle \mathcal{L}_i \cdot \mathcal{M}_i \rangle}{\langle \mathcal{M}_i \cdot \mathcal{M}_i \rangle}, \tag{2.149}$$

$$\mathcal{L}_i = \widehat{\overline{\rho}\,\widetilde{u}_i\,\widetilde{T}} - \widehat{\overline{\rho}}\,\check{\widetilde{u}}_i\,\check{\widetilde{T}}, \quad \mathcal{M}_i = -\left[\widehat{\overline{\rho}}\,\widehat{\Delta}^2\,|\check{\widetilde{S}}|\,\check{\widetilde{T}}_{,i} - \overline{\rho}\,\widehat{\Delta^2\,|\widetilde{S}|\,\widetilde{T}_{,i}} \right]. \tag{2.150}$$

Turbulent Prandtl number, Pr_t, is obtained by taking the ratio of the coefficients C_μ (equation (2.143)) and C_k (equation (2.149)).

2.5 Coupling Procedure

The procedure for coupling compressible and low Mach number codes described above into a single unsteady solver is presented in this section.

Two-dimensional view of a schematic computational domain suitable for performing simulations of film cooling problem with these two codes is shown in figure 2.6. Cooling gas from a cylindrical hole fed by a cylindrical plenum is injected at some angle onto the surface of a turbine blade, generally having some local curvature. According to the current multi-code approach, compressible code is used in the region exterior to the turbine blade surface (the top domain in figure 2.6). Low Mach number code is employed inside the film cooling hole and the plenum. Since the hole is inclined with respect to the blade surface, there exists a region of overlap between compressible and low Mach number code domains, which physically corresponds to the region above the turbine blade surface, where cooling gas injection takes place. This region of overlap is calculated by both codes. Another region of overlap exists between the two low Mach number codes, where the plenum and the film hole are intersected. Boundaries corresponding to the physical walls are shown in bold in figure 2.6. Boundaries corresponding to the domain intersection, the interface boundaries, are shown as dashed in this figure.

We concentrate now on the intersection of the compressible and the low Mach number codes and describe the coupling between them. Coupling between two low Mach number codes is more straightforward since the governing equations and numerical method used in both codes are the same. In the present formulation, we use the same interface conditions between two low Mach number codes as in compressible - low Mach number coupling.

Only one boundary of the compressible code domain intersects the low Mach number code domain: boundary corresponding to the turbine blade surface. The intersection occurs at a place, where cooling gas is injected. We call this part of the boundary an "injection boundary" for identification purposes. Variables from the low Mach number code should be supplied to the compressible code at this location, which is schematically shown by the arrow 1 in figure 2.6.

Boundaries of the low Mach number code domain intersecting the compressible code domain are the top of the cylinder and the cylindrical surface. We call the places of intersection "open boundaries", since they are not part of the walls. Variables from the compressible code should be supplied to the low Mach number code at the open boundaries, as indicated by arrows 2 in figure 2.6.
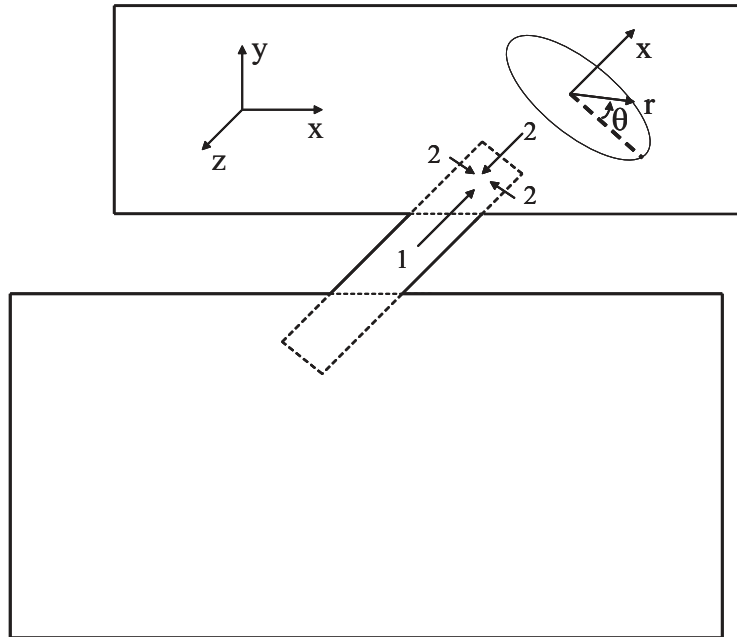
Figure 2.6: Schematic of a computational domain for film cooling simulations.

We now describe the interface conditions specified at the places of the domain intersection. We validate the particular choice of the interface conditions in the next section by showing the results of the test cases.

2.5.1 Interface Conditions for the Compressible Code

Variables, which are obtained numerically in the compressible code, are $\{\rho, u, v, w, T\}$. Specification of these five quantities is required at the grid nodes corresponding to the injection boundary of the compressible code, denoted as $\{\rho_c, u_c, v_c, w_c, T_c\}$, where the subscript "c" refers to the compressible values. One can interpolate the low Mach number code solution to the grid nodes of the injection boundary to obtain the values $\{\rho_{lm}, u_{lm}, v_{lm}, w_{lm}, T_{lm}\}$, where the subscript "lm" refers to the low Mach number values. The question is how to reconstruct the compressible values from the low Mach number values. Several methods of reconstruction have been considered.

A. Injection for the three components of velocity and the temperature. Density is obtained

from the continuity equation.

$$\rho_c \quad - \quad \text{from continuity equation}, \quad u_c = u_{lm}, \quad v_c = v_{lm}, \quad w_c = w_{lm}, \quad T_c = T_{lm}.$$

$$(2.151)$$

This is similar to the no-slip isothermal wall boundary conditions described in section 2.2, where zero values for velocities are substituted with the corresponding "lm" values.

B. Injection for all the variables.

$$\rho_c = \rho_{lm}, \quad u_c = u_{lm}, \quad v_c = v_{lm}, \quad w_c = w_{lm}, \quad T_c = T_{lm}. \tag{2.152}$$

C. Injection for $\{u, v, w, T\}$. Density is calculated from pressure through the equation of state.

$$\rho_c = \gamma M^2 p_{lm}/T_{lm}, \quad u_c = u_{lm}, \quad v_c = v_{lm}, \quad w_c = w_{lm}, \quad T_c = T_{lm}. \tag{2.153}$$

D. Riemann invariant formulation, where the interpolated values $\{\rho_{lm}, u_{lm}, v_{lm}, w_{lm}, T_{lm}\}$ are used to construct incoming quantities $\{s_{in}, w_{in}, v_{t\,in}, R_{1\,in}\}$ and the procedure described in section 2.2 is used to obtain $\{\rho_c, u_c, v_c, w_c, T_c\}$.

E. Riemann invariant formulation, but $\gamma M^2 p_{lm}/T_{lm}$ is used instead of ρ_{lm} to construct incoming quantities $\{s_{in}, w_{in}, v_{t\,in}, R_{1\,in}\}$.

Numerical tests showed that both injection and Riemann invariant formulation (methods B and D) are stable, while the method A, where the density is calculated from the continuity equation, is unstable. Injection method generally shows better accuracy than the Riemann invariant method (see section 2.6). Methods C and E, where the density is obtained from the pressure through the equation of state proved to be unstable. It is explained by the fact that pressure in low Mach number code plays different role than pressure in compressible code. Namely, it is the dynamic variable which enforces the continuity equation, rather than the thermodynamic variable coupled to density and temperature. Therefore, specifying the compressible density through the low Mach number pressure leads to unstable coupling.

As a result, method B, injection for all five variables with $\rho_c = \rho_{lm}$, is used to specify interface conditions for the compressible code at the place of intersection with the low Mach number code domain. Note that the injection method is overposed if used as the boundary

condition for the compressible code. It is, however, physically justified when used as an "interface" condition, since the interface is an interior region of the fully coupled solution and the full transfer of variables from one computational block to another is possible.

2.5.2 Interface Conditions for the Low Mach Number Code

Velocity and Temperature

In the low Mach number code, interface conditions are required at the open boundaries for the three components of velocity u_x, u_r, u_θ, temperature T, and a second order pressure $p^{(2)}$ or its gradients to solve the pressure Poisson equation. Density is obtained from the temperature through the equation of state, so no interface conditions for density are required.

In the present method, we use injection for velocity components, setting the velocity values at the interface equal to the corresponding values interpolated from the compressible code, regardless of whether the open boundary corresponds to an inflow or an outflow.

One might argue that injection method is not the right treatment for an outflow boundary. Commonly used boundary condition for an outflow is a convective condition in the form

$$\phi_t + v_{conv}\,\phi_n = 0, \tag{2.154}$$

employed in the original formulation of Pierce (2001) as well. Here ϕ stands for the convected quantity and v_{conv} is some convection velocity. In the method of Pierce (2001), convection velocity is taken to be constant over the outflow boundary and defined as the maximum outflow velocity over the boundary,

$$v_{conv} = \max_{outflow} v_n, \tag{2.155}$$

where v_n is the local velocity normal to the boundary. In the utilization of Pierce (2001), outflow boundary is a cross-sectional plane perpendicular to the centerline. Internal flow in pipes and diffusers is considered, so that large mean velocity normal to the outflow boundary is present, justifying the use of a convective condition. In the present calculations, however, some parts of an outflow boundary are represented by a cylindrical surface. Implementation of the condition (2.154) would assume that convection occurs in the radial direction, which is not true. Also, convection velocity would be hard to define in this case. Since part of a cylindrical surface corresponds to an inflow, a switch between inflow and outflow

conditions would have to be implemented. An attempt was made to treat an inflow part of the cylindrical boundary with an injection method, but an outflow part - with a convective condition. However, this resulted in an unstable method. Another drawback is that convective condition fails to provide the feedback from the second code during coupling, leading to an erroneous velocity field of the coupled solution.

For the temperature, however, it was found that the accuracy is reduced if the condition $T_{lm} = T_c$ is used when the boundary corresponds to an outflow. Enforcing the temperature at the outflow produces "wiggles" in the temperature field close to the boundary, especially when combined with an upwind-type QUICK scheme for the scalar advection (see section 2.3). To circumvent this, an injection $T_{lm} = T_c$ is used only for an inflow part of the boundary and a convective-type condition

$$T_t + v_{conv} T_n = 0 \qquad (2.156)$$

is employed at the outflow, where v_{conv} is defined by equation 2.155. Since it is not known a-priori what parts of the boundary correspond to an inflow, and what parts - to the outflow, a dynamical switch is implemented. Velocity normal to the boundary, v_n, is estimated first during each time step at each boundary node by using interpolated values from the compressible code. Nodes with $v_n \le 0$ are marked as corresponding to an inflow, and nodes with $v_n > 0$, to an outflow. Convective outflow condition works well for temperature as opposed to velocity, perhaps due to the advective nature of the temperature equation in the low Mach number formulation. This is shown via examples of a steady temperature jump and a moving entropy spot in section 2.6.

Pressure Coupling

Pressure coupling should be considered carefully when compressible and low Mach number codes are combined into a single solver. Recall that pressure in the low Mach number limit has an asymptotic expansion

$$p(\mathbf{x}, t) = p^{(0)}(t) + \gamma M^2 p^{(2)}(\mathbf{x}, t) + O(M^3). \qquad (2.157)$$

Only the second order pressure $p^{(2)}(\mathbf{x}, t)$ enters the equations of motion in the low Mach number formulation (see section 2.3), while zeroth order pressure $p^{(0)}(t)$ is the thermodynamic pressure appearing in the equation of state. Overall pressure $p(\mathbf{x}, t)$ enters the compressible equations. To determine the dynamic pressure $p^{(2)}$, Poisson equation is solved

in the low Mach number code with the Neumann boundary conditions. Taking spatial derivatives of an equation (2.157) and neglecting $O\left(M^3\right)$ terms leads to

$$\delta_{x_i}\left(p^{(2)}\left(\mathbf{x}, t\right)\right) = \frac{1}{\gamma M^2}\delta_{x_i}\left(p\left(\mathbf{x}, t\right)\right) \tag{2.158}$$

or

$$\delta_{x_i}\left(p_{lm}^{(2)}\left(\mathbf{x}, t\right)\right) = \frac{1}{\gamma M^2}\delta_{x_i}\left(p_c\left(\mathbf{x}, t\right)\right). \tag{2.159}$$

Therefore, normal derivative of pressure for the Neumann boundary conditions can be estimated from the normal derivative of the compressible pressure as

$$\delta_n\left(p_{lm}^{(2)}\left(\mathbf{x}, t\right)\right) = \frac{1}{\gamma M^2}\delta_n\left(p_c\left(\mathbf{x}, t\right)\right). \tag{2.160}$$

When Neumann boundary conditions are used, pressure $p^{(2)}\left(\mathbf{x}, t\right)$ can be found only up to an additive constant $C(t)$. To obtain pressure values consistent with the compressible code, one need to estimate this constant. To this purpose, we equate low Mach number and compressible pressure at some specific location $\mathbf{x}_0$:

$$p_c\left(\mathbf{x}_0, t\right) = p_{lm}\left(\mathbf{x}_0, t\right) = p^{(0)}\left(t\right) + \gamma M^2\left(p^{(2)}\left(\mathbf{x}_0, t\right) + C(t)\right). \tag{2.161}$$

From equation (2.161),

$$\widetilde{C}(t) = p^{(0)}\left(t\right) + \gamma M^2\, C(t) = p_c\left(\mathbf{x}_0, t\right) - \gamma M^2\, p^{(2)}\left(\mathbf{x}_0, t\right). \tag{2.162}$$

Using $\widetilde{C}(t)$, we find the overall pressure for the low Mach number code,

$$p_{lm}\left(\mathbf{x}, t\right) = \widetilde{C}(t) + \gamma M^2\, p^{(2)}\left(\mathbf{x}, t\right). \tag{2.163}$$

In practice, an additive constant $\widetilde{C}(t)$ will be different depending on the specific location $\mathbf{x}_0$, where pressure values are equalized. However, this difference is supposed to be rather small, of $O\left(M^2\right)$.

Interface Conditions for Provisional Mass Flux Components

In the fractional step formulation employed in the low Mach number code, mass flux components g_i^{k+1} are split into their provisional part and an additive correction (see section 2.3)

as

$$g_i^{k+1} = \widehat{g}_i + \delta g_i. \tag{2.164}$$

Interface conditions for the provisional mass flux components $\widehat{g}_i$ are required to advance momentum equations (2.111) at the predictor step of the fractional step method. To specify these boundary conditions, equation (2.164) can be rearranged as

$$\widehat{g}_i = g_i^{k+1} - \delta g_i. \tag{2.165}$$

Interface conditions for the mass flux g_i^{k+1} are known; an additive correction δg_i at the boundary can be estimated using the corrector step of the fractional step method, equation(2.112),

$$\delta g_i = -\Delta t \, \delta_{x_i} \left(\delta p^{(2)} \right), \tag{2.166}$$

where

$$\delta p^{(2)} = \left(p^{(2)} \right)^{k+1} - \left(p^{(2)} \right)^{k} \tag{2.167}$$

is an additive correction to the pressure. Therefore, $\delta_{x_i} \left(\delta p^{(2)} \right)$ can be expressed as

$$\delta_{x_i} \left(\delta p^{(2)} \right) = \delta_{x_i} \left(p^{(2)} \right)^{k+1} - \delta_{x_i} \left(p^{(2)} \right)^{k}. \tag{2.168}$$

The last term of an equation (2.168) is known from the previous iteration. The first term is calculated at the interface from the corresponding compressible pressure according to equation (2.159). It allows to calculate the interface conditions for provisional mass flux components as

$$\widehat{g}_i = g_i^{k+1} + \Delta t \left[\delta_{x_i} \left(p^{(2)} \right)^{k+1} - \delta_{x_i} \left(p^{(2)} \right)^{k} \right]. \tag{2.169}$$

2.5.3 Interpolation

Interpolation Method

Method used to interpolate the variables from one domain to the interface boundary nodes of another domain is discussed in this subsection. Consider first the interpolation from low Mach number domain to the injection boundary of the compressible domain. An intersection of the injection boundary with the staggered grid corresponding to the low Mach number domain is shown in figure 2.7 in two dimensions. Grid nodes of the injection boundary, to which low Mach number values should be interpolated, are specified as black circles. In order to perform interpolation, the grid cell of the low Mach number code, surrounding

each injection boundary node, is identified at the preprocessing step. Due to the staggering of the low Mach number variables, more than one low Mach number grid cell is associated with each compressible boundary node. For example, to interpolate the u values to the 3rd injection boundary point from the left in figure 2.7 (3rd black circle from the left), the grid cell corresponding to the blue rectangle is considered. To interpolate the values of v, the red grid cell is used etc. This way, all the five variables - density, temperature and the three components of velocity are obtained at each injection boundary point. However, interpolated velocities correspond to the low Mach number code local coordinate system. For three-dimensional domain, it is cylindrical, (x, r, θ). These velocities, $\{u_{lm\,x}, u_{lm\,r}, u_{lm\,\theta}\}$ (recall that subscript "lm" denotes the values interpolated from the low Mach number domain to the interface boundary of the compressible domain), are first transformed into velocities $\{u_{lm\,1}, u_{lm\,2}, u_{lm\,3}\}$, which correspond to the local cartesian system associated with the low Mach number domain, (x_1, x_2, x_3). This cartesian system has its x_1 axis aligned with the centerline of the cylinder in three dimensions. The transformation formulas are

$$
\begin{aligned}
u_1 &= u_x \\
u_2 &= u_r \cos\theta - u_\theta \sin\theta \\
u_3 &= u_r \sin\theta + u_\theta \cos\theta
\end{aligned}
\tag{2.170}
$$

(subscript "lm" is skipped for clarity). To obtain velocity components $\{u_{lm}, v_{lm}, w_{lm}\}$ in the cartesian coordinate system associated with the compressible code, another transformation is performed (subscript "lm" is again skipped)

$$
\begin{aligned}
u &= u_1 \cos\alpha - u_2 \sin\alpha \\
v &= u_1 \sin\alpha + u_2 \cos\alpha \\
w &= u_3,
\end{aligned}
\tag{2.171}
$$

where α is the angle between the x axis of the compressible domain and the centerline of the low Mach number domain (see figure 2.6 for the definition of the angle α and the sketch of the local coordinate systems).

To interpolate the variables from the compressible domain to the open boundaries of the low Mach number domain, the following process is performed. First, we rotate compressible code coordinate system (x, y, z) to match the local cartesian system associated with the low Mach number domain, (x_1, x_2, x_3). Rotated velocities $\{u_1, u_2, u_3\}$ are obtained from $\{u, v, w\}$ at the grid points of the compressible domain according to the inverse of the transformation (2.171) prior to the interpolation. This is done in order to avoid interpolation

of all three components of compressible velocity to reconstruct each of the values u_{cx}, u_{cr} and $u_{c\theta}$ at the corresponding interface boundary nodes of the staggered grid. By doing rotation first, we only need to interpolate one velocity component, u_1, to obtain streamwise velocity, u_x, and two velocity components, u_2 and u_3, to find the values of radial, u_r, and azimuthal, u_θ, velocities according to the inverse of the transformation given by equation (2.170). The same procedure is needed for the interpolation of the pressure derivatives, which are defined at the same grid nodes on the staggered grid as the velocity components. Interpolation of the scalar variables, temperature and pressure, to the cell centers of the staggered grid obviously does not require any coordinate transformation.

Bilinear interpolation is used in the present coupling procedure. Although implementation of a higher order interpolation schemes is possible, it does not lead to an increase of accuracy of the overall coupling method for two reasons. First, the low Mach number code is second order accurate in space, so second order accuracy of interpolation is consistent with it. Second, for the relatively fine meshes used in LES, an error of interpolation even in bilinear case is smaller than an inherent error of $O\left(M^2\right)$ introduced by coupling two different sets of equations. An influence of the degree of interpolation on the overall accuracy of the solution is considered in more detail in Appendix B on the example of test cases.

Approximation of the Film Hole Geometry

When film cooling configuration shown in figure 2.6 is approximated, the cylindrical cooling hole is considered. Since low Mach number code domain is cylindrical, the body-fitted mesh is used to describe the hole in the low Mach number code. Although the numerical grid is staggered in the low Mach number code, the wall boundaries are treated specially, so that the no-slip conditions are enforced exactly in the locations corresponding to the physical wall, and not in the numerical location of variables on the staggered grid (see Pierce (2001) for more details). It is not the case, however, for the compressible code. The details of the film hole exit cross-section with respect to the numerical grid at the bottom boundary of the compressible domain can be seen in figure 2.8, where the film hole wall is shown as a bold line and represents an ellipse because of the inclination angle. Due to the homogeneity of the grid in a spanwise direction, it is impossible to describe the wall of the film hole with a body-fitted mesh in the present formulation of the compressible code. It leads to the "staircase" description of the cooling hole. This is shown in more details in figure 2.9. Grid nodes which lie inside the elliptical boundary, shown in red, obtain the values of velocity, density and temperature interpolated from the low Mach number code. Grid nodes outside the elliptical

boundary, shown in blue, are treated with no-slip and adiabatic boundary conditions to represent the test plate wall. As a consequence, velocities and temperature gradients in the location corresponding to the physical film hole wall are not zero. Essentially, the compressible code sees the jet exit cross-section as having a "staircase" shape, with the boundaries corresponding to the blue line (where no-slip conditions are specified), instead of a smooth elliptical shape. This can be visualized by looking at the contours of mean vertical velocity on the bottom boundary of the compressible domain, resulting during the injection of the coolant flow from the cylindrical hole, plotted in figure 2.10 (calculations are described in chapter 5). The grid is colored according to the contour values. The diamond-shaped contours of zero vertical velocity connect the places where the no-slip conditions are enforced (in accordance with the blue line of figure 2.9. As a result of interpolation, the boundary itself, where velocity should be indentically zero, receives the values of about 0.04 to 0.06, which is seen by looking at the contour values at the boundary.

Besides the nonphysical "staircase" approximation, the effective area of the hole exit, as seen by the compressible code, is larger than in reality. Both of these deficiencies can be a source of errors in film cooling simulations. Substitution of a smooth boundary by a sharp "staircase" approximation likely produces elevated levels of turbulence. It was confirmed that a sharp corner in the intersection between the plenum and the film hole is responsible for the higher TL than a smooth corner (experiments of Johnston *et al.* (2002)). The author believes that the sharp "staircase" interface between the film hole and the test surface wall would have the same effect.

Larger effective area leads to a larger values of mass and momentum fluxes entering the compressible domain. The difference in the cross-sectional area, mass fluxes and vertical momentum fluxes exiting the low Mach number domain and entering the compressible domain is summarized in Table 2.3 together with an error introduced by the staircase approximation. Mass fluxes are estimated as

$$\mathcal{G} = \sum_{cells \subset \mathcal{A}} \rho \, v \, \Delta \, S, \tag{2.172}$$

and momentum fluxes as

$$\mathcal{I} = \sum_{cells \subset \mathcal{A}} (P + \rho \, v^2) \, \Delta \, S, \tag{2.173}$$

where $\mathcal{A}$ is the cross-sectional area for each code, sum is taken over the computational cells lying inside the cross-sectional area, P, ρ and v (vertical velocity) are estimated at the center
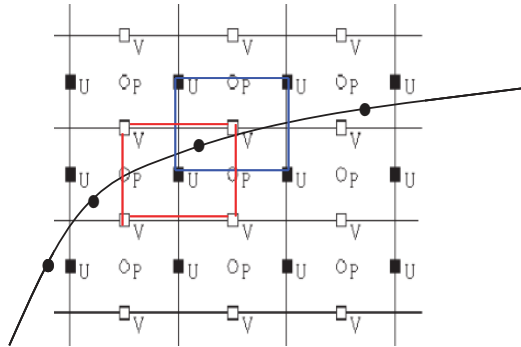
Figure 2.7: Intersection of the compressible injection boundary with the staggered grid of the low Mach number domain.

	Area	Mass flux	Momentum flux
Exiting the low Mach number domain, f_{lm}	1.37	0.358	1.514
Entering the compressible domain, f_c	1.49	0.364	1.607
Error, $(f_c - f_{lm})/f_{lm}$, %,	8.8	1.7	6.1

Table 2.3: Error introduced by the "staircase" approximation.

of the cells and ΔS is the cell area. Error is calculated as the relative difference between the value for the compressible code and the value for the low Mach number code

$$Error = \frac{f_c - f_{lm}}{f_{lm}}. \tag{2.174}$$

In spite of almost 10% difference in cross-sectional area, mass fluxes are conserved up to 1.7%. The error is larger for the vertical momentum fluxes, perhaps due to the fact that the pressure is involved in the conservation of momentum, and pressure between the low Mach number and compressible codes is difficult to couple, as discussed in section 2.6.

2.5.4 Parallelization

Parallel interface for coupling the codes is written on MPI platform. It constructs disjoint groups of processes - one group for each code. All communications within each group are performed using intracommunicators. Message passing between different groups is accomplished with the help of an intercommunicator. Time advancement of all the codes is synchronized by choosing the global time step equal to the smallest among the time steps of individual codes, as dictated by the stability requirement: $\Delta \tau = \min(\Delta \tau_1, \Delta \tau_2, \Delta \tau_3)$. Exchange of the variables across the interfaces between the computational domains of the
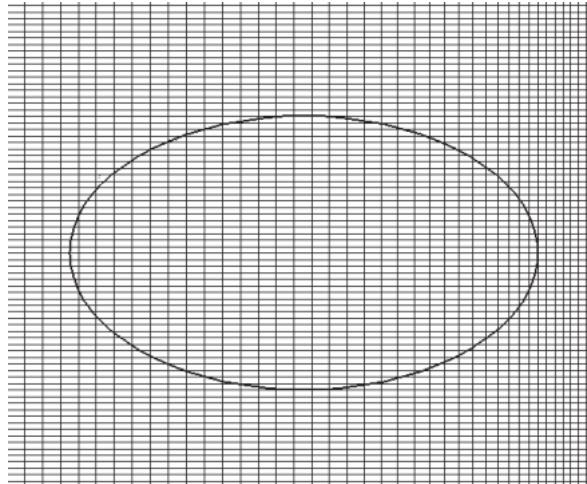
Figure 2.8: Details of the film hole exit cross-section with respect to the compressible grid.
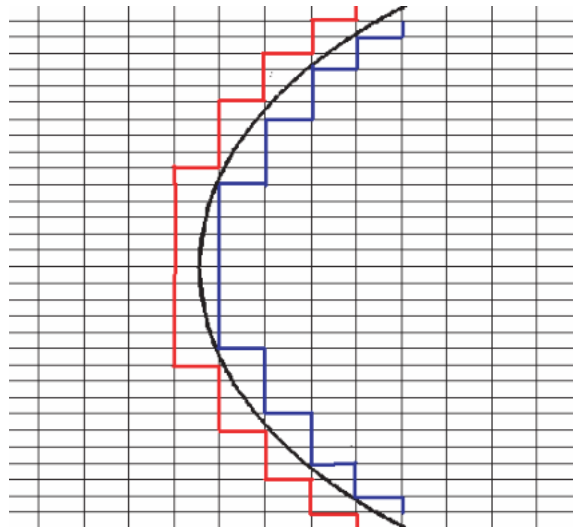
Figure 2.9: Part of the film hole exit cross-section with respect to the compressible grid, enlarged. Blue lines - nodes treated with no-slip boundary conditions; red lines - nodes obtaining the variables from the coolant flow.
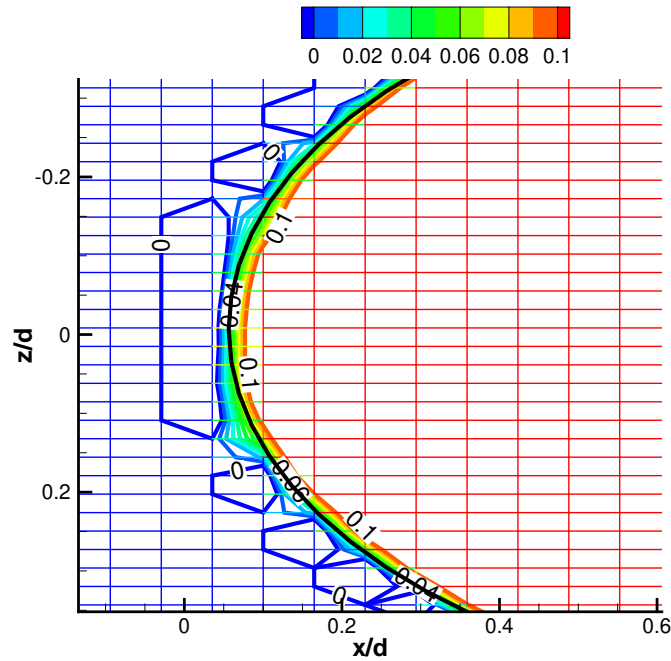
Figure 2.10: Contours of vertical velocity at the leading edge of the jet-exit cross-section in the film cooling calculations. Grid is color-coded according to the contour values.

different codes is performed at every time step, so that the coupled solver performs time-accurate unsteady computations.

2.6 Validation of the Coupling Procedure

Numerical test cases validating the choice of the coupling procedure described in section 2.5 are presented in this section. There are several aspects associated with the procedure which need to be verified in order to assess the performance of the coupling method.

1. Interface conditions.

   First aspect concerns the performance of interface conditions. Since flow information supplied from the other code is introduced at interfaces in place of boundary conditions, the reaction of each code to this new "boundary treatments" must be analyzed. This issue is especially important for the low Mach number code. Previously, this code has been used for calculating internal flow inside the cylindrical pipes and diffusers, where the flow was entering and exiting through the cross-sections perpendicular to the centerline, and the cylindrical surface represented a solid wall. In the current

simulations, due to the overlap between different domains (see figure 2.6), part of the cylindrical surface is no longer a solid wall, and the flow can enter and exit through it at random angles. Performance of the low Mach number code, when the interface conditions described in section 2.5 are used as the boundary conditions at all surfaces of the computational domain is analyzed in Appendix B. Grid convergence study is performed and an influence of the order of interpolation is tested in this appendix as well. Behavior of interface conditions for the compressible code is discussed in 2.6.2.

2. "One-way" coupling.

Existence of the overlap region between the compressible and the low Mach number codes brings another issue into consideration. Since this region is being computed by two different solvers, it is required for the convergence of the coupled solution that individual solutions are close to each other in this region. In the film cooling simulations, the overlap region is contained within the turbine blade boundary layer, where Mach number is small. Therefore, closeness of the "exact" solutions of the compressible and low Mach number equations is assumed. However, it is necessary to check whether numerical solutions are also close. Second group of tests investigates the closeness of solutions of the low Mach number code and the compressible code in the regime of low Mach number on steady and unsteady problems. It is convenient to perform these tests in a "one-way" coupling setting to isolate the difference of solutions due to the difference in numerics from the errors introduced by a mutual exchange of state variables through the interfaces. In a "one-way" coupling approach, only one code obtains information from the other code. The other code operates in a stand-alone mode, without feeling any feedback. Since low Mach number code interface has more points of contact with the compressible code due to the nature of the computational setup for the main (film cooling) problem, it is more reasonable to pass information from the compressible code to the low Mach number code for testing "one-way" coupling.

3. "Two-way" coupling.

Third group of tests concerns the performance of the "two-way" coupling procedure and the behavior of the fully coupled solution. The coupled solution is compared to both the solutions of the individuals codes and the analytical solution.

A list of implemented "one-way" and "two-way" coupling test cases is given in table 2.4. Both incompressible regime of the low Mach number code, when the disturbance has no

	"One-way" coupling	"Two-way" coupling
Incompressible regime	Taylor vortex	Taylor vortex
Variable density regime	Heated boundary layer	Entropy spot

Table 2.4: List of numerical tests to validate the coupling procedure.

variation in density and temperature; and variable density regime, with significant density and temperature variations, are considered in a framework of "one-way" and "two-way" coupling. The results of the test cases are described in more details below.

2.6.1 "One-way" coupling

Incompressible Regime

For coupling tests, when low Mach number code is run in incompressible regime, velocity disturbance in the form of a circular Taylor vortex,

$$v'_\phi = \frac{\mathcal{M}r}{16\pi\nu^2 t^2} \exp(\frac{-r^2}{4\nu t}),\ v'_r = v'_z = 0, \tag{2.175}$$

is superimposed on the uniform mean flow. Here v'_ϕ is tangential velocity, v'_r is radial velocity, v'_z is spanwise velocity and r is the distance from the center of the vortex (see Taylor (1918)). Circular Taylor vortex is an analytical solution of unsteady viscous incompressible equations. $\mathcal{M} = \int_0^\infty 2\pi r v r \mathrm{d}r$ is an invariant of the flow. Parameters t and $\mathcal{M}$ of equation (2.175) are chosen to set initial radius of the vortex R_T (R_T is the distance from the vortex center to the point of maximum velocity), and initial velocity disturbance level v'_{max}. Disturbance of $v'_{max}/U_\infty = 1\%$ is considered here.

In a "one-way" coupling formulation, low Mach number domain is placed inside the compressible code domain and information is transferred from the compressible to the low Mach number code through all the boundaries of the low Mach number code domain. Vortex is initialized in the compressible domain upstream of the low Mach number domain, convected with the mean flow and captured by the low Mach number code as it passes through it. Mach number $M_\infty = 0.05$ for the compressible code and Reynolds number $Re_{R_T} = U_\infty R_T/\nu = 330$ for both codes are considered.

Two-dimensional rectangular as well as three-dimensional cylindrical low Mach number code domains are investigated. For cylindrical configuration, the flow is quasi two-dimensional, i.e. there is no variation of flow parameters in spanwise direction in the

(a) Perpendicular domain.   (b) Inclined domain.

Figure 2.11: Vertical velocity contours for the convecting Taylor vortex.

coordinate system associated with the compressible code. Cylindrical domain is perpendicular to the main stream. For rectangular configuration, both perpendicular and inclined at 45° to the main stream domains are considered. The test case with inclined domain is conducted in order to check whether the relative skewness of the grid lines of the two codes influences the results.

Typical snapshots of the vertical velocity v calculated with both codes are overlaid in figure 2.11 for perpendicular and inclined rectangular domains. The moment when the center of the vortex is in the low Mach number code domain is shown. It can be seen that the contours of vertical velocity of the two solutions are very close to each other. The same was observed for all other variables. In fact, contours of vertical velocity show the largest difference.

Maximum difference between flow variables was calculated over the low Mach number code domain as

$$\Delta u_i = \frac{\max |u_{i\,c} - u_{i\,lm}|}{U_\infty} \tag{2.176}$$

for velocity components and

$$\Delta P = \frac{\max |p_c - p_{lm}|}{\rho_\infty U_\infty^2} \tag{2.177}$$

for pressure.

The difference in velocity is plotted versus computational time in figure 2.12 for both rectangular and cylindrical domains. The difference is larger when the center of the vortex is inside the low Mach number code domain. From figure 2.12(a) we see that orientation of the low Mach number domain does not influence the maximum difference between the solutions.

(a) Rectangular low Mach number code domain.

(b) Cylindrical low Mach number code domain.
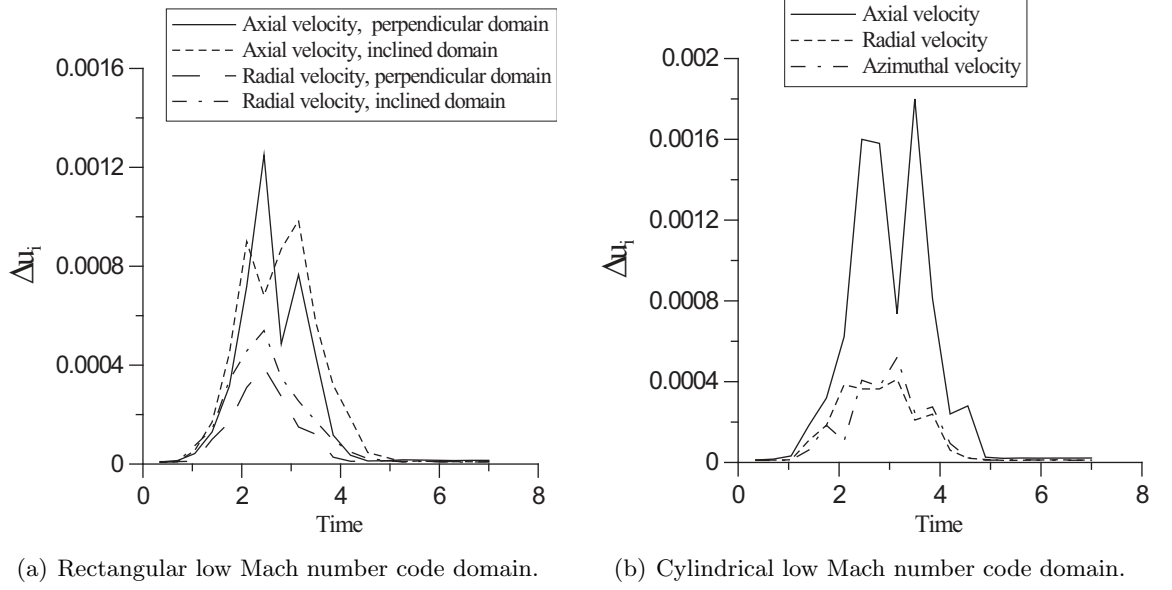
Figure 2.12: Maximum discrepancy between velocity components for convecting Taylor vortex.

The difference in pressure, when normalized with equation (2.177), is about two orders of magnitude smaller than the difference in velocity and is not plotted here. It is consistent with the fact that the pressure gradient for the Taylor vortex satisfies

$$\partial p'/\partial r = \rho \, v'^{\,2}/r. \qquad (2.178)$$

It is seen that the pressure disturbance is of the second order compared to the velocity disturbance, which explains the smaller value of the pressure difference.

It can be noticed that for the cylindrical domain the maximum difference does not exceed 0.2% and for the rectangular domain it is even less. Maximum discrepancy of 0.002 is comparable to the value of $M_\infty^2 = 0.0025$. As discussed above, error of the order of M_∞^2 is an inherent error due to the difference between the solution of low Mach number equations and the solution of compressible equations with small, but finite, M_∞.

Variable Density Regime

Laminar boundary layer above the heated wall with the temperature $T_w = 2\,T_\infty$ and Reynolds number $Re_d = U_\infty \, d/\nu_\infty = 500$ is chosen as a test case for the "one-way" coupling, when low Mach number code operates in a variable density regime. Low Mach number code

(a) Streamwise velocity.   (b) Vertical velocity.   (c) Temperature.
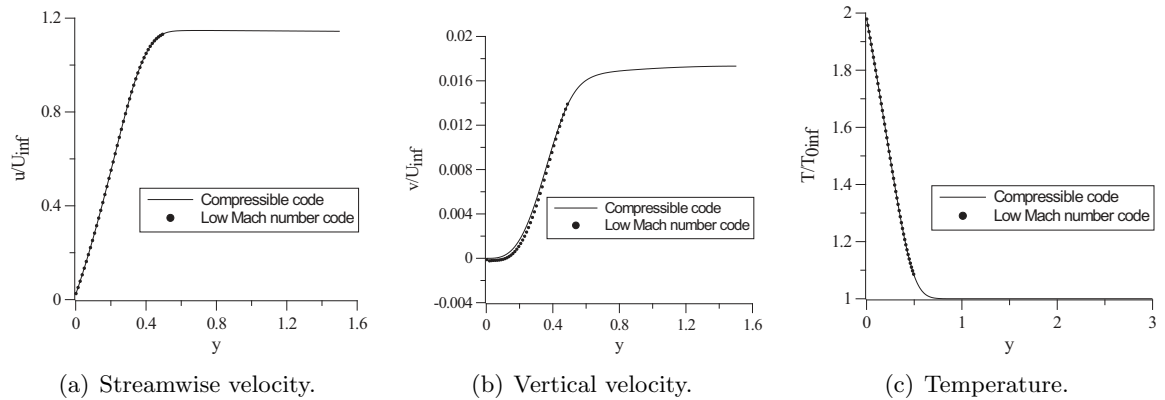
Figure 2.13: Comparison of boundary layer profiles calculated with two codes.

domain is again completely surrounded by the compressible domain, and interface condi-
tions are specified at all computational boundaries of the low Mach number code domain.
Numerical solutions of compressible and low Mach number codes are compared for the
steady problem of a laminar boundary layer above the heated wall of the previous example.
Wall-normal profiles of streamwise and vertical velocities and a temperature, taken through
the point with the maximum discrepancy between the solutions, are shown in figure 2.13.

It can be seen that the agreement between the two solutions is rather good.

Test cases described in this subsection show that compressible code and low Mach num-
ber code give very close numerical solutions for both incompressible and variable density
setting when the Mach number of the physical problem is small.

2.6.2   "Two-way" coupling

Behavior of the fully coupled solution is analyzed by passing vortical and entropy distur-
bances through the interface between low Mach number and compressible codes. "Two-way"
coupling is implemented, i.e. information between compressible and low Mach number codes
is exchanged at the interfaces as described in section 2.5. Several variations of interface con-
ditions for the compressible code are tested (testing of different interface conditions for the
low Mach number code is documented in Appendix B). The compressible interface condi-
tions being tested are (see section 2.5 for the detailed description)

A Injection for $\{u,\, v,\, w,\, T\}$, ρ is obtained from continuity.

B Injection for $\{\rho,\, u,\, v,\, w,\, T\}$.

C Injection for $\{u,\, v,\, w,\, T\}$, ρ is calculated from pressure through the equation of state.

D Riemann invariant formulation.

E Riemann invariant formulation, but ρ is calculated from pressure through the equation of state when forming Riemann invariants.

When low Mach number code is run in incompressible regime, density and temperature of unity ($\rho_{lm} = 1$, $T_{lm} = 1$) are supplied to the compressible domain to form interface conditions A through E. Stability and accuracy of the proposed interface conditions is investigated and the method with the best performance is identified. Coupled solution obtained with the chosen method is compared to both numerical solutions of individual codes and to analytical solution.

Incompressible Regime

Vortical disturbance in the form of convecting Taylor vortex (equation (2.175)) is again considered for the incompressible formulation of the low Mach number code. All parameters of the vortex are the same as in "one-way" coupling setting described previously (Reynolds number $Re_{R_T} = U_\infty R_T / \nu = 330$, peak disturbance amplitude $v'_{max}/U_\infty = 1\%$). Computational domain for this test case is shown in figure 2.14. Two-dimensional calculations are performed. Low Mach number code is located at the left of the compressible code with the region of overlap between $x = 0$ and $x = 7.7$ (all distances in this discussion are non-dimensionalized by the initial radius of Taylor vortex R_T). A uniform free-stream with velocity parallel to x-axis, $\vec{v}_\infty = (U_\infty, 0, 0)$, is taken as the undisturbed flow. Taylor vortex is superimposed on a uniform free-stream and supplied through the inflow boundary of the low Mach number code domain and is convected with the uniform main stream. The moment when the vortex is completely inside the overlap region is shown in figure 2.14. Outflow boundary of the low Mach number code domain ($x = 7.7$) gets information from the compressible code. Inflow boundary of the compressible code ($x = 0$) obtains variables from the low Mach number code.

Variation of interface conditions

Performance of the interface conditions supplied from the compressible to the low Mach number code is assessed in the beginning of this section. The present setup, however, allows the performance of interface conditions supplied from the low Mach number to the compressible code to be tested.

The quality of numerical solution of the compressible code can be judged by looking
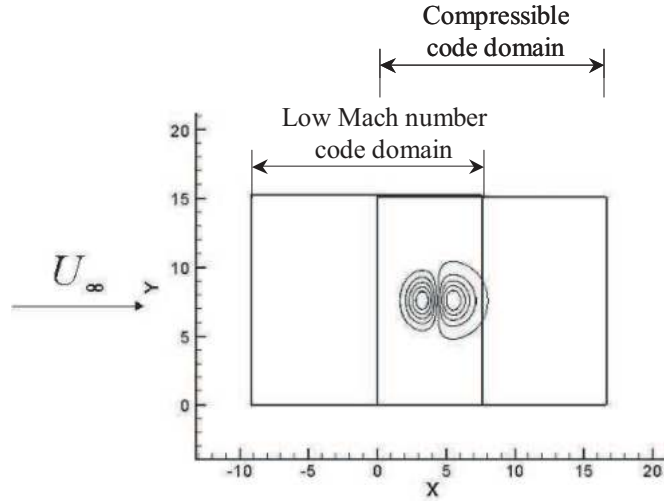
Figure 2.14: Computational domain for vortical disturbance. Vertical velocity contours are shown.

at the contours of dilatation. From equation (2.175) we can find the dilatation of the non-convecting Taylor vortex as

$$\text{div}\,\vec{v'} = \frac{1}{r}\frac{\partial}{\partial r}(rv'_r) + \frac{1}{r}\frac{\partial v'_\phi}{\partial \phi} + \frac{\partial v'_z}{\partial z} = 0, \tag{2.179}$$

since $v'_r = v'_z = 0$ and $\partial v'_\phi/\partial \phi = 0$.

When the Taylor vortex is superimposed on the uniform flow, it simply convects with it in the inviscid formulation, not producing any dilatation. Viscous effects actually generates weak dilatation for the nonlinear problem (see Colonius $et\ al.$ (1991)). However, for the present disturbance level of 1% we can consider the linearized problem and write the solution as $\vec{v} = \vec{v}_\infty + \vec{v'}$ using the principle of superposition. The dilatation of the superposed linearized solution is zero, since

$$\text{div}\,\vec{v} = \text{div}\,\vec{v}_\infty + \text{div}\,\vec{v'} = 0. \tag{2.180}$$

Another idealization comes from the fact that Taylor vortex is the solution of the incompressible equations, but a finite Mach number $M_\infty = 0.15$ is used in the compressible code.

However, this Mach number is still small enough and we can expect the values for the dilatation to be non-significant. Therefore, we can judge the accuracy of the interface conditions by looking at the dilatation levels of the numerical solution of the compressible code as the vortex is entering the computational domain.

Only methods A through D are considered in the present test problem. Maximum dilatation in the compressible domain is plotted versus x-coordinate of the center of the vortex in figure 2.15 for all four methods. We can see right away that method A is unstable. Dilatation reaches its maximum when the vortex center crosses the inflow boundary $x = 0$ for the methods B and D. This is due to the noise coming from the inflow boundary conditions. When disturbances are convected downstream further from the inflow boundary, dilatation levels come back to negligible value, which shows that numerical scheme holds the analytical value of almost zero dilatation pretty well. However, maximum dilatation levels are much larger for the Riemann invariant method (D) than for the injection(B). Method C, where density is obtained from pressure, gives the minimum dilatation levels when disturbances are crossing the domain, but fails to come back to zero dilatation level when disturbances are convected away. This method might lead to instabilities if calculations are continued further. Therefore, injection method (B), which is a simple interpolation of all five variables $\{\rho, u, v, w, T\}$ from low Mach number to compressible code gives the best overall performance for the present test case.

Behavior of the coupled solution (using injection method)

Maximum discrepancy between the components of velocity (equation (2.176)) obtained by each code in the coupled formulation is shown in figure 2.16. The difference in pressure calculated with equation (2.177) is again about two orders of magnitude smaller than the difference in velocity and not documented here.

The difference between the solutions for the fully coupled problem is even smaller compared to one-way coupling, which is probably due to the fact that two-way coupling enables simultaneous adjustment of the solutions of the two codes to each other through a feedback mechanism. It is worth noting that maximum discrepancy does not show a distinct peak as dilatation levels do, but stays at about the same level over the whole period when the vortex is inside the computational domain. This is because the maximum discrepancy is caused by the physical difference between the two equations sets being solved, and not by the performance of the interface conditions.

Vertical velocity along the horizontal line passing through the center of the vortex is
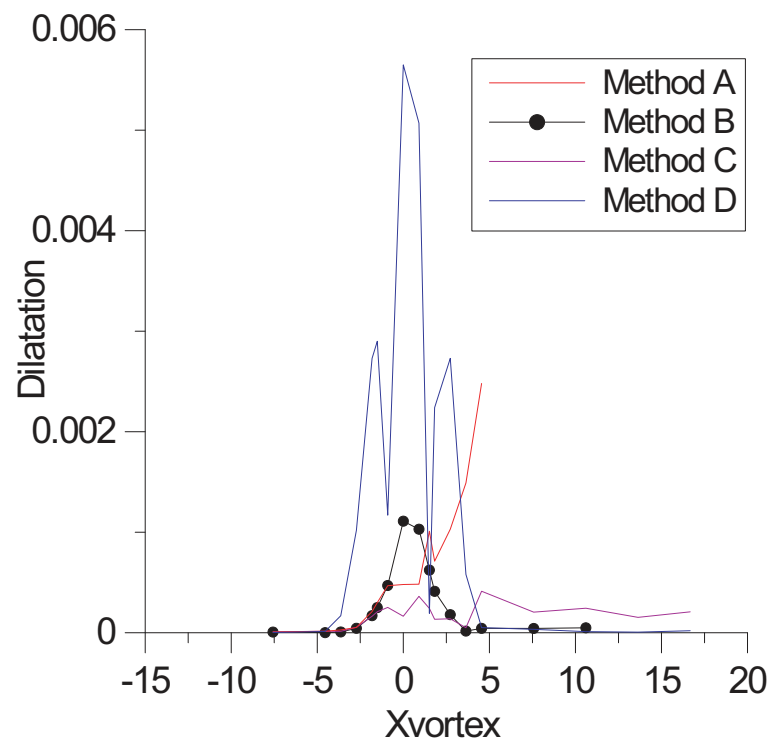
Figure 2.15: Dilatation levels in the compressible code versus x-coordinate of the vortex center.
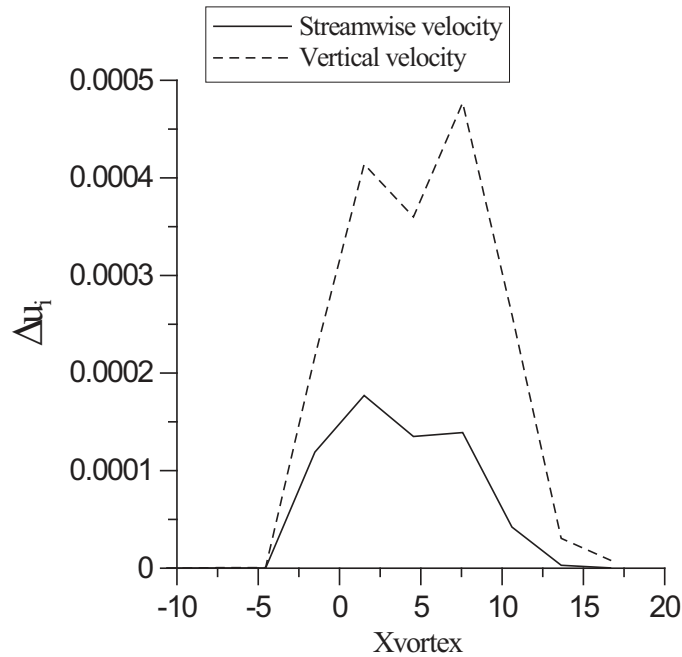
Figure 2.16: Maximum discrepancy for the coupled problem.

plotted in figure 2.17 for both the compressible and the low Mach number codes in the coupled calculation. Results of the stand-alone calculations performed with the compressible and the low Mach number codes, respectively, are also plotted for reference. Plots for the three relative positions of the vortex are shown: when the vortex enters the compressible code domain ($x_{vortex} = -1.5$, figure 2.17(a)), when it is in the center of the overlap region ($x_{vortex} = 4.55$, figure 2.17(b)) and when it exits the low Mach number code domain ($x_{vortex} = 10.6$, figure 2.17(c)).

When the vortex is far to the left from the outflow boundary of the low Mach number code domain, the difference between all four solutions is very small (figures 2.17(a) and 2.17(b)). However, the difference between the compressible solution and the solutions of the coupled calculation is larger than the difference between the two solutions of the coupled calculation in the overlap region. This is consistent with our earlier observation that solutions are closer when the codes are allowed to communicate through the feedback mechanism.

However, if we look at the profiles when the vortex is leaving the low Mach number code domain, we see some oscillations in the low Mach number code solution of the coupled calculation. These oscillations are due to the influence of the outflow interface conditions
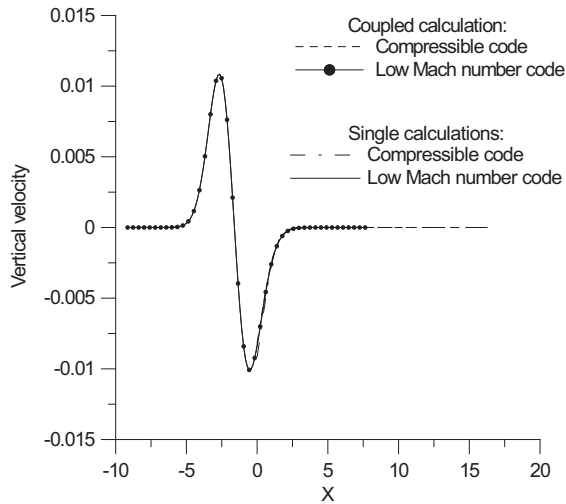
(a) Vortex enters compressible domain, $x_{vortex} = -1.5$.
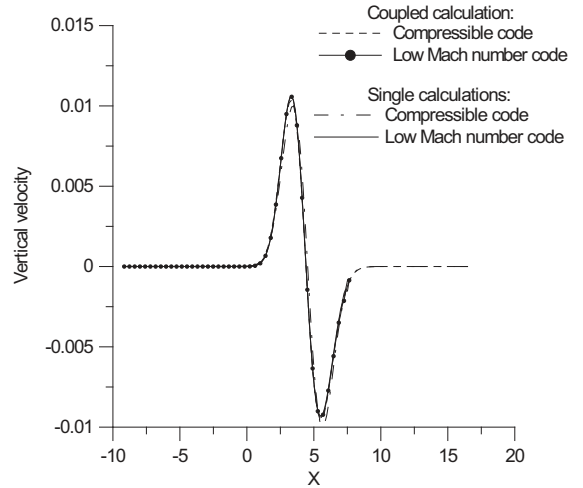
(b) Vortex in the middle of overlap, $x_{vortex} = 4.55$.
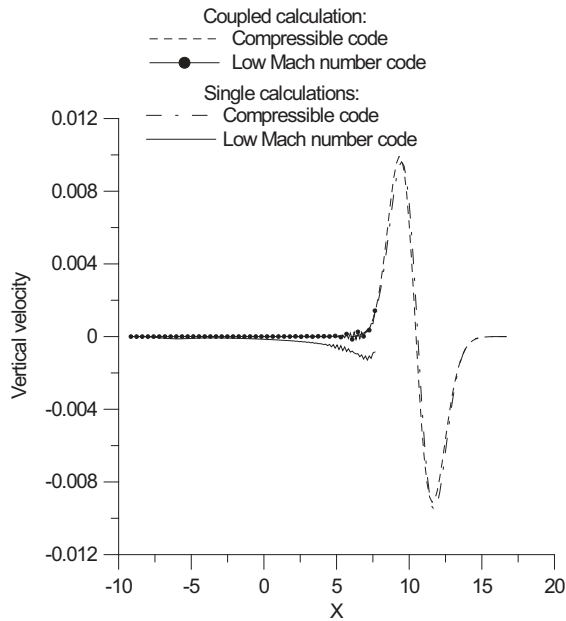
(c) Vortex exits low Mach number domain, $x_{vortex} = 10.6$.
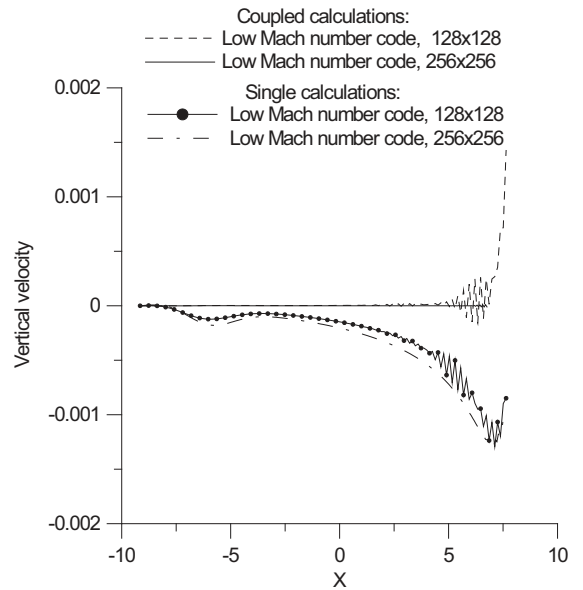
(d) Vortex exits low Mach number domain, grid size variation.

Figure 2.17: Vertical velocity along the horizontal line through the center of the vortex.

in the low Mach number code. It is interesting to note, that performance of a single low
Mach number code with convective outflow boundary conditions for the vortex leaving the
domain (see Pierce (2001)) is even worse. Not only the oscillations are not reduced in this
case, but also the mean value of the vertical velocity is significantly altered. This shows
that the present coupling procedure provides a good alternative to specifying approximate
outflow boundary conditions for the case of outgoing disturbances. To assess the influence
of a grid size on the performance of outflow boundary conditions, refined grid calculation
of both coupled and single problems was performed. The number of grid points in the
low Mach number code domain was increased from 128×128 to 256×256 with all other
parameters of the calculation left unchanged. Comparison of the vertical velocity profiles
for the vortex exiting the low Mach number code domain between original and refined
computations is made in figure 2.17(d). It can be seen that the magnitude of oscillations
is reduced with mesh refinement from 10^{-3} to 10^{-6} for the coupled problem, showing the
vast improvement of the performance of outflow interface conditions with the grid size. In
the stand-alone calculation, oscillations are also significantly reduced with grid refinement,
but velocity profile deviates even further from the correct value, showing a fundamental
drawback of the convective outflow boundary conditions in the low Mach number code
when organized outgoing disturbances are present. Reduction of oscillations at the outflow
with mesh refinement was observed in other simulations using low Mach number code.
Numerical experiments suggest the following empirical rule for choosing the grid size while
using this code in practice

$$\Delta x/L_d < 0.05, \tag{2.181}$$

(L_d is the disturbance scale). This condition usually ensures that the oscillations in the low
Mach number code due to the outflow boundary conditions are less than 0.1% of the mean
value.

Variable Density Regime

Entropy spot with the Gaussian temperature distribution given by equation (B.3), con-
vecting from low Mach number to compressible domain, is now considered for the variable
density formulation of the low Mach number code. Small and large disturbance amplitudes,
T_d, equal to 1% and 20% are tested. If viscous effects are not significant, the entropy distur-
bance simply convects with the mean flow. Reynolds number $U_\infty r_d/\nu_\infty = 6400$ is used in
the present simulation. Mach number for the compressible code is set to $M_\infty = 0.15$. Tem-
perature contours at the moment when the spot is in the overlap region (non-dimensional
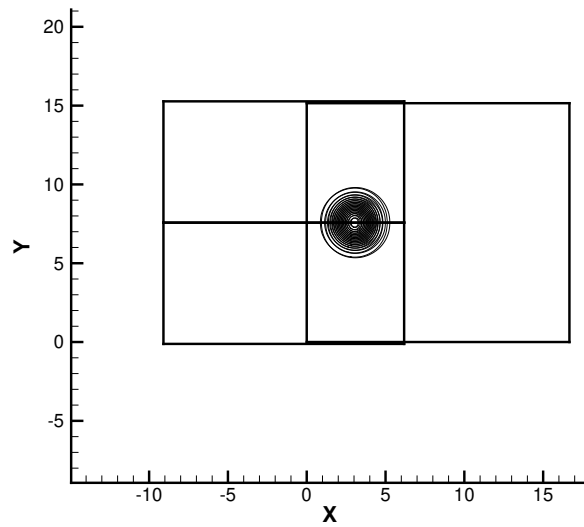
Figure 2.18: Computational domain for entropy disturbance. Temperature contours are shown. Computational time is $t\,U_\infty/r_d = 7.5$

computational time $t\,U_\infty/r_d = 7.5$) are shown in figure 2.18, all distances are normalized by the disturbance radius r_d.

Variation of interface conditions

Interface conditions supplied from the low Mach number to the compressible code are compared in the previous paragraph on the example of convecting vortical disturbance. However, density and temperature of the disturbance are constant in that case. Moreover, since the low Mach number code is run in incompressible regime, density and temperature are essentially not coupled. In the present problem, larger temperature and density variations are present, and due to the variable density setting of the low Mach number code, coupling of all the variables, such as velocities, density and temperature, is present. The author believes that this formulation offers more general setup to validate compressible interface conditions. Several variations of the interface conditions for the compressible code (methods A through E described in the beginning of the section 2.6.2) are analyzed here in the context of the entropy disturbance.

Stability

Stability of the methods A through E is assessed by looking at the dilatation levels in the compressible code for small disturbance case, $T_d = 1\%$. In case of a small disturbance amplitude, linearized formulation is a good approximation. Linear theory states that the dilatation of the entropy mode is zero when viscous dissipation is absent. Viscosity is small in the present calculation, so small values of dilatation are expected. Since numerical noise introduced by interface conditions directly affects the dilatation level, large values of this quantity is a good indication of instability. Levels of maximum dilatation in the compressible code are shown in figure 2.19 for 1% disturbance case for methods $A - E$. The first conclusion is that methods A, C and E (figure 2.19(a)), where density is not injected, but obtained either from continuity or from pressure, are unstable. This confirms the findings of the vortical disturbance case. Explanation of this fact is offered in section 2.5.

The other two other methods, B and D (figure 2.19(b)), result in bounded values of dilatation within the considered execution time. It is worth noting that coefficient of artificial dissipation is set to zero in the present calculation, which, in conjunction with rather large Reynolds number, represents quite a severe test for stability. In the case of convecting Taylor vortex, Reynolds number was sixteen times smaller and coefficient of artificial dissipation was not identically zero. Perhaps, this explains the difference in dilatation levels between these two cases (smaller for the convecting vortex case), especially after the disturbance exits the domain.

Stability properties of the interface conditions for the compressible code were extensively investigated in the context of domain decomposition method, where computational blocks calculated with the same numerical code are combined together (Berger (1985), Hesthaven (1997), Hesthaven (1998), Nördstrom & Carpenter (1999)). One of the promising methods for coupling several instances of a compressible code is the penalty method (see, for example, Carpenter *et al.* (1999)). Penalty method tries to mimic properties of continuous equations in the formulation of numerical interface closures. It uses special difference schemes satisfying the summation by parts (SBP) properties (Kreiss & Sherer (1974), Mattson & Nördstrom (2004)) and weak imposition of boundary conditions through the penalty terms (Nördstrom & Carpenter (1999)). Mathematical proofs of the strict stability of the method exist (Carpenter *et al.* (1999), Mattson & Nördstrom (2004)). Difference operators and boundary closure stencils up to any arbitrary degree of accuracy can be derived; practical applications, however, were limited so far to the 6th order of accuracy. Being an accurate and robust procedure for compressible – compressible interfaces, this method has been recently further developed to be used with the low Mach number equations and some

successful simulations of simple problems were performed for low Mach number – low Mach number coupling. Research is currently being conducted in the area of compressible – low Mach number coupling through the penalty method (Mattson *et al.* (2005)). However, the different structure of compressible and low Mach number equations complicates the formulation of interface closures which would keep the properties of the continuous problem. Moreover, it is not straightforward to extend existing stability proofs to the case of low Mach number – compressible coupling due to the different number of equations in each system resulting in the different rank of the discrete operators for each equations set.

Although theoretical background for the penalty method for low Mach number – compressible interfaces is not developed yet, penalty method was implemented in the current compressible code to perform comparison with two other stable methods, B and D. No penalization was done in the low Mach number code, where the same outflow interface conditions were used as previously. Note that penalizing just one part of the interface breaks the desired structure of the discrete operators and might cause the method to lose its nice properties.

Comparison of the dilatation levels for methods B, D and a penalty method can be seen in figure 2.19(b). Penalty method shows the smallest dilatation levels during an initial period. However, at a later time, dilatation levels for the penalty method rise to the values comparable with two other methods. Most likely, it is due to the fact that SBP properties of the method are violated due to one-sided use of the desired operators, and cancelation of boundary errors leading to an existence of energy estimate is no longer guaranteed (Mattson *et al.* (2005)).

Accuracy

To compare an accuracy of three stable compressible interface conditions – injection, Riemann invariants and a penalty, L_∞ and L_2 errors between numerical and analytical solutions are analyzed for the large disturbance case, $T_d = 20\%$. L_∞ and L_2 errors in temperature for the low Mach number code are shown in figure 2.20. It is seen that both L_∞ and L_2 errors in temperature for the low Mach number code do not depend on the coupling method. It is expected, since we do not vary the interface conditions for the low Mach number code in this test case. Errors in streamwise velocity for the low Mach number code are shown in figure 2.21. The same trend of little dependence of errors on the coupling method is observed. Errors in the low Mach number code exhibit maximum around the computational time $t\,U_\infty/r_d \sim 7$, which is seen especially for velocity errors. This time
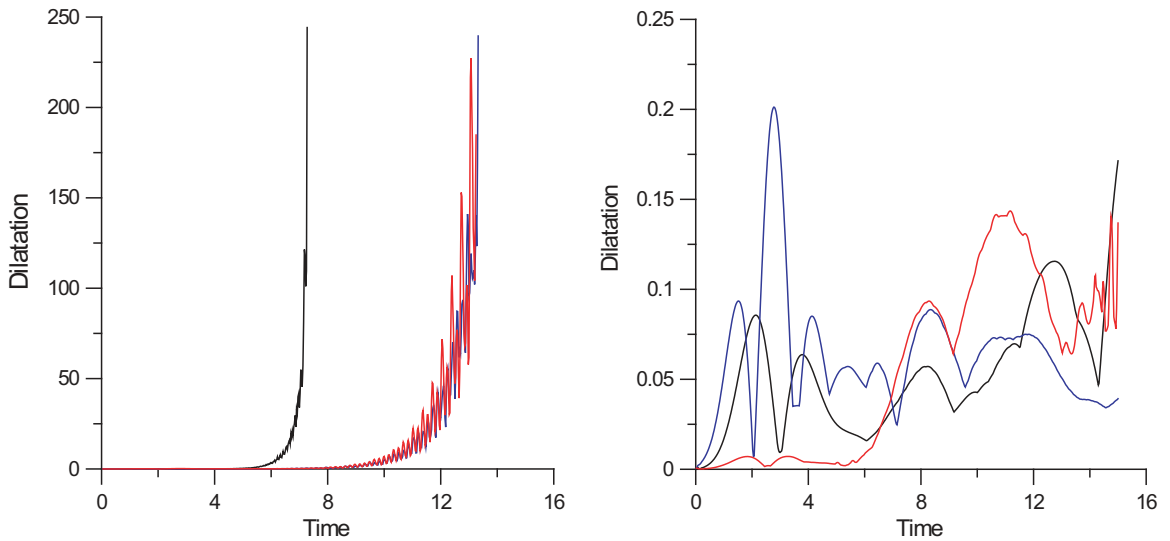
(a) Unstable methods. Black lines, density from continuity (method A); blue lines, density from pressure (method C) ; red lines, Riemann invariants with density from pressure (method E).

(b) Stable methods. Black lines, injection (method B); blue lines, Riemann invariants (method D); red lines, penalty.

Figure 2.19: Dilatation levels in the compressible code versus non-dimensional computational time, $t\,U_\infty/r_d$.

corresponds to the moment, when the disturbance crosses the outflow boundary and leaves the domain. Errors in both velocity and temperature decrease significantly after the exit of the disturbance.

For the temperature errors in the compressible code, plotted in figure 2.22, the dependence is also weak. In fact, all three methods show very similar performance. Most likely, temperature errors are dominated by viscous effects and not by interface conditions. Another confirmation of this hypothesis is the fact that temperature errors go back to zero in the low Mach number domain after the disturbance leaves it. Errors in streamwise velocity for the compressible code (figure 2.22) exhibit stronger dependence on the method. L_∞ errors are the smallest for the penalty method, followed by the injection method. Riemann invariants formulation results in the largest errors. For velocity errors in L_2 norm, trends are not as clear. Penalty method still produces the smallest errors, except for the time $t\,U_\infty/r_d \sim 6 \div 9$, when the disturbance occupies the overlap region (see figure 2.18). For the case of large, 20% disturbance amplitude, these three methods show the same general trends.

As a conclusion, all three methods show very similar behavior. Penalty method perhaps has a slight advantage over the other two methods, but does not show vast improvement

(a) L_∞ error.

(b) L_2 error.
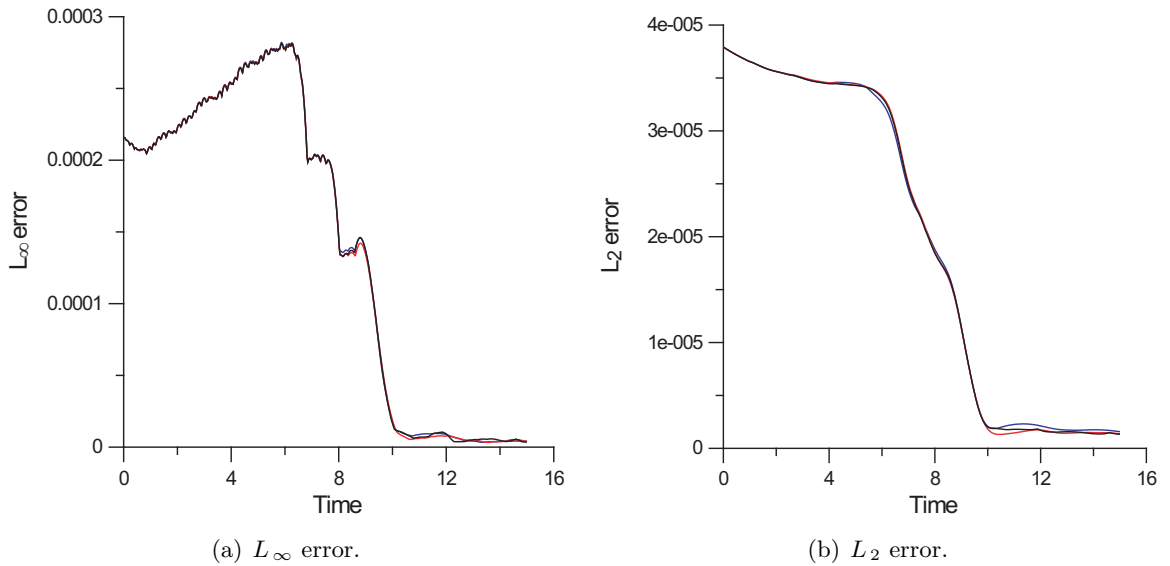
Figure 2.20: Errors in temperature versus non-dimensional computational time for the low Mach number code. Black lines, injection; blue lines, Riemann invariants; red lines, penalty.

compared to simpler injection and Riemann invariant formulations when implemented only in the compressible code. An accurate implementation of the method in both compressible and low Mach number codes is required in order to take full advantage of its superior stability and accuracy characteristics, which is postponed till theoretical and numerical background for such a coupling becomes available. Between injection and Riemann invariant methods, results are very close to each other for the entropy disturbance case; injection method performs a little better for the vortical disturbance case. Slightly better behavior of the injection method combined with its undoubted simplicity of implementation resulted in choosing injection method as the basic method for specifying interface conditions in the compressible code.

Behavior of the coupled solution (using injection method)

Profiles of the temperature are plotted along the horizontal line passing through the center of the disturbance, when it is in the region of overlap, in figure 2.24 for both 1% and 20% disturbance case calculated with the injection method. Numerical solutions for compressible and low Mach number codes, as well as analytical solution (B.3) are shown. Agreement between both numerical solutions and an analytical solution is very good showing good performance of the coupling procedure for both small and large disturbances.

(a) L_∞ error.
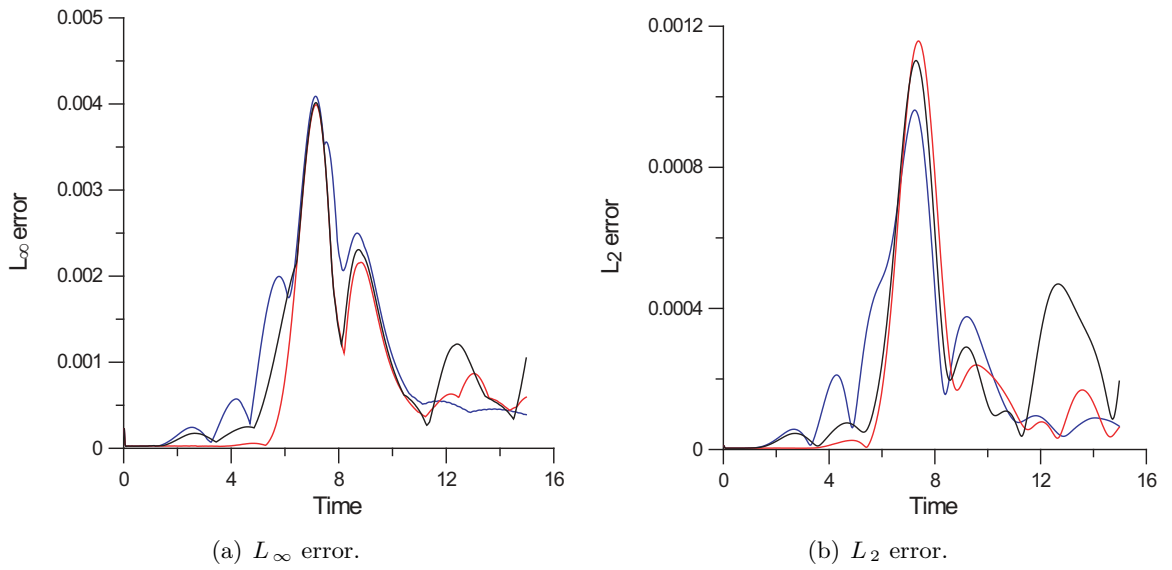
(b) L_2 error.

Figure 2.21: Errors in streamwise velocity versus non-dimensional computational time for the low Mach number code. Black lines, injection; blue lines, Riemann invariants; red lines, penalty.

(a) L_∞ error.
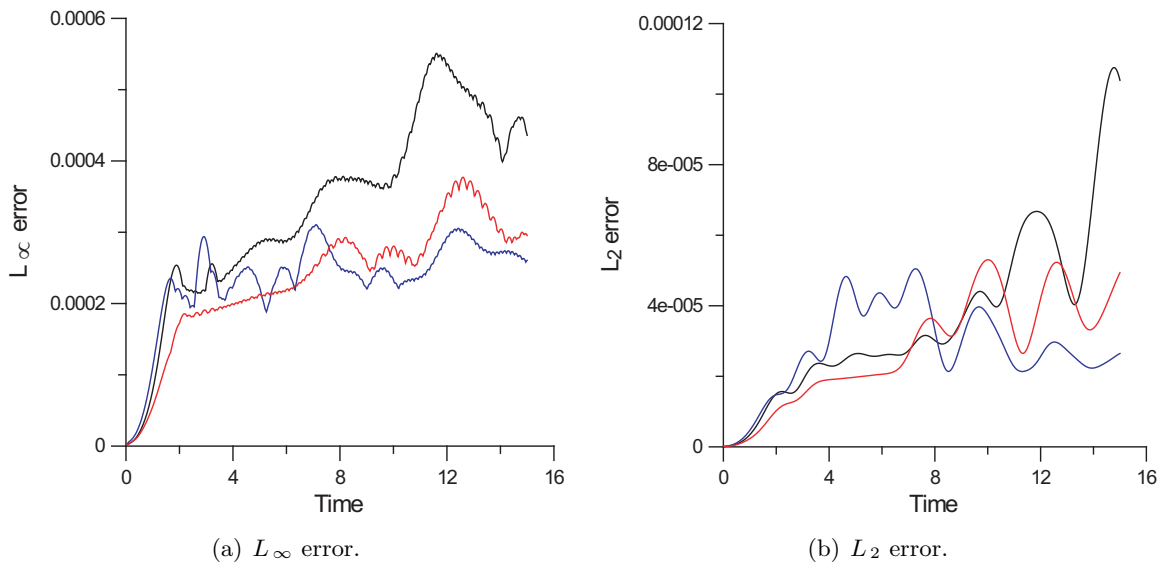
(b) L_2 error.

Figure 2.22: Errors in temperature versus non-dimensional computational time for the compressible code. Black lines, injection; blue lines, Riemann invariants; red lines, penalty.

(a) L_∞ error.

(b) L_2 error.
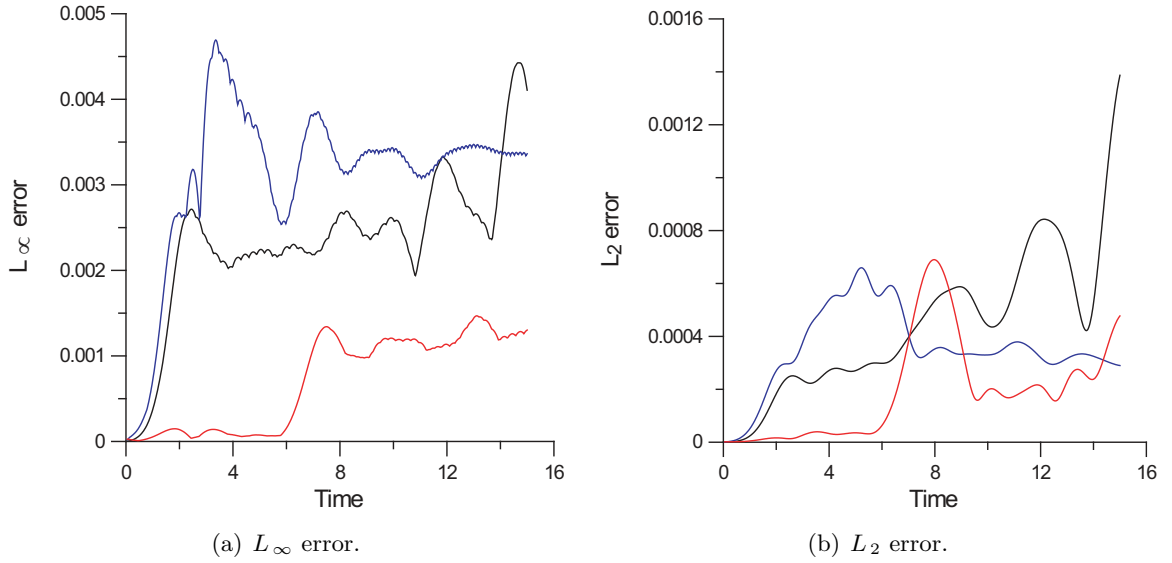
Figure 2.23: Errors in streamwise velocity versus non-dimensional computational time for the compressible code. Black lines, injection; blue lines, Riemann invariants; red lines, penalty.

(a) 1% disturbance.
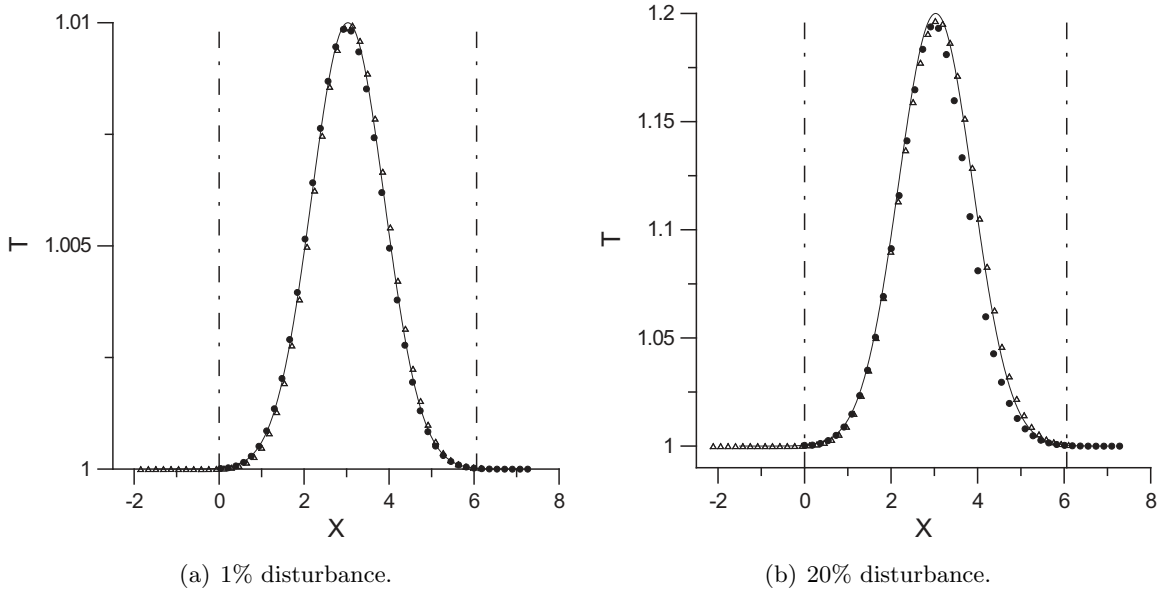
(b) 20% disturbance.

Figure 2.24: Temperature profiles through the center of the disturbance. $\bullet$, compressible code; $\triangle$, low Mach number code; ———, analytical solution; dash-dotted lines, boundaries of the overlap region.

Chapter 3

Laminar Jet in a Crossflow

3.1 Introduction

3.1.1 Previous Studies

Jet in a crossflow (JCF) can be considered as a technically relevant test problem before studying real film-cooling flows. The only difference between JCF and film-cooling flows, besides geometry, is that the temperature and the density of a jet and a crossflow are taken to be the same, while in film-cooling flows they are different. Though the difference in temperature and density definitely leads to the quantitative differences between two types of flows, many fundamental features of these flows are similar since they are caused by misalignment of momentum of injected jet relative to the mainstream, rather than by mismatch in temperature and density.

Jets in crossflow are thoroughly investigated and well documented over past years, providing reliable information for comparison with numerical results. This makes this problem suitable for testing the present computational method. There are three non-dimensional parameters pertinent to the JCF problem: jet Reynolds number $Re_j = U_j d/\nu$, crossflow Reynolds number $Re_\delta = U_\infty \delta/\nu$ and blowing ratio defined as $B = U_{jet}/U_\infty$ when $\rho_{jet} = \rho_\infty$ (here d is the jet diameter and δ is the crossflow boundary layer thickness). Many researchers have investigated cases of high blowing ratio greater than two, Kelso *et al.* (1996), Blanchard *et al.* (1999), Fric & Roshko (1994), Hasselbrink & Mungal (2001). However, high blowing ratio is representative of a different application of jets in crossflow, namely, dilution holes of gas-turbine combustors. Blowing ratio less than two are used in film cooling applications to keep the injected cold gas close to the surface. Among experimental investigations of jets in crossflow with small blowing ratio there are experiments of Gopalan *et al.* (2004), Peterson

& Plesniak (2002, 2004) and Gamussi *et al.* (2002). Gopalan et al. considered turbulent jets with flow Reynolds number $U_\infty d/\nu = 19000$, Peterson et al. were also looking at turbulent jets but emanating from the very short delivery tubes where the plenum configuration was a significant parameter. Gamussi et al. were looking at laminar jets with very low Reynolds number $U_\infty d/\nu = 100$.

There also exists many numerical investigations of JCF problem. Among them is Direct Numerical Simulations of Muppidi & Mahesh (2005) who looked at the influence of the jet velocity profile and the crossflow boundary layer thickness on the jet trajectory at two different velocity ratios, $VR = 1, 52$ and $VR = 5$.

3.1.2 Vortex Systems of Jet in a Crossflow

Basic coherent structures or vortex systems of JCF are described by many authors including Fric & Roshko (1994), Kelso *et al.* (1996), Gamussi *et al.* (2002), Blanchard *et al.* (1999). The primary feature of jets in crossflow is the counter-rotating vortex pair (CRVP). CRVP is created in the near field and occupies the entire cross-section of the jet, giving it the "kidney" shape. It carries streamwise-oriented vorticity. The length scale of CRVP is significantly greater than that of the turbulence, so CRVP is more a feature of the mean flow than the turbulence (Peterson & Plesniak (2002)). CRVP signature is observed far downstream from the jet injection, where the other vortex systems are diffused. Among other coherent structures is the horseshoe vortex system (HSV), which occurs upstream of the jet and close to the wall and is formed due to the blockage of the crossflow by the jet. Ring-like vortices (RLV), or shear-layer vortices with transverse vorticity are formed on the lateral edges of the jet. Ring-like vortices are unsteady structures, contrary to CRVP and HSV.

Many researchers who conducted experiments on jets in crossflow varying the blowing ratio noticed that the evolution of vortical structures is qualitatively different for different blowing ratios (Gamussi *et al.* (2002), Blanchard *et al.* (1999), Kelso *et al.* (1996), Fric & Roshko (1994), Gopalan *et al.* (2004)). Some of the authors observed the existence of two kinds of regimes: low-B and high-B regime, where B is the blowing ratio(Gamussi *et al.* (2002), Blanchard *et al.* (1999), Gopalan *et al.* (2004)). $B \sim 2 \div 3$ was found as a dividing line between two regimes, most likely depending on the other non-dimensional parameters describing the flow. One of the significant differences between two regimes is the structure of the wake region of the jet right above the wall. For small blowing ratio, the large zone of reverse flow occurs to the right of the jet injection. It is called the "dead

zone" by Gopalan *et al.* (2004) and DSSN vortices (downstream spiral separation node) by Peterson & Plesniak (2002) DSSN vortices are steady and spatially stationary. For high blowing ratio, the formation of the "dead zone" is not observed, but instead the unsteady vortices of alternating sign are formed by the roll-up of wall boundary layer fluid. These "wake" or "upright" vortices are described in details by Fric & Roshko (1994) and Kelso *et al.* (1996). These structures are generally not noticed for blowing ratios below two.

Another reported common feature of jets in crossflow at small velocity ratios is the existence of three-dimensional "hairpin" vortical structures(Tyagi & Acharya (2003), Blanchard *et al.* (1999), Gamussi *et al.* (2002), Gopalan *et al.* (2004)). It is believed that other vortical systems observed in low-B jets (CRVP, RLV and wall-normal vortices) constitute the base, the top part and the legs of the "hairpin" structures, respectively. Blanchard *et al.* (1999) attribute formation of the "hairpin" structures to the elliptical instability of CRVP. Gamussi *et al.* (2002) propose the mechanism of pairing of two counter-rotating longitudinal vortex tubes to form a single three-dimensional structure. Gopalan *et al.* (2004) hypothesizes that stretching of the jet vortex ring in vertical direction is a formation mechanism for the "hairpin" structures, which the authors call "semi-cylindrical vortical layer" in their paper. No "hairpin"-type structures were reported in high-B experiments. The reason for the substantial difference in jet vortical structures at small and high blowing ratios is still the subject of ongoing research.

3.2 Simulation Results

3.3 Geometry and Boundary Conditions

The case I of Muppidi & Mahesh (2005) with $VR = 1.52$ (see Table I of Muppidi & Mahesh (2005) for the detailed description) was chosen for comparison with the results of the present computational method. Schematical configuration of the geometry is shown in figure 3.1. Jet with diameter d issues perpendicular to the crossflow. Jet Reynolds number $Re_j = U_j d/\nu = 1500$, where U_j is the jet bulk velocity; blowing ratio $U_j/U_\infty = 1.52$. Characteristics of the crossflow are as follows: 80% boundary layer thickness at the inflow $\delta_{80\%} = 1.32d$, which gives crossflow Reynolds number $U_\infty \delta_{80\%}/\nu = 1300$. Mach number $M_\infty = 0.15$ is used for the crossflow in the present simulation, which is different from $M_\infty = 0$ in incompressible calculations of Muppidi & Mahesh (2005). According to the non-dimensional parameters, both jet and crossflow are in laminar regime.
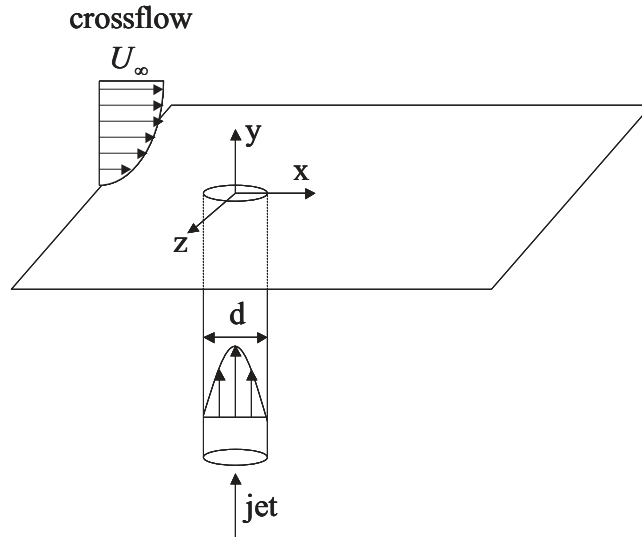
Figure 3.1: Schematics of the jet in crossflow problem.

Projection of the full computational domain onto $x - y$ plane is shown in the figure 3.2. It consists of the low Mach number code domain and the compressible code domain.

3.3.1   The low Mach Number Code Domain

Cylindrical domain with diameter d and height $2.2\,d$ is used for the calculation of the jet by the low Mach number code. The domain extends $2\,d$ below the crossflow surface, and $0.2\,d$ above, so that cylindrical region of overlap with compressible code domain exists with diameter d and height $0.2\,d$ (see the enlarged view of the region of overlap in the figure 3.2(b).) Grid of $94 \times 64 \times 64$ points with uniform distribution in streamwise, radial and circumferential directions, respectively, is used. This gives maximum cell size of $0.02\,d \times 0.008\,d \times 0.05\,d$, which satisfies the resolution requirement $\Delta x/L_d < 0.05$ given by equation 2.181 of the chapter 2. Jet parabolic profile is specified at the inflow of the domain $2\,d$ below the crossflow surface. No-slip boundary conditions are used at the pipe walls, which extend from the jet inflow to the crossflow surface. Boundary conditions described in chapter 2 are specified at the "free" boundaries, corresponding to the boundaries of the overlap region.

3.3.2 The Compressible Code Domain

Cartesian domain with dimensions $30\,d \times 10\,d \times 3\,d$ is used for the calculation of the crossflow by the compressible code. Computational grid with $204 \times 144 \times 51$ grid points is used. Grid is clustered at the region of jet injection as well as at the crossflow boundary layer. Clustering is designed so that the fine grid approximately follows the jet trajectory before it is turned by the crossflow. Every 4th point in streamwise direction and every 10th point in vertical direction is shown in figure 3.2(a), and every point is shown in the enlarged view of figure 3.2(b). The grid is uniform in the spanwise direction. Although better resolution might be required for an accurate description of the quantitative flow characteristics, it is definitely sufficient for providing a qualitative representation of the flowfield. More on the grid refinement and the limitations of the present grid can be found at the end of the current chapter, section 3.3.5. Boundary layer profile is specified at the inflow located about $10\,d$ upstream of the jet. No-slip and isothermal boundary conditions are used at the bottom wall with density obtained from the continuity equation. Wall is heated to the value of the stagnation temperature $T_{0\infty} = (1 + \frac{(\gamma-1)}{2} M^2)\, T_{\infty}$. Note that this value is different from the adiabatic wall temperature $T_{aw} = (1 + r\frac{(\gamma-1)}{2} M^2)\, T_{\infty}$, which would be the temperature of an insulated wall. Values interpolated from the low Mach number code according to the method described in chapter 2 are specified at the place of jet injection. Parameters calculated at the edge of the boundary layer are set at the top of the computational domain. At the outflow, located $20\,d$ downstream of the jet injection, parabolized Navier-Stokes equations are solved. In the spanwise direction, periodic boundary conditions are applied. Since spanwise length of the domain is $3\,d$, the present configuration corresponds to a periodic array of film-cooling holes with the pitch of $3\,d$. This configuration is different from the case of a free jet calculated by Muppidi & Mahesh (2005).

Calculations are initialized as follows. First, the steady solution for the crossflow boundary layer in absence of the jet is obtained. This solution is interpolated into the low Mach number code domain, so that the region of overlap in the low Mach number code also gets initial conditions corresponding to the crossflow boundary layer. Then jet is slowly turned on, so that the jet bulk velocity changes in time corresponding to the formula

$$U_j = \{ \begin{array}{ll} U_j^{max}\, t/t_{lag} & \text{if } t < t_{lag} \\ U_j^{max} & \text{otherwise} \end{array} .$$

Here t is the computational time, t_{lag} is the time lag equal to $2\,d/U_{\infty}$ and U_j^{max} is the
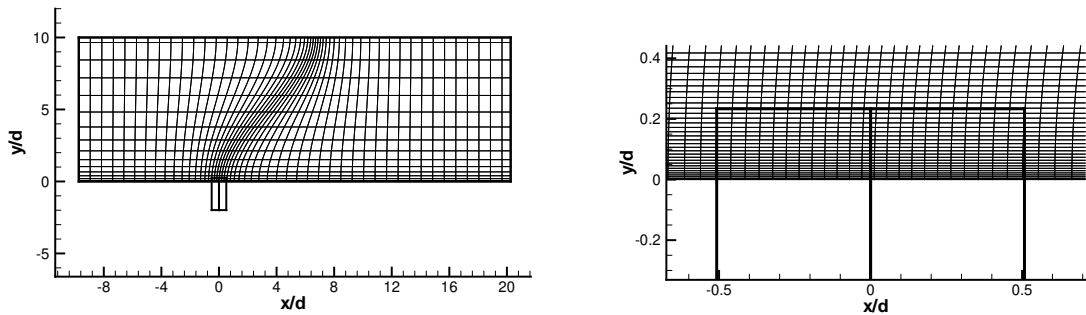
(a) The whole domain.

(b) Enlarged view of the overlap region.

Figure 3.2: Projection of the computational domain onto $x - y$ plane.

final bulk velocity. Without the slow injection, disturbances suddenly supplied to the compressible code would be too large leading to numerical instability. Solutions are advanced in time with the computational time step $0.01 \, d/U_\infty$.

3.3.3   Vorticity Dynamics

In this section we try to identify vortical structures described above in the present calculations. Although the current calculations use spanwise periodic boundary conditions and strict comparison with previous work on isolated JCF is not possible, it is still useful to make qualitative comparison.

To look at vorticity dynamics of the present calculations, we plot vorticity and streamlines at different cross-sections. Instantaneous and time-averaged normalized transverse vorticity $\omega_z \, d/U_\infty$ in $x - y$ plane taken through the center of the jet $z/d = 0$ is plotted in figure 3.3(a) and figure 3.3(b). We call this plane a center-plane in the present discussion. Only compressible code domain is shown for the sake of clarity. In the time-averaged field, only two shear layers at the lateral edges of the jet are visible, and no vortices are present. This confirms the fact that transverse vortices are non-stationary and unsteady structures. Instantaneous transverse vorticity field is much more complex, showing at least three rows of transverse vortices. Instantaneous and time-averaged in-plane velocity $\sqrt{u^2 + v^2}$ and streamlines are plotted in figure 3.4(a) and figure 3.4(b). Both compressible and low Mach

number code domains are shown. Looking at both instantaneous and time-averaged stream-lines one can notice the node point. It looks like streamlines are originating from this point and diverging in all directions. The similar node point is shown in figure 16 of Kelso *et al.* (1996) for blowing ratios B=2.2 and in figure 5(a) of Muppidi & Mahesh (2005) for the same flow regime as present calculations. The location of the node is $(x/d \sim 0.83, y/d \sim 0.27)$, which is close to $(x/d \sim 1.05, y/d \sim 0.3)$ cited by Muppidi & Mahesh (2005) It is interesting to note that the windward and leeward sides of the jet eventually collapse in the vertical center-plane. Instantaneous streamlines show the oscillations of the jet trajectory as well as formation of unsteady transverse vortices. The enlarged view of time-averaged steamlines is shown in figure 3.5(a). The horseshoe vortex is seen upstream of the jet with clockwise rotation. It is located at $(x/d = -0.82, y/d = 0.11)$ which is a little bit closer to the jet than $x/d = -1.4$ found by Muppidi et al. Hovering vortex is also observed just above the jet exit near the leading edge, consistent with observations of Muppidi & Mahesh (2005) and Kelso *et al.* (1996). Hovering vortex is only resolved in the low Mach number code do-main, since the size of the grid Δx in the compressible code domain is about five times larger than in the low Mach number code domain in the region of jet injection. Time-averaged steamlines in compressible code domain are shown in figure 3.5(b) with no hovering vortex. This explains the fact that hovering vortex in our coupled simulations extends vertically only up to to $y/d \sim 0.2$, where the low Mach number code domain ends. It persists up to $y/d \sim 0.75$ in calculations of Muppidi & Mahesh (2005). One can notice the intersection of streamlines just above the hovering vortex in figure 3.5(a) since streamlines are calcu-lated from two different flowfields – one with the hovering vortex, and the other - without it. Muppidi & Mahesh (2005) used incompressible code similar to the present low Mach number code everywhere. Incompressible code is computationally much less expensive than the fully compressible one, which allowed Muppidi & Mahesh (2005) to keep the resolution higher than in the present calculations. This observation suggests that the resolution of the compressible code in the region of the jet injection must be increased in order to capture the near-wall structures.

In order to determine the path of the jet fluid, we plot three-dimensional time-averaged streamlines originating from the various parts of the jet in figure 3.6(a). Five streamlines originating at the the center-plane (–0.1,0,0), (0,0,0), (0.1,0,0), (0.2,0,0) and (0.3,0,0) follow the jet trajectory, which is defined as the streamline originating from the center of the jet exit by Muppidi et al. However, four streamlines originating off the center-plane (0,0,–0.5), (0,0,–0.1), (0,0,0.1) and (0,0,0.5) follow much lower trajectory and occupy the region which

(a) Instantaneous vorticity.

(b) Time-averaged vorticity.
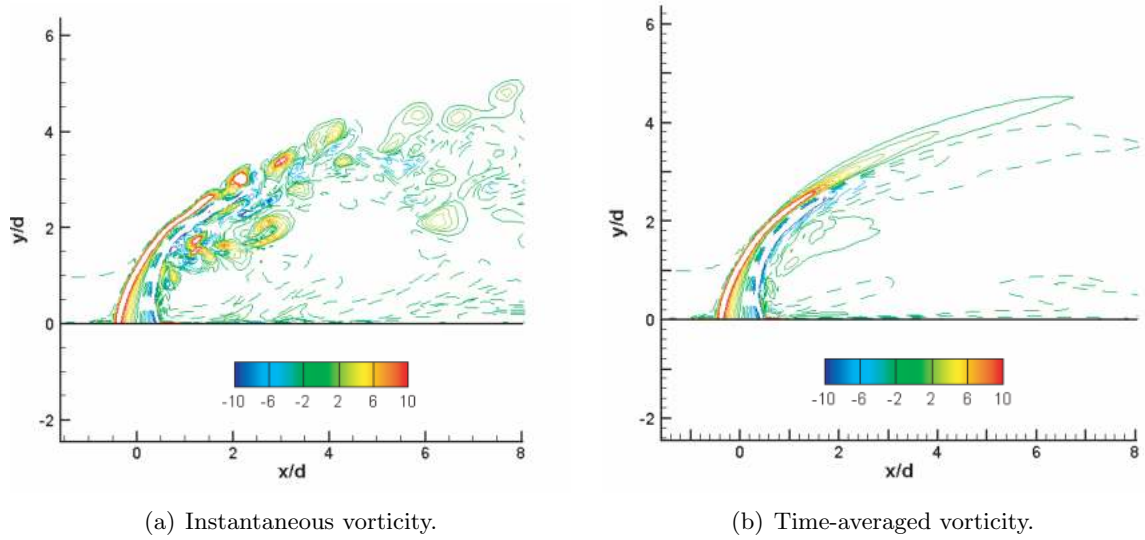
Figure 3.3: Transverse vorticity, $\omega_z\, d/U_\infty$. $x-y$ plane, $z/d = 0$. Solid lines – positive vorticity, dashed lines – negative vorticity.

(a) Instantaneous flow-field.

(b) Time-averaged flow-field.
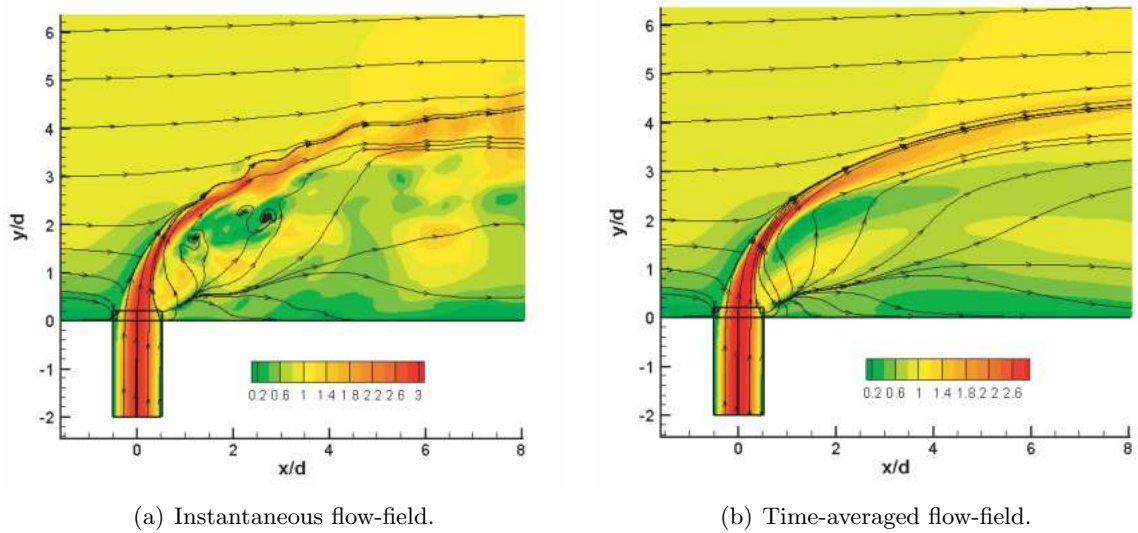
Figure 3.4: In-plane velocity, $\sqrt{u^2 + v^2}$, and streamlines. $x-y$ plane, $z/d = 0$.
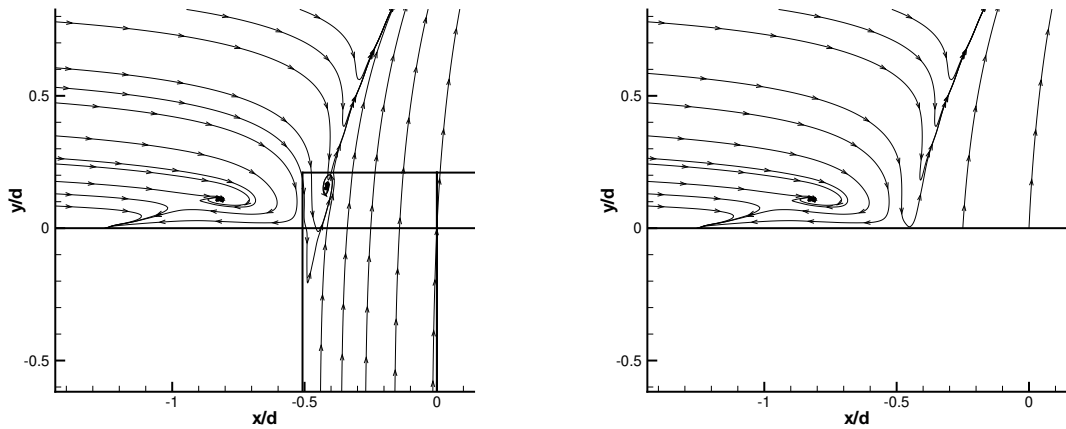
(a) Compressible and low Mach number code domains.

(b) Only compressible code domain.

Figure 3.5: Time-averaged streamlines. $x - y$ plane, $z/d = 0$. Enlarged view.

might be called the wake of the jet. The off-center-plane jet fluid follows lower trajectory since it faces stronger cross-flow, which experiences less blockage by the jet. Two streamlines which are coming from the leading edge of the jet (–0.45,0,–0.005) and (–0.45,0,0.005) bend around the jet together with the crossflow, since they don't have enough momentum to resist the crossflow and follow the jet trajectory. If we look at the $x - z$ projection of the three-dimensional streamlines in figure 3.6(b), we see that the center-plane jet fluid following the jet trajectory stays in the center-plane. The off-center-plane fluid is gathered at about $z/d \sim \pm 1$, which are the lateral boundaries of the jet wake. Fluid coming from the leading edge of the jet is lifted with the crossflow. It almost reaches the center-plane at $x/d \sim 1.5$, but later merges with the lateral boundaries of the wake. The $y - z$ projection of the trajectories (figure 3.6(c)) shows that all the jet fluid not coming from the immediate vicinity of the jet centerline is gathered into the CRVP, whose vertical and spanwise extent coincides with the extent of the jet wake.

In order to extract three-dimensional coherent structures, the isosurface of the Laplacian of pressure $P_{k,k}$ corresponding to a positive value of 5 is plotted in figure 3.7 together with three-dimensional streamlines. Since the vortex cores are associated with strong vorticity and local pressure minima, it can be shown that positive isosurfaces of $P_{k,k}$ can be used to identify coherent structures Tyagi & Acharya (2003). Coherent structures similar to the hairpin vortices observed by other authors are visible. It appears that two layers of hairpin vortices are present – above the wake region and in the wake region. The structures above

(a) Three-dimensional view.   (b) $x - z$ projection.   (c) $y - z$ projection.
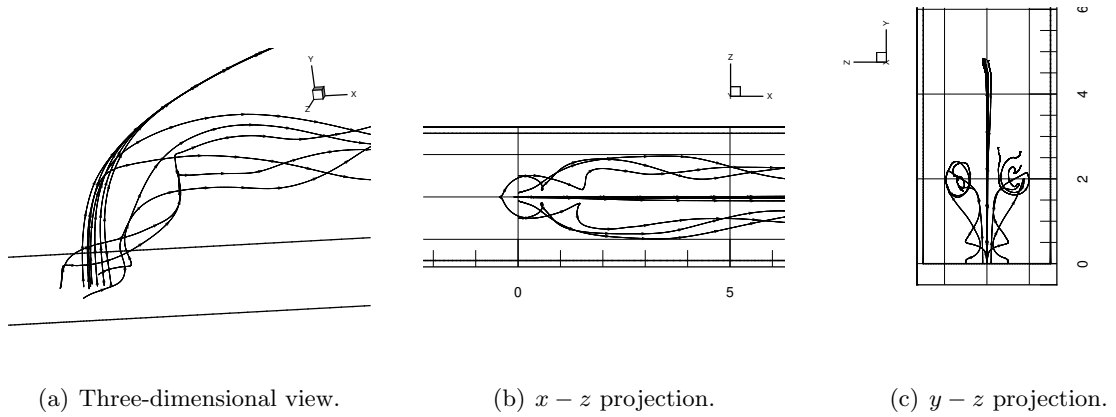
Figure 3.6: Time-averaged three-dimensional streamlines originating from the jet.
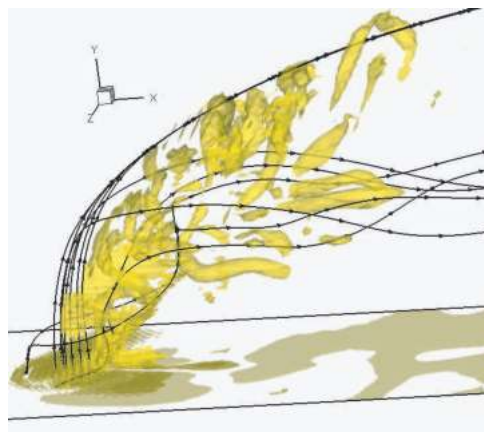
Figure 3.7: Isosurface of the Laplacian of pressure $P_{k,k} = 5$. Three-dimensional view.

(a) $x - z$ projection.   (b) $y - z$ projection.
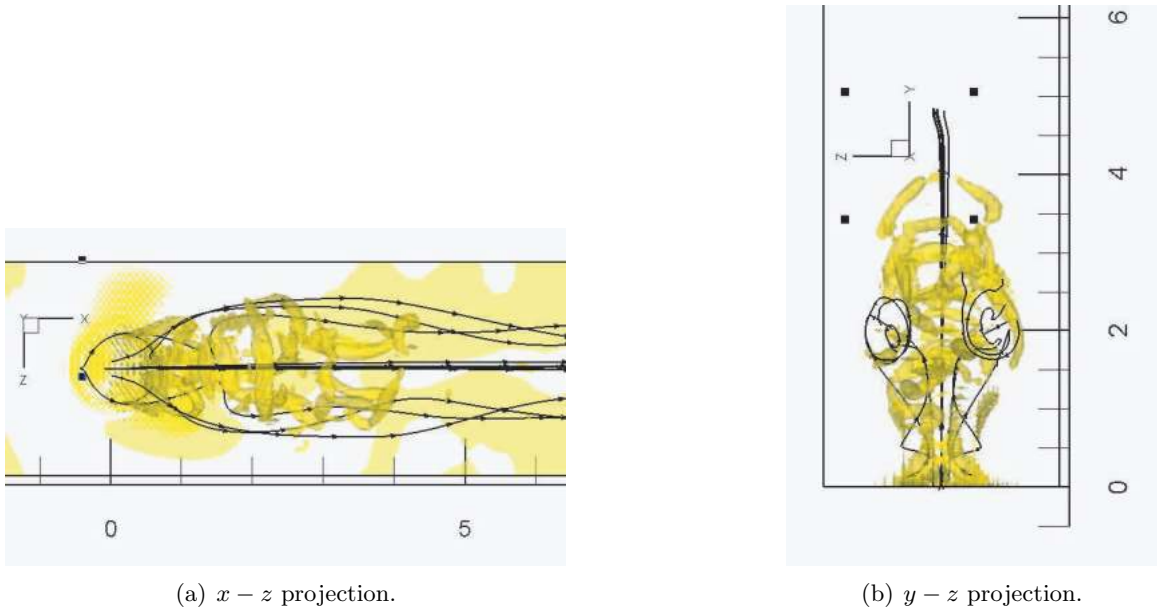
Figure 3.8: Isosurface of the Laplacian of pressure $P_{k,k} = 5$.

the wake region have their top parts linked to the jet trajectory. The lower structures are located just below the upper structures with their legs penetrating the wake region. Streamwise-oriented vortex tubes are scattered in the region of the wake corresponding to the streamwise vorticity carried by CRVP. The projection of coherent structures in $x - z$ and $y - z$ planes is shown in figure 3.8(a) and 3.8(b), respectively.

To investigate the path of the cross-flow fluid, three-dimensional streamlines originating from the different parts of the crossflow are plotted in figure 3.9(a). A streamline coming from the center of the jet is also shown to outline the jet trajectory. Several streamlines originating very close to the center-plane plane ($z/d \pm 0.01$) at different distances from the wall are shown. Streamlines originating at $y/d = 2$ and higher in the crossflow merge with the jet. Streamlines coming from $y/d = 1.5$ go around the jet deflecting only slightly from the center-plane (see also $x - z$ view in figure 3.9(b)). Trajectories coming through $y/d = 1$ deflect more and rise right behind the jet into the wake of the jet. Fluid originated from the crossflow boundary layer at $y/d = 0.5$ experiences reverse motion behind the jet and then an uplift into the jet wake. This reverse motion behind the jet creates a node point observed in figure 3.4. Also, two streamlines caught up into the upstream horseshoe vortex are shown. They go wide around the jet and rejoin together at the center-plane at $x/d \sim 3.5$. Streamlines originating at $z/d > 0.1$ and $y/d < 2$ circle around the jet, then reverse back and rise into the wake of the jet, creating DSSN vortices noticed by Peterson

(a) Three-dimensional view.

(b) $x - z$ projection.
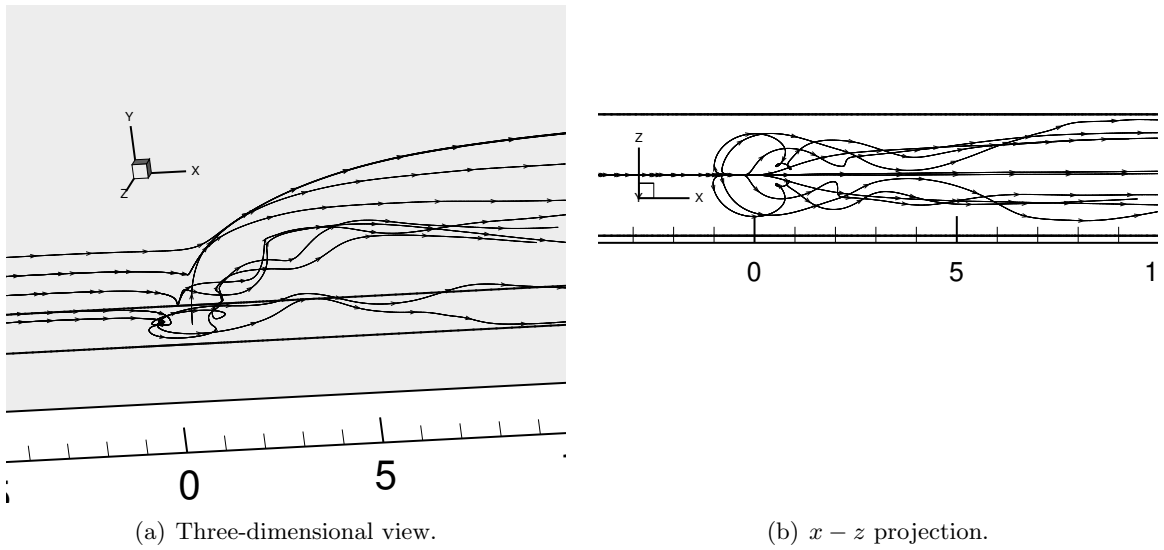
Figure 3.9: Time-averaged   om the crossflow.
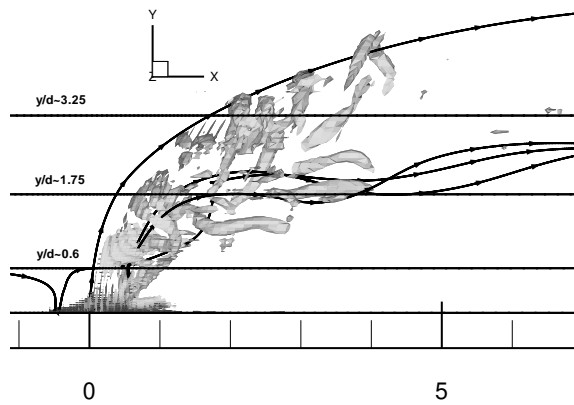
Figure 3.10: Horizontal cross-sections with respect to the coherent structures.

& Plesniak (2002). These streamlines are not plotted here for the sake of picture clarity.

To complete the picture of JCF behavior, we look at instantaneous and time-averaged normalized vertical vorticity $\omega_y \, d/U_\infty$ as well as streamlines in the horizontal cross-sections. Location of used horizontal cross-sections with respect to coherent structures is shown in figure 3.10. Several streamlines originating from the center and the edges of the jet are also plotted to mark the wake region and the jet trajectory. DSSN vortices consisting of the crossflow recirculating behind the jet are revealed in figure 3.11 in the horizontal plane $y/d \sim$ 0.6. Notice that there is almost no difference between instantaneous (figure 3.11(a)) and time-averaged (figure 3.11(b)) vorticity, showing that DSSN vortices are spatially stationary and steady structures as was noted by Peterson & Plesniak (2002). Another node point as

(a) Instantaneous vertical vortic-
ity, $\omega_z\, d/U_\infty$.

(b) Time-averaged vertical vortic-
ity, $\omega_z\, d/U_\infty$.

(c) Time-averaged in-plane veloc-
ity, $\sqrt{u^2 + w^2}$, and streamlines.
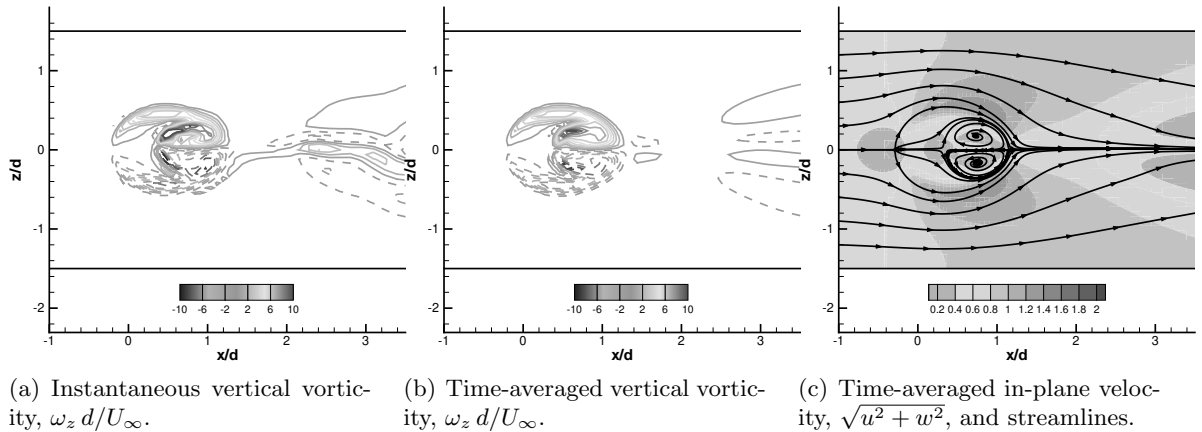
Figure 3.11: Horizontal cross-section, $y/d \sim 0.6$. Solid lines – positive vorticity, dashed
lines – negative vorticity.

well as the recirculating flow is seen in the time-averaged streamline pattern (figure 3.11(c)).
The horizontal plane coming through the wake of the jet $y/d \sim 1.75$ is shown in figure 3.12.
Instantaneous ω_y of only positive sign is found at $z/d \sim 1$ and only negative sign at $z/d \sim -1$
(figure 3.12(a)). This persistence in the vorticity sign is also reflected in the time-averaged
vorticity pattern, where two distinct vorticity lobes of the same sign and approximately the
same magnitude as instantaneous values are noticed (see figure 3.12(b)). The node point
again exists in the streamline pattern (figure 3.12(c). The node point corresponds to the lift
up of the crossflow fluid from below, which follows almost vertical path. Intersection of the
vertical streamline with the horizontal plane appears as the point of origin for the in-plane
streamline pattern. Therefore, existence of the node point in horizontal cross-section is an
indication of the wake region, where fluid is being tucked from below. The horizontal plane
passing through the legs of upper hairpin structures above the jet wake at $y/d \sim 3.25$ is
shown in figure 3.13. Vorticity pattern is completely different here than in the wake region.
Vortices of alternating sign are being shed on each side of the center-line $z/d = 0$, which
is seen in figure 3.13(a) (contours of instantaneous vorticity). Averaged vorticity has mush
smaller value than instantenous vorticity, showing that present vortical structures are of
alternating sign and they mostly cancel each other during averaging (see figure 3.13(b)).
Time-averaged streamline pattern does not have a node point, which agrees with the fact
that the horizontal plane $y/d \sim 3.25$ is above the wake region.

It is worth noting that coherent structures are only observed until $x/d \sim 5$, after which
they suddenly disappear. The disappearance of coherent structures might be caused by
the interactions among the jets which are separated by $3\,d$ in the spanwise direction in
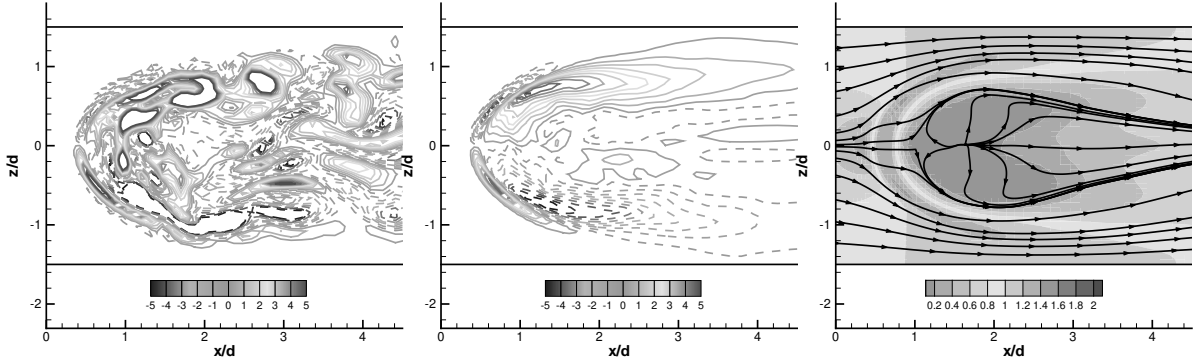
(a) Instantaneous vertical vortic-
ity, $\omega_z \, d/U_\infty$.

(b) Time-averaged vertical vortic-
ity, $\omega_z \, d/U_\infty$.

(c) Time-averaged in-plane veloc-
ity, $\sqrt{u^2 + w^2}$, and streamlines.

Figure 3.12: Horizontal cross-section, $y/d \sim 1.75$. Solid lines – positive vorticity, dashed
lines – negative vorticity.
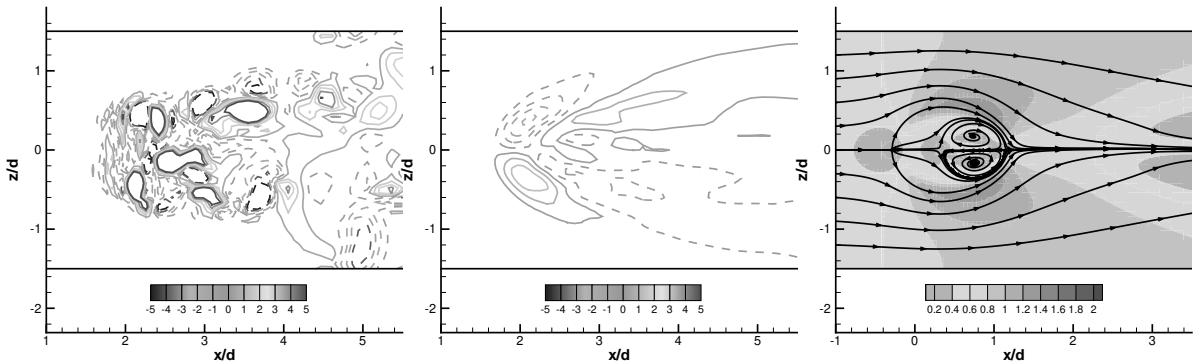
(a) Instantaneous vertical vortic-
ity, $\omega_z \, d/U_\infty$.

(b) Time-averaged vertical vortic-
ity, $\omega_z \, d/U_\infty$.

(c) Time-averaged in-plane veloc-
ity, $\sqrt{u^2 + w^2}$, and streamlines.

Figure 3.13: Horizontal cross-section, $y/d \sim 3.25$. Solid lines – positive vorticity, dashed
lines – negative vorticity.
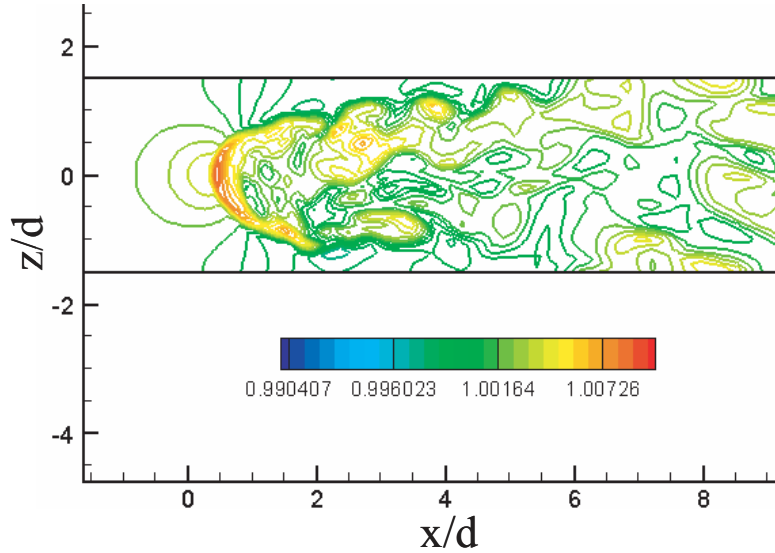
Figure 3.14: Contours of instantaneous temperature at $y/d \sim 1.75$.

the present computations or inadequate grid resolution, note grid distribution shown in figure 3.2. To look at the spanwise development of the jet, temperature contours in the horizontal plane $y/d \sim 1.75$ are plotted in the figure 3.14. Although temperature variations are small in the current computations, temperature field is still good for flow visualization since temperature plays the role of a passive scalar introduced from a jet into crossflow. Oscillations of the lateral boundary of the jet wake are observable. The lateral boundary reaches the edge of the domain $z/d = 1.5$ at $x/d \sim 5$. Coherent structures characteristic of a single jet are destroyed after this point by the interactions with the neighboring jets or dissipated by the grid which becomes coarser with the distance from the injection place.

3.3.4   Analysis of the Vorticity Dynamics

In this section we try to analyze the behavior of the vortical structures and their relations to each other. Jet fluid originating in the vicinity of the jet centerline follows the highest trajectory and stays in the center-plane. Two shear layers at the lateral edges of the jet are seen in the contours of instantaneous and time-averaged transverse vorticity (figure 3.3). When the jet trajectory starts oscillating, the vortices of alternating sign (with positive vorticity prevailing) are shed into the crossflow. These are the ring-like or shear-layer

vortices observed by other researchers (they are also sometimes called upper and lower structures). These vortices follow the jet trajectory (a streamline originating from the center of the jet). They form the top parts of the upper hairpin structures. Plot of instantaneous vertical vorticity through the legs of upper hairpin structures shown in figure 3.13(a) reveals the alternating signs of the vertical vorticity in the legs. This is in agreement with the alternating sign of the transverse vorticity of the top parts, which confirms the fact that both these vortical tubes are parts of the same hairpin structure. Both transverse and vortical vortices of alternating sign as well as upper hairpin structures occur at $x/d \sim 2 \div 4$, which again proves their interdependence. Basic mechanism suggested in the literature for the development of hairpin structures during jet-crossflow interactions is the instability of CRVP Blanchard *et al.* (1999),Gamussi *et al.* (2002). It should be noted that the upper hairpin structures, linked to RLV and jet trajectory, can not be generated this way. First, the roll-up of streamwise vortical tubes into one coherent structure would suggest that the vorticity sign of two successive structures should be the same, and not alternating, as in the present case. Second, the upper hairpin structures occur much higher than the wake region, where CRVP is located, which can be seen from figure 3.8 and figure 3.10, and their legs do not extend all the way to the wake region. Likely, the origin of the upper hairpin structures is Kelvin-Helmholtz instability of the shear layers on the leading and trailing edges of the jet, consistent with the explanation of Gamussi *et al.* (2002).

Fluid originating from off-center-plane of the jet follows lower trajectory and constitutes the wake of the jet, which extends about $1\,d$ in vertical and $2\,d$ in spanwise direction. Counter-rotating streamwise vorticity from the lateral boundaries of the jet is carried to the wake region and reorients in streamwise direction, creating strong counter-rotating vortex pair (CRVP), occupying the wake region and giving it elliptical cross-section. Lower hairpin vortex structures have their legs in the wake region. The legs are located at $z/d \pm 1$, which is also the position of the lateral boundaries of the wake region. It suggests that vertical vorticity of the legs is created by roll-up of streamwise CRVP tubes, occupying the lateral edges of the jet wake. Moreover, as the analysis of figure 3.12 shows, the instantaneous vertical vorticity in the wake region has a constant sign at the either side of the centerline $z/d = 0$, and this sign is consistent with CRVP rotation. Therefore, lower hairpin structures are possibly created by the CRVP instability mechanism proposed in Blanchard *et al.* (1999). Top part of the lower hairpin structures should, therefore, have negative transverse vorticity. Looking at figure 3.3(a) one can notice the layer of negative vorticity at $2 < x/d < 3$, $2.5 < z/d < 3$, exactly where the upper parts of the lower structures should be.

One can notice that lower hairpin structures are wider than the upper structures, having $2\,d$ versus $1.2\,d$ distance between its legs. Positive transverse vorticity in the center-plane at $1.6 < y/d < 2$ is brought from the windward side of the jet by the jet fluid which is carried around the jet and lifted up into the wake together with the crossflow fluid. Negative transverse vorticity next to the lee side of the jet occurs because of the deformation of the lee-side negative shear-layer vorticity.

3.3.5 Grid Refinement

It was noted in section 3.2 of the present chapter, that hovering vortex was resolved only in the low Mach number code domain (figure 3.5). Calculations of a laminar jet in a crossflow were repeated, where compressible grid was significantly refined in x direction, especially in the region close to the leading edge of the jet. All other parameters of the calculations were left the same. Clustering was achieved at the expense of shortening the length of the domain in a streamwise direction from $30\,d$ to $6.5\,d$. The size of the new domain can be viewed in figure 3.17, where time-averaged vertical velocity and a center streamline are also plotted. Time-averaged streamlines in the center-plane together with the computational meshes are plotted for the coarse grid in figure 3.15 and for the fine grid in figure 3.16. With the refined grid, hovering vortex is observed in both low Mach number and compressible domains, which can be seen in figure 3.16. It is interesting to note that although low Mach number domain is the same for both calculations, the size of the vortex is different in the low Mach number domain depending on the compressible code domain resolution. It again confirms the strong mutual dependence of the solutions of different codes on each other during coupling.

The jet trajectory, defined as the time-averaged streamline originating in the center of the jet exit cross-section, is compared for both grids with the results of DNS of Muppidi & Mahesh (2005) in figure 3.18. Fine grid results agree perfectly with the calculations of Muppidi & Mahesh (2005) in the near field. The failure of the jet to rise with the expected slope beyond $x/d \sim 2$ may be attributed to the very short length of the computational domain and influence of the outflow boundary conditions. For much longer domain of the coarse grid, this sudden bending is not observed; however, the overall trajectory is a little lower.
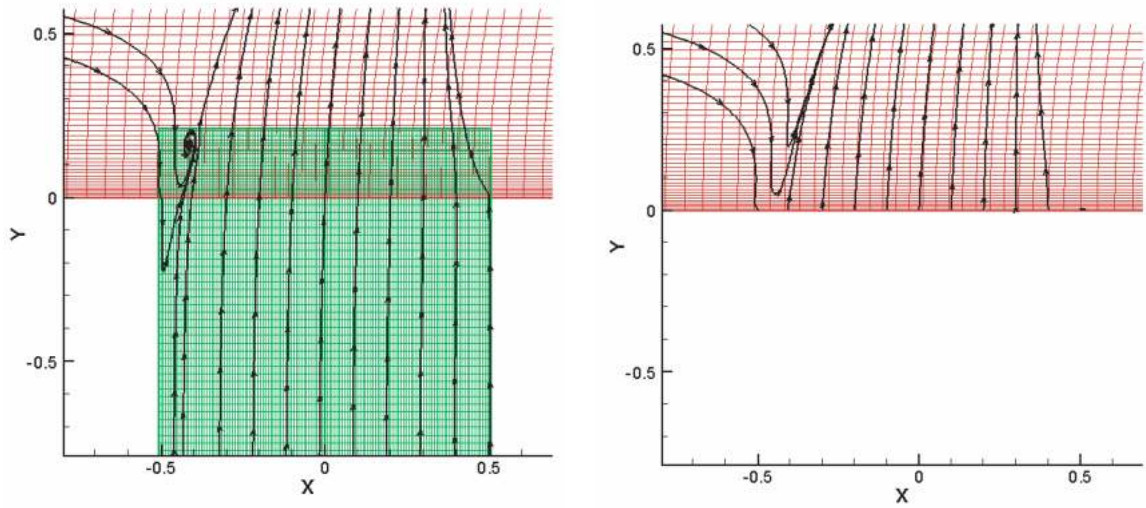
(a) Compressible and low Mach number code domains.

(b) Only compressible code domain.

Figure 3.15: Time-averaged streamlines for the coarse grid. $x - y$ plane, $z/d = 0$.
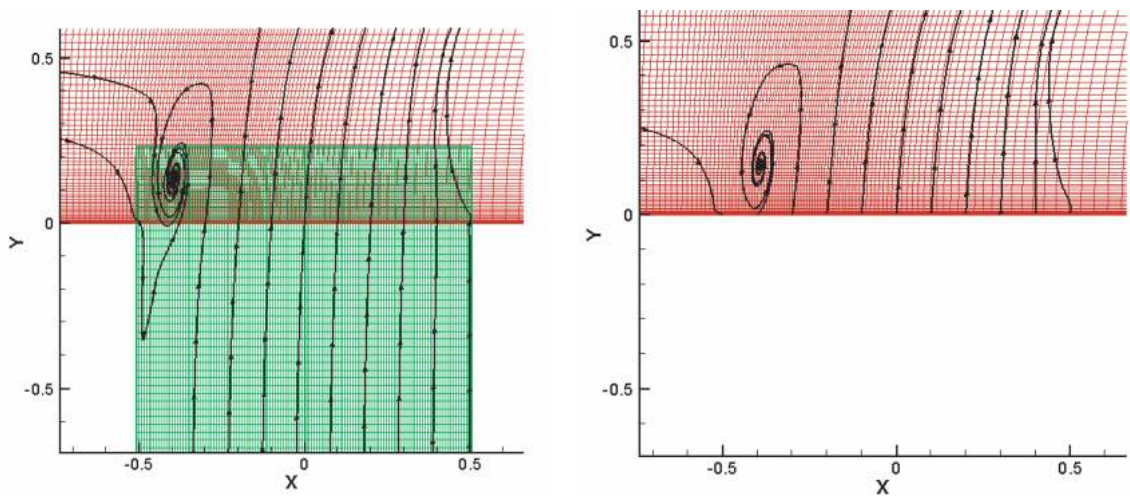
(a) Compressible and low Mach number code domains.

(b) Only compressible code domain.

Figure 3.16: Time-averaged streamlines for the refined grid. $x - y$ plane, $z/d = 0$.
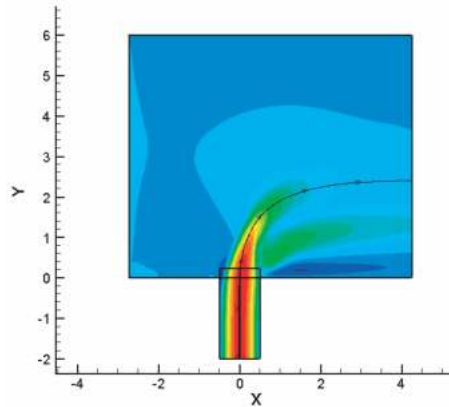
Figure 3.17: Computational domain for fine calculations. Time-averaged vertical velocity and a center streamline are also plotted.
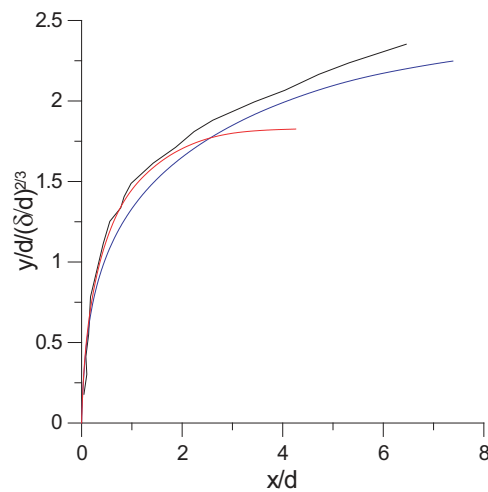
Figure 3.18: Jet trajectory. Black line, DNS of Muppidi & Mahesh (2005); blue line, coarse grid; red line, fine grid.

Chapter 4

Turbulent Boundary Layer Over a Flat Plate

4.1 Introduction

In this chapter, we present details of Large-Eddy Simulations of a turbulent boundary layer (TBL) over a flat plate. Turbulent boundary layer solution is used to specify inflow boundary conditions for LES of film cooling described in chapter 5. We choose to perform auxiliary TBL simulations to use as inflow boundary conditions for two reasons:

- No development section is needed in the main simulations to ensure that the accurate turbulent inflow is obtained, since the boundary conditions are taken from the fully-developed solution, whose accuracy is checked *a priori*.

- We only have to obtain the converged TBL solution once and use it in all subsequent calculations, as opposed to repeating the procedure all over again during each run.

Both of these considerations allow us to achieve computational savings for the overall simulations and perform the parametric and grid-refinement studies more easily. A review of existing techniques for simulating incompressible and compressible turbulent boundary layers is given in section 4.2, the description of the method employed in current simulations is presented in section 4.3, while the results of the simulations are summarized in section 4.4.

4.2   Methods for Calculating Turbulent Boundary Layers

Existing methods for calculating turbulent boundary layers can be cast into two categories: temporal methods and spatial methods. In the temporal approach (see, for example, Kleiser & Zang (1991)), periodic boundary conditions are used in the streamwise direction, besides the spanwise direction, without any change to the governing equations. The advantage of the periodic boundary conditions is apparent: no extra modeling for turbulent inflow is required. However, it can be shown by integrating the governing equations in a control volume (Xu & Martin (2004)) that streamwise periodicity assumption leads to the temporal growth of the mean streamwise velocity, thickening of the boundary layer, decrease in the turbulence production and decay of the turbulence. This leads to a non-stationary solution, contradicting the intrinsic idea behind the temporal approach. Stationary mean flow and nondecaying turbulence can be achieved by imposing a given or quasi-simultaneously computed solution through the addition of forcing terms to the basic equations. This approach makes use of the parabolic character of the boundary layer equations and the slow variation of the mean flow and turbulence statistics with streamwise location. Spalart (1988) was first to implement this approach for the simulation of incompressible TBL. He introduced a new wall-normal coordinate, applied a two-scale analysis to approximate the slow streamwise growth of the boundary layer and then added the forcing terms to the Navier-Stokes equations. Maeder *et al.* (2001) further developed the procedure of Spalart (1988) and proposed an extended temporal approach in which no *a priori* assumptions about the mean flow are required. This approach computes a flow at a series of streamwise stations, and the mean flow evolution is approximated from its upstream history. Maeder *et al.* (2001) used this method to perform direct simulation of supersonic TBL. An extended temporal approach, although efficient and promising for TBL simulations, has the disadvantage that it calls for the modification of the governing equations by introducing additional streamwise gradient terms. In the original method of Spalart (1988), a coordinate transformation that minimizes the streamwise inhomogeneity is also needed. When performing TBL simulation as an auxiliary procedure to obtain inflow conditions for the main computations, it is desirable to minimize the complexity of this auxiliary procedure, which justifies spatial methods.

The most straightforward approach to simulate a spatially developing TBL is to specify a mean flow profile at the inflow and add the turbulent fluctuations to it. Mean flow profile is usually taken from experiments or other numerical simulations which compare well with experiments. It is, however, not an easy task to generate turbulent fluctuations which retain the structure of the realistic turbulence. Lee *et al.* (1992) proposed a method for

generating turbulent fluctuations which preserve the given kinetic energy spectrum $E(k)$. This method has been used successfully for the simulation of spatially decaying compressible isotropic turbulence. However, this technique is not easily applicable to wall-bounded anisotropic flows, since it does not take the spectrum of cross-correlations into account. To try to account for anisotropy of the flow, Le & Moin (1994) extended the procedure of Lee *et al.* (1992) to prescribe the appropriate value of the Reynolds stresses (both normal and shear) in addition to the turbulent kinetic energy spectrum. They used this method to produce inflow fluctuations for DNS of a backward-facing step (Le & Moin (1994), Le *et al.* (1997)). However, the phase angle for each Fourier-component of velocity was still generated at random with this technique, which led to the improper phase information between the velocity fluctuations and lack of nonlinear energy transfer, resulting in a fairly long development section. It was found that development section of nearly 20 boundary layer thicknesses was required to recover the correct skin friction. An attempt to use this inflow generation technique for LES of the same flow over a backward-facing step (Akselvoll & Moin (1993, 1995)) showed that random fluctuations develop into realistic turbulence even slower on the coarser LES meshes. Although more sophisticated methods for artificial generation of inflow turbulence exist (see, for example, Klein *et al.* (2003), who used digital filtering of random data to reproduce a prescribed one-point second-order statistics as well as autocorrelated functions), they will always contain some degree of approximation leading to the non-realistic structure of the synthetic turbulence. To minimize the amount of modeling and empiricism in the inflow boundary conditions, researchers started looking at the possibility of applying the ideas of "input-free" self-contained methodology of temporal simulations to spatial simulations. Thus the fringe method appeared (Spalart & Hatmuff (1993)), where the simulation domain is assembled from two fringe regions at its ends and one useful region between them for data collection. Periodic boundary conditions are applied, as in temporal simulations. The method results in a spatial simulation and can take into account the streamwise pressure gradient. However, fringe method has the same disadvantage as extended temporal approach (Spalart (1988), Maeder *et al.* (2001)) that extra terms should be added to the governing equations in the fringe regions to remove mass and decrease boundary layer thickness. Lund *et al.* (1998) proposed another technique which they called a "modified Spalart method", where they make use of Spalart's ideas (Spalart (1988)) to rescale the velocity field, taken from a plane near the domain exit. But instead of using it for calculating the "growth terms" and modifying the streamwise gradients, Lund *et al.* (1998) reintroduce the rescaled velocity at the inflow boundary. Thus,

no external modeling is required for the turbulent inflow, and the simulations are completely self-contained. Modifications to the computational code are minimal, consisting of only one single subroutine for rescaling the velocity from the downstream station. Lund *et al.* (1998) successfully applied this procedure to perform LES of incompressible TBL and showed its apparent advantage when comparing to other popular techniques, such as random fluctuation method (Le & Moin (1994), Le *et al.* (1997), Akselvoll & Moin (1993), Akselvoll & Moin (1995)) and parallel inflow method(Kleiser & Zang (1991), Lund (1993), Lund & Moin (1996)). The procedure of Lund *et al.* (1998), which is now referred to as "rescaling", "rescaling-recycling" or "rescaling-reintroducing" procedure, became, perhaps, the most common and even conventional method for simulating turbulent boundary layers. A number of compressible extensions of the original incompressible formulation of Lund *et al.* (1998) are available (see, for example, Urbin & Knight (2001), Stolz & Adams (2003), Xu & Martin (2004)).

To perform Large-Eddy Simulations of compressible TBL we use the rescaling technique of Lund *et al.* (1998) and extend their method to include rescaling of density and temperature appearing in the compressible equations. Our compressibility extension is different from any of the previously proposed methods (Urbin & Knight (2001), Stolz & Adams (2003), Xu & Martin (2004)) and, perhaps, represents a hybrid of the known methods. In the next section we describe the details of the rescaling procedure used in the present simulations.

4.3   Rescaling-Recycling Procedure

The geometrical setup of the problem and the coordinate system used are shown in figure 4.1. The x-axis denotes streamwise direction, y-axis – vertical direction and z-axis – spanwise direction, respectively, with the flat plate located at $y = 0$. In LES, an instantaneous solution is represented by time-dependent Favre-filtered quantities $\widetilde{f} = \overline{\rho f}/\bar{\rho}$, where the bar denotes the filtering operation given in equation (2.119) of the chapter 2. In order to perform rescaling procedure, one must decompose this instantaneous Favre-filtered flowfield
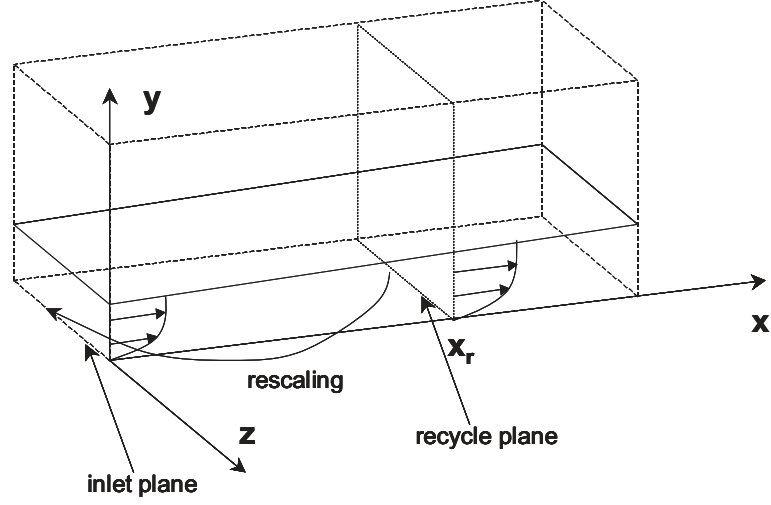
Figure 4.1: Geometrical setup of the problem.

onto a sum of mean and fluctuating components:

$$
\begin{aligned}
\tilde{\rho}\,(x,y,z,t) &= \bar{\rho}\,(x,y) &+& \rho'\,(x,y,z,t) \\
\tilde{u}\,(x,y,z,t) &= \mathcal{U}\,(x,y) &+& u'\,(x,y,z,t) \\
\tilde{v}\,(x,y,z,t) &= \mathcal{V}\,(x,y) &+& v'\,(x,y,z,t) \\
\tilde{w}\,(x,y,z,t) &= \mathcal{W}\,(x,y) &+& w'\,(x,y,z,t) \\
\tilde{T}\,(x,y,z,t) &= \mathcal{T}\,(x,y) &+& T'\,(x,y,z,t)
\end{aligned}
\tag{4.1}
$$

Here "mean" denotes an averaging in time and a homogeneous spanwise direction, so that $\{\,\bar{\rho},\,\mathcal{U},\,\mathcal{V},\,\mathcal{W},\,\mathcal{T}\,\}$ represent the average of $\{\,\tilde{\rho},\tilde{u},\tilde{v},\tilde{w},\tilde{T}\,\}$ in time and z. "Fluctuation" is the difference between the resolved instantaneous value and the mean value. Mean and fluctuating components are calculated at some downstream plane x_r, called the recycle station (see figure 4.1). The next step is to rescale the values from the recycle station in order to obtain the appropriate solution at the inlet plane x_i and specify it as inflow boundary conditions (the quantities at the recycle station are denoted with the subscript "r", and at the inlet - with the subscript "i" throughout this chapter). Due to the presence of the multiple length scales in the boundary layer, the rescaling process should be treated in a piecemeal fashion. To this purpose, two regions within the boundary layer are distinguished: the inner region with the law of the wall and the outer region with the defect law.

4.3.1 Mean Quantities

Mean Streamwise Velocity

For the incompressible TBL, the law of the wall for the mean streamwise velocity component reads (Lund *et al.* (1998))

$$\mathcal{U}^{inner} = u_\tau(x) \, f_1^{inner}(y^+), \tag{4.2}$$

where $u_\tau = \sqrt{(\nu \, \partial \mathcal{U}/\partial y)_w}$ is the friction velocity (subscript "w" denotes the wall quantities), and $y^+ = (u_\tau y)/\nu_w$ is the wall coordinate and f_1^{inner} is the universal function to be determined. The defect law is

$$\mathcal{U}_\infty - \mathcal{U}^{outer} = u_\tau(x) \, f_1^{outer}(\eta), \tag{4.3}$$

where $\eta = y/\delta$ is the outer coordinate (δ is the boundary layer thickness), $\mathcal{U}_\infty$ is the freestream velocity, and f_1^{outer} is another universal function to be determined. If we write both laws (4.2) and (4.3) for the inlet and the recycle stations, respectively, we get the following relations

$$\mathcal{U}_i^{inner} = \omega_{u_\tau} \mathcal{U}_r^{inner}(y_i^+) \tag{4.4}$$

and

$$\mathcal{U}_i^{outer} = \omega_{u_\tau} \mathcal{U}_r^{outer}(\eta_i) + (1 - \omega_{u_\tau})\mathcal{U}_\infty, \tag{4.5}$$

where

$$\omega_{u_\tau} = \frac{u_{\tau i}}{u_{\tau r}}. \tag{4.6}$$

The independent variables in (4.2) and (4.3), y_i^+ and η_i are the inner and outer coordinates of the grid nodes at the inlet station. Thus, $U_r(y_i^+)$ is the mean velocity at the recycle station, expressed as a function of y^+ and evaluated at $y^+ = y_i^+$. This evaluation require interpolation since the inner coordinates for the grid nodes at the recycle and inlet station will, in general, be different. A linear interpolation was found sufficiently accurate for this purpose. A similar interpolation is require for the outer coordinate. Scaling laws (4.2) and (4.3) are stated for the mean streamwise velocity $\mathcal{U}$ and are valid for the incompressible flow. To account for the compressibility, the same scaling laws are assumed, but written in terms of the transformed mean streamwise velocity $\hat{\mathcal{U}}$ (Bradshaw (1977))

$$\hat{\mathcal{U}}^{inner} = u_\tau(x) \, f_1^{inner}(y^+), \tag{4.7}$$

$$\hat{\mathcal{U}}_\infty - \hat{\mathcal{U}}^{outer} = u_\tau(x)\, f_1^{outer}(\eta), \tag{4.8}$$

which leads to

$$\hat{\mathcal{U}}_i^{inner} = \omega_{u_\tau}\, \hat{\mathcal{U}}_r^{inner}(y_i^+), \tag{4.9}$$

$$\hat{\mathcal{U}}_i^{outer} = \omega_{u_\tau}\, \hat{\mathcal{U}}_r^{outer}(\eta_i) + (1 - \omega_{u_\tau})\hat{\mathcal{U}}_\infty. \tag{4.10}$$

Stolz & Adams (2003) use van-Driest transformed velocity as $\hat{\mathcal{U}}$

$$\hat{\mathcal{U}} = \int_0^{\mathcal{U}} \sqrt{\frac{\bar{\rho}}{\bar{\rho}_w}}\, d\mathcal{U}, \tag{4.11}$$

Urbin & Knight (2001) also use van-Driest transformed velocity, but rewrite it for the case of adiabatic wall as

$$\hat{\mathcal{U}} = \frac{\mathcal{U}_\infty}{A} \sin^{-1}\left(A\frac{\mathcal{U}}{\mathcal{U}_\infty}\right), \tag{4.12}$$

where

$$A = \sqrt{\frac{[(\gamma-1)/2]\, M^2\, Pr_t}{1 + [(\gamma-1)/2]\, M^2\, Pr_t}}, \tag{4.13}$$

$M = \mathcal{U}_\infty/c_\infty$ is the Mach number and $Pr_t = 0.89$ is the turbulent Prandtl number. Xu & Martin (2004) define their transformed velocity as

$$\hat{\mathcal{U}} = \int_0^{\mathcal{U}} \left(\frac{\bar{\rho}_w}{\bar{\rho}}\right)^n d\mathcal{U}, \tag{4.14}$$

in the inner layer (index n is the exponent in the power law for viscosity) and use the van-Driest velocity (4.11) in the outer layer. Once the transformed velocity $\hat{\mathcal{U}}$ is rescaled according to the laws (4.9) and (4.10), one can recover the original velocity $\mathcal{U}$ through the inverse transformation. For example,

$$\mathcal{U} = \frac{\mathcal{U}_\infty}{A} \sin\left(A\frac{\hat{\mathcal{U}}}{\mathcal{U}_\infty}\right) \tag{4.15}$$

in the method of Urbin & Knight (2001);

$$\mathcal{U} = \int_0^{\hat{\mathcal{U}}} \sqrt{\frac{\bar{\rho}_w}{\bar{\rho}}}\, d\hat{\mathcal{U}}, \tag{4.16}$$

for the van-Driest transformed velocity in the integral form (4.11) used in the methods of Stolz & Adams (2003) and Xu & Martin (2004).

Mean Density and Temperature

Rescaling of the mean density $\bar{\rho}$ determines the ultimate form for the rescaling of the mean streamwise velocity $\mathcal{U}$, when the transformed velocity $\hat{\mathcal{U}}$ is defined through the mean density, as in equations (4.11) and (4.14). When fluctuations are small, to a first-order approximation, the mean density $\bar{\rho}$ and the mean temperature $\mathcal{T}$ are related by the state equation $\bar{\rho} = \mathcal{P}/R\mathcal{T}$, where R is the gas constant and $\mathcal{P}$ is the mean pressure. Since pressure is assumed constant throughout the boundary layer with zero pressure gradient, the rescaling of the mean density $\bar{\rho}$ follows the rescaling of the mean temperature $\mathcal{T}$. There are different scaling laws for the mean temperature proposed in literature. The simplest approximation is to assume a self-similar profile for the mean temperature in the inner and outer layers, respectively

$$\mathcal{T}^{inner}/\mathcal{T}_\infty = f_2^{inner}\left(y^+\right), \quad \mathcal{T}^{outer}/\mathcal{T}_\infty = f_2^{outer}\left(\eta\right). \tag{4.17}$$

Urbin & Knight (2001) and Stolz & Adams (2003) employ the scaling (4.17). However, this scaling is not physically justified for compressible flows. Moreover, with this self-similar scaling for the mean temperature and, therefore, the mean density, the compressible scaling (4.7) and (4.8) for the mean streamwise velocity degenerates to that of the incompressible case determined by equations(4.2) and (4.3) in the method of Stolz & Adams (2003).

To show this, let's assume the compressible scaling laws (4.7) and (4.8) for the transformed mean streamwise velocity $\hat{\mathcal{U}}$ and perform inverse transformation (4.16) to recover $\mathcal{U}$ from $\hat{\mathcal{U}}$. For the inner layer it reads

$$\mathcal{U}^{inner} = \int_0^{\hat{\mathcal{U}}^{inner}} \sqrt{\left(\frac{\bar{\rho}_w}{\bar{\rho}}\right)^{inner}} \, d\hat{\mathcal{U}}^{inner}. \tag{4.18}$$

We then change the independent variable in the integral (4.18) from $\hat{\mathcal{U}}^{inner}$ to y^+. Since $\hat{\mathcal{U}}^{inner}$ follows the compressible law of the wall (4.7), one can write

$$d\hat{\mathcal{U}}^{inner} = u_\tau(x) \, f_1{'}^{inner}\left(y^+\right) \, dy^+. \tag{4.19}$$

Using the the self-similarity of the mean density

$$\sqrt{(\bar{\rho}_w/\bar{\rho})^{inner}} = f_3^{inner}\left(y^+\right) \tag{4.20}$$

and substituting equations (4.19) and (4.20) into (4.18), we get

$$\mathcal{U}^{inner} = \int_0^{y^+} u_\tau(x)\, f_3^{inner}\left(y^+\right)\, f_1^{\,\prime\,inner}\left(y^+\right)\, dy^+ = u_\tau(x)\, f_4^{inner}\left(y^+\right), \qquad (4.21)$$

which is exactly the incompressible form (4.2) for the law of the wall. Following the same procedure written in terms of outer layer quantities, it is easy to show that the same degeneration occurs for the law of the wake. Compressible scaling for the mean streamwise velocity does not degenerate to the incompressible form in the formulation of Urbin & Knight (2001) because of the absence of the mean density in the inverse transformation (4.15). However, scaling laws for the mean streamwise velocity and the mean temperature are inconsistent in this case.

Xu & Martin (2004) propose to use the Waltz's equation to recover the mean temperature from the mean streamwise velocity

$$\frac{\mathcal{T}}{\mathcal{T}_\infty} = \frac{\mathcal{T}_w}{\mathcal{T}_\infty} + \frac{\mathcal{T}_{ad} - \mathcal{T}_w}{\mathcal{T}_\infty}\left(\frac{\mathcal{U}}{\mathcal{U}_\infty}\right) - r\frac{\gamma - 1}{2}M^2\left(\frac{\mathcal{U}}{\mathcal{U}_\infty}\right)^2, \qquad (4.22)$$

where $\mathcal{T}_{ad}$ is the adiabatic wall temperature given by

$$\mathcal{T}_{ad} = \mathcal{T}_\infty\left(1 + r\frac{\gamma - 1}{2}M^2\right) \qquad (4.23)$$

and r is the recovery factor, which is usually approximated as $r = \sqrt{Pr}$. Xu & Martin (2004) use the assumption that r varies little along a boundary layer, which is confirmed by the experimental data. This assumption allows them to state that the relationship between the mean temperature and the mean streamwise velocity is independent of streamwise location. It makes it possible to decouple $\mathcal{U}$ and $\mathcal{T}$ while obtaining $\mathcal{U}$ from $\hat{\mathcal{U}}$ at the inlet, knowing the relationship between $\mathcal{U}$, $\mathcal{T}$ and $\hat{\mathcal{U}}$ at the recycle station. Such formulation does not lead to the degeneration of scaling laws for the mean streamwise velocity to incompressible ones and provides consistent scaling between the mean streamwise velocity and the mean temperature.

In the present calculations, however, Mach number is quite small, $M = 0.15$. Therefore an original incompressible scaling laws for the mean streamwise velocity (4.2) and (4.3) are used, not their compressible counterparts (4.7) and (4.8), leading to the rescaling procedure (4.4) and (4.5). It allows us to avoid an additional complications arising from decoupling of the mean streamwise velocity and the temperature at the inlet necessary for high Mach

number flows. Waltz's equation (4.22) is employed to obtain the mean temperature $\mathcal{T}$ from the mean streamwise velocity $\mathcal{U}$ at the inlet.

Mean Wall-Normal and Spanwise Velocities

For the mean wall-normal velocity $\mathcal{V}$, we follow Xu & Martin (2004) and approximate it from the mean continuity equation

$$\mathcal{V} = -\frac{1}{\bar{\rho}} \int_0^y \frac{\partial \bar{\rho} \mathcal{U}}{\partial x} \, dy. \tag{4.24}$$

We estimate the order of $\partial \bar{\rho} \mathcal{U} / \partial x$ to be $(\bar{\rho}/x)\sqrt{(\bar{\rho}_w/\bar{\rho})}\, u_\tau$ and, consequently, the order of $\mathcal{V}$ to be $(y/x)\sqrt{(\bar{\rho}_w/\bar{\rho})}\, u_\tau$. So, $\sqrt{(\bar{\rho}_w/\bar{\rho})}\, u_\tau$ can be taken as the scale for $\mathcal{V}$ and the scaling laws are written as

$$\mathcal{V}^{inner} = u_\tau(x)\sqrt{\frac{\bar{\rho}_w}{\bar{\rho}}}\, f_5^{inner}(y^+) \tag{4.25}$$

in the inner layer and

$$\mathcal{V}^{outer} = u_\tau(x)\sqrt{\frac{\bar{\rho}_w}{\bar{\rho}}}\, f_5^{outer}(\eta) \tag{4.26}$$

in the outer layer. This leads to the relationships

$$\mathcal{V}_i^{inner} = \omega_{u_\tau}\omega_{\rho_w}\sqrt{\frac{\bar{\rho}_r}{\bar{\rho}_i}}\, \mathcal{V}_r\left(y_i^+\right), \quad \mathcal{V}_i^{outer} = \omega_{u_\tau}\omega_{\rho_w}\sqrt{\frac{\bar{\rho}_r}{\bar{\rho}_i}}\, \mathcal{V}_r\left(\eta_i\right), \tag{4.27}$$

where

$$\omega_{\rho_w} = \sqrt{\frac{\bar{\rho}_{w\,i}}{\bar{\rho}_{w\,r}}} \tag{4.28}$$

and ω_{u_τ} is defined in the equation (4.6). Mean spanwise velocity $\mathcal{W}$ is zero due to the spanwise statistical symmetry.

Fluctuations

The scaling suggested by Morkovin (1962), which appears appropriate to at least $M = 5$, is used in the present method. It states that the velocity fluctuations normalized by the velocity scale $\sqrt{(\bar{\rho}_w/\bar{\rho})}\, u_\tau$ are in fair agreement with the incompressible data. Applied at the recycle station and at the inlet, the scaling of u_j' ($j = 1, 2, 3$ corresponding to u', v', w') by $\sqrt{(\bar{\rho}_w/\bar{\rho})}\, u_\tau$ leads to

$$u_j'^{\,inner}_i = \omega_{u_\tau}\omega_{\rho_w}\sqrt{\frac{\bar{\rho}_r}{\bar{\rho}_i}}\, u_{j\,r}'\left(y_i^+\right), \quad u_j'^{\,outer}_i = \omega_{u_\tau}\omega_{\rho_w}\sqrt{\frac{\bar{\rho}_r}{\bar{\rho}_i}}\, u_{j\,r}'\left(\eta_i\right). \tag{4.29}$$

To a first order approximation, the state equation yields

$$\frac{p'}{\mathcal{P}} = \frac{T'}{\mathcal{T}} + \frac{\rho'}{\bar{\rho}}. \tag{4.30}$$

Neglecting $p'/\mathcal{P}$, which is very small in most cases, one gets

$$\frac{\rho'}{\bar{\rho}} = -\frac{T'}{\mathcal{T}}. \tag{4.31}$$

Thus, only the temperature fluctuations need to be rescaled. The strong Reynolds analogy (SRA) can be derived from the linearized equation

$$\frac{T_0'}{\mathcal{T}} = \frac{T'}{\mathcal{T}} + (\gamma - 1)\, M^2 \frac{\mathcal{U}\, u'}{\mathcal{T}} \tag{4.32}$$

under the assumption of negligible total temperature fluctuations $T_0'/\mathcal{T}$ (Lele (1994)). It leads to the equation

$$\frac{T'}{\mathcal{T}} = -(\gamma - 1)\, M^2 \frac{u'}{\mathcal{U}}. \tag{4.33}$$

However, a contradictory evidence about the validity of SRA can be found in literature. Simulation data of Maeder *et al.* (2001), Guarini *et al.* (2000) does not support SRA even at low Mach numbers. In contrast, experimental data of Smith & Dussauge (1996), Gaviglio (1987) gives positive prognosis about the SRA validity in the range of low to moderate Mach numbers. To avoid the uncertainty, Xu & Martin (2004) assume more general relationship between the temperature and the streamwise velocity fluctuations than that stated by SRA (4.33)

$$\frac{T'}{\mathcal{T}} = cs\, f_{amp}\, \frac{u'(t + f_{phase})}{\mathcal{U}}, \tag{4.34}$$

where t denotes the time, cs is equal to $+1$ or -1, where u' and T' are positively or negatively correlated, f_{amp} and f_{phase} are functions of y^+ in the inner layer and η in the outer layer. However, in spite of the more sophisticated reasoning behind the equation (4.34), both equations (4.33) and (4.34) lead to the same scaling law for the temperature fluctuations

$$T'_i = \frac{u'_i(t + f_{phase})}{u'_r(t + f_{phase})} \frac{\mathcal{U}_r}{\mathcal{U}_i} \frac{\mathcal{T}_i}{\mathcal{T}_r} T'_r = \omega_{u_\tau} \omega_{\rho_w} \sqrt{\frac{\bar{\rho}_r}{\bar{\rho}_i}} \frac{\mathcal{U}_r}{\mathcal{U}_i} \frac{\mathcal{T}_i}{\mathcal{T}_r} T'_r \tag{4.35}$$

for $y_r^+ = y_i^+$ in the inner layer and $\eta_r = \eta_i$ in the outer layer. Approaching the wall, U_r/U_i becomes a $0/0$ type limit and can be evaluated with the L'Hospital rule to give the following

scaling law for the temperature fluctuations at the wall (Xu & Martin (2004))

$$T'_{w\,i} = \frac{\omega_{\rho\,w}\omega_{\nu\,w}}{\omega_{u_\tau}}\sqrt{\frac{\bar{\rho}_r}{\bar{\rho}_i}}\frac{\mathcal{T}_{w\,i}}{\mathcal{T}_{w\,r}}\,T'_{w\,r},\tag{4.36}$$

where

$$\omega_{\nu\,w} = \frac{\nu_{w\,i}}{\nu_{w\,r}}.\tag{4.37}$$

Composite Solution

Once inner and outer quantities are rescaled according to their scaling laws, the inner and outer profiles are combined into a single solution valid over the entire boundary layer as

$$\begin{aligned}\mathcal{G}_i &= \mathcal{G}_i^{inner}\left[1 - W(\eta)\right] + \mathcal{G}_i^{outer}\,W(\eta),\\g'_i &= g_i^{'\,inner}\left[1 - W(\eta)\right] + g_i^{'\,outer}\,W(\eta),\end{aligned}\tag{4.38}$$

where $\mathcal{G} = \{\bar{\rho}, \mathcal{U}, \mathcal{V}, \mathcal{W}, \mathcal{T}\}$ are the mean quantities and $g' = \{\rho', u', v', w', T'\}$ are the fluctuating quantities. The weighting function $W(\eta)$ is defined as

$$W(\eta) = \frac{1}{2}\left\{1 + \tanh\left[\frac{\alpha\,(\eta - b)}{(1 - 2\,b)\,\eta + b}\right]\Big/\tanh(\alpha)\right\},\tag{4.39}$$

where $\alpha = 4$ and $b = 0.02$, following the work of Lund *et al.* (1998). When the mean and fluctuating quantities at the inflow are obtained, the total instantaneous solution is recovered from the equation (4.1) as their sum. The rescaling procedure described above requires scaling parameters u_τ and δ both at the recycle station and at the inlet. These quantities are determined from the computed solution at the recycle station, but they must be specified at the inlet. At the inlet, the target inflow boundary layer thickness δ_i is specified, which is the only control parameter introduced into the procedure. Skin friction velocity $u_{\tau i}$ can be computed from $u_{\tau r}$ as

$$u_{\tau\,i} = u_{\tau\,r}\left(\frac{\delta_i}{\delta_r}\right)^{1/8}.\tag{4.40}$$

Equation (4.40) is obtained from the standard boundary-layer correlation $u_\tau \sim \theta^{1/8}$ (see, for example, Schlichting (2000)) under the assumption that δ/θ is independent of x (θ is the momentum thickness).

	L_x	L_y	L_z	N_x	N_y	N_z	Δx^+	Δy_w^+	Δz^+
Current LES	$17\,\delta_i$	$4.5\,\delta_i$	$\pi/2\,\delta_i$	128	128	32	38	0.6	15
Lund *et al.* (1998)	$10\,\delta_i$	$3\,\delta_i$	$\pi/2\,\delta_i$	100	45	64	64	1.2	15
Stolz & Adams (2003)	$16\,\delta_i$	$4\,\delta_i$	$\pi/2\,\delta_i$	251	101	51	41	2.7	21

Table 4.1: Parameters of the numerical grid.

4.4   Implementation

4.4.1   Computational Domain and Simulation Parameters

Computational domain used for the present Large Eddy Simulations of the turbulent bound-ary layer over a flat plate is schematically shown in figure 4.1 together with the coordinate system. The grid is uniform in streamwise (x) and spanwise (z) directions; hyperbolic-tangent stretching function is employed in wall-normal (y) direction to cluster the points near the wall. Parameters of the current computational domain are summarized in table 4.1 and compared with the parameters used in LES of Lund *et al.* (1998) and Stolz & Adams (2003). The domain size and the grid resolution is comparable in all three simulations; the grid is fine enough to perform fully-resolved LES of the turbulent boundary layer without the need for wall modeling (Piomelli & Balaras (2002)). Mach number is set to $M = 0.15$ in the present simulations. Reynolds number based on the inflow boundary layer thickness $Re_{\delta i} = \mathcal{U}_\infty\,\delta_i/\nu_\infty \sim 7000$.

4.4.2   Initial and Boundary Conditions

Initial conditions for the simulations are specified to preserve the correct spectrum of the turbulent kinetic energy, as in the method of Lee *et al.* (1992). More details on the initial conditions and on the behavior of the solution during the period of initial transient are documented in Appendix C. No-slip and adiabatic boundary conditions are used at the wall. The rescaling-recycling procedure described above is implemented to obtain incoming quantities at the inflow, which are used for the formulation of subsonic inflow boundary conditions based on locally one-dimensional Riemann invariants, described in section 2. A slight modification to the procedure is implemented in the region outside of the boundary layer: instead of doing rescaling and recycling, we set the quantities equal to their free-stream values in order to avoid the drift in the streamwise mean velocity. More details can be found in Appendix C. The recycle plane is located at the distance $12.5\,\delta_i$ downstream of the inlet plane. Top boundary is treated with the Riemann invariant boundary conditions

as well, as described in chapter 2. Values corresponding to the edge of the boundary layer are used to construct an incoming Riemann invariant. All other boundaries use generic boundary conditions for the compressible code described in chapter 2.

4.4.3 Simulation Results

In this subsection, we present the results of the fully-developed boundary layer solution. The solution was advanced in time with a time step of roughly 0.1 viscous time units ($\Delta t \sim 0.1 \, \nu/u_\tau^2$). After it reached the computational time of 125 inertial timescales ($t \sim 125 \, \delta_i/\mathcal{U}_\infty$), we began accumulating the statistics. Temporal development of the velocity-derivative skewness (see Appendix C) shows, that initial transient lasts for about 80 inertial timescales, so the TBL solution is within the statistically-steady state at $t \sim 125$. The statistics were sampled over a period of $210 \, \delta_i/\mathcal{U}_\infty$. According to Spalart (1988), the typical timescale of the turbulence, i.e. the ratio of its energy to its production rate, is about $3 \, \delta^\star/\mathcal{U}_\infty$ for $Re_\theta \sim 1410$, or about $0.4 \, \delta/\mathcal{U}_\infty$ in terms of $\delta/\mathcal{U}_\infty$. So, the turbulent energy is dissipated and regenerated about 500 times during our sample period, which is more than enough for the statistics to converge. Due to the limited availability of experimental and computational data on turbulent boundary layers for the regime of low Mach number ($M = 0.15$), we compare our results with incompressible experimental and numerical data.

Streamwise Evolution of the Boundary Layer

To document the streamwise evolution of the boundary layer, we plot 99% boundary layer thickness versus Re_θ in figure 4.3. Momentum integral estimate based on the Coles' law of the wake (Coles (1956)) described in Appendix C, as well as the data from experiments of Pietrzyk *et al.* (1990) and DNS of Ferrante & Elghobashi (2004) are also plotted. Boundary layer thickness is normalized by its inflow value δ_i. Since $Re_{\theta \, i} = 910$ is the Reynolds number at the inflow in the current simulations, δ_i is taken as the boundary layer thickness corresponding to $Re_\theta = 910$ to normalize experimental data, DNS of Ferrante & Elghobashi (2004) and momentum integral estimate. Rather good agreement is obtained, where the results of the current simulations lie between the experiments of Pietrzyk *et al.* (1990) and simulations of Ferrante & Elghobashi (2004). Non-zero curvature of the graph δ/δ_i in the current LES is similar to the curvature in Code-A simulations of Ferrante & Elghobashi (2004) performed with the rescaling-recycling procedure, which might be due to the inherent properties of the procedure. Streamwise evolution of the displacement thickness $\delta^\star/\delta_i$ and momentum thickness θ/δ_i versus Re_θ is shown in figures 4.4 and 4.5, respectively. Again,

good agreement is obtained between the current simulations and DNS of Ferrante & El-ghobashi (2004), although both of the simulations produce the values of $\delta^\star$ and θ slightly higher than the experiments and the momentum integral estimate. Note that the slope of both $\delta^\star/\delta_i$ and θ/δ_i is in better agreement with the theoretical and experimental values, than that of δ/δ_i. We look at the dependence of Re_θ on the streamwise coordinate x/δ_i in figure 4.6. The origin of the coordinate system $x = 0$ is chosen to coincide with the stream-wise location, where Reynolds number $Re_\theta = 910$, for all the data presented. The growth of Re_θ with the streamwise location is a little bit overpredicted in our simulations. It follows from the momentum integral analysis, that $d\,Re_\theta/d\,Re_x = c_f/2$. Since c_f decreases with the streamwise distance, the tangent $d\,Re_\theta/d\,Re_x$ should also decrease. It increases in both the current simulations and Code-B DNS of Ferrante & Elghobashi (2004). Since Code-B simulations of Ferrante & Elghobashi (2004) are not performed with the rescaling-recycling procedure, but use the precomputed time-accurate solution at the inflow, this disagreement is probably not due to the rescaling-recycling technique. The reason for this unexpected behavior in the present simulations is an existence of a mild adverse mean pressure gradient. Plot of the mean pressure versus the streamwise distance at the edge of the boundary layer is shown in figure 4.2. Adverse pressure gradient $d\,(P/P_\infty)/d\,(x/\delta_i) \sim 1\cdot 10^{-5}$ is observed. Presence of this positive pressure gradient comes from the outflow boundary conditions. Current LES code uses parabolized Navier-Stokes equations as the outflow boundary condi-tions. DNS of Ferrante & Elghobashi (2004), where the same erroneous behavior is observed, employ convective outflow conditions of the form $\partial u_i/\partial t + U_c\,\partial u_i/\partial x = 0$. As a conclu-sion, convective outflow conditions do not perform well for the case of turbulent boundary layer and call for some improvement.

Evolution of the shape factor $H = \delta^\star/\theta$ versus Re_θ is shown in figure 4.7. Large amount of experimental and numerical data is available for the shape factor, and some of it is included in figure 4.7 in addition to the data from the sources mentioned previously. Existing data show significant scatter, with the results of the present simulations lying within the range of this scatter. We match the results of Pietrzyk *et al.* (1990) at the beginning of the calculations, converging later to the experiments of Coles (1962) and simulations of Spalart (1988). The slope of the curve is slightly higher at the beginning, but recovers the correct value towards the end of the computational domain. Note exactly the same behavior of the numerical results of Ferrante & Elghobashi (2004), although their shape factor is lower, lying below the experiments of Coles (1962), but above the simulations of Lund *et al.* (1998) and the momentum integral estimate. Similar behavior of the current
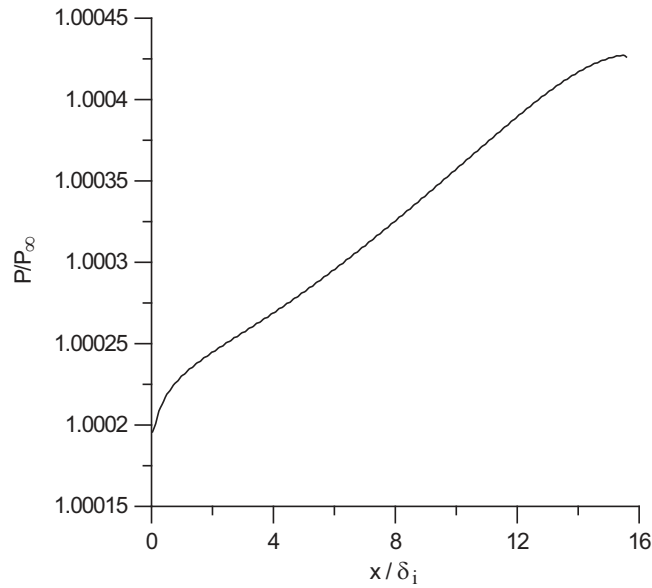
Figure 4.2: Mean pressure versus streamwise distance at the boundary layer edge shows slight adverse pressure, gradient, $d\,(P/P_\infty)/d\,(x/\delta_i) \sim 1 \cdot 10^{-5}$.

LES and DNS of Ferrante & Elghobashi (2004) again suggests that the higher slope at the beginning of the domain might be due to the rescaling-recycling procedure, confirmed by the fact that the simulations of Lund *et al.* (1998) also show similar effect, though to less extent. Local skin friction coefficient, $c_f = 2\tau_w/\rho\mathcal{U}_\infty^2$ is another important characteristics of the boundary layer measured in the experiments. The behavior of c_f versus Re_θ is plotted in figure A.6. Results of the presents simulations are within 7% of the experimental data, showing a small underestimation of the computed skin friction coefficient. Mild adverse pressure gradient introduced by the outflow boundary conditions (figure 4.2) is probably the reason for this underestimation. The correct slope of the curve is recovered towards the middle of the computational domain, consistent with the similar trend in the other documented parameters.

Mean Quantities

Mean streamwise velocity profiles $\mathcal{U}/\mathcal{U}_\infty$ versus outer coordinate y/δ are shown in figure 4.9 for the three streamwise locations along the boundary layer, corresponding to Re_θ =930, 1070 and 1260. Also shown are measurements of Murlis *et al.* (1982) for $Re_\theta = 1368$ and DNS data of Spalart (1988) for $Re_\theta = 1400$. The correct streamwise evolution of the mean velocity is recovered, showing fuller profiles with the increase in Re_θ. Results of the current
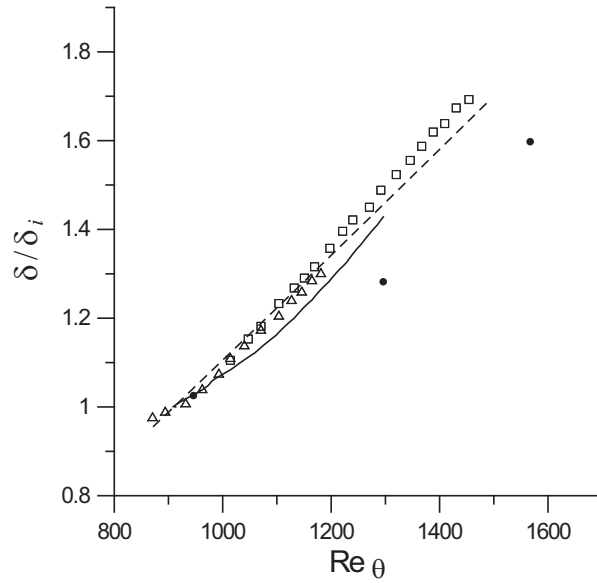
Figure 4.3: Streamwise evolution of 99% boundary layer thickness, δ/δ_i, versus Re_θ. ———, current LES; $---$, momentum integral estimate; $\bullet$, Pietrzyk *et al.* (1990); $\triangle$, Ferrante & Elghobashi (2004), Code-A: rescaling-recycling simulations; $\square$, Ferrante & Elghobashi (2004), Code-B: main simulations using Code-A as inflow conditions.
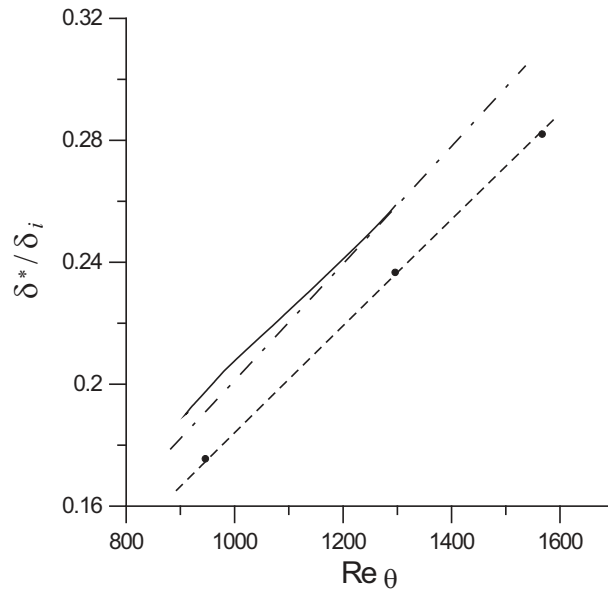
Figure 4.4: Streamwise evolution of the displacement thickness, $\delta^\star/\delta_i$, versus Re_θ. ———, current LES; $---$, momentum integral estimate; $\bullet$, Pietrzyk *et al.* (1990); $-\cdot-\cdot-$, Ferrante & Elghobashi (2004), Code-A and Code-B combined.
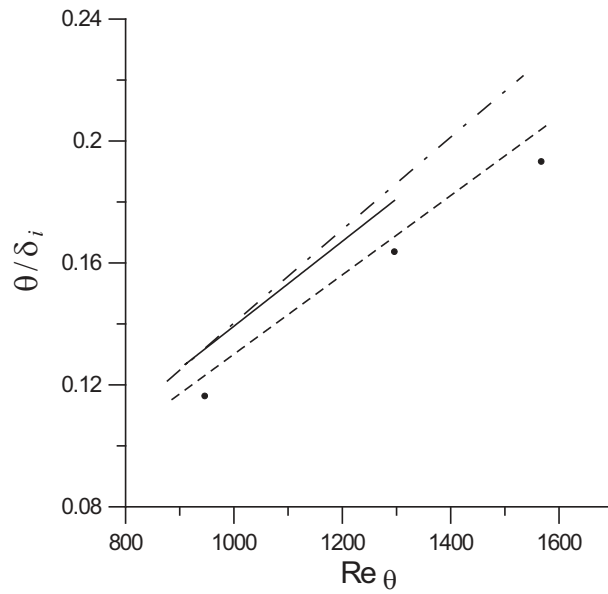
Figure 4.5: Streamwise evolution of the momentum thickness, θ/δ_i, versus Re_θ. ———, current LES; $---$, momentum integral estimate; $\bullet$, Pietrzyk *et al.* (1990); $-\cdot-\cdot-$, Ferrante & Elghobashi (2004), Code-A and Code-B combined.
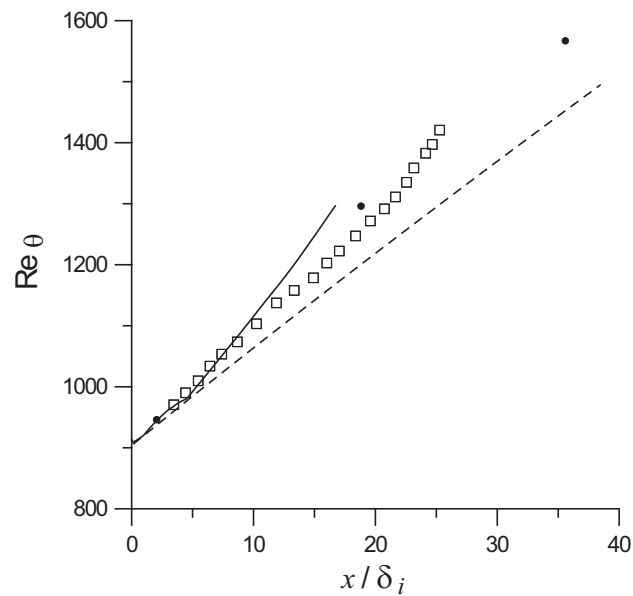
Figure 4.6: Dependence of the Reynolds number, Re_θ, on the streamwise distance, x/δ_i. ———, current LES; $---$, momentum integral estimate; $\bullet$, Pietrzyk *et al.* (1990); $\square$, Ferrante & Elghobashi (2004), Code-B.
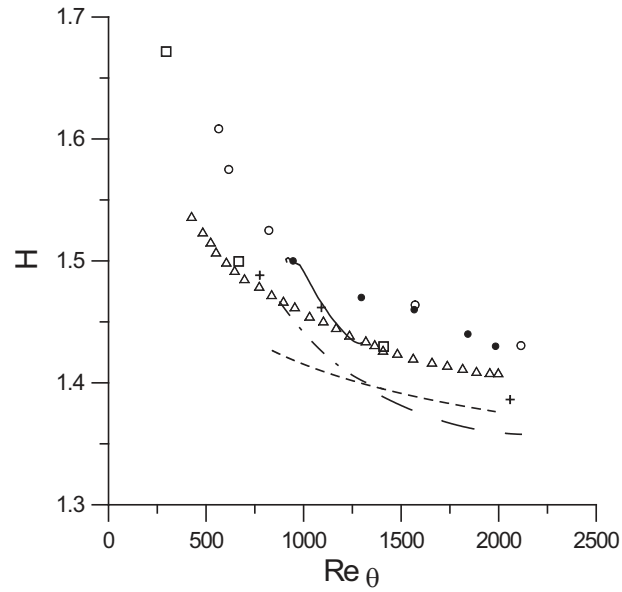
Figure 4.7: Evolution of the shape factor, $H = \delta^\star/\theta$, versus Re_θ. ———, current LES; $---$, momentum integral estimate; $\triangle$, Coles (1962); $+$, Murlis *et al.* (1982); $\square$, Spalart (1988); $\bullet$, Pietrzyk *et al.* (1990); $\circ$, Fernholz & Finley (1996); — — —, Lund *et al.* (1998); $- \cdot - \cdot -$, Ferrante & Elghobashi (2004), Code-A and Code-B combined.
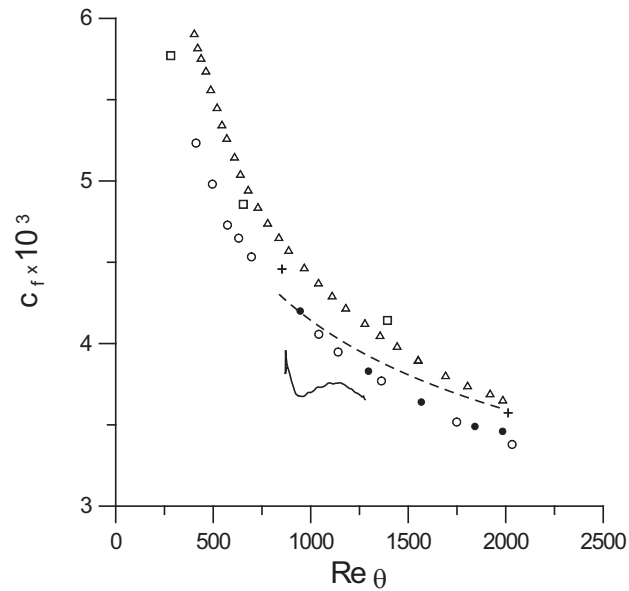
Figure 4.8: Evolution of the skin fiction coefficient, $c_f = 2\tau_w/\rho \mathcal{U}_\infty^2$, versus Re_θ. ———, current LES; $---$, momentum integral estimate; $\circ$, Hama (1954); $\triangle$, Coles (1962); $+$, Murlis *et al.* (1982); $\square$, Spalart (1988); $\bullet$, Pietrzyk *et al.* (1990).

simulations for $Re_\theta = 1260$ agree very well with the measurements of Murlis *et al.* (1982) at $Re_\theta = 1368$. Mean velocity profiles in wall units $\mathcal{U}^+ = \mathcal{U}/u_\tau$ for the same three streamwise locations are plotted in figure 4.10 versus inner coordinate y^+. Empirical law of Spalding

$$y^+ = \mathcal{U}^+ + 0.1108 \left\{ e^{0.4\mathcal{U}^+} - 1 - 0.4\mathcal{U}^+ - \frac{(0.4\mathcal{U}^+)^2}{2!} - \frac{(0.4\mathcal{U}^+)^3}{3!} - \frac{(0.4\mathcal{U}^+)^4}{4!} \right\} \quad (4.41)$$

is also plotted for comparison. Spalding law is the single formula fitting the experimental velocity distributions in the viscous layer and the transition region (Spalding (1961)). Another common empirical correlation, the logarithmic law

$$\mathcal{U}^+ = \frac{1}{k} \ln y^+ + C \quad (4.42)$$

with the standard choice of constants $k = 0.41$ and $C = 5$ (Spalart (1988)) and the viscous law of the wall $\mathcal{U}^+ = y^+$ are plotted as well. Numerical profiles closely follow the Spalding law in the viscous layer and the transition region. They also agree better with the Spalding fit in the logarithmic region than with the logarithmic law (4.42). Expected Reynolds number dependence of the numerical results is displayed in the wake region: an increase in $\mathcal{U}^+$ at the edge of the boundary layer due to the decrease in u_τ with the streamwise coordinate. Mean streamwise velocity profile in wall units at $Re_\theta = 1260$ is compared to the available experimental and numerical data in figure 4.11. The agreement of LES results with the other data is quite good. The slight discrepancy with the DNS of Spalart (1988), as well as the measurements of Pietrzyk *et al.* (1990) and DeGraaf & Eaton (2000) is observed in the logarithmic and in the wake region, where the computed mean velocity is slightly higher. The same overprediciton of the mean velocity was also reported by Lund *et al.* (1998), who state that this defect is a common feature of simulations using finite-difference methods on relatively coarse meshes and is not related to the rescaling approach. They support this claim by noting that the results of Rai & Moin (1993), obtained with the random fluctuations method, contain the similar discrepancy. An interesting observation, however, is that the current LES results agree almost perfectly with the measurements of Murlis *et al.* (1982).
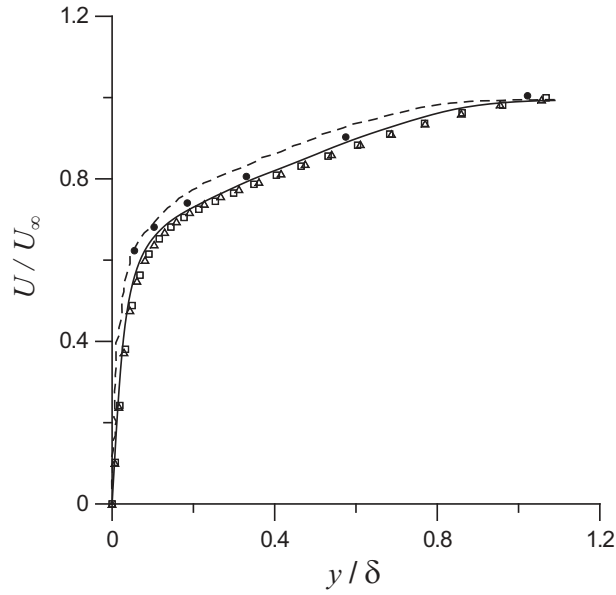
Figure 4.9: Mean streamwise velocity, $\mathcal{U}/\mathcal{U}_\infty$, versus y/δ. $\square$, $Re_\theta = 930$ (every third grid point is shown); $\triangle$, $Re_\theta = 1070$ (every third grid point is shown); ———, $Re_\theta = 1260$; $\bullet$, Murlis *et al.* (1982), $Re_\theta = 1368$; $---$, Spalart (1988), $Re_\theta = 1410$.
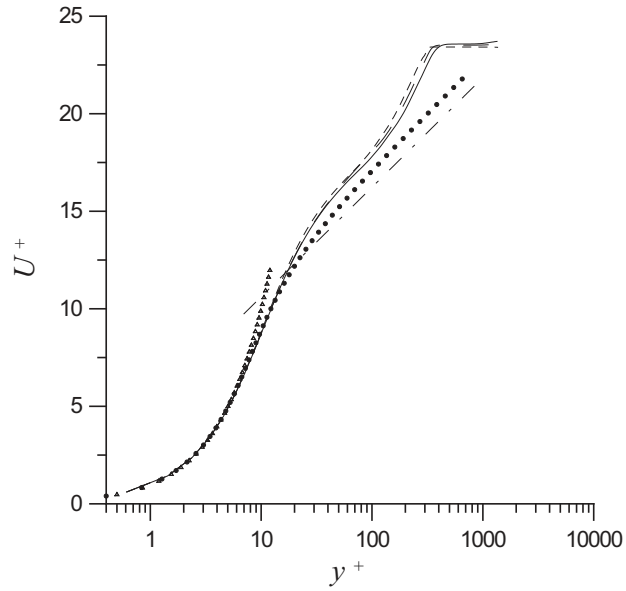
Figure 4.10: Mean streamwise velocity in wall units, $\mathcal{U}^+ = \mathcal{U}/u_\tau$, versus y^+. $---$, $Re_\theta = 930$; — — —, $Re_\theta = 1070$; ———, $Re_\theta = 1260$; $\bullet$, Spalding law: equation (C.1); $-\cdot-\cdot-$, log law: $U^+ = \ln y^+/0.41 + 5$; $\triangle$, law of the wall: $U^+ = y^+$.
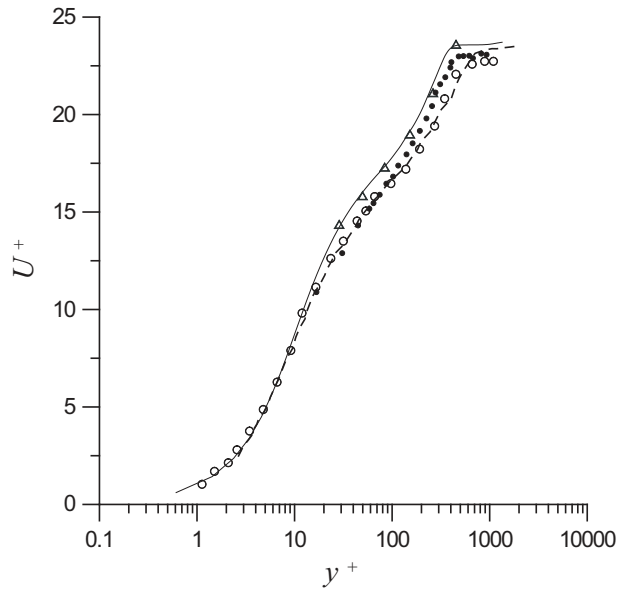
Figure 4.11: Mean streamwise velocity in wall units, $\mathcal{U}^+ = \mathcal{U}/u_\tau$, versus y^+. ———, current LES, $Re_\theta = 1260$; △, Murlis *et al.* (1982), $Re_\theta = 1368$; $- - -$, Spalart (1988), $Re_\theta = 1410$; ●, Pietrzyk *et al.* (1990), $Re_\theta = 1296$; ○, DeGraaf & Eaton (2000), $Re_\theta = 1430$.

Turbulence Quantities

Figure 4.12 shows profiles of velocity fluctuations u'^+, v'^+, w'^+ and the shear stress $u'^+ v'^+$ in wall units at three streamwise locations, Re_θ =930, 1070 and 1260, versus outer coordinate y/δ. Here and further throughout the discussion turbulence quantities are averaged in the homogeneous spanwise direction. All of the profiles generally exhibit an expected Reynolds number behavior, showing larger values of maximum intensities for larger Reynolds numbers. However, it is quite difficult to follow the trend of the fluctuations with the Reynolds number in the outer region of the boundary layer, amplified by the fact that the Reynolds numbers considered are not far apart. Comparison of the computed fluctuations and shear stress profiles at $Re_\theta = 1260$ with the available experimental and numerical data is shown in figure 4.13. The profiles are plotted versus the inner coordinate, y^+, in figure 4.13. The overall agreement is quite good. The computed profiles of v'^+, w'^+ and $u'^+ v'^+$ lie lower than the experimental data and DNS profiles of Ferrante & Elghobashi (2004), most likely due to the smaller Reynolds number in our calculations. The only significant deviation is an overprediction of the peak streamwise velocity fluctuations u'^+, in spite of the lower Reynolds number. DNS of Ferrante & Elghobashi (2004) also show the same overprediction. Moreover, this feature is also present in the LES of Lund *et al.* (1998).
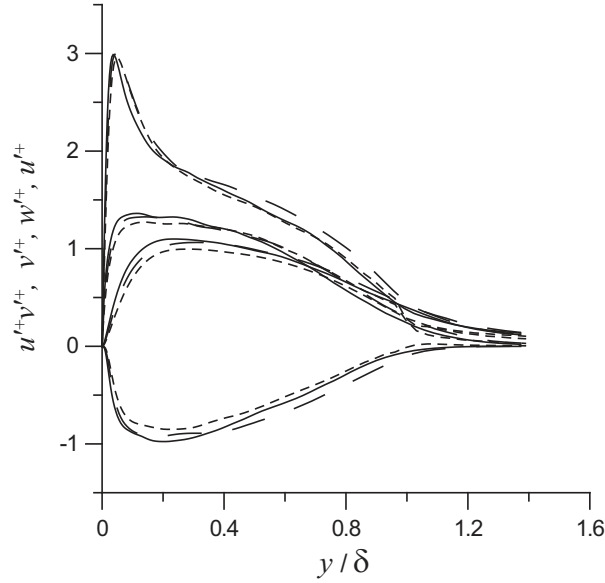
Figure 4.12: Velocity fluctuations and shear stress profiles in wall units versus y/δ. $---$, $Re_\theta = 930$; $-$ $-$ $-$, $Re_\theta = 1070$; ———, $Re_\theta = 1260$. Upper group of curves: u'^+; second from the top: w'^+; third from the top: v'^+; bottom group: $u'^+v'^+$.

Lund *et al.* (1998) hypothesize that this defect is similar to the velocity overshoot in the mean velocity profile and is related to the resolution problems and/or numerical method and not to the rescaling procedure. They support this statement, again, by noticing the similar problem in the data of Rai & Moin (1993) and other TBL calculations of Lund *et al.* (1998) performed with the methods other than rescaling-recycling technique. Resolution should not be a problem, however, in the DNS of Ferrante & Elghobashi (2004) that show the same overshoot. No further efforts has been made in the present work to isolate the effects of resolution, numerical method and the rescaling-recycling procedure, and the results were found satisfactory for the purpose of specifying time-accurate inflow conditions for Large Eddy Simulations of film cooling above the flat plate.

4.4.4 Extension to Wider Domain

When the fully-developed boundary layer solution is obtained, we extend the calculations from the original domain with $L_z = \pi/2\,\delta_i$ and $N_z = 32$ to the wider domain with $L_z = 6.8\,\delta_i$ and $N_z = 128$, required for the film cooling simulations . Grid dimensions and node count in x and y directions stay the same. In order to perform this extension, we stack four samples of an instantaneous field together in spanwise direction and continue the
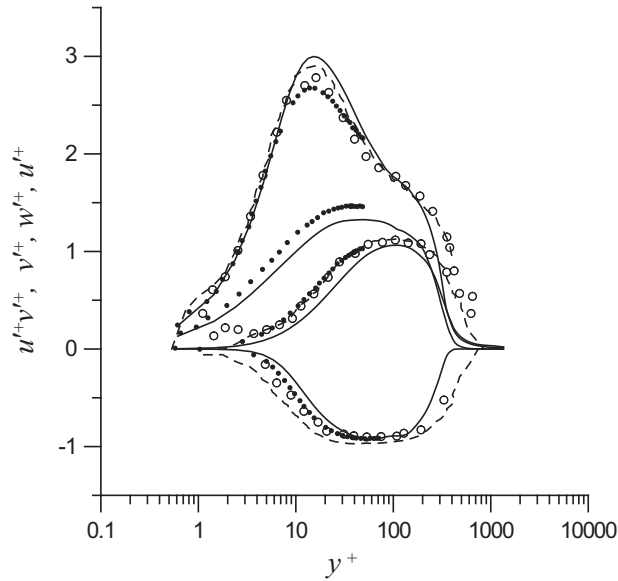
Figure 4.13: Velocity fluctuations and shear stress profiles in wall units versus y^+. ————, current LES, $Re_\theta = 1260$; •, Spalart (1988), $Re_\theta = 1410$; ○, DeGraaf & Eaton (2000), $Re_\theta = 1430$; $---$, Ferrante & Elghobashi (2004), $Re_\theta = 1430$. Upper group of curves: u'^+; second from the top: w'^+; third from the top: v'^+; bottom group: $u'^+v'^+$.

calculations on the wide domain. To visualize initial conditions for the wide domain calculations, contours of instantaneous vertical velocity in the vertical cross-section $x/\delta_i \sim 4.25$ are plotted in figure 4.14. Discontinuities due to the superposition of different solutions are visible in places, where the solutions are "glued" together. With time, these discontinuities smooth out (see figure 4.15 plotted at time $t_{wide} \sim 22\,\delta_i/\mathcal{U}_\infty$, where t_{wide} is the time of calculations on the wide domain). Wide domain calculations are run till $t_{wide} \sim 100\,\delta_i/\mathcal{U}_\infty$ before feeding the data to film cooling simulations.

Spanwise structure of the boundary layer can be visualized by looking at contours of instantaneous wall normal vorticity $\omega_y\left(\delta\nu/u_\tau^3\right)^{\frac{1}{2}}$ in a wall-parallel plane $y^+ \sim 11$, shown in figure 4.16. Near-wall streaks with the spanwise spacing of about 100 to 140 wall units are identifiable, consistent with the LES of Stolz & Adams (2003). The highly intermittent boundary layer with turbulent bursting effects can be appreciated from the density distribution in a longitudinal cross-section, figure 4.17.
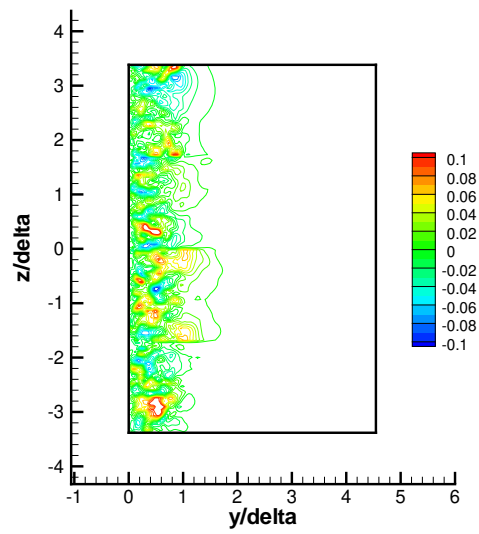
Figure 4.14: Contours of instantaneous vertical velocity in the vertical cross-section $x/\delta_i \sim$ 4.25. Initial conditions for the wide domain, $t_{wide} = 0$.
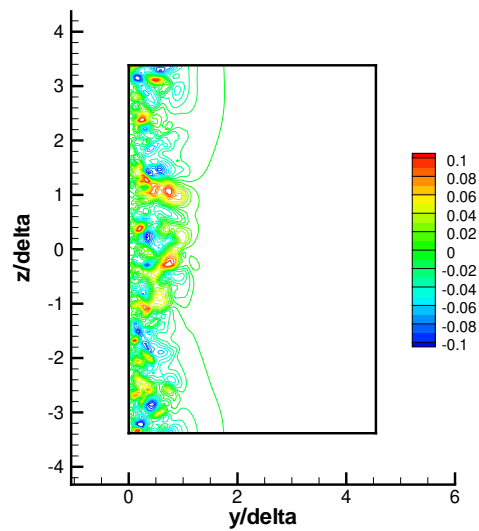
Figure 4.15: Contours of instantaneous vertical velocity in the vertical cross-section $x/\delta_i \sim$ 4.25, $t_{wide} \sim 22 \, \delta_i/\mathcal{U}_\infty$.
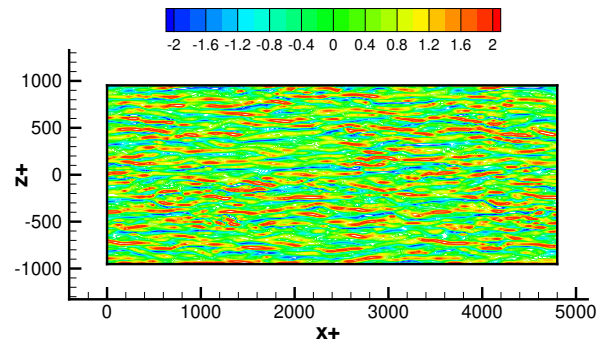
Figure 4.16: Contours of instantaneous wall-normal vorticity $\omega_y \left(\delta \nu / u_\tau^3 \right)^{\frac{1}{2}}$ in a wall-parallel plane $y^+ \sim 11$.
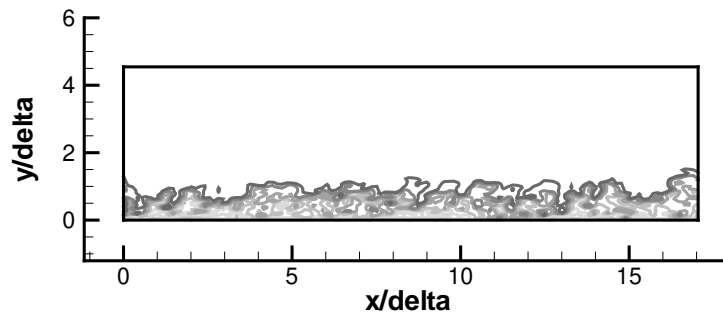
Figure 4.17: Contours of instantaneous density in a longitudinal cross-section.

Chapter 5

Simulation of Film Cooling

5.1   Introduction

This chapter concerns the numerical simulation of film cooling above the flat plate using LES technique. Experimental and numerical setup of the problem are specified in sections 5.2 and 5.3, respectively. Results of Large Eddy Simulations of the chosen cooling regime are presented next. Time-averaged flowfield is described in section 5.4. Steady phenomena associated with the flow inside the plenum, film hole and in the crossflow region are identified. Velocity field is compared to experimental values at some locations above the surface. Unfortunately, no experimental data is available for the flow inside the cooling hole and the plenum for this exact geometry. Turbulence statistics of the resulting flow are presented in section 5.5 and comparison with experiments is made. Cooling performance is discussed in section 5.6 by presenting the results of the time-averaged temperature field and adiabatic film cooling effectiveness.

5.2   Experimental Setup

Film cooling flow above the flat plate with cooling jets issued at an angle with respect to the surface is chosen as the target geometry for the present simulations. This geometry has been extensively used in many experiments. The details of the geometry are taken from experimental study of Pietrzyk *et al.* (1989), Pietrzyk *et al.* (1990) and reproduced here in figure 5.1. It consists of a large stagnation type plenum feeding an array of cylindrical film holes laterally separated by the distance $3\,d$, where d is the diameter of the hole. They are inclined at 35° with respect to the test plate. The length to diameter ratio of
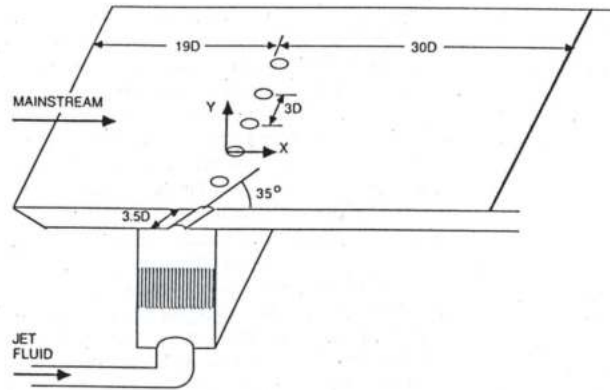
Figure 5.1: Geometry of film cooling test plate in experiments of Pietrzyk *et al.* (1989).

the cooling holes is $L/d = 3.5$. Present experimental setup is considered to be rather accurate representation of realistic gas turbine engine conditions, featuring at the same time quite simple geometry, which is easy to model and analyze. Pietrzyk *et al.* (1989) used LDV to measure three components of velocity along with normal and shear stresses at different spatial locations above the test plate for blowing ratios $B = 0.25, 0.5$ and 1 and a density ratio $DR = 1$. Pietrzyk *et al.* (1990) repeated those measurements for the flow with $B = 0.5$ and $DR = 2$. Almost identical setup, with the only difference that cooling holes were shorter, $L/d = 1.75$ instead of $L/d = 3.5$, was used by Sinha *et al.* (1991) to perform surface measurements of adiabatic film cooling effectiveness for various density and blowing ratios. Furthermore, Kaszeta *et al.* (1998) investigated effect of streamwise versus lateral injection for a similar configuration, but with $L/d = 2.3$. For streamwise injection case, two velocity ratios, $B = 0.5$ and 1, were used. He documents the mean velocity, turbulence shear stresses and eddy diffusivity at the spanwise cross-sections along the surface. Comparison of the numerical results is performed with the data of Pietrzyk *et al.* (1989) for mean velocity and turbulent stresses and with the data of Sinha *et al.* (1991) for adiabatic effectiveness.

5.3 Numerical Setup

5.3.1 Computational domain

Computational domain for performing simulations of film cooling geometry presented above is shown in figure 5.2 together with the coordinate system used. Origin of the coordinate system is located on the test plate at the leading edge of the jet. Because of the inclination

of the jet, and hence an elliptical shape of the hole exit cross-section, the trailing edge is located at $x/d \sim 1.74$. Computational domain consists of three different parts: plenum, film hole and a crossflow region. As described in chapter 2, plenum and film hole are calculated with the low Mach number code, and the crossflow region is computed with the compressible code. We summarize characteristics of each subdomain in table 5.1, all distances are expressed in terms of the film hole diameter d. For the cylindrical domains, dimensions are documented as $L \times D$, where L is the length of the cylinder and D is its diameter; for the box, $L_x \times L_y \times L_z$ dimensions are listed. Note that the length of the cylindrical domain corresponding to the cooling hole is $6.7\,d$, whereas the length of the physical hole is $3.5\,d$ (see section 5.2). This mismatch occurs due to the overlap regions of the film hole domain with the other domains both at the top and the bottom parts. The size of the overlap regions can be seen in figure 5.3, where two-dimensional projection of the numerical grid on the $x - y$ plane is plotted. Compressible code domain starts $1\,d$ upstream of the leading edge of the jet and extends to $5\,d$ downstream (see figure 5.3). Number of grid points is specified as $N_x \times N_r \times N_\theta$ for the cylindrical domains and $N_x \times N_y \times N_z$ for the box, respectively. Grid for the film hole is uniform. Since plenum is represented by a large reservoir, much larger than the film hole itself, grid stretching is required for the plenum in both axial and radial directions to ensure adequate resolution at the top wall boundary layer and in the region of high gradients next to the hole-plenum intersection, where the flow turns into the film hole. For the compressible domain, the grid is clustered in x direction to resolve the wake region below the jet, and also in y direction to resolve the wall boundary layer; the grid is uniform in z direction. Grid resolution in both x and y directions for the compressible domain is shown in figure 5.4. Generally, low Mach number code requires finer mesh than the compressible code due to an absence of any artificial dissipation in the low Mach number code. Simulations performed on coarser meshes are compared to the LES obtained with the present mesh by looking at some key features in Appendix D.

5.3.2 Simulation Parameters

Parameters identifying the simulated cooling regime are chosen to closely match those from experiments of Pietrzyk *et al.* (1989). However, density ratio of unity was used in these experiments, and no cooling effectiveness was measured. In order to compare velocity and turbulence field with the measurements of Pietrzyk *et al.* (1989) and at the same time obtain information about film effectiveness, density ratio of $DR = 0.95$ was used in the present
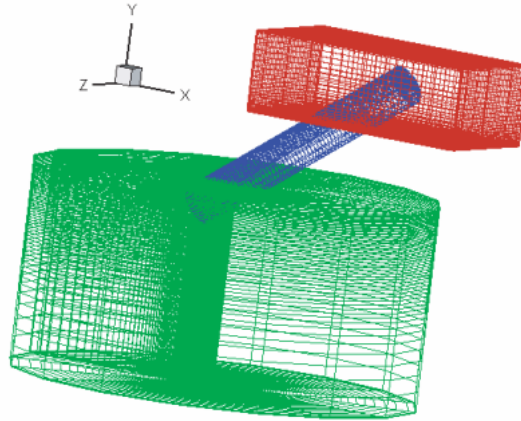
Figure 5.2: Numerical grid for film cooling simulations.
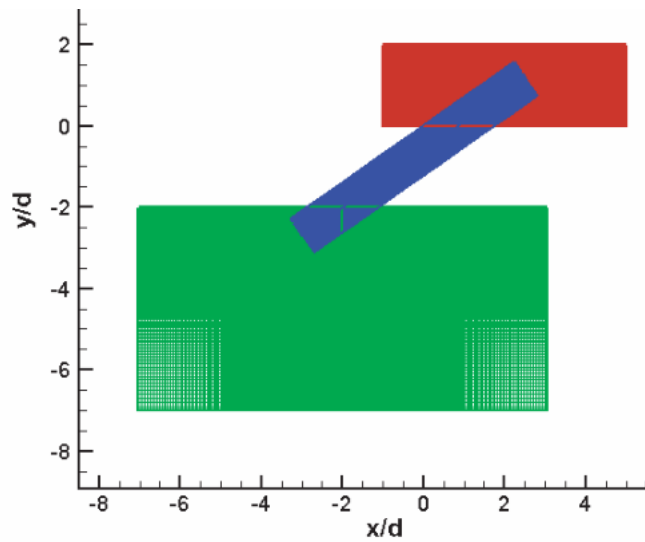
Figure 5.3: Front view of the numerical grid.

Geometry component	Plenum	Film hole	Crossflow region
Domain type	Cylinder	Cylinder	Box
Domain dimensions	$5\,d \times 5\,d$	$6.7\,d \times d$	$6\,d \times 2\,d \times 3\,d$
Number of grid points	$256 \times 512 \times 64$	$936 \times 64 \times 64$	$128 \times 128 \times 128$
Mesh type	Stretched	Uniform	Stretched
	in x and r		in x and y
Minimum resolution	$0.004d \times 0.0025d\times$	$0.007d \times 0.008d\times$	$0.025d \times 0.001d\times$
	$\times 0.1\,rad$	$\times 0.1\,rad$	$\times 0.023d$

Table 5.1: Characteristics of the numerical grid.

(a) Mesh spacing in x direction.

(b) Mesh spacing in y direction.
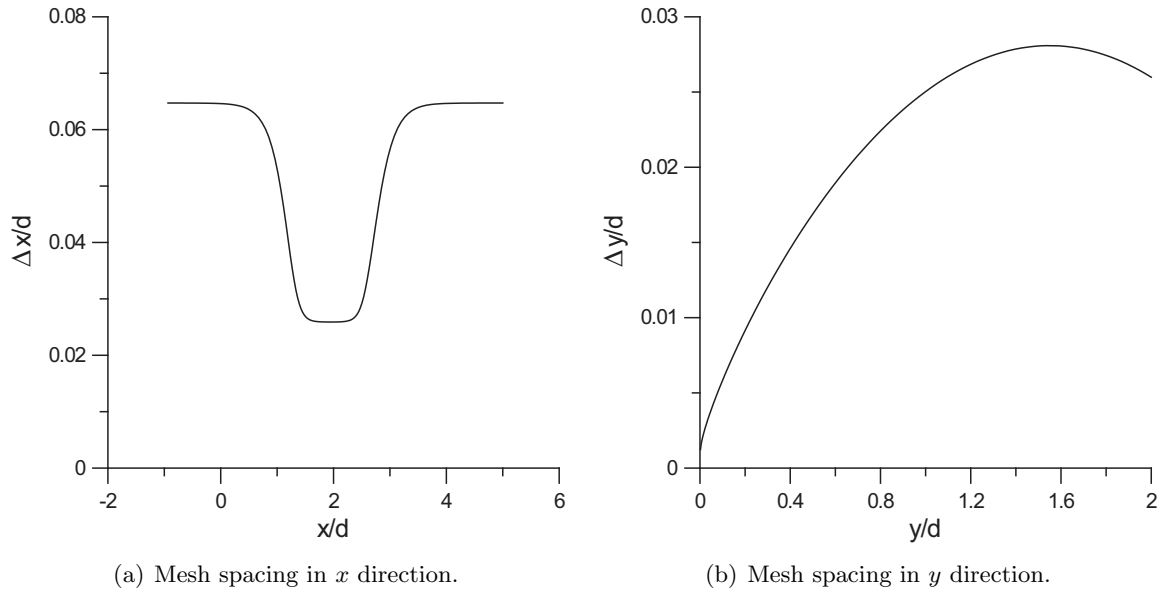
Figure 5.4: Grid resolution for the compressible domain.

	DR	VR	B	I
Experiments	1	0.5	0.5	0.25
Simulations	0.95	0.5	0.475	0.2375

Table 5.2: Comparison of flow parameters used in experiments of Pietrzyk *et al.* (1989) and in the current LES.

LES, matching the velocity ratio to the value of Pietrzyk *et al.* (1989). This slight change in density ratio led to a slight mismatch between other flow parameters, which are contrasted in table 5.2.

Mainstream boundary layer was purposely tripped in experiments to promote its transition to the turbulent state. In fact, usually film cooling experiments that use a flat plate as a test surface involve turbulent boundary layers, as opposed to experiments dealing with simulated leading edge geometry or airfoils, where approaching boundary layer is kept laminar. The reason for that comes from an attempt to match gas turbine engine environment. For the turbine component, boundary layer is laminar at the leading edge. Intensive cooling of the leading edge involving multiple jet injection, referred to as showerhead cooling, triggers the boundary layer transition. Boundary layer becomes fully turbulent by the time it reaches the flat portion of the blade. Special LES of turbulent boundary layer described in chapter 4 was performed in order to obtain realistic inflow conditions for the present simulations. Turbulent boundary layer characteristics in experiments of Pietrzyk *et al.* (1989)

	δ_i/d	δ_i^*/d	θ_i/d	$Re_{\theta i}$	Re_d
Experiments	0.52	0.089	0.059	946	16000
Simulations	0.47	0.087	0.059	938	16000

Table 5.3: Crossflow boundary layer characteristics at $x/d = -2$ for experiments of Pietrzyk *et al.* (1989) and current LES.

Component	Plenum	Film hole	Crossflow region
Inflow	Constant velocity, constant temperature	Coupling	Mainstream: turbulent b.l. Cooling gas: coupling
Outflow	Coupling	Coupling	Parabolized N.S.
Walls	No-slip, adiabatic	No-slip, adiabatic	No-slip, adiabatic
Top			Subsonic outflow

Table 5.4: Summary of the boundary conditions for each subdomain.

measured upstream of the jet injection at the location $x/d = -2$ are reported in table 5.3. Simulation parameters for the turbulent boundary layer at the same location $x/d = -2$ are also documented in this table.

5.3.3 Boundary Conditions

Boundary conditions used for each individual subdomain in the current LES are summarized in table 5.4. The reader is referred to chapter 2 for a detailed description of each specific boundary condition. Constant velocity and temperature supplied at the inflow to the plenum are determined as

$$\frac{U_{\mathrm{pl}}}{U_\infty} = \frac{VR}{(D/d)^2},$$ (5.1)

$$\frac{T_{\mathrm{pl}}}{T_\infty} = DR,$$ (5.2)

where D is the diameter of the plenum.

5.4 Velocity Flowfield

We begin the description of the velocity flowfield by looking at the cross-sectional view of the velocity magnitude contours and associated streamlines inside the plenum, film hole and in the crossflow region, taken through the $x - y$ symmetry plane of the geometry ($z/d = 0$), hereinafter referred to as a center-plane. Time-averaged quantities are presented
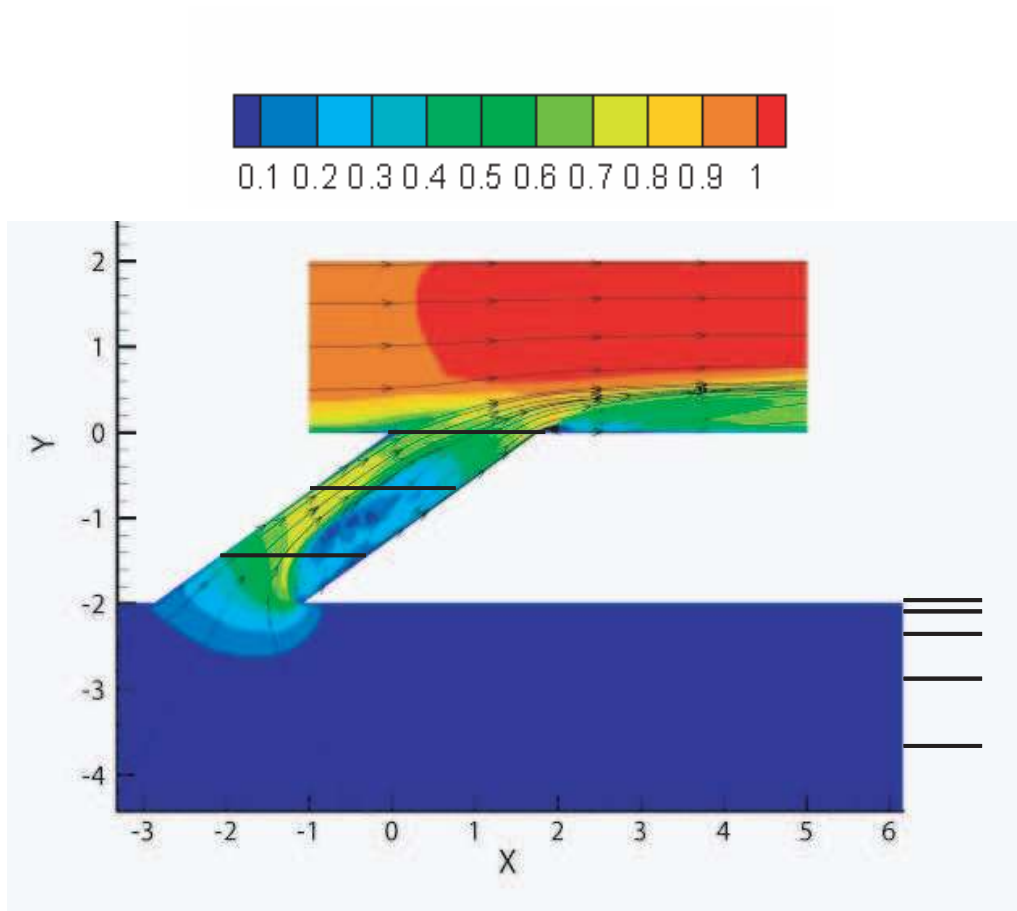
Figure 5.5: Mean velocity magnitude and streamlines inside the plenum, cooling hole and above the plate.

in figure 5.5 and instantaneous quantities, in figure 5.6. Features of the flow inside the plenum, film hole and above the test plate are analyzed below.

5.4.1   Flow Inside the Plenum

Flow in the plenum is mostly stagnating, except for the region very close to the exit, where it rapidly accelerates due to the narrow exit cross-section and turns into the film hole (see figure 5.5). The flow particles approaching the leading edge of the plenum exit cross-section turn smoothly. However, particles approaching the trailing edge of the exit cross-section have to undergo sharp 135° turn. They accelerate more rapidly, resulting in higher exit velocities, which can be seen in figure 5.7, where mean vertical velocity contours at the plenum exit cross-section are plotted. The cross-section is elliptical since it is an
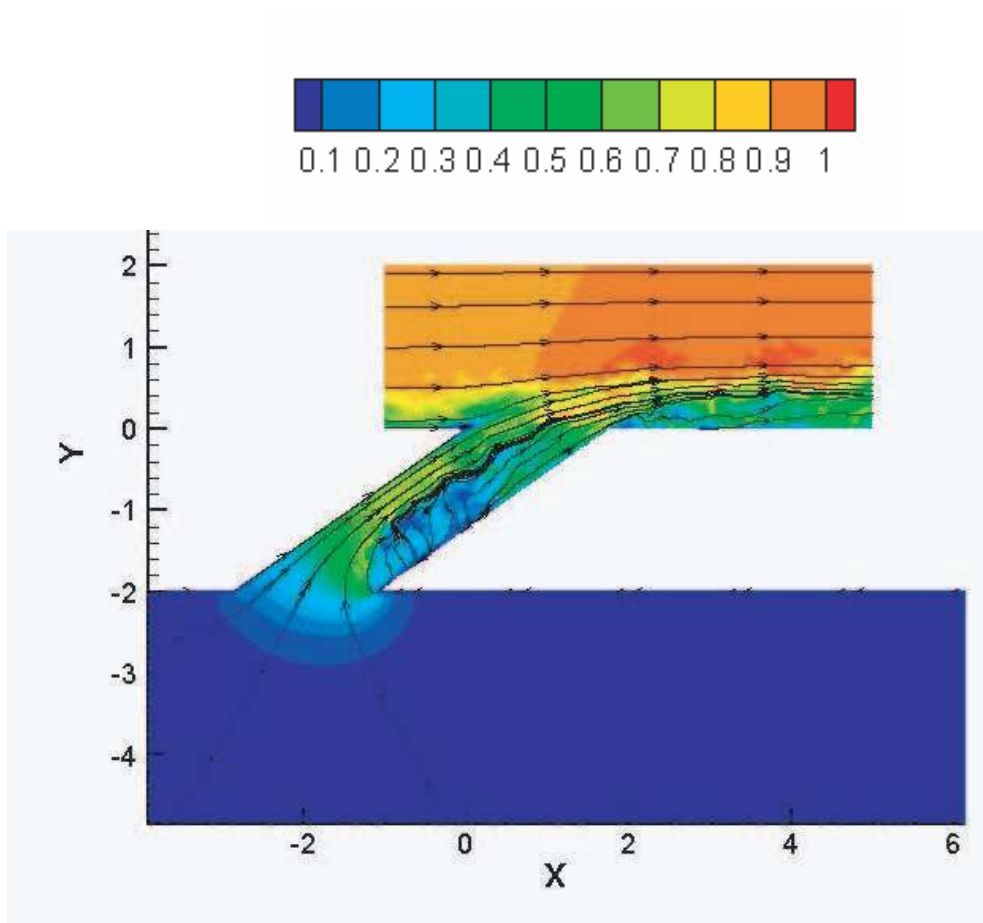
Figure 5.6: Instantaneous velocity magnitude and streamlines inside the plenum, cooling hole and above the plate.
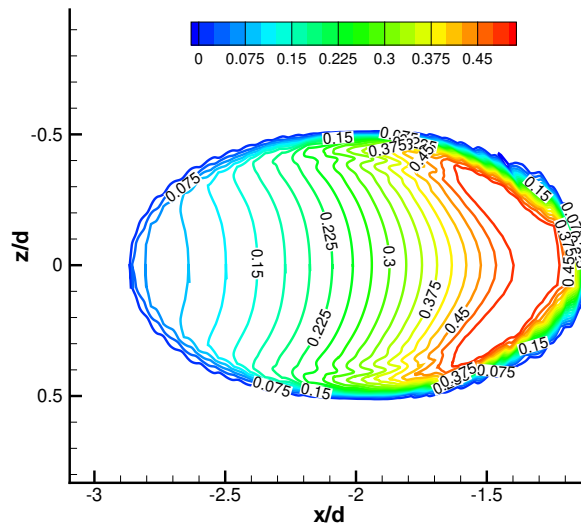
Figure 5.7: Vertical velocity contours at the plenum exit cross-section.

intersection of inclined cylindrical hole with a flat surface. Vertical velocity profiles along different horizontal lines through the center-plane of the plenum (marked in figure 5.5) are shown in figure 5.8. Skewness in velocity towards the downstream wall due to the more rapid flow acceleration near the downstream corner is evident. Note the sharp peak at the plenum exit velocity due to the quick turn at the downstream corner. Fast decay in velocity away from the plenum exit is also observed.

5.4.2 Flow inside the Film Hole

Sharp turn at the trailing edge of the plenum exit cross-section causes the flow to separate from the downstream wall of the film hole, as can be seen by looking at the close-up of the mean velocity magnitude and a streamlines inside the film hole in figure 5.9(a). This separation results in a zone of a slow moving flow next to that wall. To conserve the total mass flux, the flow accelerates upstream of this slow moving zone, producing the so-called "jetting" effect described by Leylek & Zerkle (1994), Walters & Leylek (1997), Peterson & Plesniak (2005) etc. To understand the jetting phenomenon better, contours of mean vertical velocity in two cross-sections perpendicular to the hole centerline are visualized in figure 5.9(b). The location of the cross-sections is marked in figure 5.9(a). In-plane mean streamlines for the lower cross-section are also shown. Ellipses at the bottom and the top
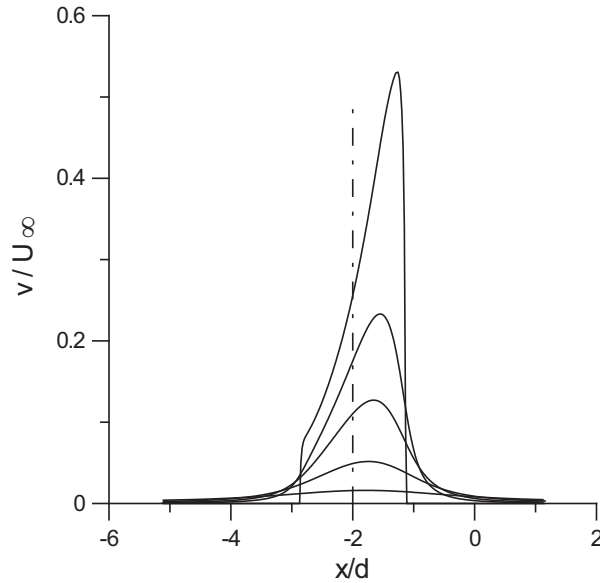
Figure 5.8: Vertical velocity along the horizontal lines through the plenum center-plane. Solid lines, from top to bottom: $(y - y_{\text{top}})/d = 0$, -0.25, -0.5, -1, -2. y_{top} is the coordinate of the top plenum wall; dash-dotted line, plenum centerline.

of the figure correspond to the plenum exit and the hole exit cross-sections, respectively. It is seen from the figure that jetting results in the recirculating flow in the transverse planes of the film hole (captured in bottom cross-section). This recirculating flow brings the fluid particles from the upstream wall (where the jetting region is located) to the downstream wall, which can also be seen by the unstable node points in a streamline pattern of figure 5.9(b) close to the downstream wall (meaning that the flow enters from out of plane into these node points). The separation zone does not extend all the way to the test plate in the current simulations due to the relatively low blowing ratio of 0.475. No recirculation is observed at the top cross-section. However, an effect of the separation zone is still noticeable at this cross-section by the existence of a low momentum flow in the middle part of the cross-section. In fact, this momentum deficit extends all the way to the hole exit resulting in an exit velocity distribution, which is the opposite to the one of a fully developed pipe flow. This is documented in figure 5.10, where mean vertical velocity contours at the film hole exit cross-section are shown. Velocity is the lowest in the central part of the cross-section, but it would be the highest there for the fully-developed laminar or turbulent pipe flow. In the compressible code, jet exit cross-section is approximated as a staircase, explaining the diamond shapes of the contour lines with zero vertical velocity at the leading edge in figure 5.10. More details on the staircase approximation together with an enlarged view of

the velocity contours can be found in section 2.5 of the chapter 2.

Vertical velocity profiles taken through the horizontal lines $y/d = -1.4$ (separation zone), $y/d = -0.7$ (end of a separation zone) and $y/d = 0$ (film hole exit) across the center-plane are shown in figure 5.11 (see the relative location of the horizontal lines across the hole in figure 5.5). Strong peak due to the jetting effect followed by a dimple due to the separation zone is observed for $y/d = -1.4$ profile. Both peak and a dimple move upstream and flatten as the flow proceeds further into the hole corresponding to a lateral growth of a separation zone and migrating of a jetting region towards an upstream wall. By the time the flow reaches the hole exit, separation effect is largely decreased, however, a slight velocity deficit in the center is still noticeable. It is interesting to note that vertical velocity peaks at the downstream corner of the hole–plate intersection. This local acceleration is probably caused by the low pressure region underneath the jet created due to the turning of the jet by the crossflow.

Comparison of jet exit velocity profiles with experimental data is presented in figure 5.12 versus x/d and in figure 5.13 versus z/d. Deficit in both streamwise and vertical velocity in the center of the jet exit cross-section due to the separation inside the hole exists extending in both streamwise and spanwise direction, showing the three-dimensionality of the separation bubble. Large spanwise velocity pointing away from the centerline is observed at the lateral edges of the jet at $x/d = 1.6$, close to the cross-section trailing edge. This indicates the beginning of a lateral diffusion of the jet. Overall, comparison with experiment is very good. The only disagreement is a slight overprediction in streamwise velocity at the downstream part of the cross-section, which can be seen from figures 5.12 and 5.13(b).

The documented flow inside the film hole shows the crucial influence of the plenum conditions on a flow inside the hole and therefore jet exit velocity distribution. Although large stagnation-type reservoir, normally used in cooling experiments and therefore modeled here, might not be representative of an actual serpentine-type plena used in real turbine engines, present findings do indicate an importance of inclusion of exact plenum conditions into film cooling simulations. The influence of plenum is transported onto the blade surface because of the short length of the cooling holes. Exact pattern of the flow inside the hole will depend on an exact geometry and, in fact, will be different for every single hole on an airfoil surface due to a different hole entrance conditions. It is arguable whether the separation inside the hole will always occur. Peterson & Plesniak (2002, 2004) studied the influence of a flow direction in the plenum on the flow inside the normally oriented cooling hole and above the test surface and showed that downstream in-hole separation occurs for
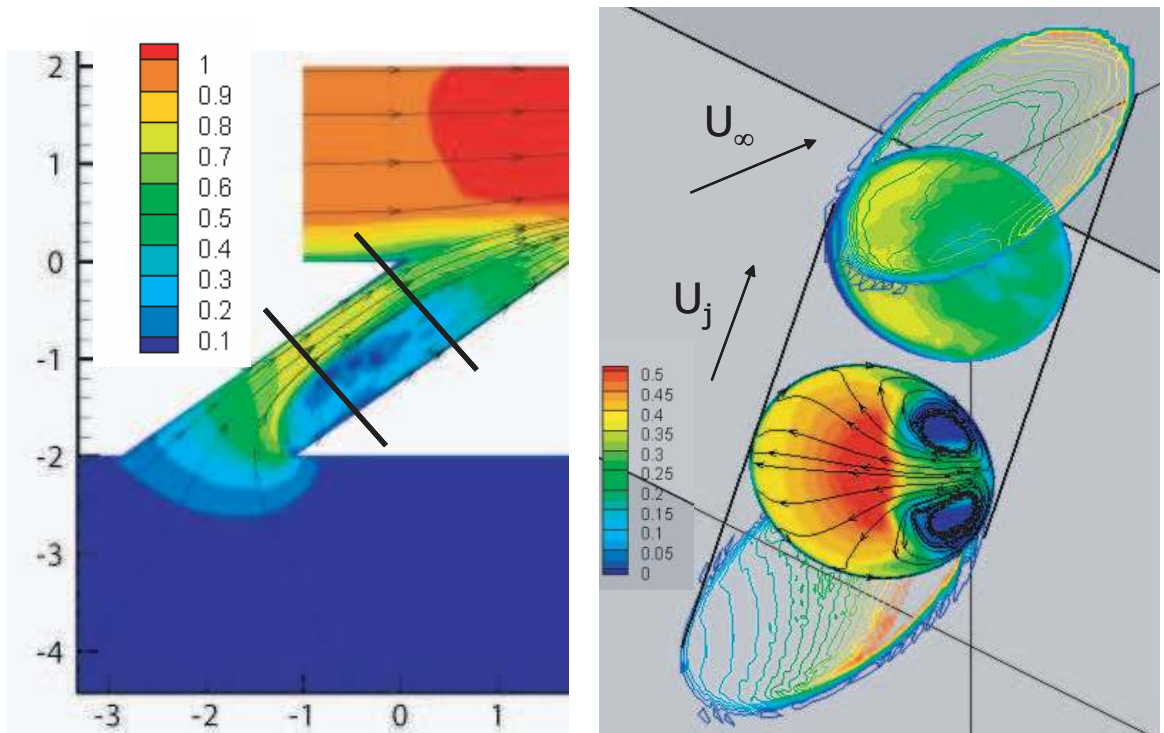
(a) Contours of mean velocity magnitude and streamlines in the center-plane.

(b) Contours of mean vertical velocity and streamlines in the cross-sections perpendicular to the hole centerline.

Figure 5.9: Flow inside the film hole.
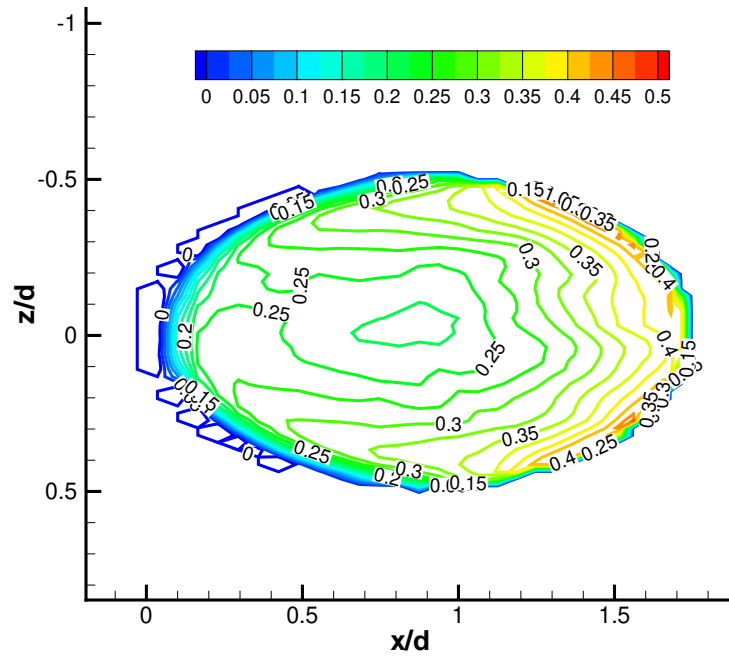
Figure 5.10: Contours of mean vertical velocity in the jet exit cross-section.
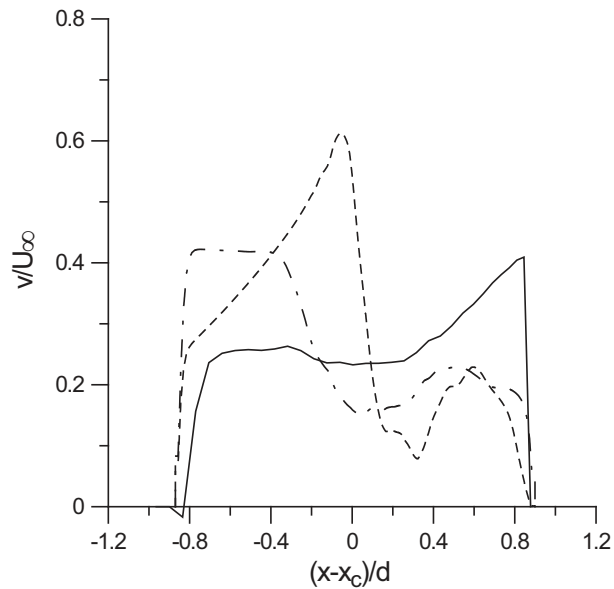
Figure 5.11: Vertical velocity profiles inside the hole along the horizontal lines through the center-plane. x_C is the streamwise coordinate of the jet centerline. Dashed line, $y/d = -1.4$; dash-dotted line, $y/d = -0.7$; solid line, $y/d = 0$ (jet exit cross-section).
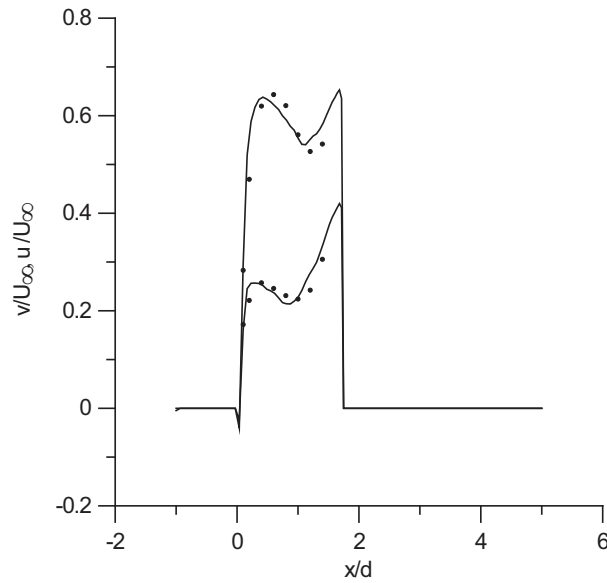
Figure 5.12: Comparison of jet exit velocity profiles with experiment. Profiles taken along the horizontal line $y/d = 0$ in the center-plane. Lines, calculations; symbols, experiments (Pietrzyk *et al.* (1989)). Top line, streamwise velocity; bottom line, vertical velocity

(a) Along a spanwise line $x/d = 1$

(b) Along a spanwise line $x/d = 1.6$
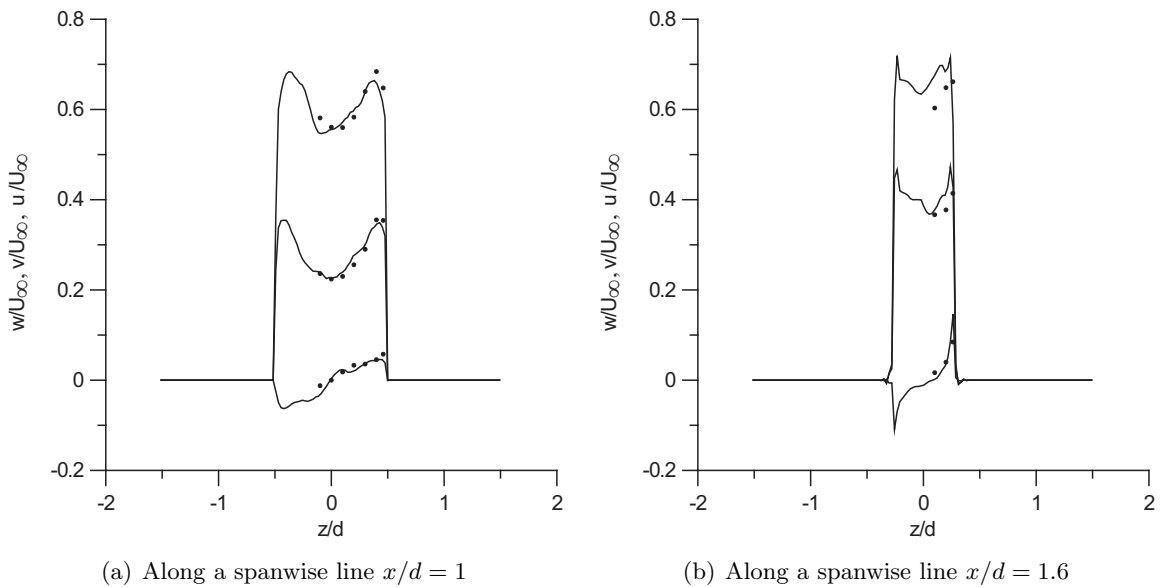
Figure 5.13: Comparison of jet exit velocity profiles with experiment. Lines, calculations; symbols, experiments (Pietrzyk *et al.* (1989)). Top curve, streamwise velocity; middle curve, vertical velocity, bottom curve, spanwise velocity.

the counter-flow plenum, and upstream in-hole separation for the co-flow plenum. They also concluded that the influence of a plenum conditions on jet-mainstream interaction during film-cooling is extremely high.

5.4.3   Flow above the Test Plate

Three-Dimensional View

Jet-mainstream interaction occurs above the test plate, making the structure of the flow in this region highly three-dimensional and complex. To visualize the three-dimensionality of the flow and its coherent steady vortical structures, mean three-dimensional streamlines in the crossflow region are plotted in figure 5.14. Contours of vertical velocity at the wall are also shown marking the film hole boundary. Among steady vortical structures visible in the figure are horseshoe vortex upstream of the hole and another three-dimensional vortical structure downstream of the hole. Magnified view of both of these vortex systems is presented in figure 5.15. Horseshoe vortex occurs as a result of a blockage of the crossflow by the jet. Not being able to penetrate through the jet, boundary layer vorticity is transported around its circumference, gradually reorienting in streamwise direction. In case of a normal injection, horseshoe vortex gets entrained into the jet quite fast due to a strong upstream secondary motion in the jet wake. In the present case of inclined jet, however, upstream secondary motion is not as strong, and the horseshoe vortex persists far downstream, as can be seen in figure 5.14 (only one leg of the horseshoe vortex is captured in figure. A symmetrical leg on the other side of the jet exists as well). The downstream vortex occurs due to the entrainment of a crossflow fluid bending around the jet back to the center-plane by the low pressure zone created behind the jet due to the crossflow blockage. Being pushed towards the center-plane, the crossflow fluid is entrained into the vortical motion bringing it down to the wall and back underneath the jet. A similar structure was observed by Peterson & Plesniak (2002, 2004) in case of a normal jet injection and was named a downstream spiral separation node (or DSSN vortex). Because of the existence of a spiral node in the streamline pattern for the currently observed vortex, it will be referred to as DSSN vortex as well.

Cross-Sectional Views

Front View

   A signature of the horseshoe vortex at the upstream corner of the hole and the DSSN
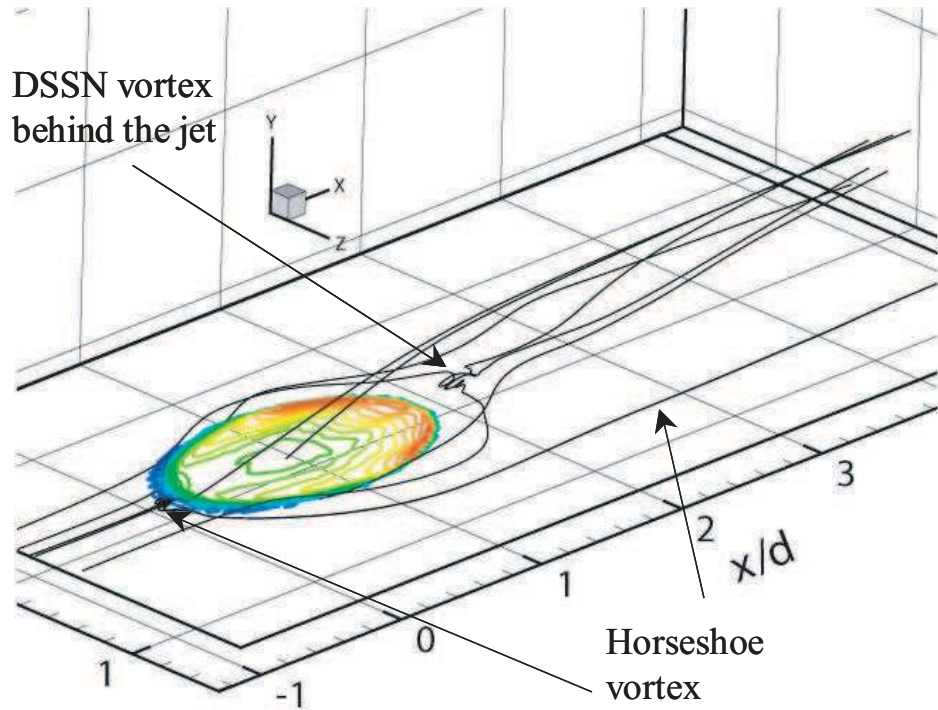
Figure 5.14: Three-dimensional mean streamlines in the crossflow region.

(a) Horseshoe vortex upstream of the jet

(b) DSSN vortex behind the jet
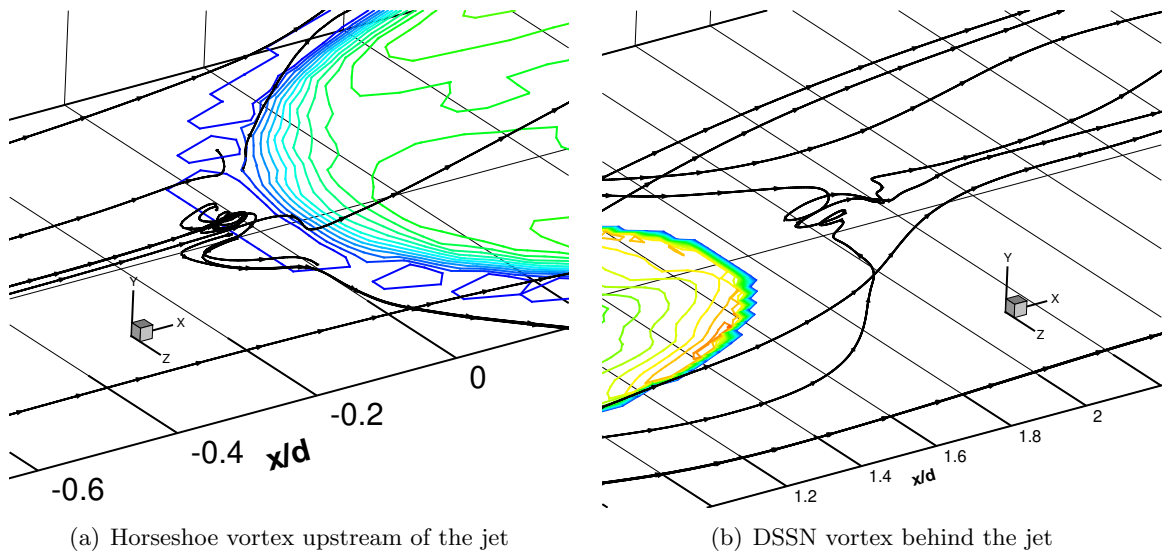
Figure 5.15: Magnified view of the crossflow vortex systems.

vortex downstream of the hole is visible on the center-plane view in figure 5.5. Convergence of the jet streamlines after injection indicates a jet lift-off and is compensated by a spanwise spreading. The low-momentum wake between the jet and the wall is visible, which consists of an entrained crossfow fluid and a jet fluid shed from the lateral edges of the jet. To assess a streamwise location of the horseshoe and the DSSN vortex, a magnified view of the two-dimensional $x - y$ projection for both of these vortical systems is presented in figure 5.16. Horseshoe vortex (figure 5.16(a)) is originated right before the jet injection, $x/d \sim -0.05$, and lies very close to the wall, at $y/d \sim 0.01$. Another interesting phenomenon seen in figure 5.16(a) is the crossflow ingestion into the hole creating a vortex next to the upstream wall with a vorticity sign opposite to that of a horseshoe vortex. This vortex is similar to a hanging vortex observed in normal jets (Iourokina & Lele (2005), Muppidi & Mahesh (2005)). Looking at DSSN vortex (figure 5.16(b)), one can notice that the streamlines create a pattern of an unstable vortex, located at $x/d \sim 2$, $y/d \sim 0.07$. Being entrained into the vortex, some of the fluid proceeds downstream towards the wall, some merges with the wake of the jet, and some impinges on the wall right beneath the vortex and reverses the direction to join with the lower part of the jet.

Now we look at the mean velocity profiles and compare them with experimental values. Streamwise and vertical velocity profiles along the horizontal lines $y/d = 0.15$ (through the DSSN vortex) and $y/d = 0.3$ (through the wake of the jet) at the center-plane are shown in figure 5.17. The gap in vertical velocity due to the flow separation completely disappears by $y/d = 0.15$ showing that the jet recovers from the influence of the in-hole separation. The gap still exists, however, in the streamwise velocity profile. Overall, the values of u are increasing and the values of v are decreasing with the distance from the wall, corresponding to the bending of the jet. Right behind the hole trailing edge, both u and v drop significantly, marking the low momentum region associated with DSSN vortex. No negative values for u and v, however, are observed at $y/d = 0.15$, which would be expected for the recirculating flow. This is because the vortex exists closer to the wall; vortex core is observed at about $y/d \sim 0.07$ and the region of reverse flow lies beneath it. Unfortunately, no measurements were performed below $y/d = 0.15$, and comparison with experiments is not possible. Computational profiles of u and v plotted at $y/d = 0.05$ indeed show the negative values at $x/d \sim 2$ for both streamwise and vertical velocity (figure 5.18).

No gap due to the in-hole separation is visible at $y/d = 0.3$. Both streamwise and vertical velocity profiles acquire usual jet-like parabolic form. Streamwise velocity upstream of the jet at $y/d = 0.3$ is larger compared to $y/d = 0.15$ consistent with the boundary

(a) Horseshoe vortex upstream of the jet

(b) DSSN vortex behind the jet
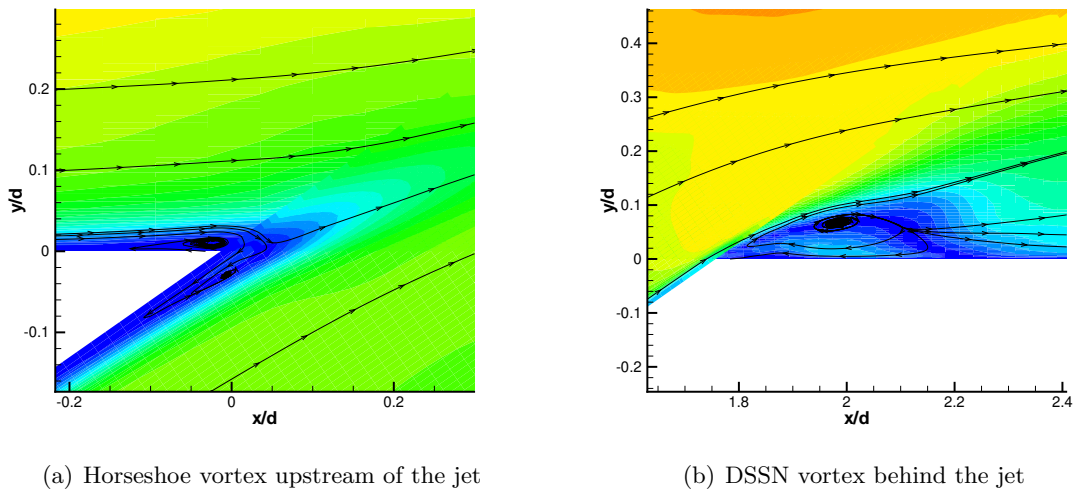
Figure 5.16: Magnified view of the crossflow vortex systems.

layer velocity distribution. Both streamwise and vertical velocity profiles are smoother at $y/d = 0.3$, indicating that sharp gradients occurring during the initial interaction between the jet and the crossflow are smoothing out.

Transverse View

To document the spanwise development of the jet, we first look at the spanwise cross-sections along different streamwise locations. Velocity magnitude contours together with the mean streamlines for the planes cutting through the film hole exit are plotted in figures 5.19 and 5.20 and those downstream of the film hole exit, in figures 5.21 and 5.22. Roll up of the shear layer vorticity on the lateral sides of the exit cross-section is noticeable at $x/d = 1$. These vortices grow in size as the observer moves downstream and start entraining crossflow fluid, creating a recirculating motion from the lateral sides of the jet to the wall and up into the wake, forming counter-rotating vortex pair (CRVP). The location of CRVP corresponds to the wake of the jet. Another vortex pair with the circulation opposite to that of CRVP is seen next to the wall at $z/d = \pm 1$. Contrary to CRVP, these vortices do not expand laterally and remain of approximately the same size. These are the legs of a horseshoe vortex seen in figure 5.14. Interaction between the jets (due to periodicity) also comes into play as the jets expand laterally, and is quite significant by $x/d = 5$, showing that another pair of vortices is formed between the jet cores (lateral edges of the transverse cross-section).

We plot velocity distribution at three spanwise cross-sections, $x/d = 1$, $x/d = 3$ and

(a) $y/d = 0.15$ (b) $y/d = 0.3$
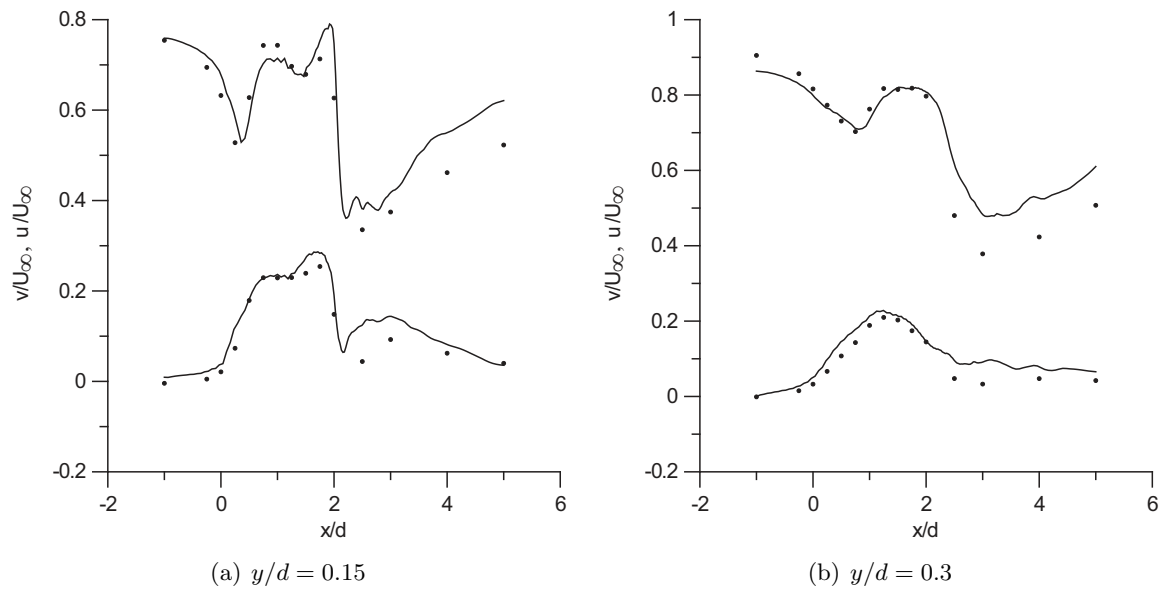
Figure 5.17: Velocity profiles along the horizontal lines in the center-plane. Top curve, streamwise velocity; bottom curve, vertical velocity. Solid line, simulations; symbols, experiments (Pietrzyk *et al.* (1989)).
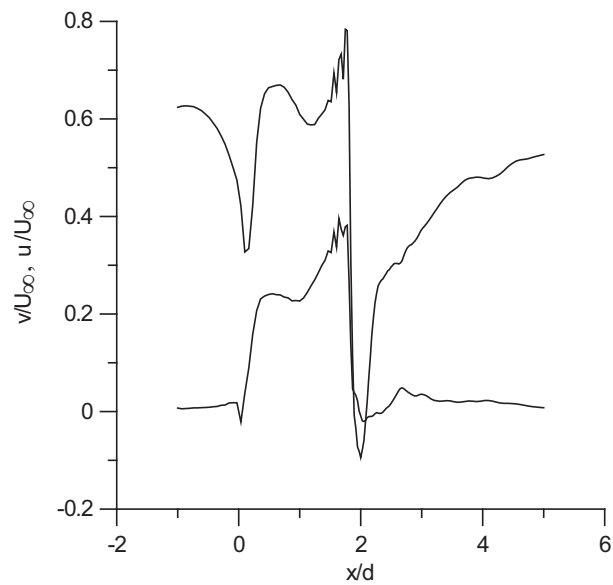
Figure 5.18: Velocity profiles along the horizontal line $y/d = 0.05$ in the center-plane. Top curve, streamwise velocity; bottom curve, vertical velocity.

$x/d = 5$, in figures 5.23, 5.24 and 5.25, respectively. Profiles along the lines $y/d = 0.15$ and $y/d = 0.3$ are documented for each cross-section. At $x/d = 1$, streamwise velocity profile is almost uniform across z, indicating that inclined jet with relatively low momentum ratio starts bending in a crossflow direction right away. However, at this streamwise location, it still penetrates vertically into crossflow, which can be judged from the high values of vertical velocity at both $y/d = 0.15$ and $y/d = 0.3$. Notice high values of spanwise velocity away from the center-plane at $x/d = 1$, showing fast lateral spreading of the jet during the initial period of interaction. At $x/d = 3$, streamwise velocity profile is significantly different from the one at $x/d = 1$, with the large gap in the middle. This gap is due to the wake underneath the jet, where crossflow fluid is being entrained by CRVP. A narrow spike of vertical velocity is seen at $y/d = 0.15$, which is much weaker at $y/d = 0.3$. This spike is quite different from the wider top-hat profile at $x/d = 1$ due to the jet penetration. It corresponds to the bulk upward vertical motion induced by CRVP. Note that spanwise velocity at $y/d = 0.15$ reversed its sign, pointing now towards the center-plane, corresponding to CRVP entraining motion. Spanwise velocity still points away from the center-plane at $y/d = 0.3$, since CRVP does not yet extend vertically to $y/d = 0.3$. Magnitude of spanwise velocity is highly reduced, however, showing that the strong spanwise expansion is now over. At $x/d = 5$, lateral entrainment by CRVP exists at both $y/d = 0.15$ and $y/d = 0.3$ indicated by the sign of spanwise velocity. Note that values absolute values of both spanwise and vertical velocity are now very small, since CRVP motion becomes slower as its radius grows. Gap in streamwise velocity is also not as large now, because of the lateral mixing of the crossflow with the wake fluid. It is interesting to note a waving in streamwise velocity for $y/d = 0.15$ for all three spanwise cross-sections occurring at $z/d \sim \pm 1$, apparently associated with the horseshoe vortex. It looks like horseshoe vortex is moving with a lower speed than the rest of the fluid. Waving in streamwise velocity at $y/d = 0.3$ also exists, though not as pronounced. This trend is somewhat noticeable in experimental data as well, especially at $x/d = 3$. Slight oscillations in vertical velocity also exists at $y/d = 0.15$ for $x/d \geq 3$, due to the interaction between the jets observed in figures 5.21 and 5.22.

Horizontal View

Near-wall structure of the jet-crossflow interaction varies significantly with blowing ratio in case of normal jet injection. At high blowing ratio, unsteady upright vortices exists in the wake, reorienting boundary layer vorticity in vertical direction and bringing crossflow fluid into the wake. Vortex shedding resembles the Karman vortex street more and more

(a) $x/d = 1$

(b) $x/d = 1.2$
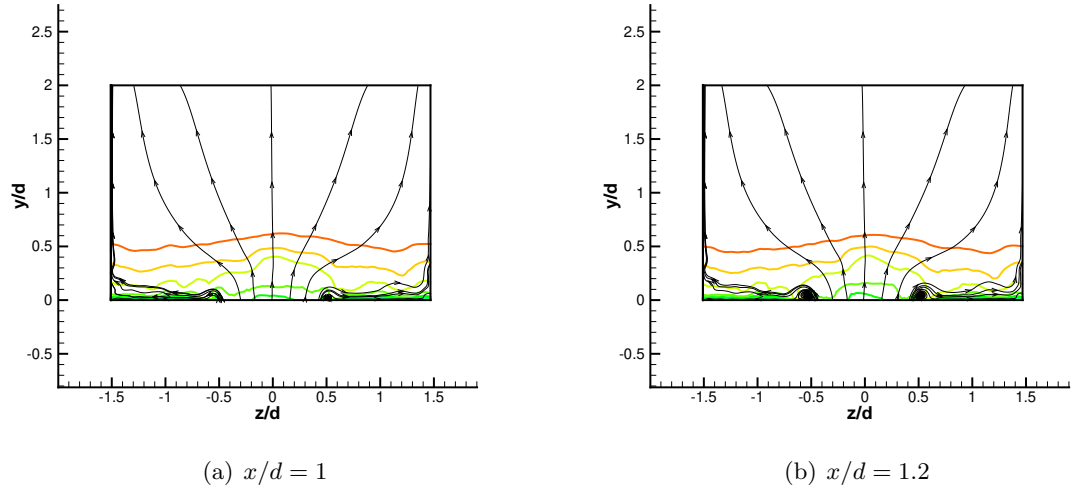
Figure 5.19: Velocity magnitude and mean streamlines at the transverse planes cutting through the film hole exit.

(a) $x/d = 1.4$

(b) $x/d = 1.6$
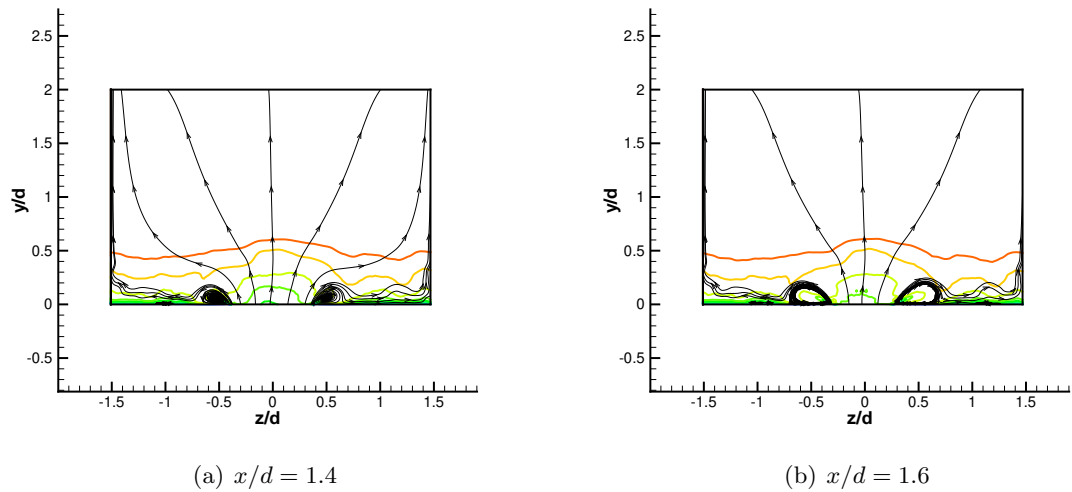
Figure 5.20: Velocity magnitude and mean streamlines at the transverse planes cutting through the film hole exit.

(a) $x/d = 2$ (b) $x/d = 3$
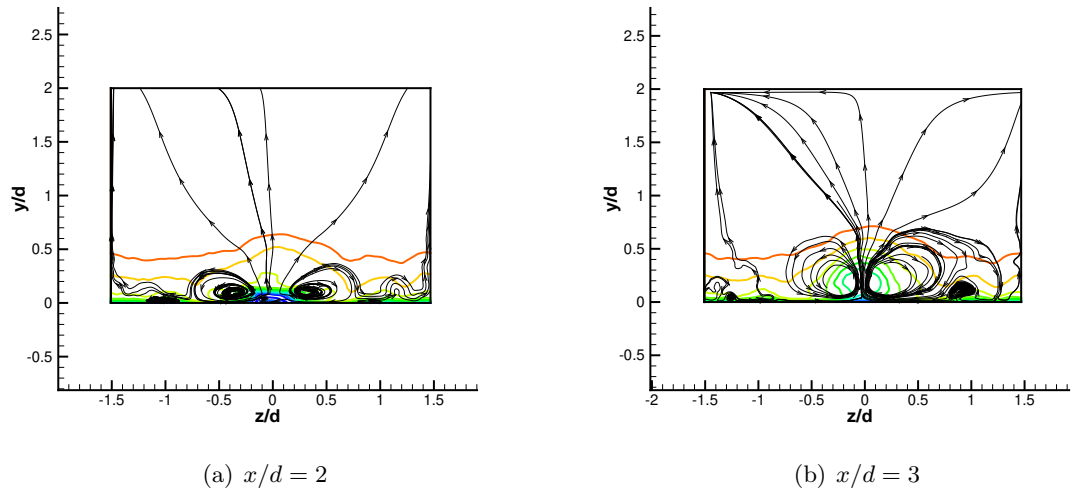
Figure 5.21: Velocity magnitude and mean streamlines at the transverse planes downstream of the film hole exit.

(a) $x/d = 4$ (b) $x/d = 5$
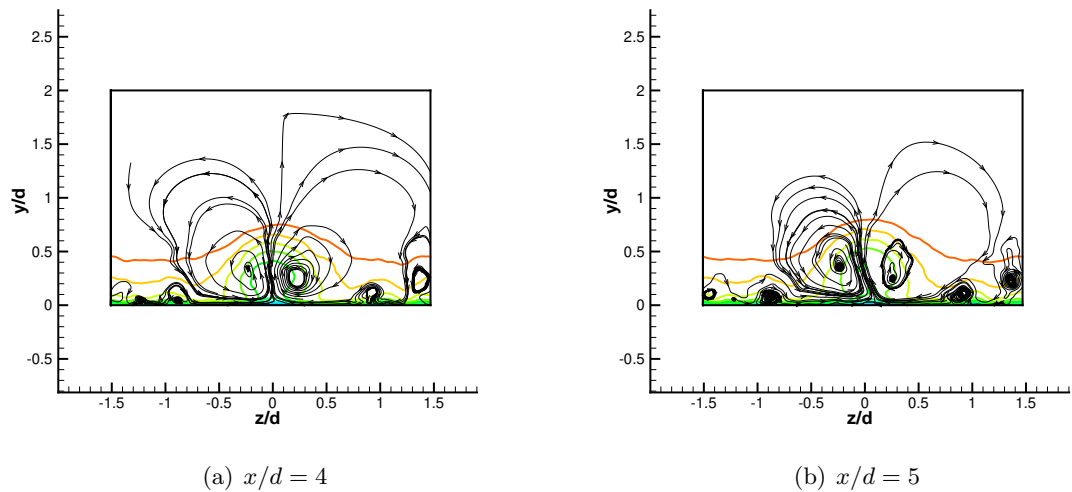
Figure 5.22: Velocity magnitude and mean streamlines at the transverse planes downstream of the film hole exit.

(a) $y/d = 0.15$

(b) $y/d = 0.3$
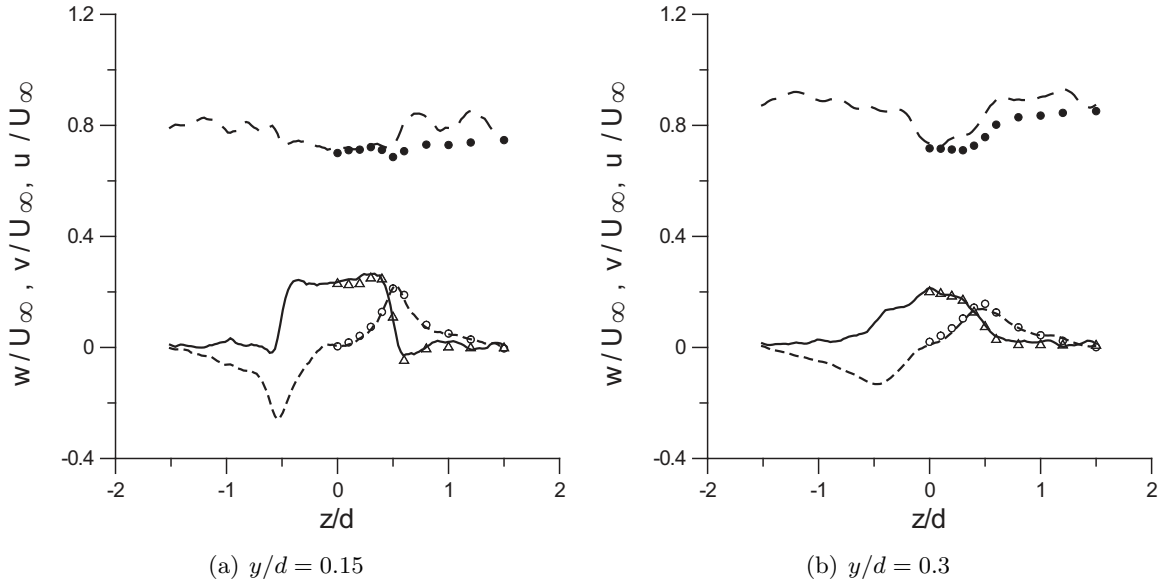
Figure 5.23: Velocity profiles for the transverse plane $x/d = 1$. Lines, simulations; symbols, experiments (Pietrzyk *et al.* (1989)). — — —, •; streamwise velocity; ———, $\triangle$, vertical velocity; $---$, $\circ$, spanwise velocity.

(a) $y/d = 0.15$

(b) $y/d = 0.3$
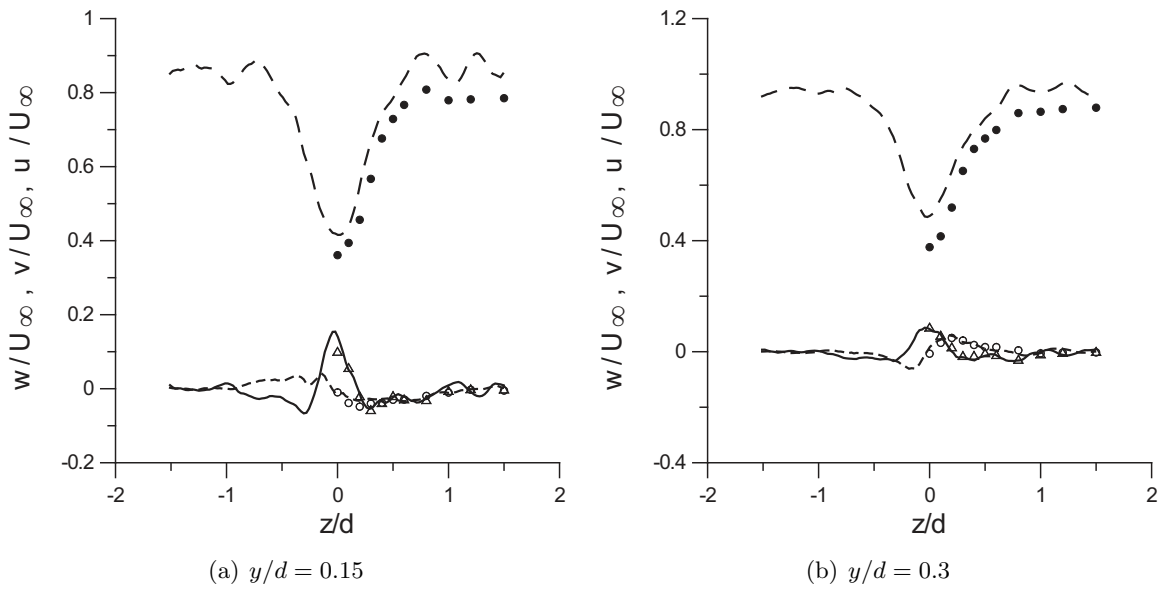
Figure 5.24: Velocity profiles for the transverse plane $x/d = 3$. Lines, simulations; symbols, experiments (Pietrzyk *et al.* (1989)). — — —, •; streamwise velocity; ———, $\triangle$, vertical velocity; $---$, $\circ$, spanwise velocity.

(a) $y/d = 0.15$ (b) $y/d = 0.3$
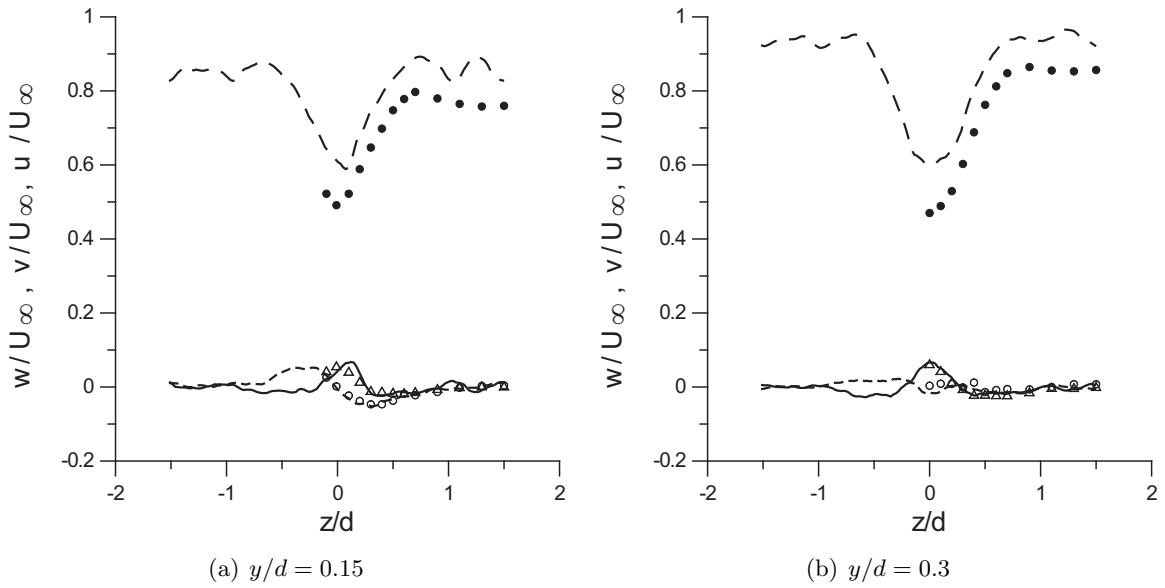
Figure 5.25: Velocity profiles for the transverse plane $x/d = 5$. Lines, simulations; symbols, experiments (Pietrzyk *et al.* (1989)). — — —, ●; streamwise velocity; ———, △, vertical velocity; − − −, ○, spanwise velocity.

with increase in the blowing ratio. The near-wall structure is completely different for low-momentum normal jets. Large "dead" zone exists behind the jet with almost no flow, occupied by two slowly recirculating vortices. The flow behind low-momentum inclined jet does not follow any of these two scenarios. No vortex shedding occurs, and no "dead" zone is formed. Instead, two small recirculating vortices exist close to the wall at the lateral edges of the jet. Flow initially bending around the jet rapidly converges back towards the center-plane. This pattern can be seen in figure 5.26, where mean spanwise velocity and streamlines at the horizontal $y/d = 0.015$ cross-section are presented. Two recirculating vortices behind the jet are visible, corresponding to the large values of spanwise velocity towards the center-plane. Node point at $x/d \sim 2.1$ is observed, coinciding with the location of DSSN vortex described earlier. Therefore, recirculating motion in the near-wall horizontal cross-section is associated with the backward motion of the fluid underneath DSSN vortex into the jet and, seen in figure 5.16(b). The three-dimensional mechanism of DSSN vortex seems to be completely different from the dynamics of upright vortices of the high-momentum normal jets, since it brings fluid from the wake to the wall, whereas upright vortices bring the fluid from the wall to the wake. DSSN vortex can possibly be of the same nature as the "dead zone" with the slow moving recirculating flow behind the low-momentum normal jets, but significantly reduced in size due to the inclination of the jet. It is undoubtedly associated
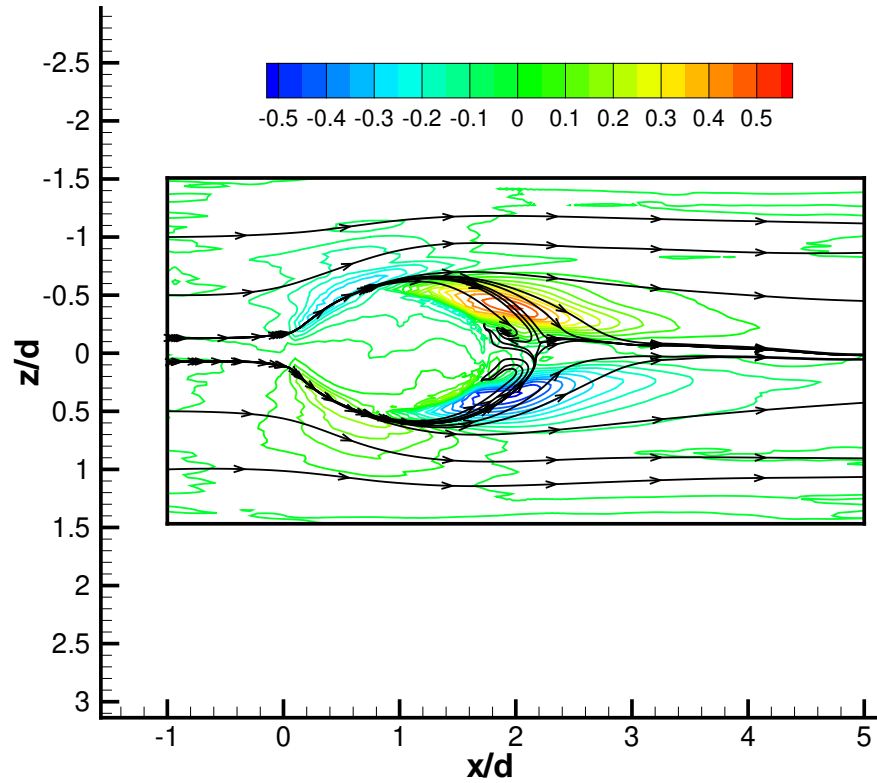
Figure 5.26: Mean spanwise velocity and streamlines in the horizontal $y/d = 0.015$ cross-section.

with the jet lift-off, and its streamwise, as well as vertical spreading most likely depends on the blowing ratio.

As far as comparison of mean velocity flowfield with experiments is concerned, the overall agreement is very good. An only disagreement seems to be a slight overprediction of streamwise velocity, especially in the far field.

5.5   Turbulence Statistics

Turbulence field and its comparison with experiments is presented in this section. Turbulence statistics was accumulated over a period of $t \sim 48\, d/\mathcal{U}_\infty$. This sampling interval is large enough to achieve the convergence of the mean quantities. However, it is not sufficient for the convergence of the second moments and the derived quantities. Limited averaging

time results in spiky profiles for these quantities, which will be smoothed out by adding more samples. Importance of SGS turbulence model is assessed in Appendix D.

5.5.1 Front View

Normal Stresses

Turbulent Kinetic Energy

Contours of turbulence kinetic energy (TKE), $\sqrt{k}/U_\infty$, where $k = (u'^2 + v'^2 + w'^2)/2$, in the center-plane for the plenum, film hole and a crossflow region are plotted in figure 5.27. There are three dominant regions of high kinetic energy, with TKE levels greater than 18%.:

1. The corner between the plenum and the downstream film hole wall, where the flow undergoes sharp 135 degree turn. Some peculiar behavior of TKE near the jet centerline close to the intersection with the plenum is most likely a numerical artifact: due to a proximity of the centerline, the grid cell volumes become very small; in a control volume formulation of the low Mach number code, it means that the area next to the centerline is the most susceptible to numerical instabilities (or the formation of "wiggles"). Given the high level of unsteadiness introduced by the proximity of a sharp corner, some numerical noise is accumulated in this region. Recall that no artificial dissipation is used in low Mach number code to remove the energy from the high wave number components.

2. A shear layer between the separated region next to the downstream hole wall and the "jetting" region. Johnston *et al.* (2002) believe that Kelvin-Helmholtz instability of this shear layer leads to a turbulence production in this region. This shear layer carries high levels of turbulence into the crossflow region, explaining why the sharp corner from the plenum enhances the turbulence levels above the test plate (see also Johnston *et al.* (2002)). To get a better estimate of the levels of turbulence brought into crossflow by the incoming jet due to the flow separation inside the hole, contours of TKE levels in a jet exit cross-section are plotted in figure 5.28. Indeed, turbulence levels of up to 14% are noticeable in the middle of the cross-section.

3. Immediately behind the trailing edge of the hole exit cross-section, corresponding to the location of a DSSN vortex.

Root Mean Square (RMS) Values of Velocity Fluctuations

To look at the contribution of fluctuations of different velocity components to the turbulent kinetic energy, contours of u_{rms}, v_{rms} and w_{rms} in the center-plane are shown in figures 5.29, 5.30 and 5.31, respectively. The overall structure of u_{rms}, v_{rms} and w_{rms} is similar. High levels of all three components of turbulent fluctuations exist in the recirculation region behind the jet, vertical velocity fluctuations showing the smallest value. Main differences occur in the near field after the jet injection. u_{rms} is maximum in the shear layer between the jet and a crossflow, while v_{rms} show the highest value in the jet wake, beneath the shear layer. They perhaps correspond to the vertical fluctuations induced by CRVP bringing the flow from the wall into the wake. The w_{rms} has a maximum next to the wall, probably also associated with CRVP, representing the lateral entrainment of fluid towards the centerline. The different locations of maximum levels for u_{rms} and w_{rms} explains two local maxima of TKE in the far field (see figure 5.27): one right next to the wall due to w' fluctuations and another in the shear layer due to u' fluctuations.

Comparison with Experiments

Measurements of the two components of the fluctuating velocity, u_{rms} and v_{rms}, are performed in the center-plane by Pietrzyk *et al.* (1989). They are visualized in terms of a turbulence level (TL) defined as

$$TL = \sqrt{u'^2 + v'^2}/U_\infty. \tag{5.3}$$

Contour plot of TL from the present simulations is shown in figure 5.32. Corresponding plot from experiments is reproduced in figure 5.33. The overall structure of TL for simulations and experiments is very similar. Turbulence of about 12% is observed at the upstream shear layer; levels of $14 - 16\%$ are reached in the middle of the jet exit cross-section (due to the shear layer inside the hole discussed earlier); the highest turbulence levels are in the downstream shear layer. Contour line of 18% spreads till $x/d \sim 4$ and $y/d \sim 0.5$ in both simulations and experiments and contour line of 16% lasts beyond $x/d = 5$, reaching $y/d \sim 0.6$ at $x/d = 5$. Perhaps, a major disagreement is the extension of high TL zone of $> 18\%$ all the way towards the wall and existence of TL much higher than 18% in the recirculation region close to the trailing edge of the jet exit cross-section. Maximum value and an increment for the contour levels of figure 5.32 are chosen to coincide with the same quantities in figure 5.33 to facilitate direct comparison with experiments. But in fact, maximum levels of as high as 30% are observed in the present LES in the recirculation region. The reason for such a high levels of turbulence in this region in the simulations is

not clear, especially taking into account that velocity field shows very good agreement, and TL in all other regions of the flow seem to be reproduced rather accurately. Most likely, this is connected with the numerical treatment of the corner between the film hole wall and the test surface. Recall, that the elliptical jet exit cross-section is approximated with the sharp staircase boundary in the present method due to the code limitation (see figure 2.8 of chapter 2). An overprediction of TL in a region close to the downstream corner can be further seen in figure 5.34, where TL profiles along the horizontal lines $y/d = 0.15$ and $y/d = 0.3$ in the center-plane are plotted. Disagreement at $y/d = 0.3$, further from the wall, is much smaller.

$u'v'$ **Shear Stress**

Contours of normalized $u'v'$ shear stress in the center-plane are plotted in figure 5.35 for the present simulations and in figure 5.36 for the experiments of Pietrzyk *et al.* (1989). Quite a good agreement is again obtained for the majority of the flow. Upstream shear layer, with $u'v' \sim -0.002$, is reproduced quite accurately, having similar values and shapes of the contour lines. Maximum levels of $u'v'$ shear stress are found in the interface between the jet fluid and the low momentum wake and show the peak value of -0.007, consistent with experiments. The largest disagreement occurs right above the jet exit. In experiments, an extensive region of positive shear stress ($+0.001$) is observed above the jet exit at $0.2 < x/d < 1$. This positive shear stress is probably originated in the shear layer between the separated flow and a "jetting" region in the film hole. It is interesting, that region of positive stress of the same level ($\sim +0.001$) is observed in the present simulations near the upstream corner of the hole–plate intersection, but it is much more narrow and does not spread as far in streamwise direction. The $u'v'$ shear stress inside the film hole is plotted in figure 5.37, where the region above the flat plate is also shown. The shear stress contours inside the hole and above the flat plate agree pretty well, and an underprediction of the positive stress in the middle of the jet exit starts in the hole. The region of large positive shear due to the flow separation in the hole is indeed formed, but it does not spread all the way to the jet exit. Narrow layer of positive shear which is observed in the simulations at the leading edge of the jet exit comes from the boundary layer and not from the jetting region. Perhaps, larger sampling interval will smooth the unsteadiness in the shear stress contours in the middle of the film hole and lead to an elongation of the positive shear region.

$u'v'$ shear stress profiles along the vertical lines $x/d = 1$ and $x/d = 2$ in the centerplane are compared with the experimental data in figure 5.38. The line $x/d = 1$ comes through

the region of positive shear stress, and it is clearly seen that the positive peak in $u'v'$ shear stress is missed in the calculations. Line $x/d = 2$ comes through the region of negative stress, and agreement between experiments and simulations is good.

5.5.2 Transverse View

Turbulence Quantities

To get a better understanding of a three-dimensional structure of the turbulence field produced during jet-crossflow interaction, contours of all six components of the Reynolds stress tensor are plotted in the transverse plane $x/d = 4.5$ in figure 5.40 for normal stresses and 5.41 for shear stresses, respectively. All three components of the normal stresses have pretty much the same spanwise distribution and a similar magnitude of about 12% for this cross-section, with u_{rms} reaching 16%. As was noted before, maximum of u_{rms} occurs in the shear layer above the wake region, v_{rms} has the highest values in the wake region and w_{rms} peaks next to the wall.

The components of the shear stresses (figure 5.41) differ more from each other. $u'v'$ stress has a simple structure in the far field, it occupies the region between the jet and the low momentum wake and has large negative value (see also figures 5.35, 5.36). The $u'w'$ stress, responsible for the lateral growth of the jet, has two lobes with the opposite sign on each side of the centerplane. The $v'w'$ stress is the most irregular, and does not follow any particular pattern, it also has the smallest value of all the three components. Perhaps, a much longer averaging time is required for $v'w'$ stress than for the two other shear stresses to reach the similar levels of convergence. It is worth noting, the averaging time of $t \sim 48\,d/\mathcal{U}_\infty$ is apparently not enough to obtain a converged pattern for all of the shear stresses.

Comparison of the off-centerplane development of a turbulence fluctuations with experiments is performed by looking at the spanwise profiles of the turbulence kinetic energy $\sqrt{k}/U_\infty$ plotted along the horizontal line $y/d = 0.15$ in transverse cross-section $x/d = 3$ and $x/d = 5$ in figure 5.39. Except for an overprediction of TKE at the center-plane at $x/d = 3$ discussed previously, the agreement of spanwise development of TKE is very good. Off-centerplane development of shear stresses is compared for $u'v'$ and $u'w'$ profiles along the vertical line passing through $x/d = 3$, $z/d = 0.2$ in figure 5.42; and along the vertical line passing through $x/d = 5$, $z/d = 0.3$ in figure 5.43. The location of the vertical lines is chosen, so that they pass through the region with the maximum $u'w'$ stresses. Agreement is reasonable, no underprediction of $u'w'$ stress next to the wall is observed, as opposed to
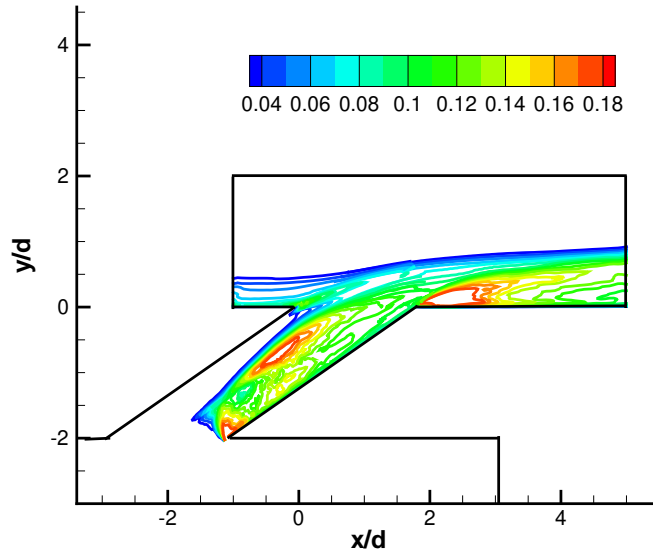
Figure 5.27: Contours of turbulence kinetic energy, $\sqrt{k}/U_\infty$, in the center-plane for the plenum, film hole and a crossflow region.

typical RANS simulations (see figure 1.1 of chapter 1), which means that the lateral growth of the jet is modeled correctly, confirmed by the good agreement in spanwise development of velocity documented in section 5.4.

Turbulent Eddy Viscosity and Temperature Diffusivity

As was discussed in chapter 1, RANS eddy viscosity turbulence models (algebraic and two-equation) assume that the shear stresses are connected to the mean rate of strain through a single coefficient, called eddy viscosity (equation (1.6). As a result, principal axis of the stress tensor are assumed to be aligned with the principal axis of the rate of strain tensor. In reality, the relation between these two tensors might be much more complex, and single coefficient is often not sufficient to describe it. It is possible to evaluate the anisotropy of the eddy viscosity coefficient, μ_t by, looking at its components, $\mu_{t,xy}$, $\mu_{t,xz}$ and $\mu_{t,yz}$ defined as

$$\mu_{t,xy} = -\frac{1}{2}\frac{\overline{u'v'}}{\bar{S}_{xy}}, \ \mu_{t,xz} = -\frac{1}{2}\frac{\overline{u'w'}}{\bar{S}_{xz}}, \ \mu_{t,yz} = -\frac{1}{2}\frac{\overline{v'w'}}{\bar{S}_{yz}}. \tag{5.4}$$
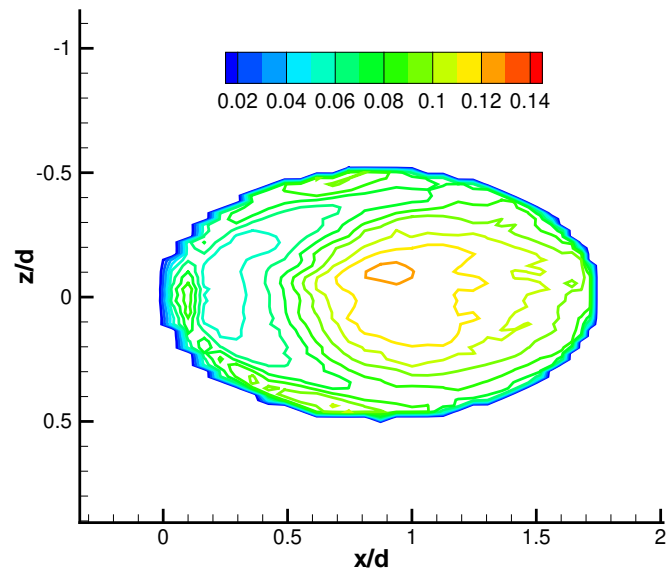
Figure 5.28: Contours of turbulence kinetic energy, $\sqrt{k}/U_\infty$, at the jet exit cross-section.
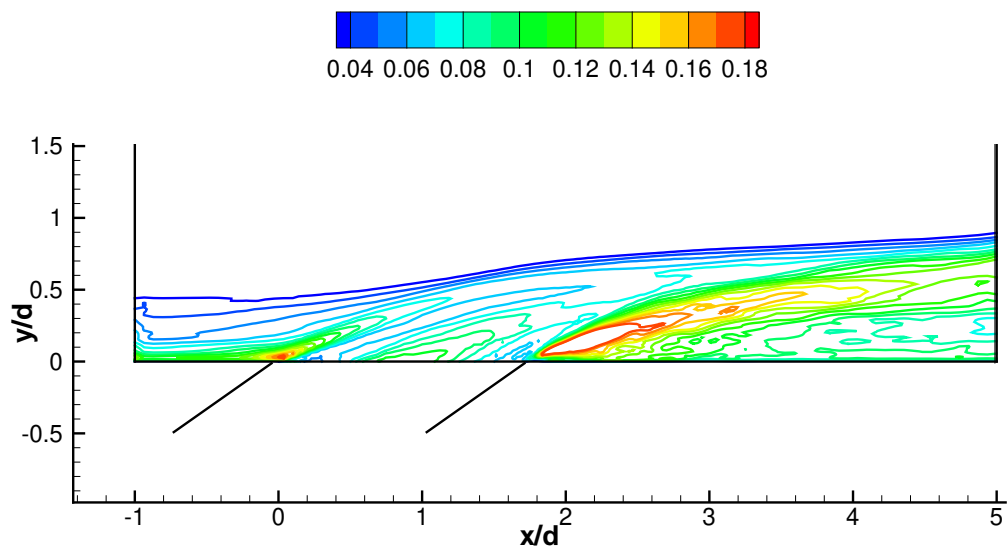
Figure 5.29: Contours of u_{rms} in the center-plane.
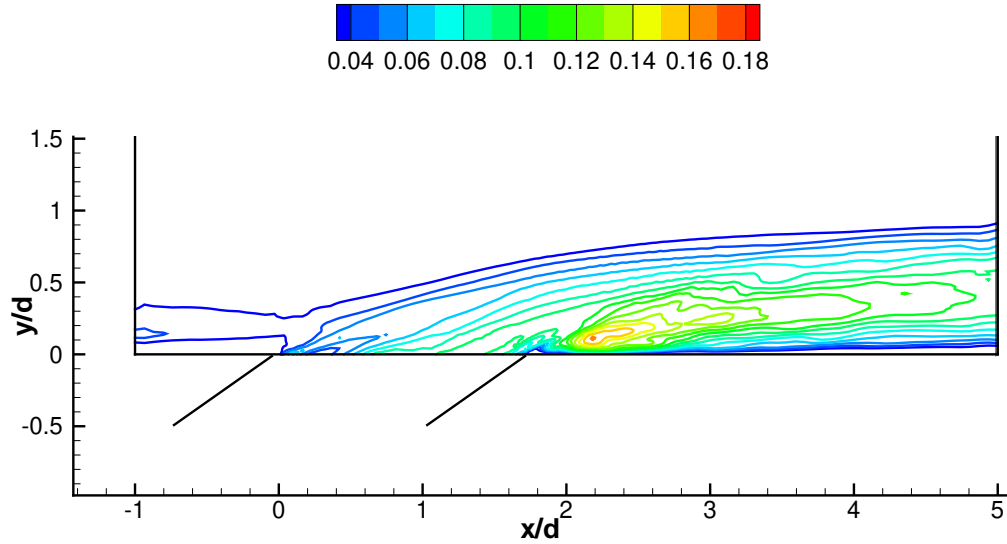
Figure 5.30: Contours of v_{rms} in the center-plane.

Three components of an "eddy viscosity vector" are plotted in figure 5.44 for the transverse plane $x/d = 2.5$. It is seen that the distribution of these components is indeed different. $\mu_{t,\,xy}$ has large positive value in the jet wake and in the shear layer above it, it turns negative in the lower portion of the wake and practically zero close to the wall. $\mu_{t,\,xz}$, on the other hand, has large positive values close to the wall, corresponding to the lateral turbulent mixing. Distribution of $\mu_{t,\,yz}$ shows three regions with the high values: in the center-plane close to the wall (wake region) and higher from the wall at $x/d \sim \pm 5$, in the cores of CRVP vortices, corresponding to the vertical mixing promoted by CRVP. To quantify the differences in $\mu_{t,\,xy}$, $\mu_{t,\,xz}$ and $\mu_{t,\,yz}$ more closely, we plot the lateral distribution of all three components for $y/d = 0.05$ (very close to the wall), $y/d = 0.15$ (in the wake region) and $y/d = 0.5$ (in the shear layer above the wake) in figure 5.46. Near the wall, the xy component is practically zero between $z/d = -0.3$ and $z/d = 0.3$, whereas yz component is ~ -0.03 near the center-plane, and xz component is $\sim 0.02 - -0.04$ at $z/d \sim \pm 0.1$. In the wake, xy component has the same peak value as yz component, but with the different location of peaks (center-plane versus $z/d \sim -0.2$), but xz component is about 3 times larger at the center-plane. In the shear layer, xy component is almost constant with the value of 0.003. xz component peaks at the center-plane with -0.005 value, and yz component has
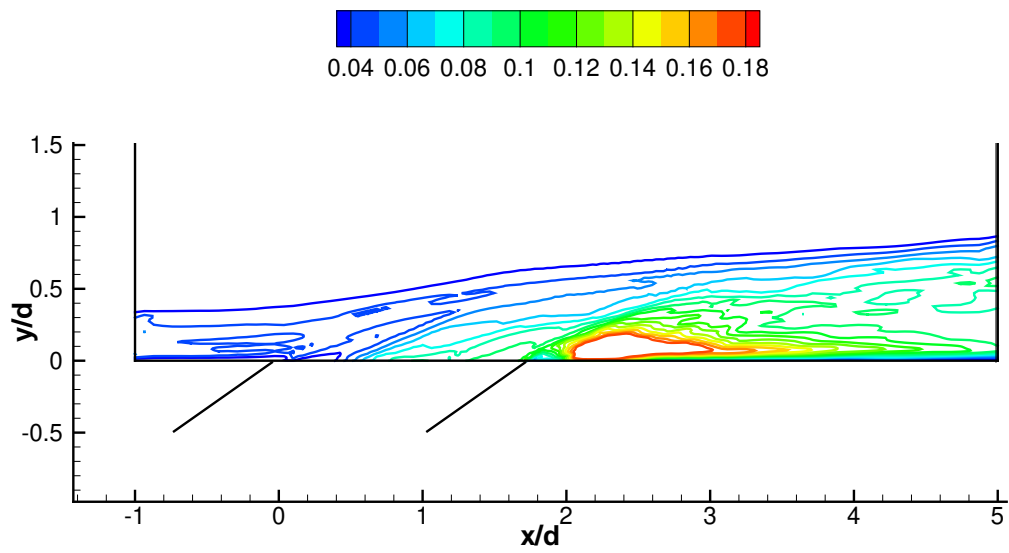
Figure 5.31: Contours of w_{rms} in the center-plane.
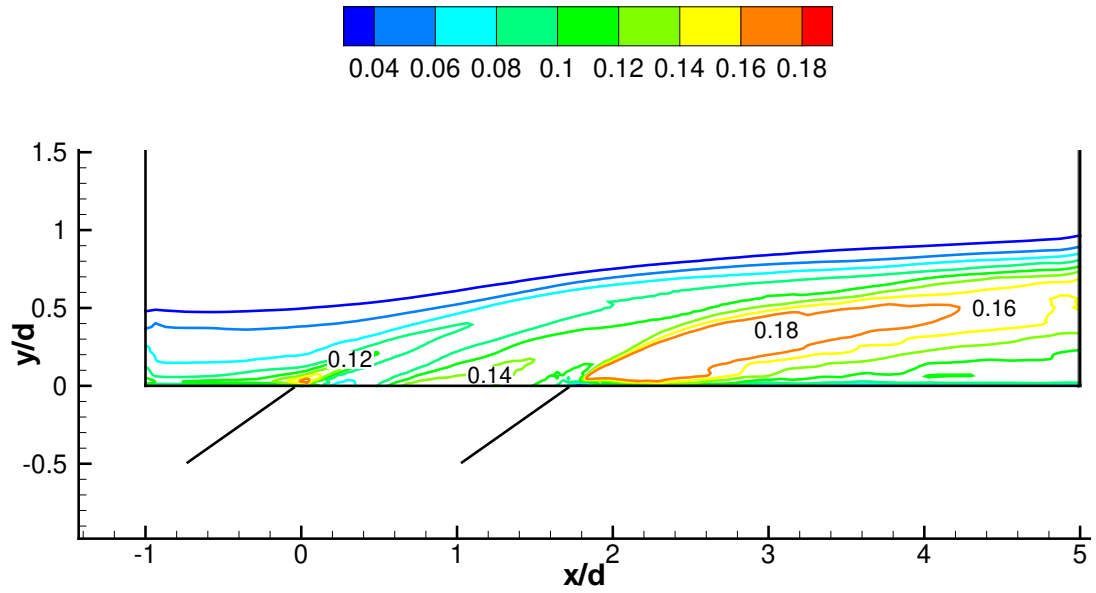
Figure 5.32: Contours of turbulence level, $\sqrt{u'^2 + v'^2}/U_\infty$, in the center-plane.
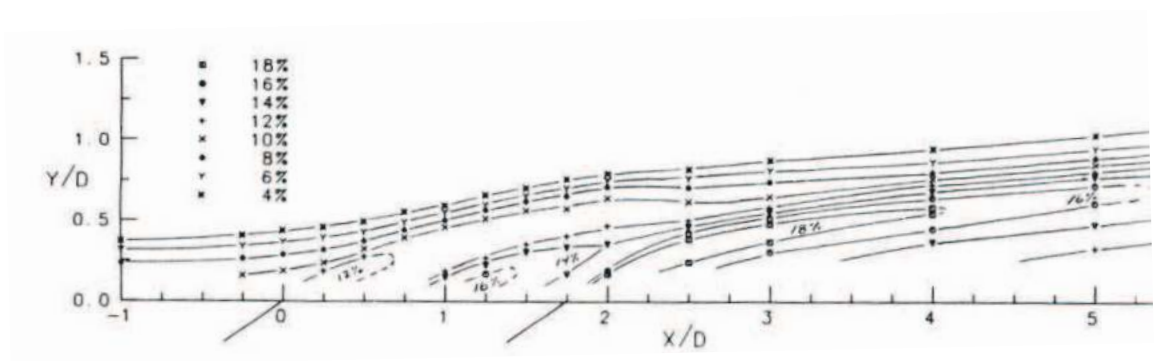
Figure 5.33: Contours of turbulence level, $\sqrt{u'^2 + v'^2}/U_\infty$, in the center-plane. Data of Pietrzyk *et al.* (1989).

(a) $y/d = 0.15$ (b) $y/d = 0.3$
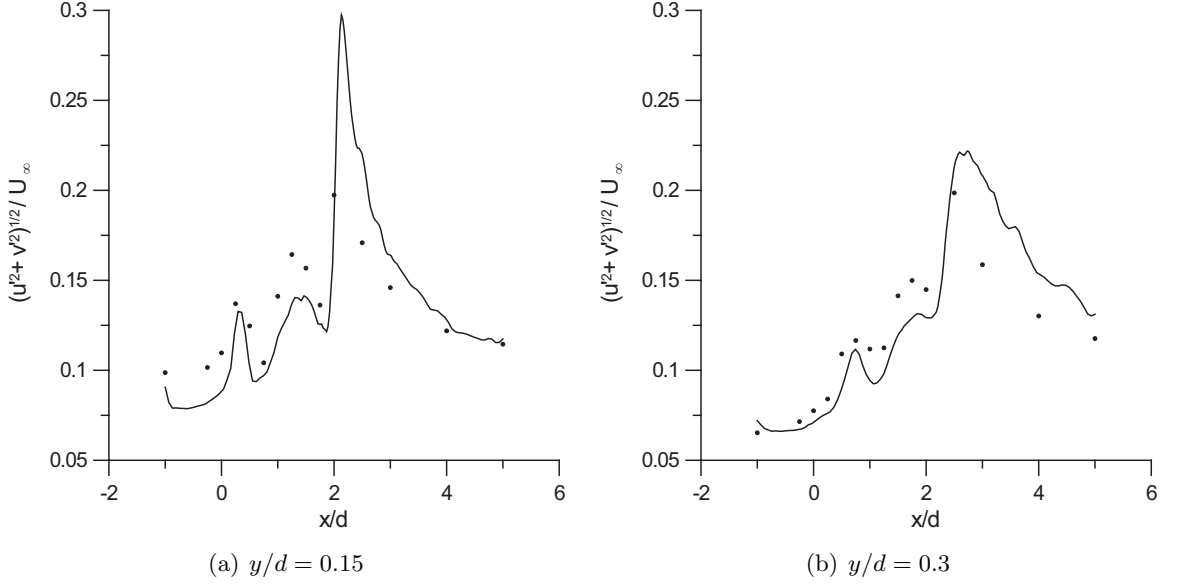
Figure 5.34: Profiles of in-plane turbulent kinetic energy $\sqrt{u'^2 + v'^2}/U_\infty$ along the horizontal lines above the test plate in the center-plane. Lines, simulations; symbols, experiments (Pietrzyk *et al.* (1989)).

an antisymmetric distribution with the same overall level.

It was mentioned in Acharya *et al.* (2001) that an assumption of an isotropy of eddy viscosity effectively means that $\mu_{t,xz}$ and $\mu_{t,yz}$ have the value of $\mu_{t,xy}$ (since the models are tuned to predict the $u'v'$ shear stress correctly). Present calculations show that the xy component is actually the smallest of all the three components and not a good representation of the overall eddy viscosity. For example, $\mu_{t,xz}$ is severely underestimated near the wall if taken equal to $\mu_{t,xy}$. This precludes the correct description of a lateral mixing, leading to an underprediction of a spanwise growth.

Another quantity which is assumed isotropic in RANS models is the thermal diffusivity, k_t, relating the turbulent heat fluxes $\overline{u'_j T'}$ to the mean temperature gradient $\overline{T},_j$:

$$\overline{u'_j T'} = -k_t \overline{T},_j . \tag{5.5}$$

Three components of a thermal diffusivity obtained by dividing turbulent heat fluxes by the corresponding mean temperature gradient, are plotted in figure 5.45 for the spanwise cross-section $x/d = 2.5$. Overall, $k_{t,y}$ distribution is similar to $\mu_{t,xy}$ and $k_{t,z}$ is similar to $\mu_{t,xz}$. It is seen even from the contour plots, that the streamwise component of the thermal diffusivity, $k_{t,x}$ is about five times larger than the other two components. This is further
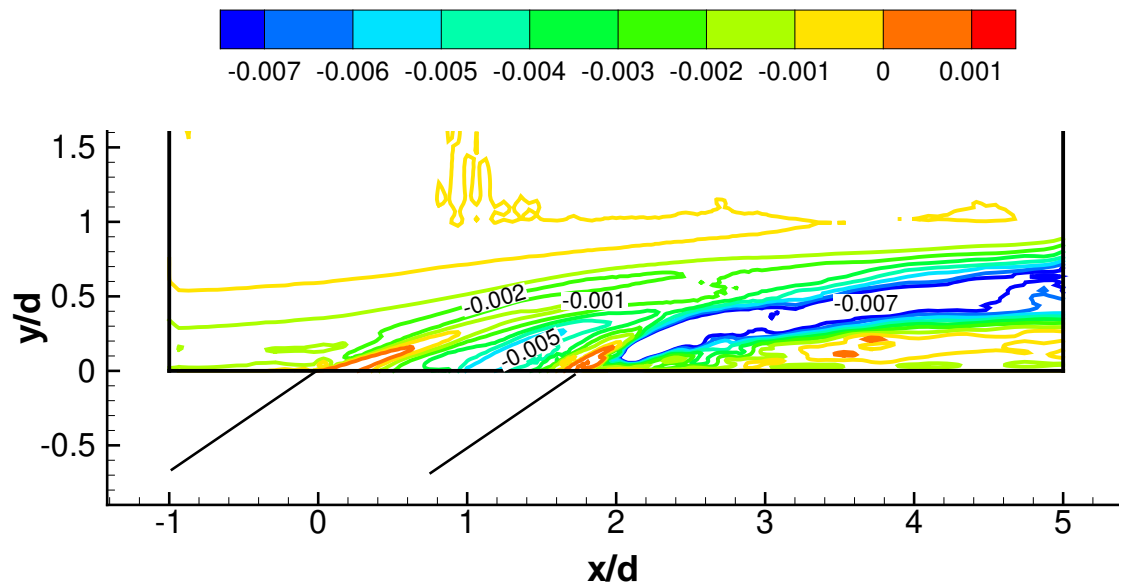
Figure 5.35: Contours of $u'v'$ shear stress in the center-plane.
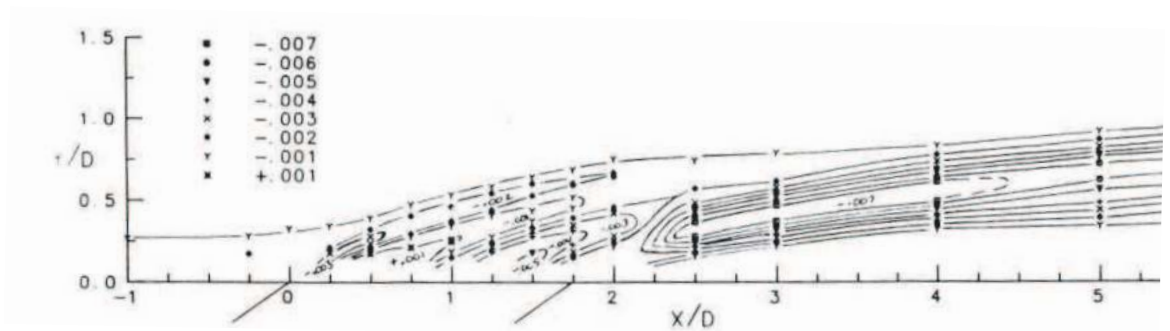
Figure 5.36: Contours of $u'v'$ shear stress in the center-plane. Data of Pietrzyk et $al.$ (1989).
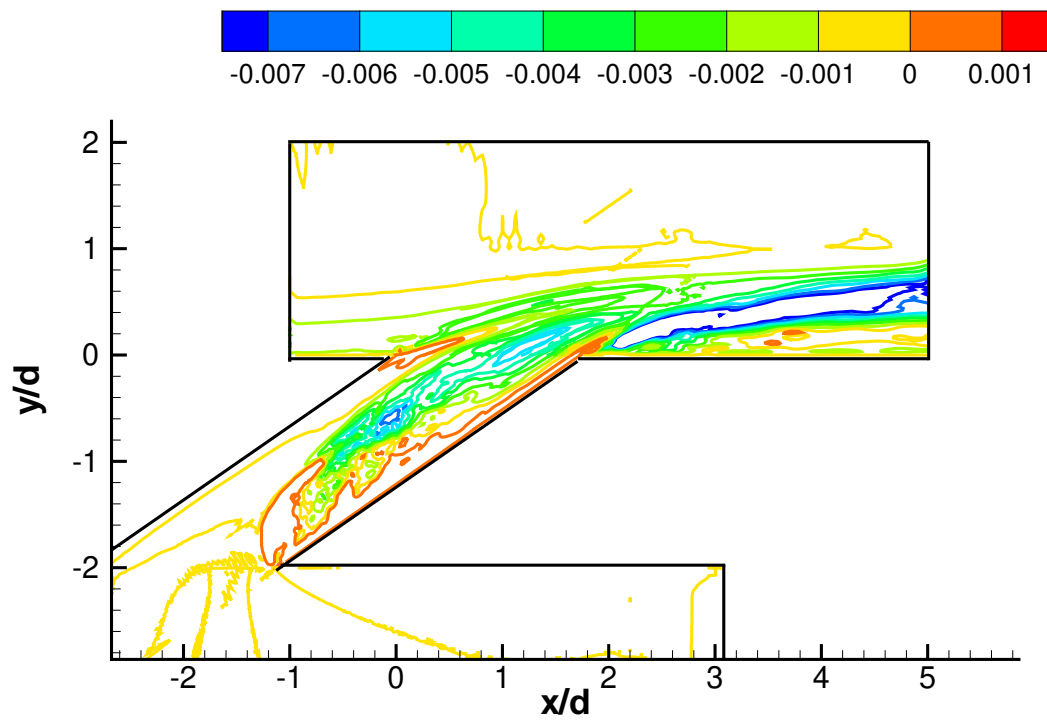
Figure 5.37: Contours of $u'v'$ shear stress in the center-plane for the film hole and the crossflow region.

(a) $x/d = 1$

(b) $x/d = 2$
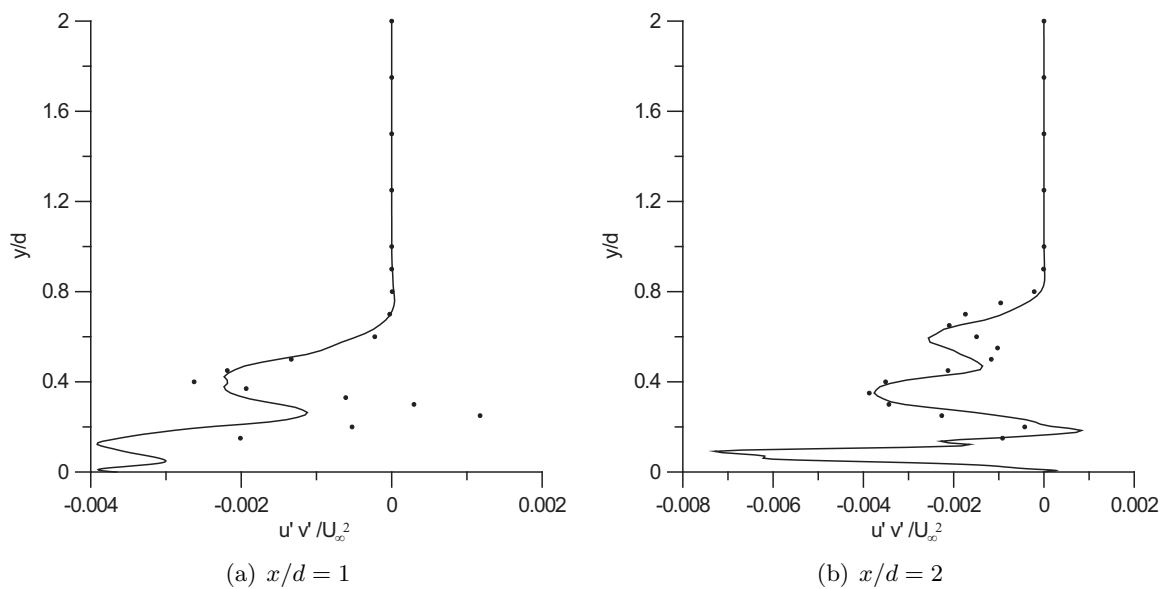
Figure 5.38: Vertical profiles of $u'v'/U_\infty^2$ in the center-plane. Lines, simulations; symbols, experiments (Pietrzyk *et al.* (1989)).

(a) $x/d = 3$

(b) $x/d = 5$
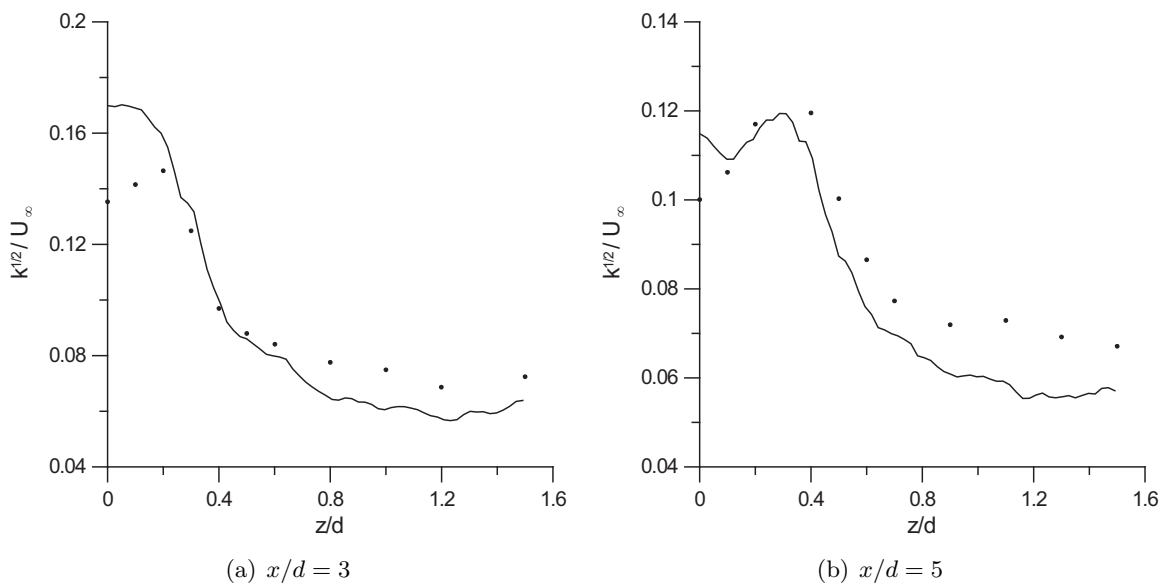
Figure 5.39: Profiles of turbulent kinetic energy $\sqrt{k}/U_\infty$ along the horizontal line $y/d = 0.3$. Lines, simulations; symbols, experiments (Pietrzyk *et al.* (1989)).

	1	2	3
μ_t	-0.0008	0.014	0.008
k_t	0.009	0.003	-0.005
Pr_t	0.27	1.6	

Table 5.5: Three components of eddy viscosity, thermal diffusivity and minimum and maximum Prandtl number, $y/d = 0.05$, $z/d = 0.1$.

demonstrated in figure 5.47, where lateral distribution of $k_{t,x}$, $k_{t,y}$ and $k_{t,z}$ is plotted for the horizontal positions $y/d = 0.15$, $y/d = 0.25$ and $y/d = 0.5$. Larger values of $k_{t,x}$ are visible at $y/d = 0.15$ (reaching negative values of almost -0.4 off the center-plane) and $y/d = 0.25$. They are the most pronounced in the shear layer, at $y/d = 0.5$. $k_{t,y}$ is practically zero in the shear layer, $k_{t,z}$ has a small negative values, however, $k_{t,x}$ is significantly larger, 5 to 8 times in some spanwise locations. It is possible that over-prediction of the vertical penetration of RANS models comes from modeling negligible $k_{t,y}$ component with the large $k_{t,x}$ values, which would result in overestimation of vertical mixing. To estimate turbulent Prandtl number, we take three representative points, $y/d = 0.05$, $z/d = 0.1$ (near-wall, off-center), $y/d = 0.15$, $z/d = 0$ (wake, at the center-plane) and $y/d = 0.5$, $z/d = 0.2$ (shear layer, off-center). The values of the three components of eddy viscosity and thermal diffusivity for these three points are summarized in tables 5.5, 5.6 and 5.7. Column 1 corresponds to $\mu_{t\,xy}$ and $k_{t\,x}$; column 2, $\mu_{t\,xz}$ and $k_{t\,y}$; column 3, $\mu_{t\,yz}$ and $k_{t\,z}$.

Turbulent Prandtl number is defined as

$$Pr_t = \frac{\mu_t}{k_t}. \tag{5.6}$$

In tables 5.5, 5.6 and 5.7 we list the minimum (in column 1) and the maximum (in column 2) values among all the possible combinations arising from dividing different components (for clarity, we considered only the positive values of the coefficients). The range of Pr_t from 0.008 to 3.71 is observed. Therefore, in some locations it is significantly different from 0.9 (the range of 0.8 to 1.0 is assumed in most of the turbulence models, 0.9 being the typical value).

5.6   Film Cooling Performance

Complex interaction between jet and a crossflow and three-dimensional vortical structures occurring as a result of this interaction have a direct effect on film cooling performance.

	1	2	3
μ_t	0.012	0.026	0.004
k_t	0.03	0.007	0.015
Pr_t	0.13	3.71	

Table 5.6: Three components of eddy viscosity, thermal diffusivity and minimum and maximum Prandtl number, $y/d = 0.15$, $z/d = 0$.

	1	2	3
μ_t	0.003	0.002	0.0008
k_t	0.1	0.007	0.002
Pr_t	0.008	1	

Table 5.7: Three components of eddy viscosity, thermal diffusivity and minimum and maximum Prandtl number, $y/d = 0.5$, $z/d = 0.2$.

(a) u_{rms}

(b) v_{rms}

(c) w_{rms}
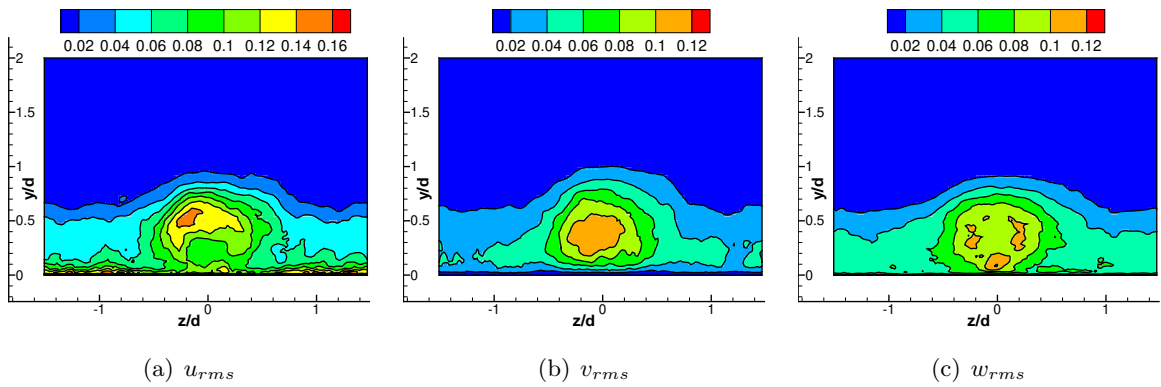
Figure 5.40: Contours of normal stresses in the spanwise cross-section $x/d = 4.5$.

(a) $u'v'$ stress

(b) $u'w'$ stress

(c) $v'w'$ stress
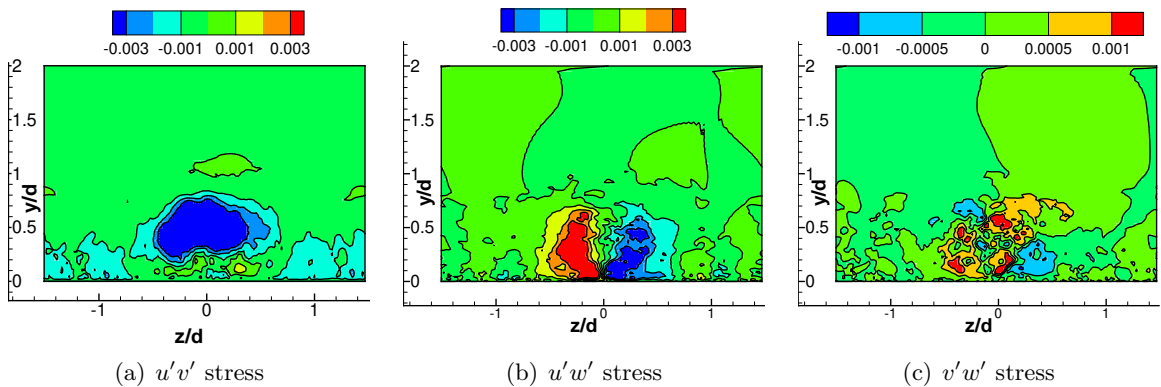
Figure 5.41: Contours of shear stresses in the spanwise cross-section $x/d = 4.5$.

(a) $u'v'$ shear stress
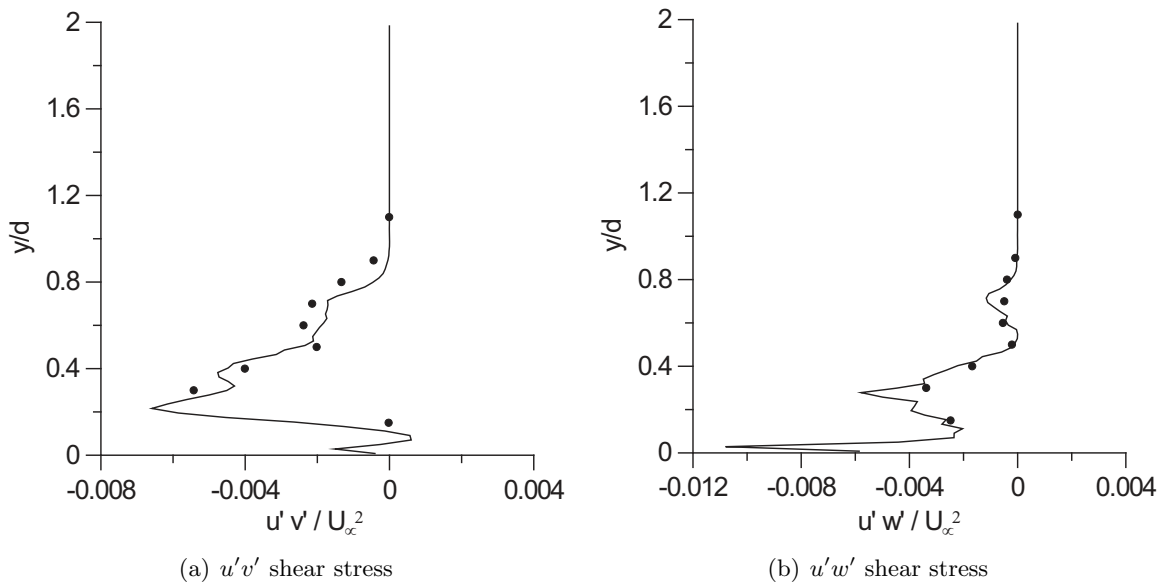
(b) $u'w'$ shear stress

Figure 5.42: Shear stress profiles along the vertical line for off-center location $x/d = 3$, $z/d = 0.2$. Lines, simulations; symbols, experiments (Pietrzyk *et al.* (1989)).

(a) $u'v'$ shear stress
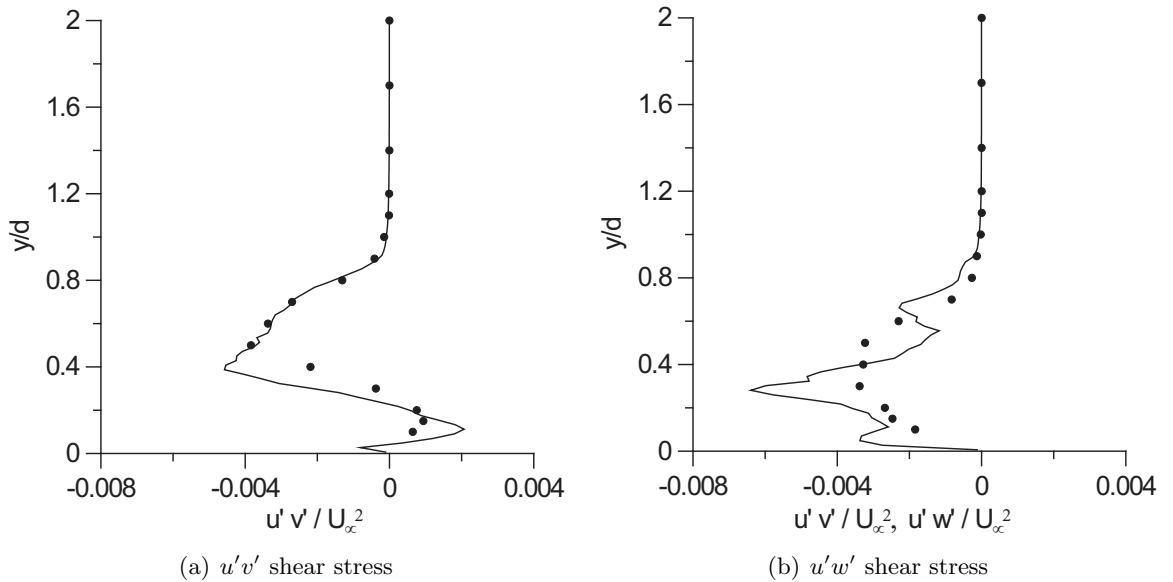
(b) $u'w'$ shear stress

Figure 5.43: Shear stress profiles along the horizontal line for off-center location $x/d = 5$, $z/d = 0.3$. Lines, simulations; symbols, experiments (Pietrzyk *et al.* (1989)).

(a) $\mu_{t,\,xy}$

(b) $\mu_{t,\,xz}$

(c) $\mu_{t,\,yz}$
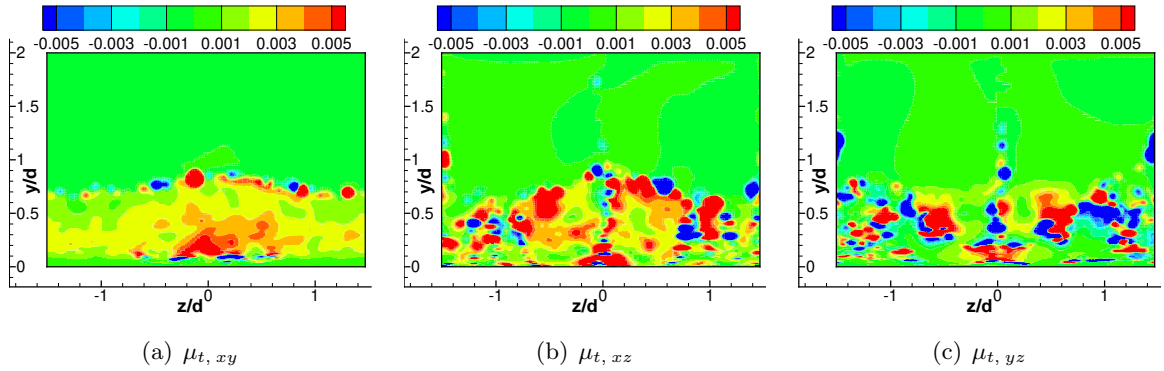
Figure 5.44: Contours of different components of eddy viscosity in the spanwise cross-section $x/d = 2.5$.

(a) $k_{t,\,x}$

(b) $k_{t,\,y}$

(c) $k_{t,\,z}$
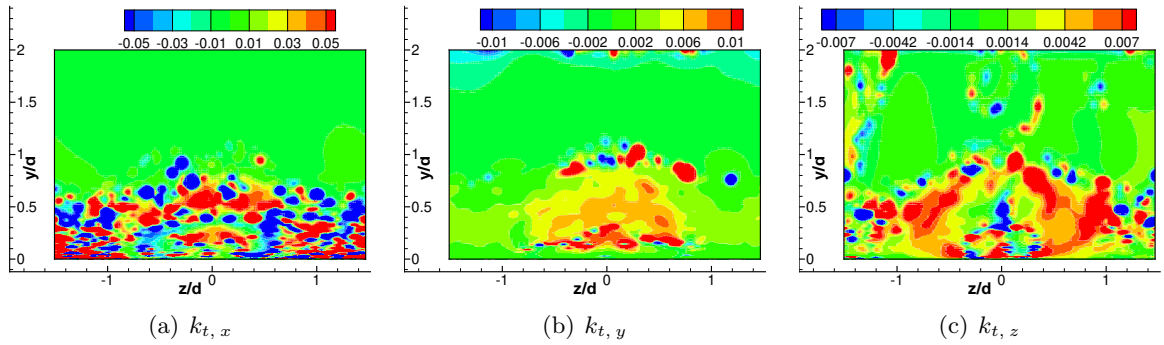
Figure 5.45: Contours of different components of thermal diffusivity in the spanwise cross-section $x/d = 2.5$.

(a) $y/d = 0.05$, near the wall

(b) $y/d = 0.15$, in the wake

(c) $y/d = 0.5$, in the shear layer
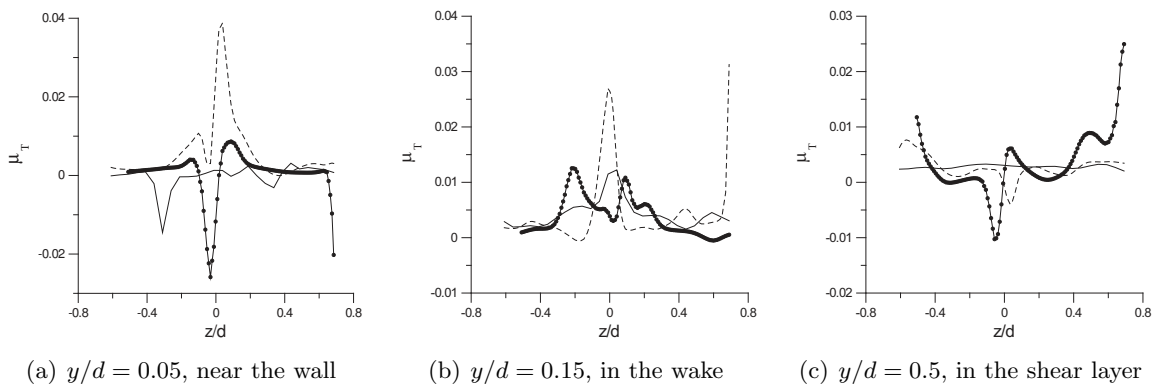
Figure 5.46: Plots of different components of eddy viscosity at $x/d = 2.5$. Solid line, $\mu_{t,\,xy}$; dash line, $\mu_{t,\,xz}$; line+symbols, $\mu_{t,\,yz}$).

(a) $y/d = 0.15$, near the wall   (b) $y/d = 0.25$, in the wake   (c) $y/d = 0.5$, in the shear layer
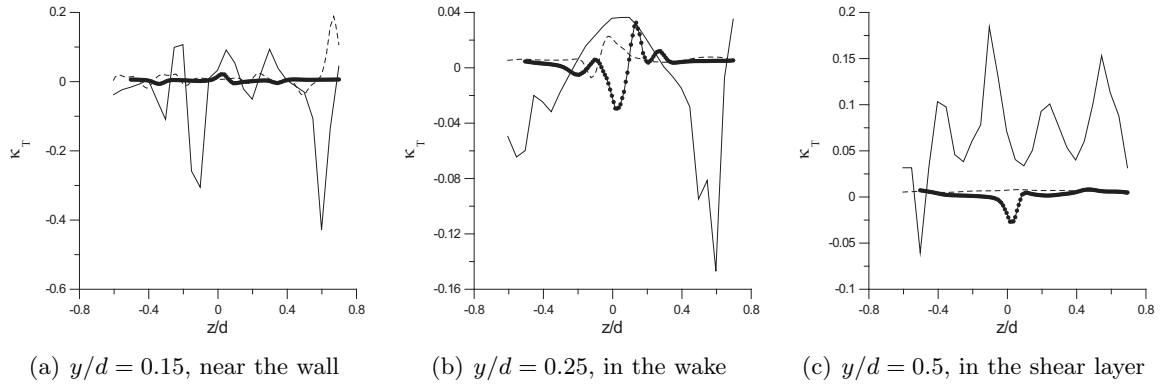
Figure 5.47: Plots of different components of thermal diffusivity at $x/d = 2.5$. Solid line, $k_{t,x}$; dash line, $k_{t,y}$; line+symbols, $k_{t,z}$).

The desired behavior of an injected gas for an efficient cooling would be to stay as close to the surface as possible providing good cooling coverage. However, all of the vortical systems associated with the jet-crossflow interaction play against it. Horseshoe vortex carries crossflow boundary layer fluid around the jet. As it was seen, horseshoe vortex spreads far downstream without dissipating for the case of an inclined jet. This strong self-contained structure keeps crossflow fluid circulating around its legs, preventing it from mixing with the jet flow. Therefore, it can create a barrier for a spanwise spreading of the jet, necessary for providing cooling coverage between the holes. Another drawback of a horseshoe vortex is bringing some of the crossflow fluid inside the film hole, thereby increasing the coolant temperature and heating an upstream hole wall, known as hot gas ingestion. Perhaps, the most detrimental effect on film cooling performance is that of a DSSN vortex, attracting hot crossflow fluid from the lateral edges of the jet towards the center-plane and then pushing it right down on the wall behind the jet. This effect is called the "jet lift-off" by film cooling practitioners and can actually cause the situation when no jet fluid comes in contact with the wall behind the trailing edge of the cooling hole. This means that this part of the surface gets no cooling coverage. This effect can be demonstrated by contours of the normalized mean temperature in the center-plane in figure 5.48. Normalized temperature is defined as

$$\Theta = \frac{T - T_\infty}{T_j - T_\infty} \tag{5.7}$$

and corresponds to 0, when the temperature is equal to the free-stream temperature, and to 1, when it is that of a coolant. Region with hotter flow is visible behind the jet, starting

from the trailing edge of the cooling hole and spreading till $x/d \sim 3$. Coolant jet reattaches to the surface further downstream, reducing the wall temperature. Temperature contours at the wall are seen in figure 5.49. Jet lift-off and reattachment are noticeable. It is interesting to note an asymmetric pattern in the temperature contours, probably due to an unsteady lateral oscillations of the jet. Normalized mean temperature in the spanwise cross-sections is plotted in figure 5.50 for $x/d = 2$ and $x/d = 3$, and in figure 5.51 for $x/d = 4$ and $x/d = 5$. The beginning of the jet lift-off right after the coolant injection is clearly visible at $x/d = 2$, where the contour of minimum temperature (corresponding to maximum Θ) are elevated from the wall. The effect of CRVP on the temperature field is seen in the cross-section $x/d = 3$, where two mushroom-like lobes corresponding to the legs of CRVP, are formed. The region with the lowest temperature corresponds to the cores of CRVP, and the wall temperature underneath the cores is larger due to the crossflow entrainment. The role of CRVP in cooling performance is destructive since it brings hot crossflow fluid underneath the jet, promoting the jet lift-off and increasing the wall temperature. At $x/d = 4$, the jet cross-section acquires the wake-like form, with the minimum temperature located in the middle of the cross-section. Contours of minimum temperature are still elevated from the wall. By $x/d = 5$ the jet reattachment occurs, resulting in the propagation of the minimum temperature contours all the way to the wall.

Comparison of film cooling performance with experiments is complicated by the fact than no film cooling measurements were obtained for exact configuration simulated here and studied experimentally by Pietrzyk et $al.$ (1989). Sinha et $al.$ (1991) documents film cooling effectiveness for similar configuration but with the shorter cooling holes ($L/d = 1.75$ instead of $L/d = 3.5$) for a range of blowing parameters. The closest regime of Sinha $et\,al.$ to the one simulated here is the regime with $DR = 1.2$ and $B = 0.5$. Flow parameters of the current LES and this regime of Sinha $et\,al.$ are contrasted in table 5.8. Comparison of centerline film cooling effectiveness η_c with experimental values is documented in figure 5.52(a). Film cooling effectiveness is defined as

$$\eta = \frac{T_w - T_\infty}{T_j - T_\infty}, \tag{5.8}$$

where T_w is the adiabatic wall temperature. With respect to the normalized temperature plotted in figures 5.48– 5.50, film cooling effectiveness is just Θ_w. The first thermocouple junction in experiments of Sinha et $al.$ (1991) was positioned one diameter downstream of the trailing edge of the cooling hole, which is $x/d = 2.74$ in the present coordinate system. DSSN vortex is located closer to the hole, so it was not captured by experiments. Downstream of DSSN vortex, where there are measurement points, simulated effectiveness

seems to be higher than the experimental one. It might be associated with the longer film hole in the simulations, resulting in a weaker effect of in-hole separation and, as a consequence, more uniform exit velocity profile and higher cooling performance. It is worth noting that experimental uncertainty is the largest close to the coolant injection due to the complexity of the flow in this region. Unfortunately, near field measurements are the only data we can compare to due to the limited length of the computational domain. In addition, effectiveness near the jet centerline is very sensitive to a spanwise location and can vary by a large amount with only slight deviation from the centerline, which can be seen in figure 5.49. Also, due to a spanwise wiggling of the jet, the geometrical centerline can be different from the physical centerline, and comparison of the near-field centerline effectiveness becomes extremely complicated. This also has been observed in the investigation of Walters & Leylek (1997), who obtained better agreement in centerline effectiveness with experiments of Sinha *et al.* (1991) after the correction for the jet skewness have been incorporated. Laterally-averaged effectiveness $\bar{\eta}$ (figure 5.52(b)) exhibits similar trend: predicted effectiveness is larger than experimental, perhaps showing the better performance of the longer cooling holes.

Very good agreement with experimental data in mean velocity profiles, documented in section 5.4, and favorable agreement in turbulence statistics (section 5.5) gives the reason to believe that current LES can be trusted in the prediction of the temperature field as well. Then disagreement in film-cooling effectiveness documented in this section can indeed be attributed to either the difference in the film hole length or to the uncertainty of the experimental data in the near field of the jet injection. Perhaps, another LES with an exact match in the length of the hole, as well as other cooling parameters, is needed to shed more light on this issue.

Lateral spreading of the jet can be estimated by looking at the lateral distribution of the local cooling effectiveness. It is plotted for $x/d = 2.74$ (or $x/d = 1$ counting from the trailing edge of the jet, the first measurement point in experiments of Sinha *et al.* (1991)) in figure 5.53(a). It is seen that the distribution of the effectiveness is asymmetric. The spanwise location of the geometrical centerline is shown as a dash-dotted line. As discussed earlier, the asymmetry of the jet is also clearly visible in figures 5.49 and 5.50 showing the temperature contours on the wall and in the spanwise cross-section. Experimental measurements of the lateral spreading by Sinha *et al.* (1991) are available at $x/d = 2.74$ for the regime with density ratio $DR = 2$ and momentum ratio $I = 0.32$. Although the density ratio of $DR = 0.95$ is significantly different in the current LES, cooling effectiveness scales

with the momentum ratio, and density ratio by itself is not very important parameter, as discussed in Sinha *et al.* (1991), Bogard & Thole (2006) etc. Momentum ratio of $I = 0.2375$ of the current LES is somewhat close, and comparison with the experiments is useful. Lateral distributions of the effectiveness between the simulations and experiments is compared in figure 5.53(b). Since slightly different regimes are being compared (recall also the difference in L/d between simulations and experiments), the overall values of effectiveness are not expected to match. Therefore, effectiveness normalized by its maximum value, η/η_{max} is compared. Also, correction for the jet skewness has been made (the mismatch between the geometrical and the physical centerlines), as in Walters & Leylek (1997) by shifting the spanwise coordinate in the simulation by z_{max}, which is the lateral position of the point with maximum effectiveness (or physical centerline). Good agreement is observed after these corrections are made. The only slight difference between the simulations and experimental data is at the lateral edges of the cross-section, $(z - z_{max})/d < -1$. Experimental data goes all the way to zero, but computational data stays constant at some non-zero level. This is due to the non-zero value of Mach number in the simulations (experiments are performed in incompressible regime). In the absence of film cooling, adiabatic wall temperature $T_{w\,nc}$ is related to freestream temperature T_∞ as:

$$T_{w\,nc} = \left(1 + r\frac{(\gamma - 1)}{2}M^2\right) T_\infty, \tag{5.9}$$

where "nc" stands for "no cooling". When equation (5.8) is used to obtained film cooling effectiveness, the effectiveness without the cooling is

$$\eta_{nc} = \frac{r(\gamma - 1)}{2} M^2 \frac{1}{T_j/T_\infty - 1}, \tag{5.10}$$

slightly greater than zero. This disagreement is due to the mismatch in the definitions used for film cooling effectiveness.

As discussed earlier, RANS simulations feature an underprediction of the lateral spreading of the jet. Current LES is definitely free of this deficiency.
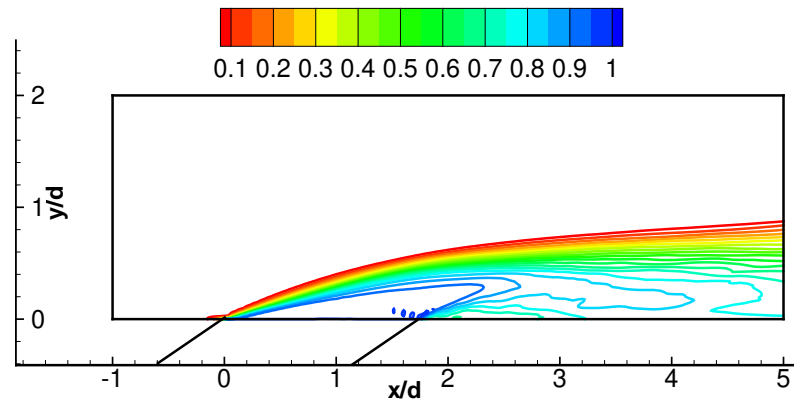
Figure 5.48: Normalized mean temperature, Θ, at the center-plane.
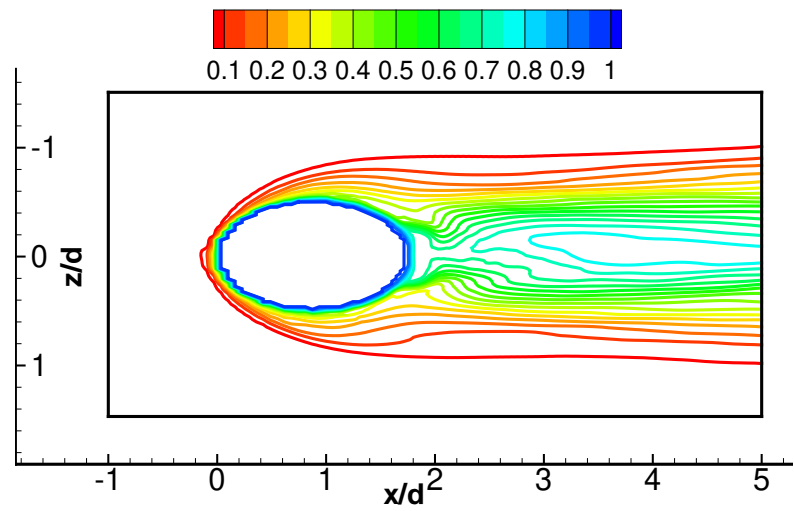
Figure 5.49: Normalized mean temperature, Θ, at the wall.

(a) $x/d = 2$

(b) $x/d = 3$
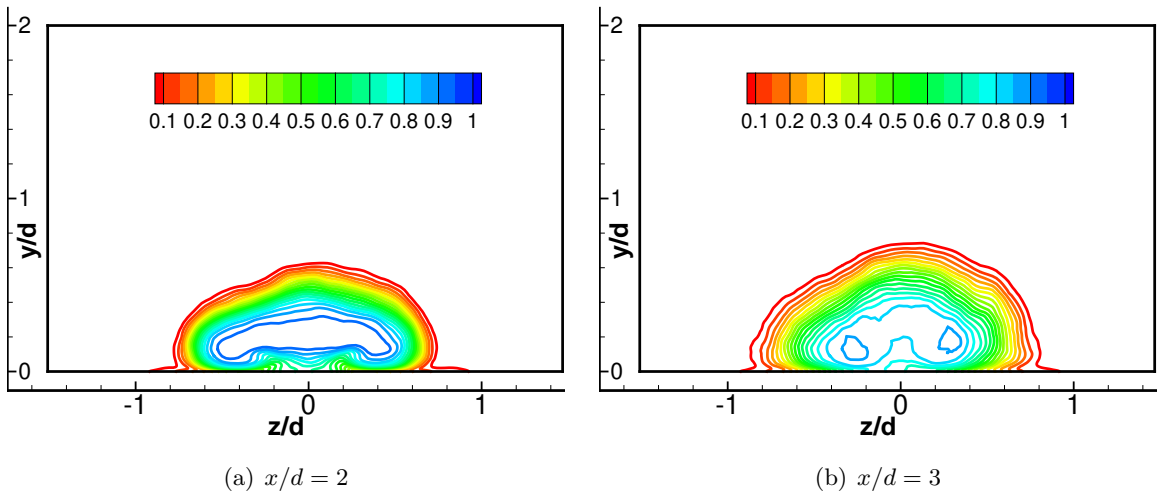
Figure 5.50: Normalized mean temperature, Θ, in the spanwise cross-sections.

(a) $x/d = 4$

(b) $x/d = 5$
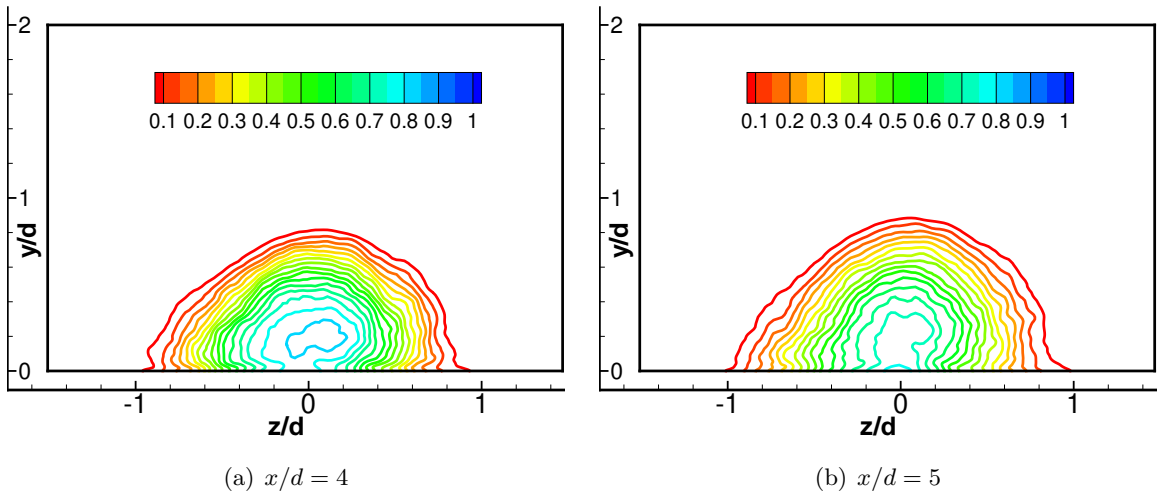
Figure 5.51: Normalized mean temperature, Θ, in the spanwise cross-sections.

	DR	VR	B	I	L/d
Experiments	1.2	0.42	0.5	0.208	1.75
Simulations	0.95	0.5	0.475	0.2375	3.5

Table 5.8: Comparison of the flow parameters between the closest regime of experiments of Sinha *et al.* (1991) and the current LES.

(a) Centerline effectiveness

(b) Laterally averaged effectiveness
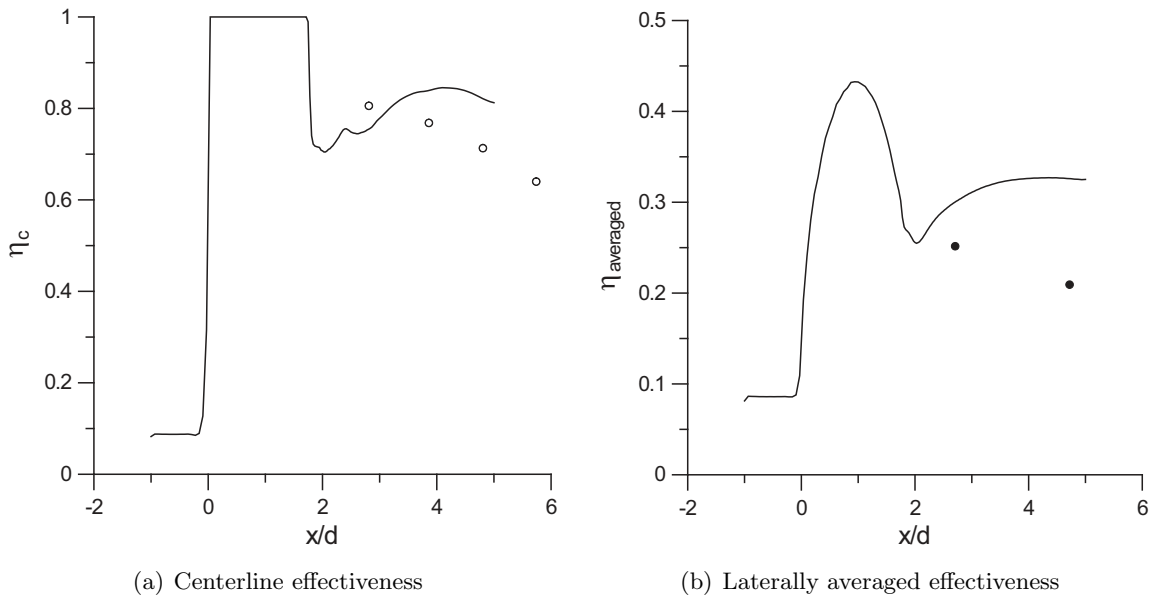
Figure 5.52: Adiabatic film cooling effectiveness. Lines, simulations; symbols, experiments (Sinha *et al.* (1991)).

(a) Solid line, local adiabatic effectiveness; dash-dotted line, position of the geometrical centerline.

(b) Comparison with experiments for the effectiveness normalized by its maximum value. Only one half of the cross-section is plotted. Line, simulations; symbols, experiments (Sinha *et al.* (1991)). z_{max}, spanwise coordinate of the local maximum.
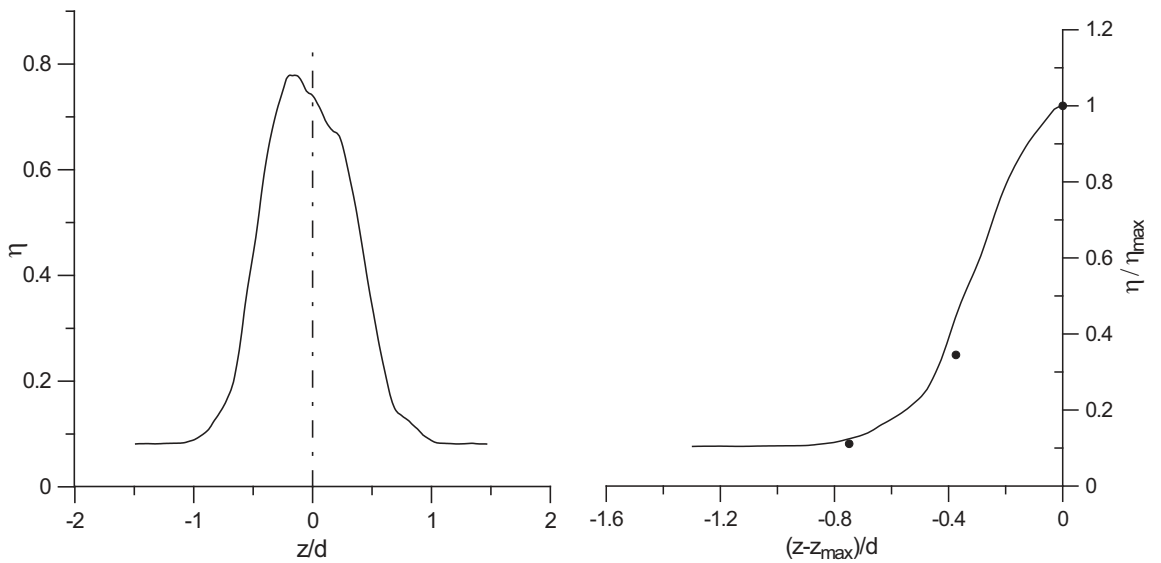
Figure 5.53: Lateral distribution of adiabatic film cooling effectiveness at $x/d = 2.74$.

Chapter 6

Concluding Remarks

The high pressure turbine of a gas turbine engine operates in an extremely complex environment, featuring turbulent flow with high temperature non-uniformities, or streaks, coming from the combustor, cooling jets issuing from the surface, which also carry turbulence produced due to the interactions with the supply plenum. Although there have been many studies of film cooling, both experimental and computational, the complexity of the problem always leaves room for more discoveries. With the present simulations, we intended to study the film cooling flow behavior and connect the underlying flow physics to the cooling properties of the design. The lessons we learned from this study are the following. The sharp corner of the plenum, which makes the flow to turn very suddenly into the hole, creates a separation zone inside the hole and a jetting region upstream of this separation zone. The effects are larger with larger blowing ratio and shorter delivery holes. Another impact of this sharp corner is generation of turbulence by creating the region of very high local shear between the rapidly accelerating flow in the "jetting region" and a stagnating separation zone. Increased turbulence levels inside the jet increase the mixing of the jet with the crossflow, which is usually associated with the increase in heat transfer coefficient and fast diffusion of the coolant core, leading to decreased cooling performance. An effect of the in-hole separation itself can also be linked to decreased cooling efficiency for two reasons: first, it changes jet exit velocity distribution and creates velocity deficit in the center of jet exit cross-section. Such a velocity distribution leads to an increase in effective velocity ratio due to the blockage or effective area reduction, promoting the jet lift-off. Another reason for reduced effectiveness is that the recirculation zone inside the hole due to the separation has a direction of rotation corresponding to the rotation of the Counter-Rotating Vortex Pair (CRVP), resulting in higher jet trajectory and smaller lateral spreading, negative for

cooling performance. The practical recommendation would be to design supply channels taking this effect into account, with either avoiding in-hole separation or trying to reduce it.

Negative influence of all of the vortical structures on film cooling performance is almost discouraging. However, by understanding the mechanisms how the reduction in effectiveness occur, one might be able to design the ways to overcome it. Such an accurate documentation has been performed in the present study by carefully looking at the flow streamlines originating inside the crossflow and showing how, where and why they impinge on either film hole wall (horseshoe vortex) or the blade wall (DSSN vortex). The strength of DSSN vortex is certainly linked to the in-hole flow development and the blowing ratio, increasing with the increase in blowing ratio and in-hole non-uniformity.

On the numerical side of the study, successful development of a coupled solver which combines different numerical codes solving different sets of equations is definitely an accomplishment, since it might find use in multiscale multiphysics simulations, such as the flow through the entire gas turbine engine, accurate prediction of the helicopter noise etc. Development of this capability allowed us to include the plenum into the simulations, where the flow is very slow, and simultaneously retain the capability of having a compressible crossflow, which is especially important for the leading edge film cooling, where the flow is usually in high subsonic or transonic regime. These simulations became first Large Eddy Simulations of film cooling flows known to the author, which incorporate plenum into the model and therefore provide a realistic description of the coolant entrance conditions impossible to accurately model due to the high complexity. Finally, it was shown that both the eddy viscosity and thermal diffusivity of the turbulence field associated with JCF flows are anisotropic, thus explaining why RANS turbulence models, which have a built-in assumption of an isotropic values for these coefficients, are inherently incapable of capturing the correct behavior of spanwise shear stress and, as a consequence, the lateral spreading of the jet. Comparison with experiments for the mean velocity profiles and film cooling effectiveness distribution in the lateral direction, as well as direct comparison of spanwise shear stresses confirmed that LES does not suffer from this shortcoming.

Future Directions

Running present LES simulations for a longer time in order to obtain better convergence in turbulence statistics is desired. In addition to adiabatic film cooling effectiveness, another important parameter for evaluating the overall cooling performance, heat transfer coefficient augmentation due to blowing, could be assessed. The simulations would also benefit from

further grid refinement, especially in the upstream part of the jet cross-section. Significant clustering has been made next to the trailing edge to resolve the shear layer between the jet and its wake. However, phenomena requiring high resolution, such as upstream shear layer and the turbulence coming from the separated pipe flow, exists in the upstream part as well. Also, different cooling regimes could be considered, such as higher blowing ratio, density ratio, skewing of the jet etc. Comparison of the different regimes with the present base case would be of interest. It would also be important to investigate the influence of incoming free-stream turbulence on film cooling performance using LES, since the flows exiting the combustion chamber in gas turbine engines are highly turbulent.

As a future development of an existing capability, it would be especially interesting to perform Large Eddy Simulations of leading edge film cooling. Surface curvature was listed amongst the crucial parameters influencing the cooling performacne, and not much is understood about this effect. Existing experimental finding are contradictory and no accurate numerical investigations, such as Large Eddy simulations, has been done for these configurations at all, except for the ongoing effort of Rozati & Tafti (2006). The developed computational approach has all the necessary capabilities for such simulations to be conducted. Compressible code, which takes care of the flow in the crossflow region, is written in curvilinear coordinates, making the transition from the flat plate to the curved surface straightforward. Understanding of leading edge heat transfer studied by many authors, but in the presence of film cooling, would shed more light on this complex problem.

Appendix A

Laminar Compressible Boundary Layer

A.1 Self-Similar Solution

Self-similar analytic solution for the laminar compressible boundary layer over a flat plate is chosen for the validation of the numerical method for the compressible code. Compressible boundary layer equations for the flow over a flat plate can be written as:

Continuity:
$$\frac{\partial(\rho\,u)}{\partial\,x} + \frac{\partial(\rho\,v)}{\partial\,y} = 0. \tag{A.1}$$

Momentum:
$$\rho\left(u\frac{\partial\,u}{\partial\,x} + v\frac{\partial\,u}{\partial y}\right) = -\frac{d\,p}{d\,x} + \frac{\partial}{\partial\,y}\left(\mu\frac{\partial\,u}{\partial\,y}\right), \tag{A.2}$$

$$\frac{\partial\,p}{\partial\,y} = 0. \tag{A.3}$$

Energy:
$$\rho\,u\frac{\partial\,\Theta}{\partial\,x} + \rho\,v\frac{\partial\,\Theta}{\partial y} = \frac{\partial}{\partial\,y}\left\{\mu\left(\frac{1}{Pr}\frac{\partial\,\Theta}{\partial\,y} + \frac{Pr-1}{Pr}\frac{\partial}{\partial\,y}\left(\frac{u^2}{2\,c_p\,T_0}\right)\right)\right\}. \tag{A.4}$$

State:
$$p = \rho\,R\,T. \tag{A.5}$$

Here ρ is the density, T is the temperature, u and v are velocity components in x and y directions, respectively, p is the pressure, μ is the viscosity, k is the thermal conductivity,

Pr is the Prandtl number

$$Pr = \frac{\mu \, c_p}{k}, \tag{A.6}$$

c_p is the specific heat capacity at constant pressure. The function Θ in equation (A.4) is the non-dimensional total enthalpy defined as

$$\Theta = \frac{c_p \, T + u^2/2}{c_p \, T_0} - 1, \tag{A.7}$$

Here and further the subscript "e" refers to the values at the edge of the boundary layer and the subscript "0" denotes the total, or stagnation, quantities. Since $\partial p / \partial y = 0$, therefore $p(x) = p_e(x)$ at every streamwise coordinate x, and the state equation (A.5) leads to the following simple relationship between the density and the temperature:

$$\rho(x, y) \, T(x, y) = \rho_e(x) \, T_e(x). \tag{A.8}$$

To obtain self-similar solutions to equations (A.1)–(A.4), Illingworth (1949) and Stewartson (1949) proposed a transformation, which reduces these equations to the form very close to the incompressible one. For these transformations, Pr can be arbitrary, but constant. The viscosity law $\mu(T)$ is assumed to be linear

$$\frac{\mu}{\mu_0} = b \frac{T}{T_0}. \tag{A.9}$$

Parameter b is chosen to approximate the Sutherland law at the wall

$$b = \sqrt{\frac{T_w}{T_0}} \frac{T_0 + S_0}{T_w + S_0}. \tag{A.10}$$

The Illingworth-Stewartson transformation introduces new coordinates $\tilde{x}$ and $\tilde{y}$ defined as

$$\tilde{x} = \int_0^x b \frac{p_e \, c_e}{p_0 \, c_0} \, dx, \tag{A.11}$$

$$\tilde{y} = \frac{c_e}{c_0} \int_0^y \frac{\rho}{\rho_0} \, dy, \tag{A.12}$$

where c is the speed of sound. From (A.11) and (A.12) we have

$$\frac{\partial}{\partial x} = \frac{\partial \tilde{x}}{\partial x} \frac{\partial}{\partial \tilde{x}} + \frac{\partial \tilde{y}}{\partial x} \frac{\partial}{\partial \tilde{y}}, \tag{A.13}$$

$$\frac{\partial}{\partial y} = \frac{\partial \tilde{y}}{\partial y} \frac{\partial}{\partial \tilde{y}}. \tag{A.14}$$

The stream function $\psi(x, y)$ is introduced as

$$\frac{\partial \psi}{\partial y} = \frac{\rho}{\rho_0} u, \quad \frac{\partial \psi}{\partial x} = -\frac{\rho}{\rho_0} v. \tag{A.15}$$

If we define transformed velocities $\tilde{u}$ and $\tilde{v}$ as

$$\tilde{u} = \frac{\partial \psi}{\partial \tilde{y}}, \quad \tilde{v} = -\frac{\partial \psi}{\partial \tilde{x}}, \tag{A.16}$$

we can express

$$u = \frac{c_e}{c_0} \tilde{u}, \tag{A.17}$$

$$v = -\frac{\rho}{\rho_0} \left(\tilde{u} \frac{\partial \tilde{y}}{\partial x} - \tilde{v} \frac{\partial \tilde{x}}{\partial x} \right). \tag{A.18}$$

The next step is to substitute the transformations defined by (A.11)–(A.14), (A.17)–(A.18) into the compressible boundary layer equations (A.1)–(A.4):

$$\frac{\partial \tilde{u}}{\partial \tilde{x}} + \frac{\partial \tilde{v}}{\partial \tilde{y}} = 0, \tag{A.19}$$

$$\tilde{u} \frac{\partial \tilde{u}}{\partial \tilde{x}} + \tilde{v} \frac{\partial \tilde{u}}{\partial \tilde{y}} = \tilde{u}_e \frac{d \tilde{u}_e}{d \tilde{x}} (1 + \Theta) + \nu_0 \frac{\partial^2 \tilde{u}}{\partial \tilde{y}^2}, \tag{A.20}$$

$$\frac{\partial p}{\partial \tilde{y}} = 0, \tag{A.21}$$

$$\tilde{u} \frac{\partial \Theta}{\partial \tilde{x}} + \tilde{v} \frac{\partial \Theta}{\partial \tilde{y}} = \nu_0 \left\{ \frac{1}{Pr} \frac{\partial^2 \Theta}{\partial \tilde{y}^2} - \frac{1 - Pr}{Pr} \left(\frac{(\gamma - 1) M^2/2}{1 + (\gamma - 1) M^2/2} \right) \frac{\partial^2}{\partial \tilde{y}^2} \left[\left(\frac{\tilde{u}}{\tilde{u}_e} \right)^2 \right] \right\}, \tag{A.22}$$

where ν_0 is the kinematic viscosity coefficient $\nu_0 = \mu_0/\rho_0$, M is the Mach number $M = u_e/c_e$. External flow is assumed isentropic throughout this analysis. Pressure gradient dp/dx is eliminated from the equation (A.2) as

$$\frac{d p}{d x} = \frac{d p_e}{d x} = -\rho_e u_e \frac{d u_e}{d x}. \tag{A.23}$$

Equations (A.19)–(A.22) are solved with the following boundary conditions.
For velocities:

$$\tilde{u} = \tilde{v} = 0 \text{ at } \tilde{y} = 0, \quad \tilde{u} = \tilde{u}_e(\tilde{x}) \text{ at } \tilde{y} \to \infty. \tag{A.24}$$

For non-dimensional enthalpy:

$$\frac{\partial \Theta}{\partial \tilde{y}} = 0 \text{ at } \tilde{y} = 0, \quad \Theta = 0 \text{ at } \tilde{y} \to \infty \tag{A.25}$$

for adiabatic wall,

$$\Theta = \Theta_w\left(\tilde{x}\right) \text{ at } \tilde{y} = 0, \quad \Theta = 0 \text{ at } \tilde{y} \to \infty \tag{A.26}$$

for isothermal wall.

Note that the continuity equation (A.19) and y-momentum equation (A.21) have exactly the same form as in incompressible case. X-momentum equation (A.20) differs from its incompressible counterpart only by the factor $(1+\Theta)$ multiplying the term $\tilde{u}_e \, d\,\tilde{u}_e/d\,\tilde{x}$, which accounts for the pressure gradient. Self-similar solutions to the equations (A.19)–(A.22) can be obtained for problems with the specific distribution of an external velocity profile $\tilde{u}_e\left(\tilde{x}\right)$.

We now consider the case of a compressible boundary layer over a flat plate with zero pressure gradient $dp/dx = 0$. Than the external flow is uniform and external velocity is constant $\tilde{u}_e\left(\tilde{x}\right) = \tilde{U}_\infty$. The term $(1+\Theta)\,\tilde{u}_e \, d\,\tilde{u}_e/d\,\tilde{x}$ in equation (A.20) is identically zero in this case, which means that the energy equation is completely decoupled from the rest of the system. So, velocity profile in transformed coordinates does not depend on temperature distribution for a compressible boundary layer over a flat plate with zero pressure gradient. Moreover, equations (A.19)–(A.21) now have exactly the same form as incompressible equations for $d\,p/d\,x = 0$. The case of a boundary layer over a flat plate with zero pressure gradient in incompressible case was first considered by Blasius (1908). Following the similarity transformation he proposed:

$$\eta = \tilde{y}\sqrt{\frac{\tilde{U}_\infty}{\nu_0 \tilde{x}}}, \tag{A.27}$$

$$\psi = \sqrt{\nu_0 \, \tilde{x} \, \tilde{U}_\infty} f(\eta), \tag{A.28}$$

and assuming for the non-dimensional total enthalpy

$$\Theta = \Theta\left(\eta\right), \tag{A.29}$$

we get the following form for the equations (A.20) and (A.22):

$$2f''' + ff'' = 0, \tag{A.30}$$

$$2\,\Theta'' + Prf\Theta' = 2\,(1 - Pr)\left[\frac{(\gamma - 1)\,M^2/2}{1 + (\gamma - 1)\,M^2/2}\right](f'^2)'', \tag{A.31}$$

with boundary conditions

$$f = f' = 0 \text{ at } \eta = 0, \quad f' = 1 \text{ at } \eta \to \infty \tag{A.32}$$

and

$$\Theta' = 0 \text{ at } \eta = 0, \quad \Theta = 0 \text{ at } \eta \to \infty \tag{A.33}$$

for adiabatic wall,

$$\Theta = \Theta_w \text{ at } \eta = 0, \quad \Theta = 0 \text{ at } \eta \to \infty \tag{A.34}$$

for isothermal wall.

Self-similar solution can only exists for an isothermal wall if the non-dimensional total enthalpy Θ_w, and therefore the temperature T_w, is constant at the wall and $\tilde{x}$-dependence is eliminated. Note that the continuity equation (A.19) is exactly satisfied by introducing the stream function in the form of (A.16). Equation (A.30) possesses the well-known solution documented by Blasius (1908). Equation (A.31) can be solved after the solution $f(\eta)$ is obtained for a given Prandtl number Pr and Mach number M. The case $Pr = 1$ leads to an especially simple solution. In this case equation (A.31) takes the form

$$2\,\Theta'' + f\Theta' = 0, \tag{A.35}$$

and Mach number dependence is eliminated.
In the case of adiabatic wall,

$$\Theta \equiv 0 \tag{A.36}$$

is a solution to the equation (A.35) with boundary conditions (A.33).
If the wall is isothermal, the function

$$\Theta(\eta) = \Theta_w\left[1 - f'(\eta)\right] = \Theta_w\left(1 - \frac{\tilde{u}}{\tilde{U}_\infty}\right) \tag{A.37}$$

satisfies the equation (A.35) and boundary conditions (A.34).

The temperature can be recovered from the non-dimensional enthalpy Θ as

$$T = \left[1 + \Theta(\eta) - \frac{u^2}{2\,c_p T_0} \right] T_0. \tag{A.38}$$

Both solutions (A.36) and (A.37) can be combined to obtain a single formula for the temperature

$$\frac{T}{T_\infty} = 1 + \frac{\gamma - 1}{2} M^2 \left[1 - \left(\frac{u}{U_\infty} \right)^2 \right] + \frac{T_w - T_{ad}}{T_\infty} \left[1 - \frac{u}{U_\infty} \right], \tag{A.39}$$

where

$$T_{ad} = T_\infty (1 + \frac{\gamma - 1}{2} M^2) \tag{A.40}$$

is an adiabatic wall temperature. Equality $\tilde{u}/\tilde{U}_\infty = u/U_\infty$ together with the isentropic relationships is used to derive equation (A.39) from equation (A.38). This equation is exact for Prandtl number $Pr = 1$. The following approximation is often used for arbitrary Prandtl number:

$$\frac{T}{T_\infty} = 1 + r\frac{\gamma - 1}{2} M^2 \left[1 - \left(\frac{u}{U_\infty} \right)^2 \right] + \frac{T_w - T_{ad}}{T_\infty} \left[1 - \frac{u}{U_\infty} \right], \tag{A.41}$$

with

$$T_{ad} = T_\infty (1 + r\frac{\gamma - 1}{2} M^2), \tag{A.42}$$

where $r = \sqrt{Pr}$ is a recovery factor. For all skipped details of the derivation of the self-similar solution for the compressible boundary layer over a flat plate the reader is referred to Schlichting (2000).

A.2   Numerical Tests

Laminar compressible boundary layer over a flat plate with zero pressure gradient is used to test the numerical method and boundary conditions described in section 2.2. Two-dimensional rectangular domain with the size $15\,\delta$ in streamwise direction, $4\,\delta$ in vertical direction and 128×128 grid points is used, where δ is the inflow boundary layer thickness. The grid distribution is uniform in x-direction and it is clustered near the wall in y-direction to resolve the boundary layer. Reynolds number $Re = U_\infty \delta / \nu_\infty = 8000$ and Prandtl number $Pr = 1$ are used. Viscosity law is assumed to be linear according to equations (A.9), (A.10). Two values of Mach number, $M = 0.15$ and $M = 0.8$, and two types of wall boundary conditions, adiabatic and isothermal wall with $T_w/T_0 = 0.8$, are considered. Self-similar

analytic solution, described in section A.1, is used to set initial quantities. For inflow and top boundary conditions based on Riemann invariants, as described in section2.2, analytic solution is used to specify the values of incoming characteristics. Figures A.1 and A.2 show profiles of streamwise velocity $\tilde{u}/\tilde{U}_\infty$, vertical velocity $\tilde{v}/\tilde{U}_\infty/\sqrt{Re_{\tilde{x}}}$ ($Re_{\tilde{x}} = \tilde{U}_\infty \tilde{x}/\nu_0$) and normalized temperature $(T - T_w)/(T_\infty - T_w)$ for the case $M = 0.15$ with adiabatic and isothermal wall, respectively. Note the scaling of vertical velocity with $1/\sqrt{Re_{\tilde{x}}}$ in these and subsequent figures, so that the re-scaled vertical velocity is of the same order as stream-wise velocity and normalized temperature for plotting convenience. It can be seen that the normalized temperature and streamwise velocity fall approximately on the same curve for isothermal wall in case of low Mach number, since linear dependence of temperature on streamwise velocity in equation (A.39) dominates the quadratic dependence. Linear term is identically zero for adiabatic wall; thus only the quadratic term retains, and profiles do not collapse. Figures A.3 and A.4 show the same profiles for $M = 0.8$. Both for adiabatic and isothermal wall an excellent agreement is obtained between the numerical and analytical solution for both Mach numbers. Vertical velocity is usually more sensitive to numerical errors and inaccuracies in the boundary condition formulation than other variables in the boundary layer. Note that computed vertical velocity profile exactly coincides with the analytical solution for $M = 0.15$ (figures A.1 and A.2). A very slight disagreement in vertical velocity is noticeable for high Mach number case $M = 0.8$ (figures A.3 and A.4). Perhaps, more sophisticated, non-reflecting boundary conditions are required for simulating high-Mach number boundary layers on short domains with higher degree of accuracy.

Streamwise development of the boundary layer is documented in figures A.5 and A.6 for the case $M = 0.8$ for both adiabatic and isothermal wall with $T_w/T_0 = 0.8$. 99% boundary layer thickness $\tilde{\delta}$, displacement thickness

$$\tilde{\delta}^\star = \int_0^\infty \left(1 - \frac{\tilde{u}}{\tilde{U}_\infty} \right) d\tilde{y}, \tag{A.43}$$

and momentum thickness

$$\tilde{\theta} = \int_0^\infty \frac{\tilde{u}}{\tilde{U}_\infty} \left(1 - \frac{\tilde{u}}{\tilde{U}_\infty} \right) d\tilde{y} \tag{A.44}$$

are plotted versus $Re_{\tilde{x}} = \tilde{U}_\infty \tilde{x}/\nu_0$ in figure A.5. Theoretical values $\tilde{\delta} \sim 4.9\,\tilde{x}/\sqrt{Re_{\tilde{x}}}$, $\tilde{\delta}^\star = 1.7208\,\tilde{x}/\sqrt{Re_{\tilde{x}}}$ and $\tilde{\theta} = 0.664\,\tilde{x}/\sqrt{Re_{\tilde{x}}}$, obtained from the similarity solution, are also plotted in the figure. An agreement between the computational and theoretical curves is

excellent. Skin friction coefficient

$$c_f = \frac{\tau_w}{\frac{1}{2}\,\rho_w\,U_\infty^2} \tag{A.45}$$

is plotted against $Re_w = U_\infty\,x/\nu_w$ in figure A.6 together with its theoretical value

$$c_f = \frac{0.664}{\sqrt{Re_w}}. \tag{A.46}$$

Agreement is again very good. Note a very short development length in the case of isothermal wall, over which the influence of inflow boundary conditions is noticeable. It persists for only about 2 grid points even for high value of Mach number $M = 0.8$. No development length exists for the case of adiabatic wall. Results for lower Mach number $M = 0.15$ show equally good agreement.
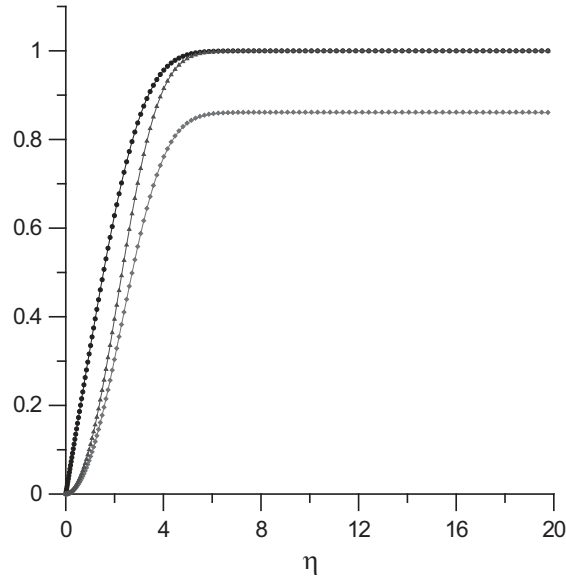
Figure A.1: Comparison of boundary layer profiles. $Re = 8000$, $Pr = 1$, $M = 0.15$, adiabatic wall. Lines – similarity solution, symbols – computation. Upper curve: streamwise velocity $\tilde{u}/\tilde{U}_\infty$; middle curve: temperature $(T-T_w)/(T_\infty-T_w)$; lower curve: vertical velocity $\tilde{v}/\tilde{U}_\infty/\sqrt{Re_{\tilde{x}}}$.
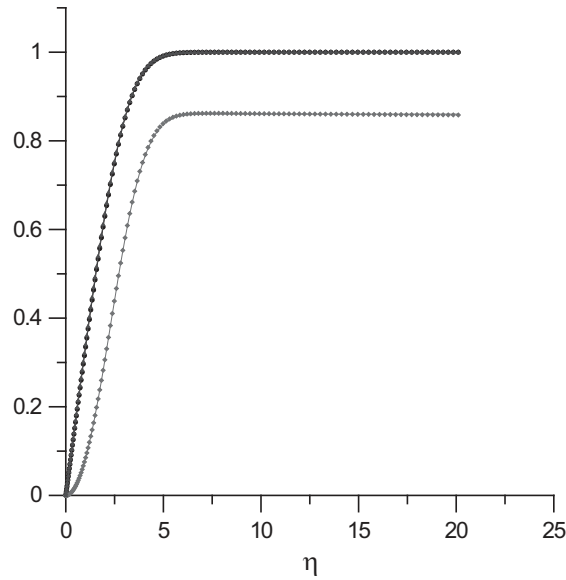
Figure A.2: Comparison of boundary layer profiles. $Re = 8000$, $Pr = 1$, $M = 0.15$, $T_w/T_0 = 0.8$. Lines – similarity solution, symbols – computation. Upper curves: streamwise velocity $\tilde{u}/\tilde{U}_\infty$ and temperature $(T - T_w)/(T_\infty - T_w)$; lower curve: vertical velocity $\tilde{v}/\tilde{U}_\infty/\sqrt{Re_{\tilde{x}}}$.
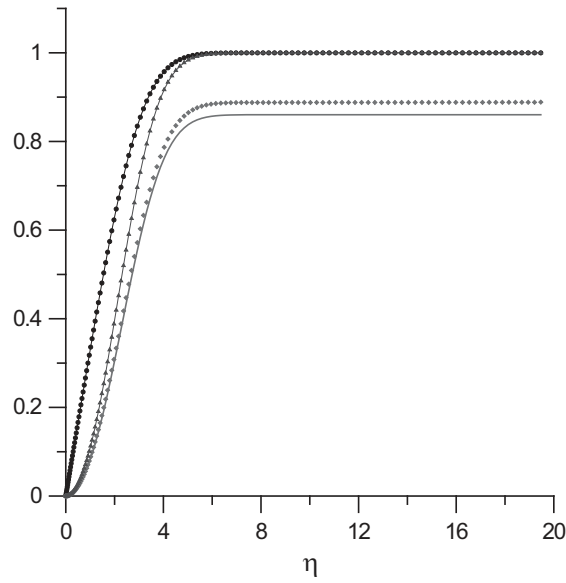
Figure A.3: Comparison of boundary layer profiles. $Re = 8000$, $Pr = 1$, $M = 0.8$, adiabatic wall. Lines – similarity solution, symbols – computation. Upper curve: streamwise velocity $\tilde{u}/\tilde{U}_\infty$; middle curve: temperature $(T - T_w)/(T_\infty - T_w)$; lower curve: vertical velocity $\tilde{v}/\tilde{U}_\infty/\sqrt{Re_{\tilde{x}}}$.
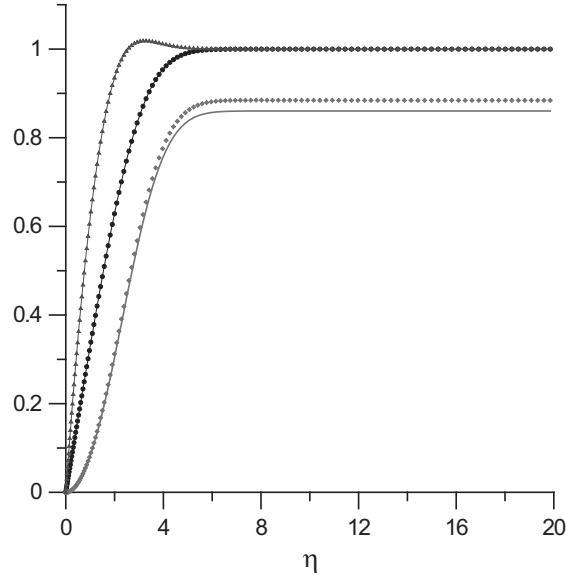
Figure A.4: Comparison of boundary layer profiles. $Re = 8000$, $Pr = 1$, $M = 0.8$, $T_w/T_0 = 0.8$. Lines – similarity solution, symbols – computation. Upper curve: temperature $(T - T_w)/(T_\infty - T_w)$; middle curve: streamwise velocity $\tilde{u}/\tilde{U}_\infty$; lower curve: vertical velocity $\tilde{v}/\tilde{U}_\infty/\sqrt{Re_{\tilde{x}}}$.

(a) Adiabatic wall.

(b) Isothermal wall, $T_w/T_0 = 0.8$.
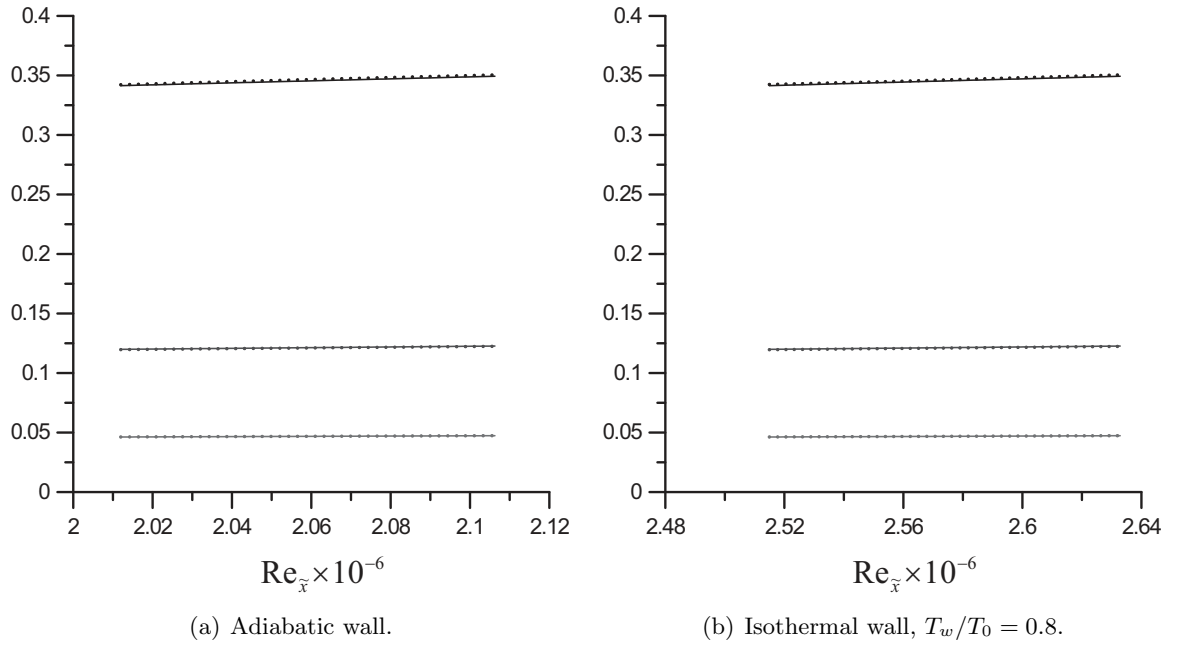
Figure A.5: Streamwise development of the boundary layer. $Re = 8000$, $Pr = 1$, $M = 0.8$. Lines – similarity solution, symbols – computation. Upper curve: 99% boundary layer thickness $\tilde{\delta}$; middle curve: displacement thickness $\tilde{\delta}^\star$; lower curve: momentum thickness $\tilde{\theta}$.

(a) Adiabatic wall.

(b) Isothermal wall, $T_w/T_0 = 0.8$.
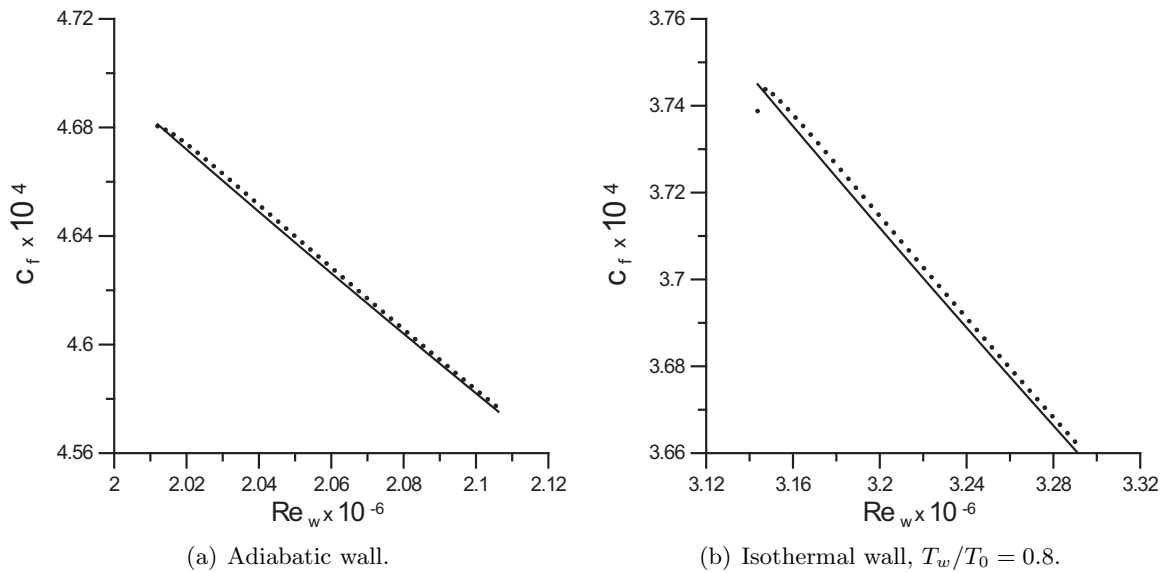
Figure A.6: Skin friction coefficient, c_f, versus $Re_w = U_\infty x/\nu_w$. $Re = 8000$, $Pr = 1$, $M = 0.8$. Lines – similarity solution, symbols – computation.

Appendix B

Interface Conditions: Low Mach Number Code

Performance of interface conditions for the low Mach number code is assessed in this appendix. Since this code has been previously used for calculating internal flow inside the cylindrical pipes and diffusers, cylindrical surface used to represent a solid wall. In the present formulation, part of the cylindrical surface is no longer a solid wall, and the flow can enter and exit through it at random angles. Such a dramatic change in the role performed by a cylindrical surface calls for a thorough investigation of the behavior of the new interface conditions. Several methods which can be used for specifying interface conditions are compared in section B.1. The method with the best overall behavior is identified. Grid convergence study is performed in section B.2.

B.1   Variation of Interface Conditions

Behavior of the interface conditions for the low Mach number code is tested first by applying exact solution at all the boundaries of the low Mach number code domain. Several variations of specifying interface conditions are investigated. The method showing the best performance is identified.

B.1.1   Temperature jump

The following problem is chosen as the first test case to assess the performance of the low Mach number interface conditions. Two gases with different temperatures are moving parallel to each other with the same constant speed U_∞, so that the temperature interface
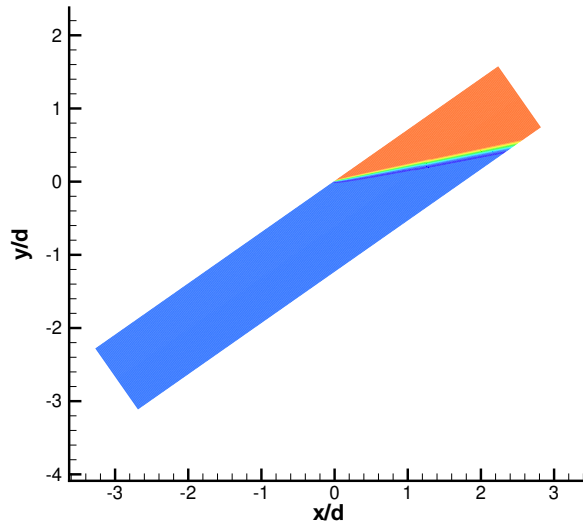
Figure B.1: Temperature field for the steady temperature jump.

is formed. Reynolds number $Re = U_\infty\, d/\nu_\infty = 8000$ is considered, which is equal to the Reynolds number used in the film cooling simulations (d is the pipe diameter).Temperature interface is inclined at some angle with respect to the centerline of the cylindrical domain, as shown in figure B.1, where the temperature field is plotted in a cross-sectional plane containing the centerline. Upper gas has a temperature $T = T_\infty$ shown in red and lower gas has $T = 0.8\, T_\infty$ shown in blue. This problem is representative of a sharp temperature interface between the jet and crossflow formed at an angle with respect to the hole centerline in film cooling simulations. Computational grid is uniform in all directions, with the resolution $\Delta\, x \sim 0.02\, d$, $\Delta\, r \sim 0.008\, d$, $\Delta\, \theta = 0.1\, rad$.

Several ways of specifying interface conditions were tested. First tests concerned conditions for velocity described in section 2.5. Combination of convective outflow conditions with an injection at the inflow proved to be unstable. So, injection method for both inflow and outflow was chosen to specify velocities at the interface.

Two variations of the interface conditions for the temperature are compared in the present test case:

- Injection conditions. Temperature is specified using an injection method $T_{lm} = T_{an}$ at all grid nodes of the free boundaries, where subscript "an" stands for analytical solution.

- Combination of injection and convective conditions. Injection $T_{lm} = T_{an}$ is used when the boundary corresponds to an inflow, convective-type condition $T_t + v_{conv} T_n = 0$ is employed at an outflow.

L_∞ and L_2 errors defined as

$$L_\infty(u_i) = \frac{\max |u_{i\,numer} - u_{i\,an}|}{U_\infty}, \quad L_\infty(T) = \frac{\max |T_{numer} - T_{an}|}{T_\infty} \tag{B.1}$$

$$L_2(u_i) = \frac{1}{U_\infty} \sqrt{\frac{\sum (u_{i\,numer} - u_{i\,an})^2}{N}}, \quad L_2(T) = \frac{1}{T_\infty} \sqrt{\frac{\sum (T_{numer} - T_{an})^2}{N}} \tag{B.2}$$

are plotted in figure B.2 for the three components of velocity and in figure B.3 for the temperature. Combination of injection and convective interface conditions for the temperature show superior results for the present test case. It is noticeable, that the temperature errors are larger than the velocity errors. Moreover, L_∞ errors in temperature show unrealistically large values of $13 - 14\%$, while the values of L_2 errors of $\sim 1\%$ seem to be more reasonable. The reason for such a high values of L_∞ temperature errors is that the interface has a finite thickness of $0.1\,d$ due to the viscous effects in the present calculations. Cusp interface with zero thickness was used for calculating errors, which explains large values for maximum errors in temperature. L_2 errors are much smaller, since the difference in solutions due to the finite interface thickness is felt only by a few grid points.

B.1.2 Entropy spot

Same temperature interface conditions were also tested on the problem of a moving entropy spot, where temperature disturbance in the form of

$$T' = T_d \exp\left(-(r - r_c)^2 / r_d^2\right) \tag{B.3}$$

was superimposed on the uniform mean flow moving at an angle with respect to the pipe centerline. Here r_c is the position of the disturbance center. Disturbance amplitude $T_d = 1.2\,T_\infty$ and radius $r_d = 0.2\,d$ were considered. Reynolds number is $Re = U_\infty d/\nu_\infty = 8000$, as in the previous example. Temperature field is shown in figure B.4 for the moment when the disturbance is entering the domain (computational time $= 1.8$), when it is in the middle of the domain (computational time $= 3$) and when it is exiting it (computational time $= 5$). Note that the direction of the free-stream velocity is chosen so that the disturbance

(a) L_∞ error.
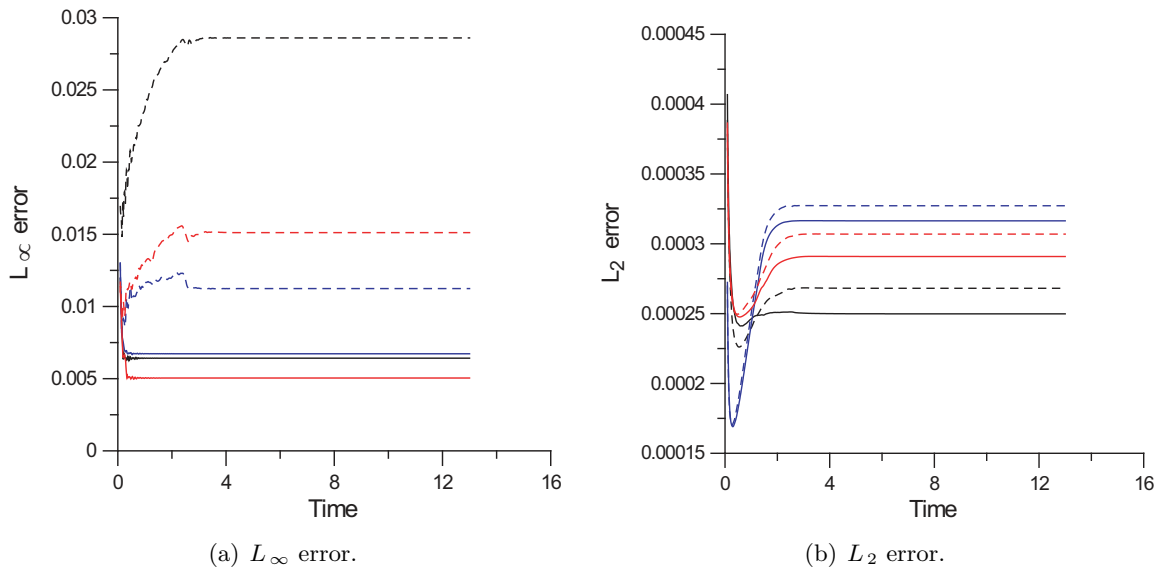
(b) L_2 error.

Figure B.2: Error in velocity versus computational time for different temperature interface conditions. Black lines, axial velocity; blue lines, radial velocity; red lines, azimuthal velocity. Solid lines, injection+convective; dashed lines, injection.

(a) L_∞ error.

(b) L_2 error.

Figure B.3: Error in temperature versus computational time for different temperature interface conditions. Solid lines, injection+convective; dashed lines, injection.
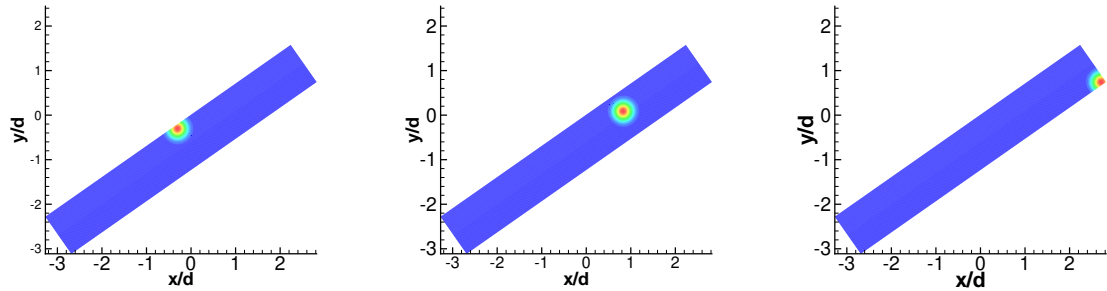
(a) Disturbance is entering the domain, computational time = 1.8.

(b) Disturbance is in the middle of the domain, computational time = 3.

(c) Disturbance is exiting the domain, computational time = 5.

Figure B.4: Temperature field for the moving entropy spot.

exits through the corner of the domain, representing the most rigorous test case for the interface conditions. The L_∞ and L_2 errors with respect to an analytical solution for the three components of velocity and for the temperature are plotted in figures B.5 and B.6, respectively, for an injection and injection+convective temperature interface conditions. L_∞ error has a distinct spike at the time when the disturbance is crossing the outflow boundary. L_2 error is distributed more broadly over the time when the disturbance is inside the domain. It has two local maxima for the velocity, corresponding to the disturbance entering and exiting the domain. It is interesting to note that both interface conditions give the same value of L_2 error in temperature. Overall, injection+convective method again produces more accurate solution.

The influence of the number of iterations in the Poisson solver on the accuracy of the numerical solution is documented in figure B.7. L_2 error of the temperature is plotted in figure B.7(a) for $N_{iter} = 1$, 2, 3 and in figure B.7(b) for $N_{iter} = 3$, 5, 7. Injection+convective temperature interface conditions are implemented. It is seen that one iteration results in an unstable solution. Accuracy is significantly improved going from 2 to 5 iterations. However, the error stays practically the same after 5 iterations. This confirms the conclusion of Pierce (2001) that $4 - 5$ iterations is an optimum number of iterations for calculating variable density flows.

An attempt was made to vary the definition of convective velocity v_{conv} in equation (2.156) in the implementation of outflow convective conditions for the temperature. v_{conv} equal to the mean outflow velocity and to the local outflow velocity was tested in addition to the maximum outflow velocity defined by equation (2.155). However, very little sensitivity of the results on the way v_{conv} is defined was detected, so the original formulation of Pierce

(a) L_∞ error.

(b) L_2 error.
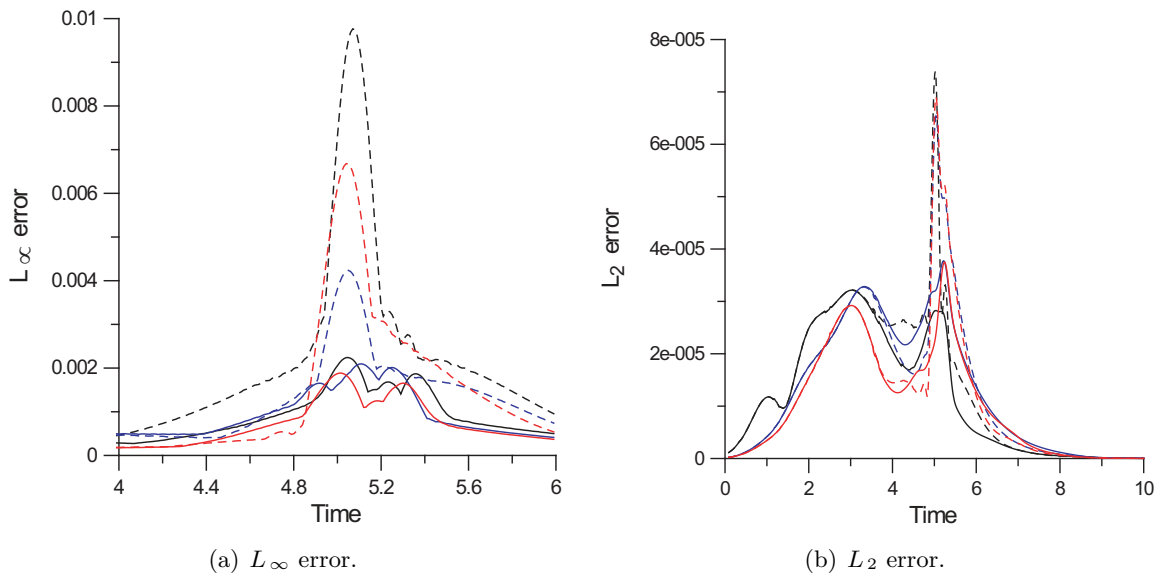
Figure B.5: Error in velocity versus computational time for different temperature interface conditions. Black lines, axial velocity; blue lines, radial velocity; red lines, azimuthal velocity. Solid lines, injection+convective; dashed lines, injection.
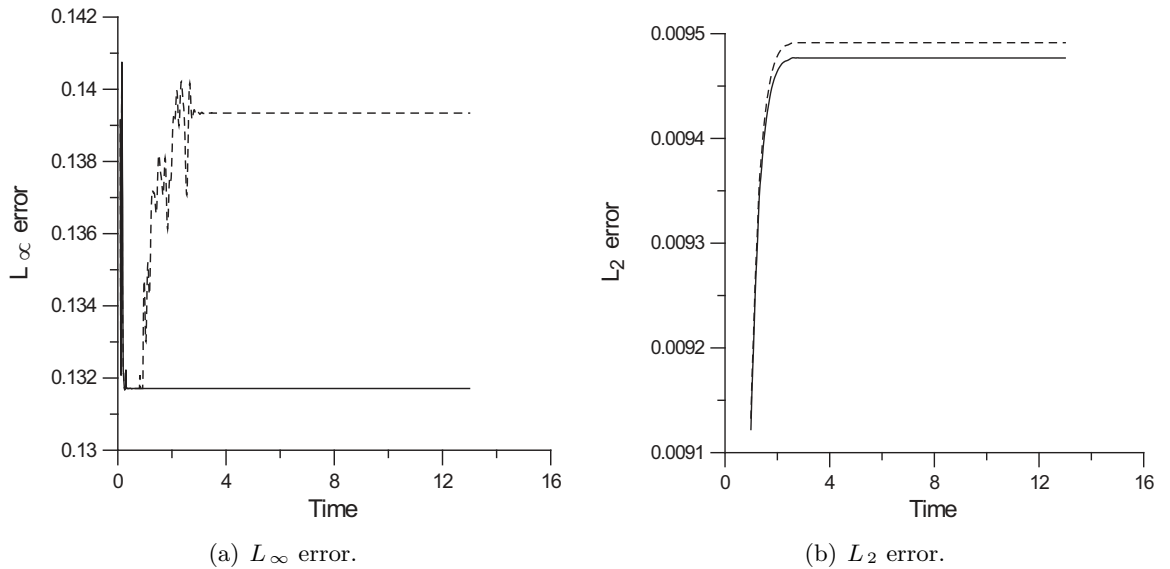

(a) L_∞ error.

(b) L_2 error.
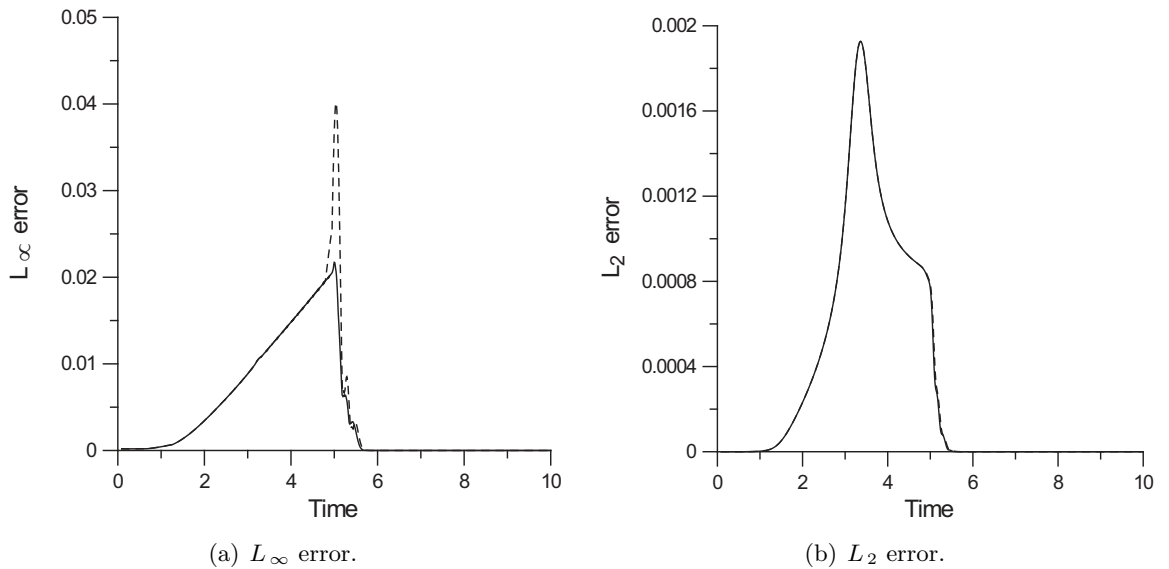
Figure B.6: Error in temperature versus computational time for different temperature interface conditions. Solid lines, injection+convective; dashed lines, injection.
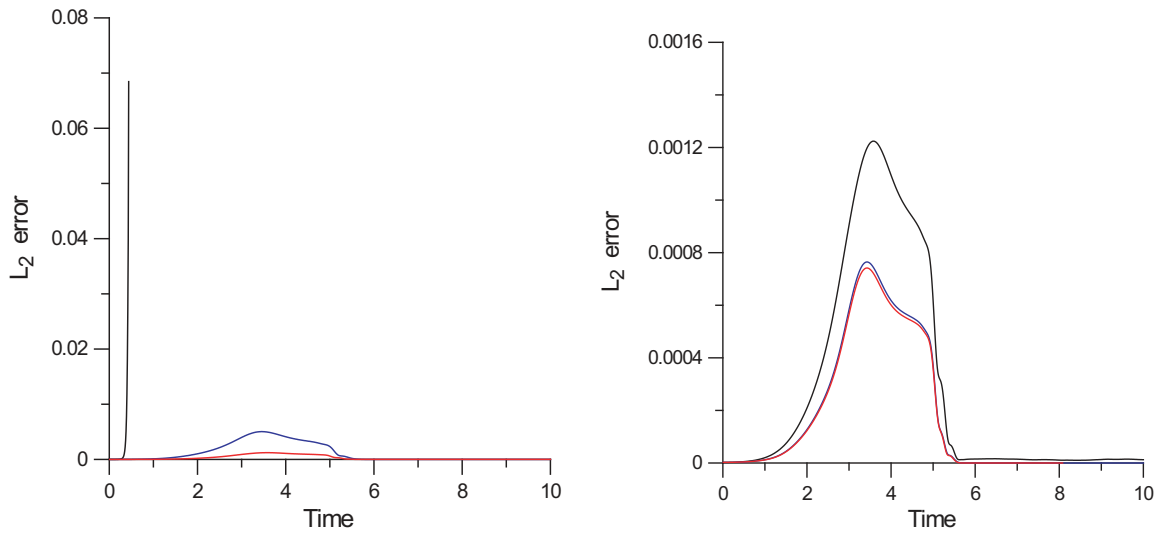
(a) Black line, 1 iteration; blue line, 2 iterations; red line, 3 iterations.

(b) Black line, 3 iterations; blue line, 5 iterations; red line, 7 iterations.

Figure B.7: Influence of number of iterations. L_2 error in temperature versus computational time.

(2001) (equation (2.155)) is left unchanged.

It is shown here that the coupling method for the low Mach number code described in section 2.5 of the chapter 2 with injection+convective interface conditions for the temperature performs well for steady and unsteady problems. In all the calculations reported throughout this manuscript, this method is used to specify interface conditions for the low Mach number code, when it is run in variable density regime. For the incompressible regime, interface conditions are the same, but with the temperature omitted from the formulation. Grid convergence study, performed to further investigate the accuracy of the current method, is documented in section B.2 of this appendix.

B.2 Grid Convergence Study

This part of the appendix is concerned with the behavior of the solution of the low Mach number code with grid refinement when interface conditions described in section 2.5 of chapter 2 and tested in the previous section, are implemented. The problem of decaying vortices is considered first (B.2.1). Grid convergence study is performed first when an analytical solution is specified at the low Mach number domain boundaries. Analytical solution imposed onto the compressible grid and interpolated to the low Mach number domain boundaries with bilinear and fourth order interpolation is considered further. Finally,

numerical solution of the compressible code interpolated to the boundaries of the low Mach number code is specified as interface conditions in the example of a laminar boundary layer above the heated wall B.2.2.

B.2.1 Decaying vortices

The test case of decaying vortices having the following analytical solution is considered first:

$$
\begin{aligned}
u\,(x,\,y,\,t) &= -\cos x \sin y\, e^{-2\,t} \\
v\,(x,\,y,\,t) &= \sin x \cos y\, e^{-2\,t} \\
w\,(x,\,y,\,t) &= 0 \\
p^{(2)}\,(x,\,y,\,t) &= -\tfrac{1}{4}(\cos 2\,x + \cos 2\,y)\, e^{-4\,t} \\
T\,(x,\,y,\,t) &= \text{const.}
\end{aligned}
\tag{B.4}
$$

Exact boundary conditions

Exact boundary conditions are first specified at all computational boundaries to establish the base case. L_∞ error between the numerical and analytical solutions, defined by

$$
L_\infty(u_i) = \frac{\max |u_{i\,numer} - u_{i\,an}|}{\max |u_{i\,an}|},
\tag{B.5}
$$

is documented in figure B.8 versus number of grid points in x direction, N_x. Grid convergence shows the second order behavior of the error for the velocities and the pressure for both two-dimensional and three-dimensional calculations, as expected from the second order accuracy of the low Mach number code. Another important quantity is plotted in figure B.8(a) together with the error curves – magnitude of the correction velocity. Correction velocity is introduced to ensure the solvability condition for the Poisson equation, which requires the sum of the mass fluxes over the boundaries of the computational domain to be identically zero. Although exact solution specified at the boundaries satisfies this requirement in the continuous sense, numerical approximation of the mass flux integral is not identically zero due to discretization errors. The value of velocity at each grid point at the outflow boundary is corrected by a small amount to drive this integral approximation to the machine zero. The net correction is split equally among the nodes of the outflow boundary, resulting in the same value of the correction velocity at each node, which is calculated as

$$
v_{corr} = -\frac{\sum (\rho\,v)_n\,\Delta\,S_n}{N_b},
\tag{B.6}
$$

(a) Two-dimensional calculations.

(b) Three-dimensional calculations.
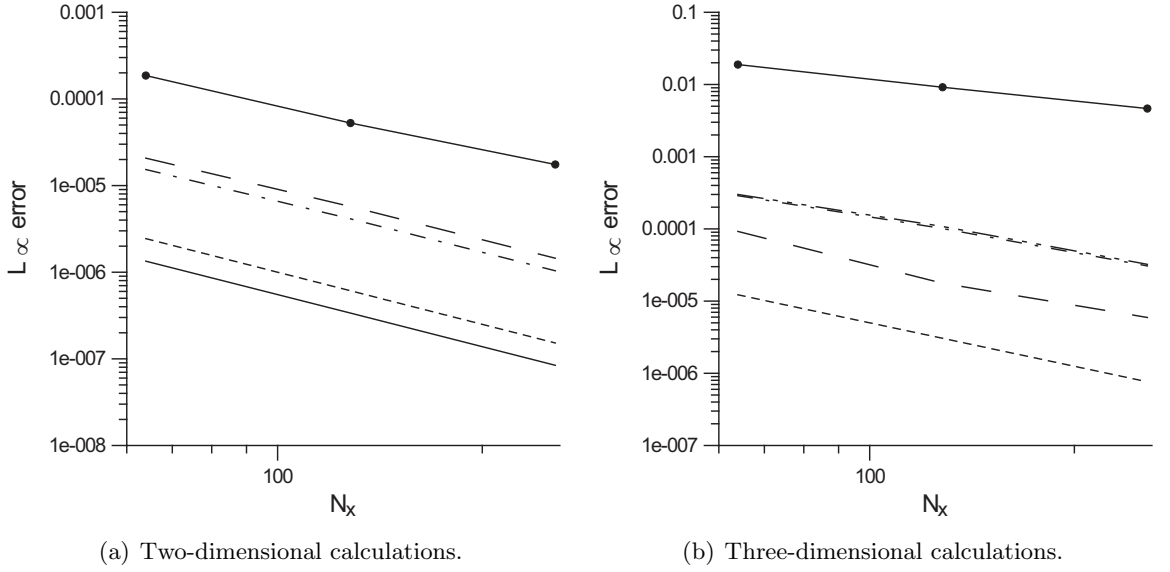
Figure B.8: L_∞ error versus number of grid points the low Mach number domain, decaying vortices, exact boundary conditions. — — —, u error; — · —, v error; — · · · —, w error; —●—, P error; - - - - , quadratic law, $1/N_x^2$; ——, magnitude of the correction velocity.

where N_b is the number of boundary nodes at the outflow boundary and ΔS_n is the cell area. Correction velocity in figure B.8(a) also shows the second order convergence with the grid size, consistent with the overall accuracy of the numerical discretization scheme.

Interpolated boundary conditions

To test an effect of interpolation on the grid convergence, the low Mach number code domain is placed inside the compressible code domain. Time-dependent analytical solution of decaying vortices (B.4) is imposed on the compressible grid. This analytical solution is interpolated from the compressible grid to the boundaries of the low Mach number grid and used to specify time-dependent interface boundary conditions. Bilinear interpolation and fourth-order Hermite interpolation are tested.

Bilinear interpolation

For bilinear interpolation, no dependence of errors on the grid size of the low Mach number domain is observed. However, errors do depend on the grid size of the compressible domain. The variation of L_∞ error with the number of grid points of the compressible domain is shown in figure B.9. Second order convergence with the compressible domain grid size is obtained, consistent with the accuracy of interpolation method. Absolute values

(a) Two-dimensional calculations.

(b) Three-dimensional calculations.
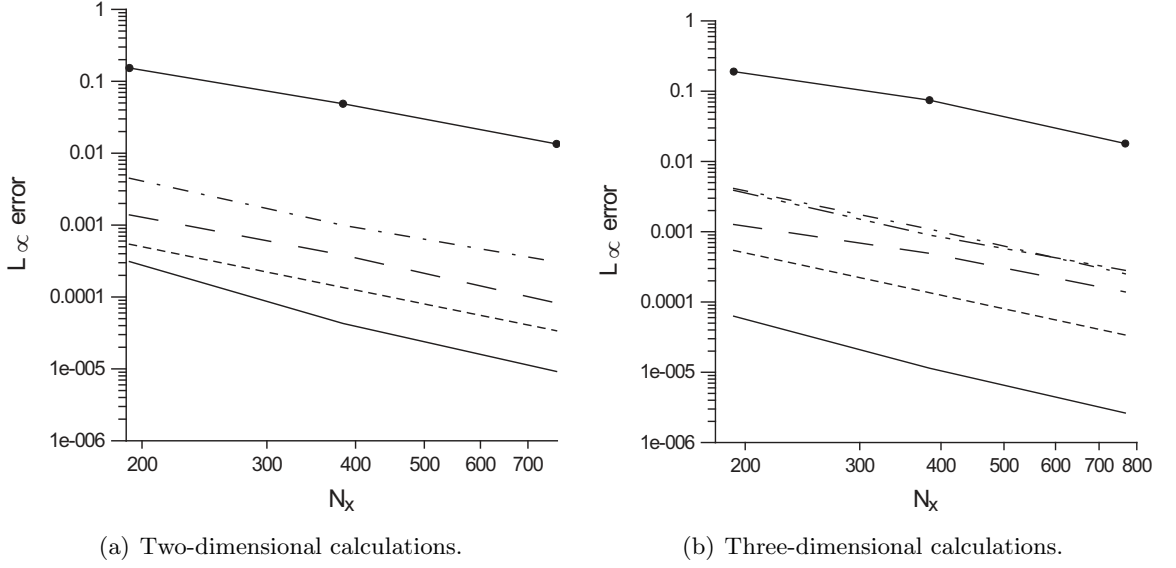
Figure B.9: L_∞ error versus number of grid points of the compressible domain, decaying vortices, bilinear interpolation. — — —, u error; — $\cdot$ —, v error; — $\cdot\cdot\cdot$ —, w error; —•—, P error; - - - - , quadratic law, $1/N_x^2$; ——, magnitude of the correction velocity.

of errors and of the correction velocity are almost two orders of magnitude larger for bilinear interpolation, than for exact boundary conditions.

Fourth order interpolation

Behavior of the errors is the opposite when the fourth order interpolation is employed. No dependence on the compressible grid size is observed. However, second order convergence with the low Mach number grid size is recovered, as in the case of exact solution at the boundaries. This can be seen in figure B.10. L_∞ error when the analytical solution is specified at the boundaries is also plotted in this figure (blue lines). It is noticeable that the plots for the exact boundary conditions and for the fourth order interpolated boundary conditions fall almost on top of each other.

The behavior of the errors can be explained in terms of the correction velocity. As already discussed, an analytical value for the correction velocity is zero for the case of decaying vortices. For an exact boundary conditions, numerical value of v_{corr} is not zero because of the discretization errors of the estimation of the mass flux integral $\sum (\rho v)_n \Delta x_n$. For interpolated boundary conditions, both discretization of the mass flux integral and the difference between interpolated and analytical values due to the interpolation determine the value of v_{corr}. When the correction velocity is small, smaller than approximation errors introduced by the scheme, approximation errors are the dominant source of errors, and the

(a) Two-dimensional calculations.

(b) Three-dimensional calculations.
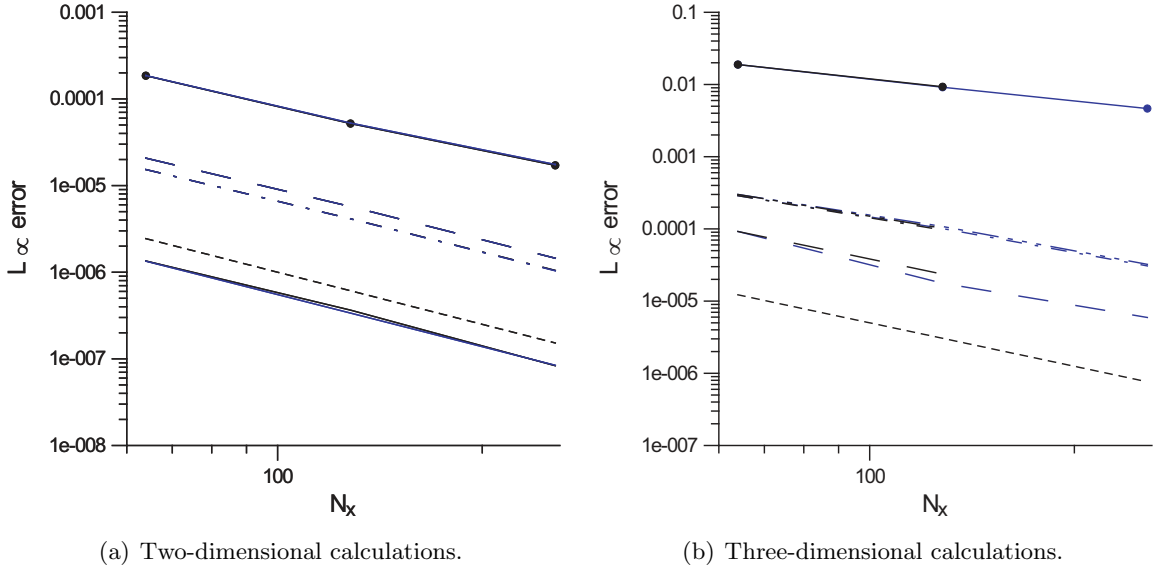
Figure B.10: L_∞ error versus number of grid points of the low Mach number domain, decaying vortices, fourth order interpolation. — — —, u error; — $\cdot$ —, v error; — $\cdot\cdot\cdot$ —, w error; —•—, P error; - - - - , quadratic law, $1/N_x^2$ ——, magnitude of the correction velocity; blue lines, exact boundary conditions.

accuracy of the solution scales with the grid size according to the order of the numerical scheme. This is observed in the cases with exact boundary conditions and with fourth order interpolation scheme, where the errors show the second order convergence with the low Mach number grid size. The insensitivity of errors to the compressible grid size in the case of fourth order interpolation scheme is explained by the fact that interpolation errors are smaller than approximation errors of the low Mach number numerical method even for the coarsest compressible grid. v_{corr} for both of these cases is smaller than 10^{-6}. For bilinear interpolation, to the contrary, interpolation errors are large and they lead to $v_{corr} \sim 10^{-4}$, that is larger than approximation errors of the numerical method. Interpolations errors in this case determine the accuracy of the solution. Since errors due to bilinear interpolation scale with the compressible grid size with the second order, this is the reason why L_∞ errors of the solution scale the same way. No dependence on the low Mach number grid size is observed, since approximation errors are smaller than interpolation errors.

B.2.2 Boundary layer above the heated wall

Laminar boundary layer above the heated wall with the temperature $T_w = 2T_\infty$ and Reynolds number $Re_d = U_\infty d/\nu_\infty = 500$ is another test case for the grid convergence

study. Low Mach number code domain is again completely surrounded by the compressible domain, and interface conditions are specified at all computational boundaries of the low Mach number code domain. The crucial difference between this test case and the previous test case of decaying vortices is that **numerical** solution of the compressible code is interpolated to the boundaries of the low Mach number domain, and not an **analytical** solution. Compressible code is run to convergence with Mach number $M_\infty = 0.05$. Dependence of the L_∞ error on a grid size of the low Mach number code for all the variables u, v, w, P, T, ρ is shown in figure B.11 for both bilinear and fourth order interpolation. No variation of the compressible code grid size was performed. Correction velocity magnitude is $\sim 3.6 \cdot 10^{-4}$ independent of the low Mach number code grid size and an order of interpolation. Correction velocity is dominated in this case by the difference of analytical solutions of the compressible and low Mach number equations and not by interpolation or discretization errors.

It is seen that the errors for u and v velocities and the pressure follow the trend of a correction velocity and do not depend on either grid size or an order of interpolation. On the other hand, the errors for w, T and ρ do depend on both the grid size and the order of interpolation. Errors for T and ρ show the second order convergence with the low Mach number grid size for both bilinear and fourth order interpolation, while the error for w behaves with the first order accuracy for the bilinear interpolation and with the second order accuracy for the fourth-order interpolation. One might conclude that the correction velocity determines the errors for u, v and P, making them independent of a grid size and an order of interpolation. In fact, the error in pressure for bilinear interpolation even increases slightly with the grid size, which might be due to the fact that better resolution in this case leads to a slight increase in correction velocity. w velocity is less susceptible to the correction velocity influence, but still feels it, especially in the case of bilinear interpolation, which results in a decrease of the order of accuracy. This smaller sensitivity of w to the correction velocity is perhaps due to the two-dimensionality of the boundary layer solution. Temperature, calculated from the energy equation and not coupled to the Poisson system, and density, determined from the temperature, are not influenced at all by the correction velocity and show an expected second order convergence with the grid size and an increase in accuracy with the order of interpolation.

The difference of analytical solutions of compressible and low Mach number equations scales with M_∞^2, where M_∞ is the Mach number of the compressible code. This difference is inherent when compressible and low Mach number codes are coupled and will result in a
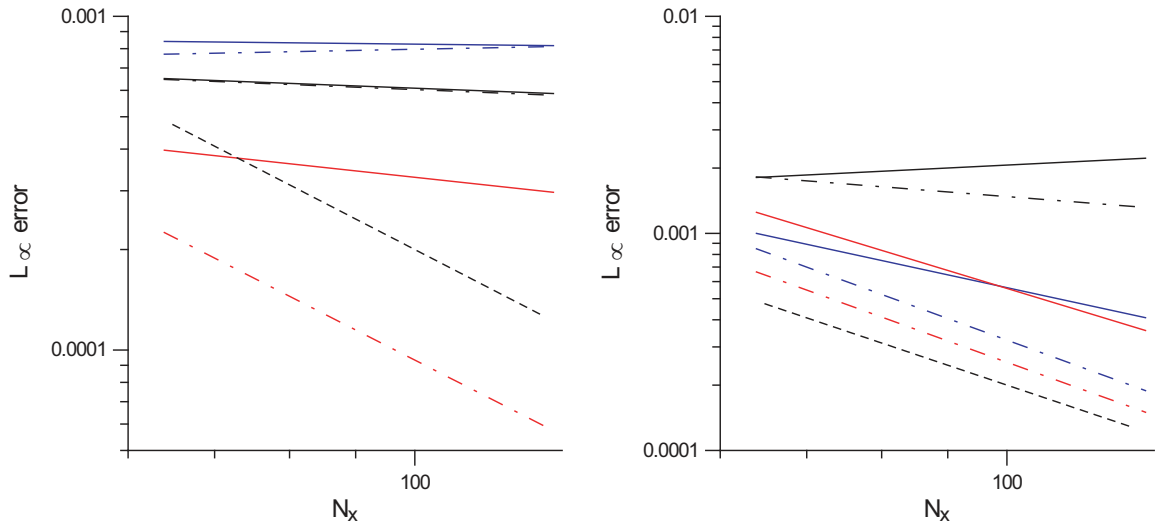
(a) Errors for u, v, w. Black lines, u errors; blue lines, v errors; red lines, w errors.

(b) Errors for P, T, ρ. Black lines, P errors; blue lines, T errors; red lines, ρ errors.

Figure B.11: L_∞ error as a function of the low Mach number code grid size, laminar boundary layer above the heated wall. Solid lines, bilinear interpolation; dash-dotted lines, fourth order interpolation; dashed line, quadratic law, $1/N_x^2$.

correction velocity for the low Mach number code of the same order of M_∞^2. For relatively fine meshes used in LES and practical Mach numbers for the compressible code ($\geq\sim 0.1$) this "analytical" error is going to be the dominant source of errors for both the low Mach number and the compressible code solutions. This error does not depend on the order of interpolation. Therefore, bilinear interpolation can be used without sacrificing the accuracy of the overall solution and providing for the gain in computational efficiency.

Appendix C

Details of the Turbulent Boundary Layer LES

C.1 Initial Conditions

Initial conditions for the simulations of the turbulent boundary layer are obtained by summing the mean profile and the turbulent fluctuations for the five variables $\{\rho,\, u\ v,\, w,\, T\}$. Mean profile for the streamwise velocity is obtained by superimposing the Spalding law of the wall

$$y^+ = \mathcal{U}^+_{wall} + 0.1108 \left\{ e^{0.4\mathcal{U}^+_{wall}} - 1 - 0.4\mathcal{U}^+_{wall} \frac{(0.4\mathcal{U}^+_{wall})^2}{2!} - \frac{(0.4\mathcal{U}^+_{wall})^3}{3!} - \frac{(0.4\mathcal{U}^+_{wall})^4}{4!} \right\} \tag{C.1}$$

and the law of the wake in the form of Schlichting (2000)

$$\frac{\mathcal{U}_\infty - \mathcal{U}_{wake}}{u_\tau} = \frac{1}{0.41} \ln(\eta) \tag{C.2}$$

as

$$\mathcal{U} = \mathcal{U}_{wall}\left[1 - W(\eta)\right] + \mathcal{U}_{wake}\, W(\eta), \tag{C.3}$$

using the weighting function $W(\eta)$ of Lund *et al.* (1998), defined in section 4. The mean vertical velocity is obtained by integrating the incompressible counterpart of the mean continuity equation

$$\mathcal{V} = -\int_0^y \frac{\partial \mathcal{U}}{\partial x} dy, \tag{C.4}$$

using the approximate relations of Schlichting (2000),

$$\frac{\mathcal{U}}{\mathcal{U}_\infty} = \left(\frac{y}{\delta}\right)^{1/7} \tag{C.5}$$

and

$$\frac{7}{72}\frac{d\,\delta}{d\,x} = 0.0225 \left(\frac{\nu}{\mathcal{U}_\infty \delta}\right)^{1/4}, \tag{C.6}$$

to get

$$\mathcal{V} = \frac{72}{56} \cdot 0.0225 \left(\frac{\nu}{\mathcal{U}_\infty \delta}\right)^{1/4} \eta^{8/7}. \tag{C.7}$$

The mean spanwise velocity is set to zero. The mean temperature is obtained from the mean streamwise velocity through the Waltz's equation. The mean density is calculated from the mean temperature through the equation of state.

Initial turbulence field to use with the rescaling-recycling procedure is often generated as random fluctuations of some specified amplitude (Lund *et al.* (1998)). Needless to say, such a crude guess can significantly delay the convergence of the solution to the state with the correct turbulence structure (simulation of Lund *et al.* (1998) was run initially for 1100 inertial timescales $\delta_i/\mathcal{U}_\infty$ to eliminate starting transients, which is quite expensive). Besides the slow convergence rate, even more significant problem can occur if simulations are started from the random disturbance field. To illustrate this problem, we turn to the paper of Ferrante & Elghobashi (2004), who tried to implement random initial conditions to perform DNS of a turbulent boundary layer. As a result, they observed fast temporal decay of $u_i'u_j'$ throughout the domain and consequent relaminarization of the TBL. It was first proposed, that the reason for this temporal decay is that the rescaling is not able to sustain the required magnitude of the cross correlation $u'v'$ necessary for the production of the turbulent kinetic energy (TKE) when starting with the initial condition $u'v' = 0$. But specifying the realistic profiles for the four correlations u', v', w' and $u'v'$ did not cure the fast temporal decay of TKE. Only after the realistic TKE spectrum $E(k)$ was prescribed in addition to $u_i'u_j'$ profiles in the initial field, the production rate of TKE was sustained. It was argued that the combination of a realistic $E(k)$ and a non-vanishing $u'v'$ is required to ensure the correct initial temporal behavior when performing DNS of TBL. Since Lund *et al.* (1998) did not encounter similar relaminarization problem starting with the random disturbance field in their LES, Ferrante & Elghobashi (2004) concluded that this is specific to DNS that additional effort is required in constructing initial solution to ensure its correct development at the early stages of the computations.

In the current LES, however, we encountered a similar problem of fast temporal decay of the turbulence if random fluctuations are specified initially. We then reconstructed an isotropic turbulence field with the prescribed TKE spectrum $E(k)$. The velocity fluctuations were further rescaled to satisfy specific intensities u', v' and w', as in the method of Le & Moin (1994). However, we skip the rotation step, necessary to ensure the correct value for the correlation $u'v'$; it is zero in our initial field. This procedure was found sufficient to prevent the temporal decay of initial disturbances and led to the correct turbulence characteristics of the fully-developed boundary layer. Apparently, it was the realistic TKE spectrum and not the value of the initial cross-correlation $u'v'$ (which is zero in our case) that was required to ensure the correct temporal development of the current LES.

The procedure implemented here to produce an isotropic turbulence field with the prescribed energy spectrum is the same as used by Xiong (2004) to specify initial conditions for his LES of homogeneous isotropic turbulence. TKE spectrum is set as

$$E(k) \propto k^4 \exp[-2(k/k_p)^2], \tag{C.8}$$

where the peak wave number k_p is equal to 4. This method is similar to the method of Lee *et al.* (1992), with the difference that the reconstructed turbulence field is solenoidal, i.e. the incompressibility condition $\mathbf{k} \cdot \hat{\mathbf{u}} = 0$ is satisfied. The procedure of synthesizing an incompressible isotropic turbulence field with the prescribed TKE spectrum is well described in Durbin & Petterson Reif (2000). There was no specific need for the strict imposition of the incompressibility condition in the current compressible simulations. The procedure of Xiong (2004) was used since it was validated against experiments of Comte-Bellot & Corrsin (1971) and numerical data of Lee *et al.* (1992), and is known to lead to a realistic isotropic turbulence field. Analytical functions $f(\eta) = A\,\eta \exp{(-B\,\eta)}$ were specified for the turbulence intensities u', v' and w', where the coefficients A and B were chosen to ensure the best fit between the analytical and experimental profiles. Density and temperature fluctuations were initially set to zero, but they became non-zero after the first time step due to the compressibility of the equations and the rescaling-recycling procedure.

To demonstrate that initial conditions described above lead to the correct temporal development of the turbulent boundary layer, we plot the value of velocity-derivatives skewness defined as

$$S_u = [\frac{1}{3} \sum_{i=1}^{3} \langle (\partial u_i'/\partial x_i)^3 \rangle][\frac{1}{3} \sum_{i=1}^{3} \langle (\partial u_i'/\partial x_i)^2 \rangle]^{-\frac{3}{2}}, \tag{C.9}$$
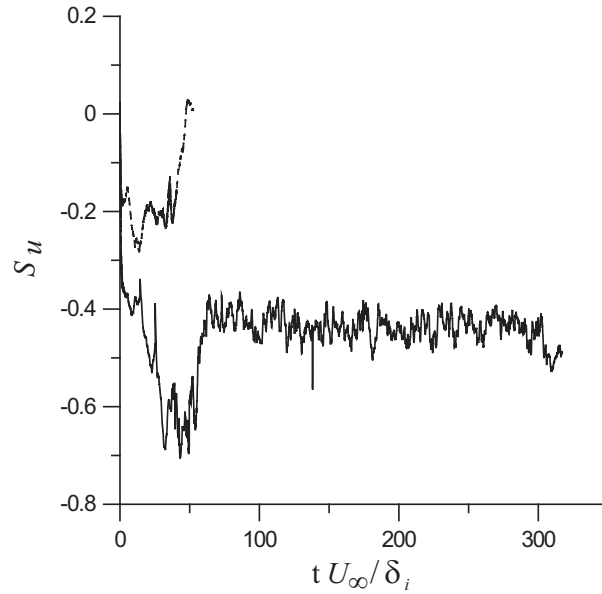
Figure C.1: Time-development of the velocity-derivative skewness, S_u, versus non-dimensional time, $t\mathcal{U}_\infty/\delta_i$. $- - -$, random fluctuations as initial disturbances; ———, initial disturbances with the specified TKE spectrum and turbulence intensities.

averaged over the whole length and width of the domain and the height of $0 \leq y \leq 0.7\,\delta_i$, versus non-dimensional time $t\mathcal{U}_\infty/\delta_i$ in Fig. C.1. This skewness is related to the process of vortex stretching and nonlinear energy transfer from small to large wavenumbers. When random fluctuation field is specified as initial conditions, the value of S_u vanishes as time increases (see figure C.1). As soon as this effect was realized, the calculations were stopped at time $t \sim 50\,\delta_i/\mathcal{U}_\infty$. When initial field with the correct TKE spectrum is specified, after some initial transient S_u reaches the typical value of $-0.4 - 0.5$ and stays at this level. This fact shows that the proper energy transfer rate is sustained throughout the simulations. In addition, the transient time needed to recover the realistic turbulence structure is reduced to about 80 inertial timescales $\delta_i/\mathcal{U}_\infty$ in our simulations, as opposed to 1100 in the simulations of Lund *et al.* (1998), which started from the random disturbance field.

C.2 Inflow Boundary Conditions Outside of the Boundary Layer

Sagaut *et al.* (2004) performed an evaluation of three proposed rescaling-recycling methods (Urbin & Knight (2001), Schröder *et al.* (2001) and Stolz & Adams (2003)) for a long time integration ($t \sim 105\,\delta_i/\mathcal{U}_\infty$) and reported that all of these methods lead to a temporal

drift in either δ, or $\delta^\star$, or both, from its target values. In some cases, quite a substantial drift of up to 20% was observed over the integration time of 105. In order to avoid this drift, Sagaut *et al.* (2004) proposed to fix the mean turbulent boundary layer profile at the inflow and to rescale only the fluctuations. However, this measure seems to be quite strong. Since the turbulent fluctuations influence the mean profile, fixing the mean profile prevents the solution from developing consistently, introduces an ad-hoc assumption into the computations (which one strongly desires to minimize) and deprives the rescaling-recycling method from its major attractiveness of being "input-free".

In the present simulations, we have also encountered a temporal drift in the boundary layer thickness if the rescaling-recycling procedure is used for the entire inflow boundary. The plot of the computed inflow boundary layer thickness δ_i^{comp} normalized by its target value δ_i versus non-dimensional time $t\mathcal{U}_\infty/\delta_i$ is shown in figure C.2. It is clear from the figure that the computed boundary layer thickness increases with time. It was observed that the reason for this increase is the drift in the mean streamwise velocity outside of the boundary layer. To demonstrate this effect, contours of the mean streamwise velocity in $x - y$ plane are shown in figure C.3 for the simulation time $t \sim 215\,\delta_i/\mathcal{U}_\infty$. Statistics were collected within the last 25 inertial timescales. Recall that 99% boundary layer thickness is defined as the y-coordinate, where the mean streamwise velocity is equal to 99% of its free-stream value. The contour levels are zoomed into the values from $0.98\mathcal{U}_\infty$ to $\mathcal{U}_\infty$ in figure C.3. Streamwise velocity at the edge of the boundary layer diminishes with time, pushing the location with $\mathcal{U} = 0.99\mathcal{U}_\infty$ outside of the actual boundary layer, leading to erroneously large estimate for the boundary layer thickness. This drift effect is pronounced even over short sampling period of $25\,\delta_i/\mathcal{U}_\infty$. The drift occurs, because the rescaling-recycling procedure is applied both in the boundary layer and above the boundary layer. Fluctuations are determined as the difference between the instantaneous and the mean solution. During initial transient, an instantaneous solution necessarily deviates from its mean even in the regions of steady flow, since inaccuracies in initial and boundary conditions together with the discretization errors create acoustic disturbances, which propagate through the domain till they leave it. These small disturbances, which are actually only numerical artifacts, are mistakenly treated as the "turbulent fluctuations" in the region outside of the boundary layer, where they do not exist in reality. If rescaled and recycled, these "fluctuations" deteriorate the solution and lead to the long-term drift in the mean velocity, observed in the current simulations. To remedy the situation, it was proposed to apply rescaling and recycling procedure only within the boundary layer. Above the boundary layer edge, we set

the inflow quantities equal to their free-stream values, leading to the correct mean profile and zero values for the fluctuations. This procedure is much less strict than fixing the mean velocity profile throughout the entire boundary layer proposed by Sagaut *et al.* (2004). It is also more physically justifiable and leads to the correct development of the boundary layer.

Temporal behavior of the boundary layer thickness normalized by its target value for the proposed modified rescaling-recycling method is shown in figure C.2. After initial transient time of about 120 inertial timescales (which is close to the time necessary for the correct velocity derivative skewness to develop, see figure C.1), boundary layer thickness recovers its target value within a 2% error and sustains it throughout the computations. Contours of mean streamwise velocity at time $t \sim 335\, \delta_i/\mathcal{U}_\infty$ for the modified method are shown in figure C.4. The region with $0.98\mathcal{U}_\infty < \mathcal{U} < \mathcal{U}_\infty$ is a narrow band at the edge of the boundary layer, as it should be. Note, that the statistics was accumulated this time over a large period of $t \sim 210\, \delta_i/\mathcal{U}_\infty$. If there would be a drift in the mean velocity, it would definitely manifest itself over such a long integration time. Temporal behavior of the Reynolds number based on inflow momentum thickness, $Re_{\theta\,i}$, is plotted in figure C.5. After initial transient time of about 120 inertial timescales (the same transient time as for the boundary layer thickness), it reaches its equilibrium value of $Re_{\theta\,i} \sim 910$. Note, that we do not compare the momentum thickness to its target value, but only to its equilibrium value, since fixing the target values for both boundary layer thickness and momentum thickness makes the problem overspecified (see Lund *et al.* (1998)).

C.3   Momentum Integral Analysis

The momentum integral analysis leading to the estimates used in section 4 for evaluating the streamwise evolution of the boundary layer is presented here. It can also be found in Lund *et al.* (1998). In this analysis, the mean velocity profile is assumed to obey the Coles' law of the wake (Coles (1956)) over the entire extent of the layer:

$$\mathcal{U}^+ = \frac{1}{k}\, \ln(y^+) + B + \frac{2\Pi}{k}\, \sin^2\left(\frac{\pi}{2}\, \eta\right), \tag{C.10}$$

where $\mathcal{U}^+ = \mathcal{U}/u_\tau$ $y^+ = y\,u_\tau/\nu$, $\eta = y/\delta$. k, B are constants and Π is a parameter that depends on the pressure gradient, which are set to $k = 0.41$, $B = 0.5$, $\Pi = 0.5$, respectively, following Lund *et al.* (1998). The boundary layer thickness, δ, is defined as the position,
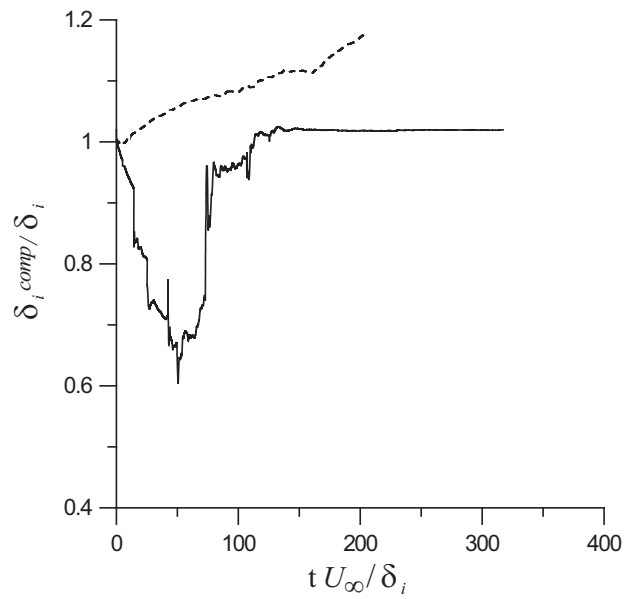
Figure C.2: Time-development of the computed inflow boundary layer thickness, δ_i^{comp}/δ_i, versus non-dimensional time, $t\,\mathcal{U}_\infty/\delta_i$. $---$, original rescaling-recycling method, ———, modified rescaling-recycling method.
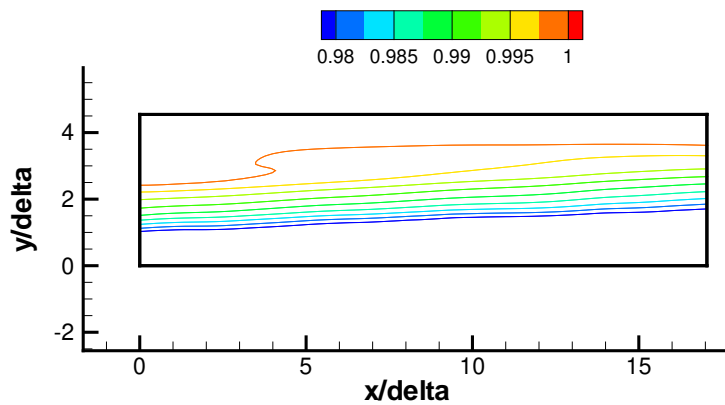
Figure C.3: Contours of the mean streamwise velocity in $x-y$ plane for the original rescaling-recycling method.
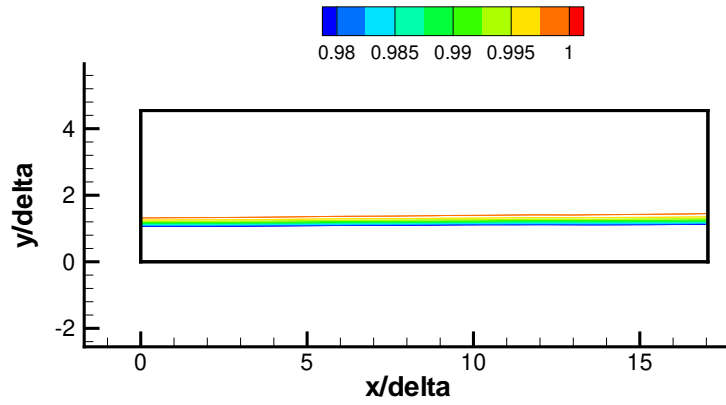
Figure C.4: Contours of the mean streamwise velocity in $x - y$ plane for the modified rescaling-recycling method.
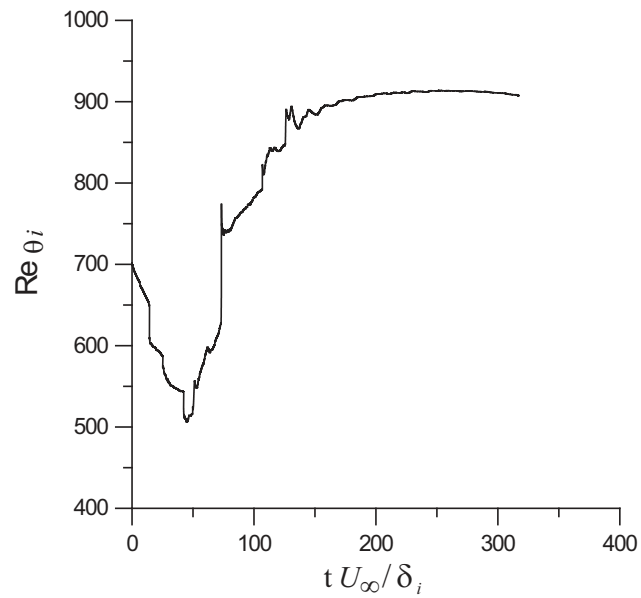
Figure C.5: Time-development of the Reynolds number based on inflow momentum thickness, $Re_{\theta i}$, versus non-dimensional time, $t\mathcal{U}_{\infty}/\delta_i$, with the modified rescaling-recycling method.

where $\mathcal{U} = \mathcal{U}_\infty$. Making use of this condition, relation (C.10) implies

$$Re_\delta = \frac{\mathcal{U}_\infty \delta}{\nu} = \lambda \exp\left[k\left(\lambda - B\right) - 2\,\Pi\right], \tag{C.11}$$

where λ is the wall friction parameter

$$\lambda = \frac{\mathcal{U}_\infty}{u_\tau} = \sqrt{\frac{2}{c_f}}. \tag{C.12}$$

Using (C.11) and (C.12), one can rewrite equation (C.10) as

$$\frac{\mathcal{U}}{\mathcal{U}_\infty} = 1 + \frac{1}{k\,\lambda}\left\{\ln(\eta) + 2\,\Pi\left[\sin^2\left(\frac{\pi}{2}\eta\right) - 1\right]\right\}. \tag{C.13}$$

Displacement and momentum thickness can be obtained by integrating relation C.13:

$$\delta^\star = \left(\frac{1 + \Pi}{k\,\lambda}\right)\delta, \tag{C.14}$$

$$\theta = \left\{\frac{1 + \Pi}{k\,\lambda} - \frac{1}{k^2\lambda^2}\left[2 + 2\,\Pi\left(\frac{\mathrm{Si}\,(\pi)}{\pi} + 1\right) + \frac{3}{2}\,\Pi^2\right]\right\}\delta, \tag{C.15}$$

where $\mathrm{Si}\,(\pi) \simeq 1.852$ is the sine integral evaluated at π. The streamwise distance is determined by integrating the relation (see, for example, Schlichting (2000))

$$2\,\frac{d\,\theta}{dx} = c_f \tag{C.16}$$

while using (C.12) to yield

$$x - x_i = \int_{\lambda_i}^{\lambda} \lambda^2 \frac{d\,\theta}{d\lambda}\,d\,\lambda, \tag{C.17}$$

where the subscript "i" denotes the inflow station (the location where $Re_\theta = 910$ for the present comparison, see chapter 4). Expressions (C.11), (C.14), (C.15) and (C.17) contain the wall shear parameter λ as an independent variable. The plots in chapter 4 referring to the momentum integral estimates were generated by stepping through the values of λ and then rearranging the outputs to produce the functions of Re_θ or x.

Appendix D

Supplement to Chapter 5

D.1   Grid Refinement

An important issue while performing numerical simulations is the choice of the computational grid. The problem of choosing the grid is always intriguing since there are no particular rules on assessing the necessary resolution beyond some general considerations. For LES, one of these considerations is that the grid size should be smaller than the size of the energy-containing eddies, since the goal of LES is to resolve such eddies. However, the size of these eddies is generally unknown. For the flows studied extensively, such as turbulent boundary layer, channel flow etc., previous LES experiences give an idea about the require grid resolution. When one moves to the simulation of more complex phenomena, such as JCF flows, where past LES efforts are limited or even absent, the choice of the grid becomes a difficult task. The situation is complicated by the fact that different scales of motion exist in different geometrical locations, so that the efficient distribution of grid points is sought for. One should also take into account that each LES run takes considerable amount of time, and there is a limited opportunity for trying out different grids computationally.

Three computational grids are compared in this study. First two are concerned with the change of the mesh in the compressible subdomain. The third grid uses finer resolution in the film hole and the plenum, having the compressible mesh the same as Grid 2. The relative comparison of the three grids can be found in table D.1. Only the differences are highlighted. All other grid parameters, which are not altered, can be found in table 4.1 of chapter 5.

Mesh spacing inside the compressible subdomain from Grid 1 to Grid 2 (same as Grid

3) is changed only in x direction (by redistribution of grid points, the total grid size of $128 \times 128 \times 128$ nodes stays the same). Mesh in y direction is the same as the one used in chapter 4 and is shown to be adequate to resolve the upstream turbulent boundary layer. Although, besides TBL phenomena, there is also a shear layer forming between the jet and the wake in y direction, y-mesh is believed to be accurate enough. The z mesh is uniform with more than 42 points per jet diameter and should be sufficient. Resolution in x-direction is compared for the Grid 1 and Grid 2 (Grid 3) in figure D.1. Grid 1 has uniform distribution of points in x direction, giving about 17 points per jet diameter, which is less than half as the z mesh. Apparently, this resolution is not enough to accurately describe the complex interactions occurring immediately after the jet injection, where the DSSN vortex resides. It manifests itself in strong overprediction of vertical velocity with Grid 1 in that region shown in figure D.2, where time-averaged vertical velocity at the centerplane along the horizontal line $y/d = 0.15$ is compared with the experimental data of Pietrzyk *et al.* (1989). Severe clustering of grid points in the wake region for Grid 2 and Grid 3 (figure D.1) remedies the situation. Grid 3, having the same resolution in the compressible subdomain as Grid 2, and improved resolution inside the film hole and the plenum, leads to the vertical velocity profile above the flat surface very similar to that of the Grid 2 (figure D.2). It means that the resolution inside the hole is superior to that above the flat surface even for the coarser hole mesh (Grids 1 and 2) and is not the dominant source of errors in the wake region. Film cooling effectiveness for all three grids is compared in figure D.3. It is seen that Grid 1 exaggerates a decrease in film effectiveness due to the DSSN vortex, with Grids 2 and 3 showing smaller decrease. Larger level of oscillations for Grid 2 computations might be due to smaller averaging time.

Although no difference between Grid 2 and Grid 3 solutions is noticeable in the crossflow region, Grid 3 shows major improvement in the plenum and film hole region. As it can be inferred from table D.1, Grid 3 is three times finer in the axial direction for the film hole (radial and azimuthal directions being unchanged; this refinement choice is associated with the fact that the axial resolution of Grid 2 inside the hole is the coarsest among (x_j, r_j, θ_j)) and has significantly better resolution in the plenum for both axial and radial directions. Mean vertical velocity profiles taken at the exit from the plenum are compared for Grid 2 and Grid 3 in figure D.4. Large grid to grid oscillations present in Grid 2 are completely absent in Grid 3, resulting in well-resolved smooth flowfield. Analysis of the results showed that the oscillations were dictated by the lack of y-resolution in the top wall plenum boundary layer and x-resolution in the region of fast acceleration and sharp turning at the downstream

	Grid 1	Grid 2	Grid 3
Crossflow region	Uniform	Clustered	Clustered
(compressible subdomain)	$x_{min}/d \sim 0.059$	$x_{min}/d \sim 0.025$	$x_{min}/d \sim 0.025$
Film hole	$312 \times 64 \times 64$	$312 \times 64 \times 64$	$936 \times 64 \times 64$
Plenum	$256 \times 128 \times 64$	$256 \times 128 \times 64$	$256 \times 512 \times 64$
	$10\,d \times 10.516\,d$	$10\,d \times 10.516\,d$	$5\,d \times 5\,d$

Table D.1: Variation in parameters of the different grids.
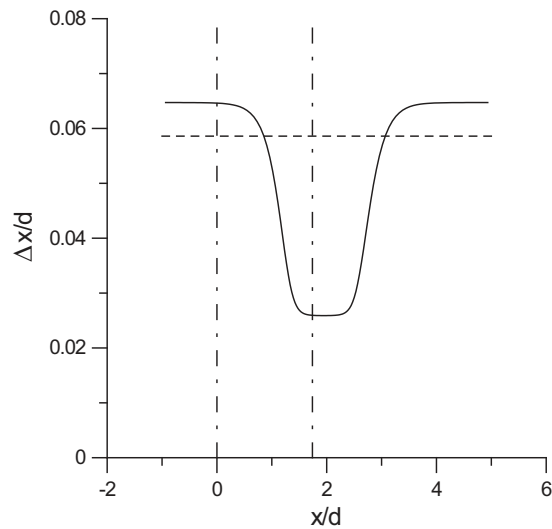
Figure D.1: Mesh spacing in streamwise direction. Dashed line, Grid 1; solid line, Grid 2 and Grid 3; dash-dotted lines, x coordinates of the leading and trailing edges of the hole exit cross-section in the centerplane.

corner of the plenum–hole connection.

Grid 3 is the default grid for documenting the simulation results in chapter 5.

D.2   SGS Turbulence Model

The importance of SGS turbulence model in the present calculations can be assessed by looking at the ratio of subgrid (SGS) turbulent viscosity to the laminar viscosity μ_t/μ, where SGS turbulent viscosity is defined by

$$\mu_t = C_\mu\, \overline{\rho}\, \Delta^2\, |\widetilde{S}|, \tag{D.1}$$
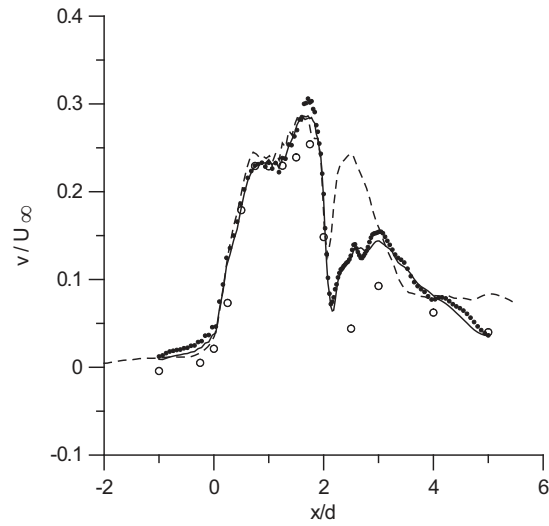
Figure D.2: Time-averaged vertical velocity profiles at the centerplane along the horizontal line $y/d = 0.15$. Dashed line, Grid 1; •, Grid 2; solid line, Grid 3; ○, experiments of Pietrzyk *et al.* (1989).
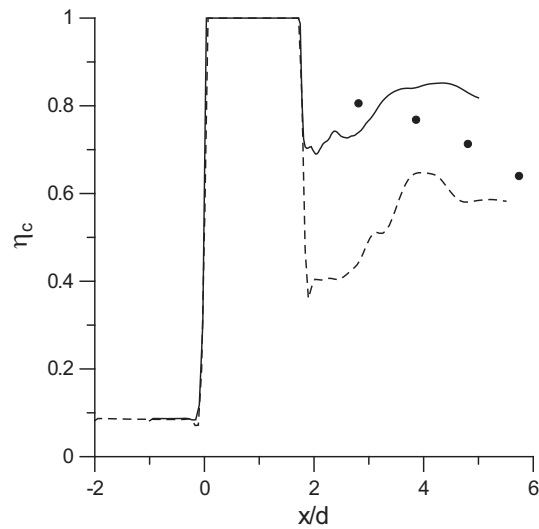
Figure D.3: Centerline film cooling effectiveness. Dashed line, Grid 1; •, Grid 2; solid line, Grid 3; ○, experiments of Sinha *et al.* (1991)
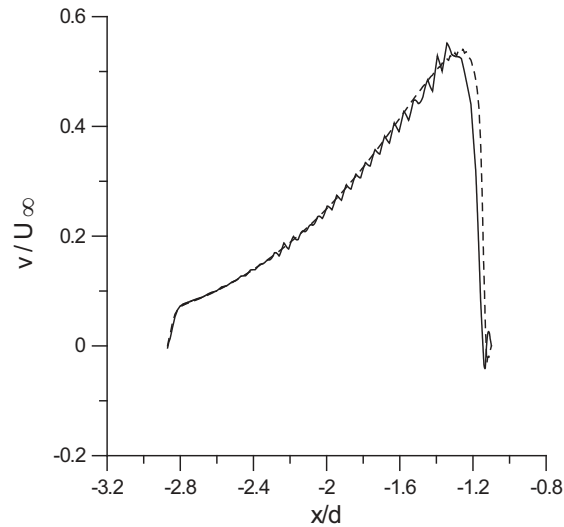
Figure D.4: Time-averaged vertical velocity profiles at the centerplane at the plenum exit. Dashed line, Grid 3; solid line, Grid 2.

and the coefficient C_μ is determined by the dynamic procedure (equation 2.143) described in the section 5.5 of the chapter 2. Ratio μ_t/μ is plotted at the centerplane for the plenum, film hole and the crossflow region in figure D.5. The peak values of SGS turbulent viscosity reach about five times the value of the laminar viscosity (the color scale of the figure is selected to show the structure of μ_t in more detail). It is seen that the model plays practically no role in the plenum. Inside the hole, largest values of μ_t are observed in the separated region next to the downstream wall. In the crossflow region, turbulent viscosity is the most significant in the wake below the jet. The horizontal view of μ_t/μ in the crossflow region for $y/d = 0.3$ can be seen in figure D.6. Plane $y/d = 0.3$ passes through the wake region of the jet. Spots of high turbulent viscocity downstream of the jet injection corresponding to high turbulent mixing are visible.

D.3 Artificial Dissipation Scheme

As described in section 2.2 of chapter 2, coefficient of artificial dissipation σ_d is not constant in the present model, but proportional to the high-order derivatives of the rate of strain
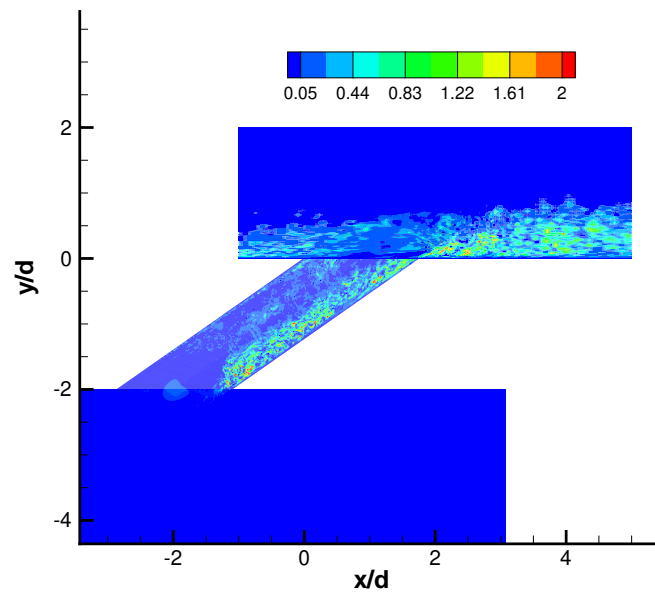
Figure D.5: Ratio of subgrid turbulent viscosity to the laminar viscosity, μ_t/μ. Centerplane view.
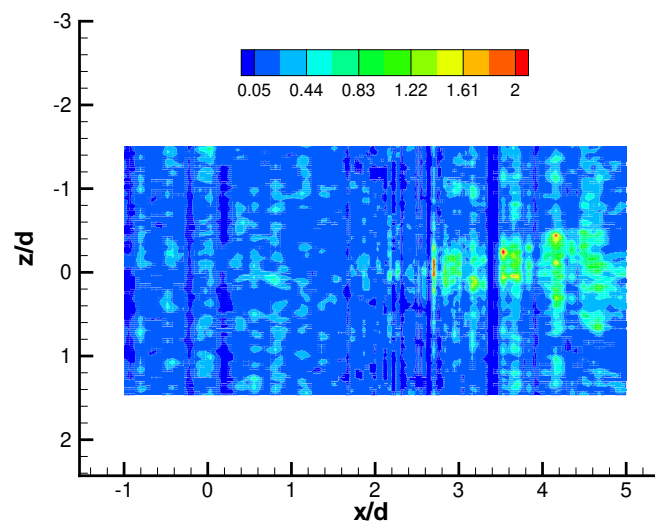
Figure D.6: Ratio of subgrid turbulent viscosity to the laminar viscosity, μ_t/μ. Horizontal view, $y/d = 0.3$.

(a) Artificial dissipation term.

(b) Dominant convective term, $u\,\partial T/\partial x$.

Figure D.7: Comparison of artificial dissipation term and a dominant convective term in the energy equation. Center-plane view.

(equation (2.70). The artificial dissipation term

$$D = -\sigma_d\left(\xi, \eta,\, z,\, t\right)\left(\Delta\,\xi^4\frac{\partial^4 U}{\partial\,\xi^4} + \Delta\,\eta^4\frac{\partial^4 U}{\partial\,\eta^4} + \Delta\,z^4\frac{\partial^4 U}{\partial\,z^4}\right) \tag{D.2}$$

added to the right-hand side of the equations is compared to the dominant convective term in the left-hand side for the energy equation in figure D.7 and for three momentum equations in figures D.8–D.10. Center-plane view is plotted. For the energy equation, the ratio between the artificial dissipation term and the terms in the left-hand side is about 1/500, since temperature gradients are small due to the small temperature variation in the present calculations. For the momentum equations, the ratio is about 1/20. However, the most of the dissipation is added in the region right after the jet injection, where the highest TKE levels (higher than in the experiments) are observed. The dissipation is high there due to the strong gradients of velocity introduced by the sharp corner. In all other regions of the flow, where good comparison with experiments is observed, dissipation is about an order of magnitude smaller, leading to the ratio of 1/200. Artificial dissipation term is about the same order of magnitude as the SGS model term.

(a) Artificial dissipation term.

(b) Dominant convective term, $\rho\, u\, \partial u/\partial x$.
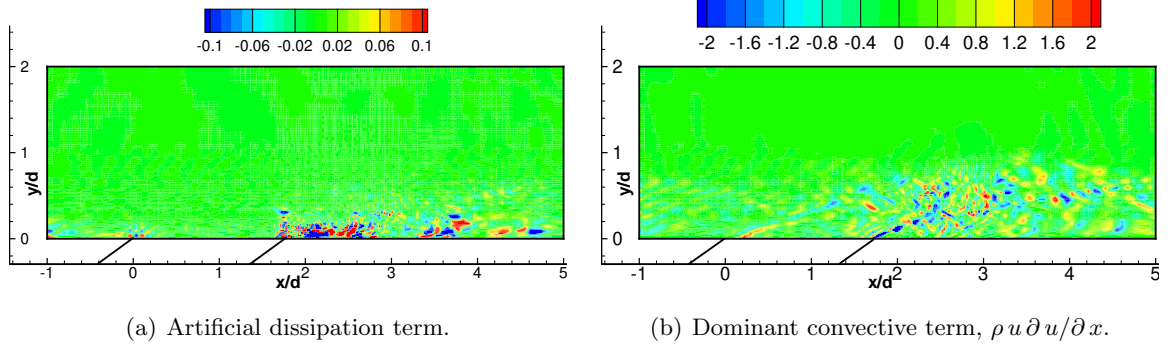
Figure D.8: Comparison of artificial dissipation term and a dominant convective term in the x-momentum equation. Center-plane view.

(a) Artificial dissipation term.

(b) Dominant convective term, $\rho\, u\, \partial v/\partial x$.
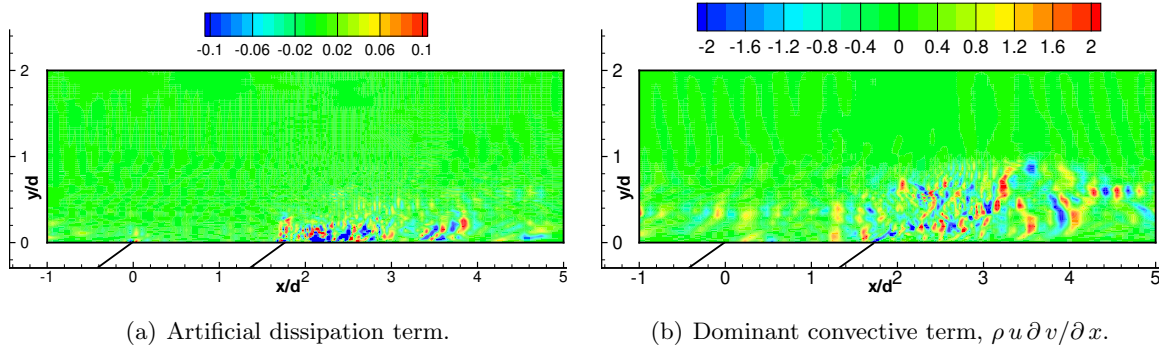
Figure D.9: Comparison of artificial dissipation term and a dominant convective term in the y-momentum equation. Center-plane view.

(a) Artificial dissipation term.

(b) Dominant convective term, $\rho\, u\, \partial w/\partial x$.
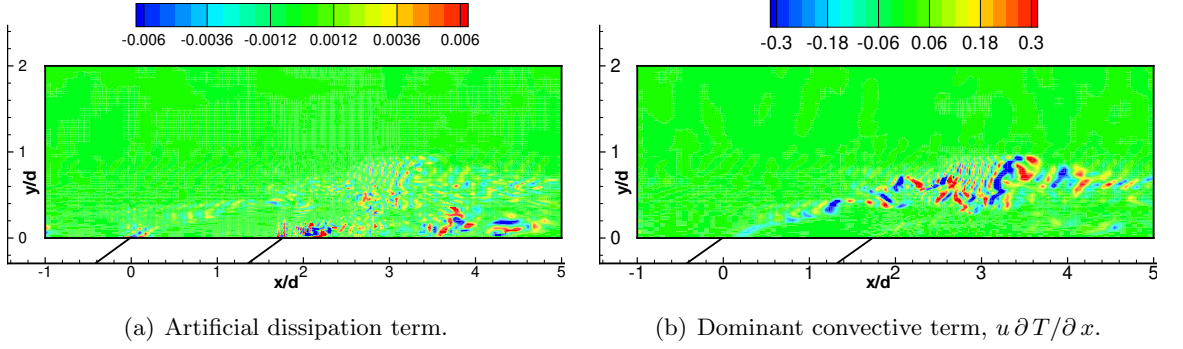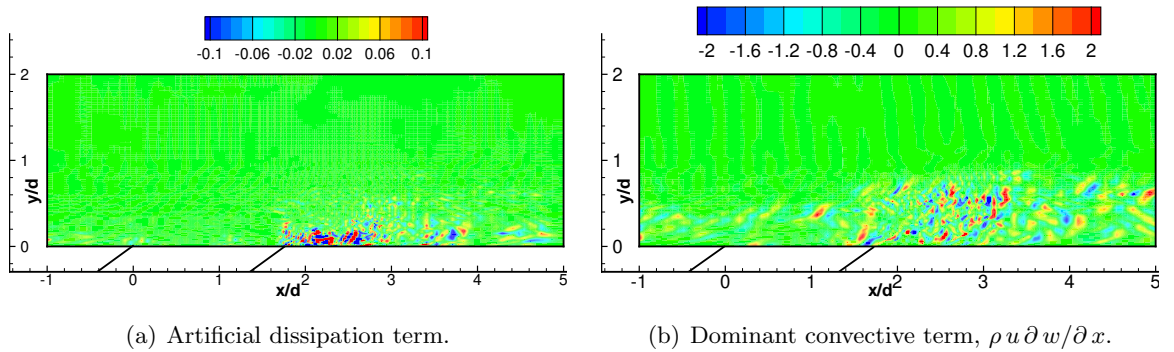
Figure D.10: Comparison of artificial dissipation term and a dominant convective term in the z-momentum equation. Center-plane view.

Bibliography

ABIDE, S. & VIAZZO, S. 2005 A 2d compact fourth-order projection decomposition method. *Journal of Computational Physics* **206** (2), 252–276.

ABRAMOVICH, G. N. 1963 *The theory of turbulent jets*. MIT Press, Cambridge, MA.

ACHARYA, S., TYAGI, M. & HODA, A. 2001 Flow and heat transfer predictions for film cooling. In *Heat Transfer in Gas Turbine Systems*, , vol. 934, pp. 110–125. Annals of the New York Academy of Sciences.

AJERSCH, P., ZHOU, J.-M., KETLER, S., SALCUDEAN, M. & GARTSHORE, I.S. 1995 Multiple jets in a crossflow: Detailed measurements and numerical simulations. *ASME Paper* 95-GT-9.

AKSELVOLL, K. & MOIN, P. 1993 Application of the dynamic localization model to large eddy simulation of flow over a backward-facing step. *Engineering Applications to Large Eddy Simulation* . ASME, New York, edited by U. Piomelli.

AKSELVOLL, K. & MOIN, P. 1995 Large eddy simulation of turbulent confined coannular jets and turbulent flow over a backward facing step. In *Report TF–63*. Thermosciences Division, Department of Mechanical Engineering, Stanford University.

BALDAUF, S., SCHEURLEN, M., SCHULZ, A. & WITTIG, S. 2002 Correlation of film-cooling effectiveness from thermographic measurements at enginelike conditions. *Journal of Turbomachinery* **124**, 686–698.

BALDWIN, B. S. & LOMAX, H. 1978 Thin layer approximation and algebraic model for separated flows. *AIAA Paper* 78-257.

BEAM, R. M. & WARMING, R. 1978 An implicit factored scheme for the compressible Navier-Stokes equations. *AIAA Journal* **16** (4), 393–402.

BERGELES, G., GOSMAN, A. D. & LAUNDER, B. E. 1978 The turbulent jet in a cross stream at low injection rates - a three-dimensional numerical treatment. *Numerical Heat Transfer* **1**, 217–242.

BERGER, M. J. 1985 Stability of interfaces with mesh refinement. *Mathematical Computing* **45**, 301–318.

BERGER, M. J. 1987 On conservation at grid interfaces. *SIAM Journal on Numerical Analysis* **24**, 967–984.

BERGER, M. J. & OLIGER, J. 1984 Adaptive mesh refinement for hyperbolic partial differential equations. *Journal of Computational Physics* **53**, 484–512.

BERHE, M. K. & PATANKAR, S. V. 1996 A numerical study of discrete-hole film cooling. *ASME Paper* 96-WA/HT-8.

BLANCHARD, J. N., BRUNET, Y. & MERLEN, A. 1999 Influence of a counter rotating vortex pair on the stability of a jet in a cross flow: an experimental study by flow visualizations. *Experiments in Fluids* **26**, 63–74.

BLASIUS, H. 1908 Grenzschichten in Fl´ussigkeiten mit kleiner Reibung. *Z.Math. Phys.* **56**, 1–37.

BOGARD, D. G. & THOLE, K. A. 2006 Gas turbine film cooling. *Journal of Propulsion and Power* **22** (2), 249–270.

BRADSHAW, P. 1977 Compressible turbulent shear layers. *Annual Review of Fluid Mechanics* **9**, 33.

BRILEY, W. R. & MCDONALD, H. 1975 Solution of the three-dimensional compressible Navier-Stokes equations by an implicit technique. In *Proceedings of the Fourth International Conference on Numerical Methods in Fluid Dynamics, Lecture Notes in Physics*, , vol. 35, pp. 105–110. Springer-Verlag, Berlin.

BUNKER, R. & BAILEY, J. 2001 Film cooling discharge coefficient measurements in a turbulated passage with internal crossflow. *ASME Journal of Turbomachinery* **123** (4), 774–780.

BURD, S. & SIMON, T. 1997 The influence of coolant supply geometry on film coolant exit flow and surface adiabatic effectiveness. *ASME Paper* 97-GT-025.

BURD, S. W. & SIMON, T. W. 1999 Measurements of discharge coefficients in film cooling. *Transactions of the ASME. The Journal of Turbomachinery* **121** (2), 243–248.

CALI, P. M. & COUAILLIER, V. 2000 Conservative interfacing for overset grids. *AIAA Paper* 2000-1008. In 38th AIAA Aerospace Sciences Meeting and Exhibit, Reno, NV.

CARATI, D. & EIJNDEN, E. V. 1997 On the self-similarity assumption in dynamic models for large eddy simulations. *Physics of Fluids* **9**, 2165–2167.

CARPENTER, M. H., NORDSTRÖM, J. & GOTTLIEB, D. 1999 A stable and conservative interface treatment of arbitrary spatial accuracy. *Journal of Computational Physics* **148**, 341–365.

CHANG, S. L. & CHIEN, L. S. 2003 Domain decomposition algorithms for fourth-order nonlinear elliptic eigenvalue problems. *Journal of Computational Physics* **191** (2), 476–501.

CHESSHIRE, G. & HENSHAW, W. D. 1994 A scheme for conservative interpolation on overlapping grids. *SIAM Journal of Scientific Computing* **15** (4), 819–845.

CHIEN, J. C. & SCHETZ, J. A. 1975 Numerical solution of the three dimensional Navier-Stokes equations with applications to channel flows and a buoyant jet in a cross flow. *ASME Journal of Applied Mechanics* **42**, 575–579.

COLES, D. 1962 The turbulent boundary layer in a compressible fluid. In *Report No. R-403-PR*. The Rand Corporation, Santa Monica, California.

COLES, D. E. 1956 The law of the wake in a turbulent boundary layer. *Journal of Fluid Mechanics* **1**, 191.

COLLIS, S. S. 1997 A computational investigation of receptivity in high-speed flow near a swept leading edge. PhD thesis, Stanford University.

COLONIUS, T., LELE, S. K. & MOIN, P. 1991 The free compressible viscous vortex. *Journal of Fluid Mechanics* **230**, 45–73.

COMTE-BELLOT, G. & CORRSIN, S. 1971 Simple Eulerian time correlation of full and narrow-band velocity signals in grid generated "isotropic" turbulence. *Journal of Fluid Mechanics* **48**, 273–337.

COOK, A. W. & CABOT, W. H. 2004 A high-wavenumber viscosity for high-resolution numerical methods. *Journal of Computational Physics* **195**, 594–601.

COOK, A. W. & CABOT, W. H. 2005 Hyperviscosity for shock-turbulence interactions. *Journal of Computational Physics* **203**, 379–385.

DAILERY, L. D. & PLETCHER, R. H. 1996 Evaluation of multigrid acceleration for precondioned time-accurate Navier-Stokes algorithms. *Computers and Fluids* **25** (8), 791–811.

DEGRAAF, D. B. & EATON, J. K. 2000 Reynolds-number scaling of the flat-plate turbulent boundary layer. *Journal of Fluid Mechanics* **422**, 319–346.

DURBIN, P. A. & PETTERSON REIF, B. A. 2000 *Statistical Theory and Modeling for Turbulent Flows*. John Wiley and Sons.

EATON, J. K. 2006 Private communication.

ETHRIDGE, M., CUTBIRTH, J. & BOGARD, D. 2001 Scaling of performance for varying density ratio coolants on an airfoil with strong curvature and pressure gradients effects. *Transactions of the ASME. The Journal of Turbomachinery* **123**, 1–7.

FAN, L. N. 1967 The path of a jet directed at large angles to a subsonic free stream. *Tech. Rep.*. California Institute of Technology, KH-R-15.

FERNHOLZ, H. H. & FINLEY, P. J. 1996 Incompressible zero-pressure gradient turbulent boundary layers: An assessment of the data. *Progress in Aerospace Sciences* **32**, 245.

FERRANTE, A. & ELGHOBASHI, S. E. 2004 A robust method for generating inflow conditions for direct simulations of spatially-develping turbulent boundary layers. *Journal of Computational Physics* **198**, 372–387.

FIORINA, B. & LELE, S. K. 2005 An artificial nonlinear diffusivity method for supersonic reacting flows with shocks. *Journal of Computational Phyics* (submitted).

FOSTER, N. W. & LAMPARD, D. 1980 The flow and film cooling effectiveness following injection through a row of holes. *Journal of Engineering for Power* **102**, 584–588.

FRIC, T. F. & ROSHKO, A. 1994 Vortical structure in the wake of a transverse jet. *Journal of Fluid Mechanics* **279**, 1–47.

GAMUSSI, R., GUJ, G. & STELLA, A. 2002 Experimental study of a jet in a crossflow at very low reynolds number. *Journal of Fluid Mechanics* **454**, 113–144.

GARG, V. K. & GAUGLER, R. E. 1995 Leading edge film cooling effects on turbine blade heat transfer. *ASME Paper* 95-GT-275.

GARG, V. K. & GAUGLER, R. E. 1997a Effect of coolant temperature and mass flow on film cooling of turbine blades. *International Journal of Heat and Mass Transfer* **40**, 435–445.

GARG, V. K. & GAUGLER, R. E. 1997b Effect of velocity and temperature distribution at the hole exit on film cooling of turbine blades. *ASME Journal of Turbomachinery* **119**, 343–351.

GAVIGLIO, J. 1987 Reynolds analogies and experimental study of heat transfer in the supersonic boundary layer. *International Journal of Heat and Mass Transfer* **30**, 911.

GERMANO, M., PIOMELLI, U., MOIN, P. & CABOT, W. H. 1991 A dynamic subgrid-scale eddy viscosity model. *Physics of Fluids, A3* pp. 1760–1765.

GHOSAL, S., LUND, T. S., MOIN, P. & AKSELVOLL, K. 1995 A dynamic localization model for large-eddy simulation of turbulent flows. *Journal of Fluid Mechanics* **286**, 229–255.

GHOSAL, S. & MOIN, P. 1995 The basic equations for the large eddy simulation of turbulent flows in complex geometry. *Journal of Computational Physics* **118**, 24–37.

GOLDSTEIN, R. J. & STONE, L. D. 1997 Row-of-hole film cooling of curved walls at low injection angles. *Transactions of the ASME. The Journal of Turbomachinery* **119** (3), 574–579.

GOPALAN, R., ABRAHAM, B. M. & KATZ, J. 2004 The structure of a jet in cross flow at low velocity ratios. *Physics of Fluids* **16** (6), 2067–2087.

GRITSCH, M., SHULTZ, A. & WITTIG, S. 2001 Effect of crossflows on the discharge coefficient of film cooling holes with varying angles of inclination and orientation. *ASME Journal of Turbomachinery* **123** (4), 781–787.

GRIVÉS, E. LE 1978 Mixing process induced by the vorticity associated with the penetration of a jet into a cross flow. *Journal of Engineering for Power* **100**, 465–475.

GUARINI, S. E., MOSER, R. D., SHARIFF, K. & WRAY, A. 2000 Direct numerical simulations of a supersonic turbulent boundary layer at Mach 2.5. *Journal of Fluid Mechanics* **414**, 1.

GUERRA, J. & GUSTAFFSON, B. 1986 A numerical method for incompressible and compressible flow problems with smooth solutions. *Journal of Computational Physics* **63**, 377–397.

GUSTAFFSON, B. 1987 Unsymmetric hyperbolic problems and the Euler equations at low mach numbers. *Journal of Scientific Computing* **2**, 123–136.

GUSTAFFSON, B. & STOOR, H. 1991 Navier-Stokes equations for almost incompressible flow. *SIAM Journal on Numerical Analysis* **28**, 1523–1547.

HAHN, S. & CHOI, H. 1997 Unsteady simulation of jets in a cross flow. *Journal of Computational Physics* **134**, 342–356.

HALE, C., PLESNIAK, M. & RAMADHYANI, S. 2000 Film cooling effectiveness for short film cooling holes fed by a narrow plenum. *ASME Journal of Turbomachinery* **122** (3), 553–557.

HAMA, F. R. 1954 *Trans. Soc. Nav. Arch. Mar. Eng.* **62**.

HARLOW, F. H. & WELCH, J. E. 1965 Numerical calculation of time-dependent viscous incompressible flow. *Physics of Fluids* **8**, 2182–2189.

HASSELBRINK, E. F. & MUNGAL, M. G. 2001 Transverse jets and jet flames. *Journal of Fluid Mechanics* **443**, 1–68.

HAY, N., LAMPARD, D. & SALUJA, C. L. 1985 Effects of cooling films on the heat transfer coefficient on a flat plate with zero mainstream pressure gradient. *ASME J. Eng. Gas Turbines Power* **107**, 105–110.

HESTHAVEN, J. S. 1997 A stable penalty method for compressible Navier-Stokes equations. II. One-dimensional domain decomposition schemes. *SIAM Journal on Scientific Computing* **18** (3), 658–685.

HESTHAVEN, J. S. 1998 A stable penalty method for compressible Navier-Stokes equations. III. Multidimensional domain decomposition schemes. *SIAM Journal on Scientific Computing* **20** (1), 62–93.

HODA, A. & ACHARYA, S. 2000 Predictions of a film coolant jet in crossflow with different turbulence models. *ASME Journal of Turbomachinery* **122**, 558–569.

HOUZEAUX, G. & CODINA, R. 2004 A dirichlet/neumann domain decomposition method for incompressible turbulent flows on overlapping subdomains. *Computers and Fluids* **33** (5), 771–782.

ILLINGWORTH, C. R. 1949 Steady flow in the laminar boundary layer over a gas. *Proceedings of the Royal Society* **A 199**, 533.

IOUROKINA, I. V. & LELE, S. K. 2005 Towards largy eddy simulation of film-cooling flows on a model turbine blade leading edge. *AIAA Paper* 2005-0670. In 43rd AIAA Aerospace Sciences Meeting and Exhibit, Reno, NV.

JOHNSTON, J. P., MOISER, B. P. & KHAN, Z. U. 2002 Vortex generating jets; effects of jet-hole inlet geometry. *International Journal of Heat and Fluid Flow* **23**, 744–749.

KAPADIA, S. & ROY, S. 2003 Detached eddy simulation of trubine blade cooling. *AIAA Paper* 2003–3632. In 36th Thermophysics Conference, Orlando, FL.

KARAGOZIAN, A. R. 1986 An analytical model for the vorticity associated with a transverse jet. *AIAA Journal* **24** (3), 429–436.

KASZETA, R. W. & SIMON, T. W. 2000 Measurement of eddy diffusivity of momentum in film cooling flows with streamwise injection. *ASME Journal of Turbomachinery* **122** (1), 178–183.

KASZETA, R. W., SIMON, T. W., OKE, R. A., W., S. & BURD 1998 Flow measurements in film cooling flows with lateral injection. *ASME Paper* 98-GT-54.

KELSO, R. M., LIM, T. T. & PERRY, A. E. 1996 An experimental study of round jets in cross-flow. *Journal of Fluid Mechanics* **306**, 111–144.

KIM, C. N., KARAGOZIAN, A. R. & NGUYEN, T. T. 1985 Vortex modeling of single and multiple dilution jet mixing in a crossflow. *AIAA Paper* 85–1580.

KLEIN, M., SADIKI, A. & JANICKA, J. 2003 A digital filter based generation of inflow data for spatially developing direct numerical or large eddy simulations. *Journal of Computational Physics* **186**, 652.

KLEISER, L. & ZANG, T. 1991 Numerical simulation of transition in wall-bounded shear flows. *Annual Review of Fluid Mechanics* **23**, 495–537.

KODZWA, P. 2005 Measurements of film cooling performance in a transonic single passage model. PhD thesis, Deparment of Mechanical Engineering, Stanford University.

KOPRIVA, D. A. 1991 Multidomain spectral solution of the Euler gas-dynamics equations. *Journal of Computational Physics* **96**.

KOPRIVA, D. A. 1994 Multidomain spectral solution of compressible viscous flows. *Journal of Computational Physics* **115**.

KOPRIVA, D. A. & KOLIAS, J. H. 1996 A conservative staggered-grid chebyshev multido-main method for compressibe flows. *Journal of Computational Physics* **125** (2), 475–488.

KREISS, H. O. & SHERER, G. 1974 Finite element and finite difference methods for hyper-bolic partial differential equations. In *Mathematical Aspects of Finite Elements in Partial Differential Equations*. Academic Press, Inc.

KRUSE, H. 1984 Measurements of film cooling effectiveness and heat transfer on a flat plate. pp. 451–461. Washington, DC, Hemisphere Publishing Corp.

LAKEHAL, D., THEODORIDIS, G. S. & RODI, W. 1998 Computationf of film cooling of a flat plate by lateral injection from a row of holes. *International Journal of Heat and Fluid Flow* **40**, 418–430.

LE, H. & MOIN, P. 1994 Direct numerical simulation of turbulent flow over a backward-facing step. In *Report TF–58*. Thermosciences Division, Department of Mechanical Engineering, Stanford University.

LE, H., MOIN, P. & KIM, J. 1997 Direct numerical simulation of turbulent flow over a backward-facing step. *Journal of Fluid Mechanics* **330**, 349.

LEE, S., LELE, S. K. & MOIN, P. 1992 Simulation of spatially evolving turbulence and the applicability of Taylor's hypothesis in compressible flow. *Physics of Fluids* **A 4** (7), 1521–1530.

LELE, S. K. 1994 Compressibility effects on turbulence. *Annual Review of Fluid Mechanics* **26**, 211–254.

LELE, S. K. 1998 Direct numerical simulations of compressible turbulent flows: fundamentals and applications. In *Transition, Turbulence and Modeling*, pp. 421–488. Kluwer Academic Publishers.

LEONARD, B. P. 1979 A stable and accurate convective modelling procedure based on quadratic upstream interpolation. *Computational Methods in Applied Mechanics and Engineering* **19**, 59–98.

LEYLEK, J. H. & ZERKLE, R.D. 1994 Discrete-jet film cooling: A comparison of computational results with experiments. *Transactions of the ASME. The Journal of Turbomachinery* **116**, 358–368.

LILLY, D. K. 1992 A proposed modification of the Germano subgrid-closure method. *Physics of Fluids, A4* pp. 633–635.

LIU, K. & PLETCHER, R. 2005 Large eddy simulation of discrete-hole film cooling in a flat plate turbulent boundary layer. *AIAA Paper* 2005–4944. In 35th AIAA Fluid Dynamics Conference and Exhibit.

LUND, T. S. 1993 Large eddy simulation of a boundary layer with concave streamwise curvature. In *Annual Research Briefs*, p. 91. Center for Turbulence Research, Stanford University.

LUND, T. S. & MOIN, P. 1996 Large-eddy simulation of a concave wall boundary layer. *International Journal of Heat and Fluid Flow* **17**, 290.

LUND, T. S., WU, X. & SQUIRES, K. D. 1998 Generation of turbulent inflow data for spatially-developing bounday layer simulations. *Journal of Computational Physics* **140**, 233–258.

LUTUM, E. & JOHNSON, B. 1999 Influence of the hole length-to-diameter ratio on film cooling with cylindrical holes. *ASME Journal of Turbomachinery* **121** (2), 209–216.

MAEDER, T., ADAMS, N. A. & KLEISER, L. 2001 Direct simulation of turbulent supersonic boundary layers by an extended temporal approach. *Journal of Fluid Mechanics* **429**, 187–216.

MANNA, M., BENOCCI, C. & SIMONS, E. 2005 Large eddy simulation of turbulent flows via domain decomposition techniques. *International Journal for Numerical Methods in Fluids* **48** (4), 367–422.

MANNA, M., VACCA, A. & DEVILLE, M. O. 2004 Preconditioned spectral multi-domain discretization of the incompressible NavierStokes equations. *Journal of Computational Physics* **201** (1), 204–223.

MARGASON, R. J. 1968 The path of a jet directed at large angles to a subsonic free stream. *Tech. Rep.*. NASA-TN-D-4919.

MATTSON, K., IOUROKINA, I. & HAM, F. 2005 Stable and accurate coupling between compressible and incompressible flow solvers. In *Annual Research Briefs*. Center for Turbulence Research, Stanford University.

MATTSON, K. & NÖRDSTROM, J. 2004 Summation by parts operators for finite difference approximations of second derivatives. *Journal of Computational Physics* **199** (2).

MCCROSKEY, W. J. 1995 Vortex wakes of rotocraft. *AIAA Paper* 95–0530. In 33rd AIAA Aerospace Sciences Meeting and Exhibit, Reno, NV.

MITTAL, R. & MOIN, P. 1997 Suitability of upwind-biased finite difference schemes for large-eddy simulation of turbulent flows. *AIAA Journal* **35**, 1415–1417.

MOHSENI, K. & COLONIUS, T. 2000 Numerical treatment of polar coordinate singularities. *Journal of Computational Physics* **157**, 787–795.

MOIN, P., SQUIRES, K., CABOT, W. & LEE, S. 1991 A dynamic subgrid-scale model for compressible turbulence and scalar transport. *Physics of Fluids, A3* (11), 2746–2757.

MORKOVIN, M. V. 1962 Effects of compressibility on turbulent flows. In *Mécanique de la Turbulence*, pp. 367–380. CNRS, Paris, ed. A. Favre.

MULDOON, F. & ACHARYA, S. 1999 Numerical investigation of the dynamical behavior of a row of square jets in crossflow over a surfacee. *ASME Paper* 99-GT-217. In IGTI Intl. Gas Turbine Conference, Indianapolis.

MÜLLER, B. 1999 Low mach number asymptotics of the Navier-Stokes equations and numerical implicatons. In *30th Computational Fluid Dynamics*, pp. 821–831. Von Karman Institute for Fluid Dynamics, Lecture Series 1999–03.

MUPPIDI, S. & MAHESH, K. 2005 Study of trajectories of jets in crossflow using direct numerical simulations. *Journal of Fluid Mechanics* **530**, 81–100.

MURLIS, J., TSAI, H. M. & BRADSHAW, P. 1982 The structure of trubulent boundary layers at low Reynolds number. *Journal of Fluid Mechanics* **122**, 13–56.

NÖRDSTROM, J. & CARPENTER, M. H. 1999 Boundary and interface conditions for high order finite difference methods applied to Euler and Navier-Stokes equations. *Journal of Computational Physics* **148**.

PARTER, S. V. 1999 On the overlapping grid method for elliptic boundary value problems. *SIAM Journal on Numerical Analysis* **36** (3), 819–852.

PETERSON, S. D. & PLESNIAK, M. W. 2002 Short-hole jet-in-crossflow velocity field and its relationship to film-cooling performance. *Experiments in Fluids* **33**, 889–898.

PETERSON, S. D. & PLESNIAK, M. W. 2004 Evolution of jets emanating from short holes into crossflow. *Journal of Fluid Mechanics* **503**, 57–91.

PETERSON, S. D. & PLESNIAK, M. W. 2005 The effect of streamwise injection on the flow structure and skin friction distribution of a row of multiple jets-in-crossflow. Int. Conf. on Jets, Wakes and Separated Flows, ICJWSF-2005, Toba-shi, Mie, Japan.

PFEIFFER, H. P., KIDDER, L. E., SCHEEL, M. A. & TEUKOLSKY, S. A. 2003 A multidomain spectral method for solving elliptic equations. *Computer Physics Communications* **152** (3), 253–273.

PIERCE, C. D. 2001 Progress-variable approach for large eddy simulaiton of turbulent combustion. PhD thesis, Deparment of Mechanical Engineering, Stanford University.

PIETRZYK, J. R., BOGARD, D .G. & CRAWFORD, M. E. 1989 Hydrodynamic measurements of jets in crossflow for gas turbine film cooling applications. *Transactions of the ASME. The Journal of Turbomachinery* **111**, 139–145.

PIETRZYK, J. R., BOGARD, D .G. & CRAWFORD, M. E. 1990 Effects of density ratio on the hydrodynamics of film cooling. *Transactions of the ASME. The Journal of Turbomachinery* **112**, 438–443.

PIOMELLI, U. & BALARAS, E. 2002 Wall-layer models for large-eddy simulations. *Annual Review of Fluid Mechanics* **34**, 349–374.

PLETCHER, R. H. & CHEN, K.-H. 1993 On solving the compressible Navier-Stokes equations for unsteady flows at very low mach numbers. *AIAA Paper* 1993-3368.

PULLIAM, T. H. 1993 Time accuracy and the use of implicit methods. *AIAA Paper* 93-3360.

RAI, M. M. 1987 Navier-Stokes simulations of blade-vortex interaction using high-order accurate upwind schemes. *AIAA Paper* 87-0543.

RAI, M. M. & MOIN, P. 1993 Direct numerical simulation of transition and turbulence in a spatially evolving boundary layer. *Journal of Computational Physics* **109**, 169.

RAMSEY, J. W. & GOLDSTEIN, R. J. 1971 Interaction of a heated jet with a deflecting stream. *ASME Journal of Heat Transfer* **94**, 365–372.

REHM, R. G. & BAUM, H. R. 1978 The equations of motion for thermally driven buoyant flows. *Jorunal of Reseacrh of the National Bureau of Standards* **83**, 297–308.

RENAUD, F. & GAUTHIER, S. 1997 A dynamical pseudo-spectral domain decomposition technique: Application to viscous compressible flows. *Journal of Computational Physics* **131** (1), 89–108.

ROZATI, A. & TAFTI, D. 2006 Analysis of flow physics and jet-mainstream interaction in leading edge filmcooling using large eddy simulation. *ASME Paper* FEDSM2006-98063. In 2nd Joint U.S.-European Fluids Engineering Summer Meeting, Miami, FL.

SAGAUT, P., GARNIER, E., TROMEUR, E., LARCHEVÊQUE, L. & LABOURASSE, E. 2004 Turbulent inflow condition for large-eddy simulation of compressible wall-bounded flows. *AIAA Journal* .

SCHLICHTING, H. 2000 *Boundary-layer theory*, 8th edn. Berlin; New York: Springer.

SCHLÜTER, J. U., PITSCH, H. & MOIN, P. 2002 Consistent boundary conditions for integrated les/rans simulations: Les outflow conditions. *AIAA Paper* 2002-3121. 32nd AIAA Fluid Dynamics Conference and Exhibit, St.Louis, MO.

SCHLÜTER, J. U., PITSCH, H. & MOIN, P. 2003*a* Boundary conditions for les in coupled simulations. *AIAA Paper* 2003-0069. In 41st AIAA Aerospace Sciences Meeting and Exhibit, Reno, NV.

SCHLÜTER, J. U., SHANKARAN, S., KIM, S., PITSCH, H., ALONSO, J. & MOIN, P. 2003*b* Integration of rans and les flow solvers for simultaneous flow computations. *AIAA Paper* 2003-0085.

SCHLÜTER, J. U., WU, X., KIM, S., SHANKARAN, S., ALONSO, J. J. & PITSCH, H. 2005 A framework for coupling reynolds-averaged with large-eddy simulations for gas turbine applications. *Journal of Fluids Engineering, Transactions of the ASME* **127** (4), 806–815.

SCHMIDT, D., SEN, B. & BOGARD, D. 1996 Film cooling with compound angle holes: Adiabatic effectiveness. *ASME Journal of Turbomachinery* **118**, 807–813.

SCHRÖDER, W., MEINKE, M., EWERT, R. & EL-ASKARY, W. 2001 Les of a turbulent flow around a sharp trailing edge. In *Direct and Large-Eddy Simulation - IV*, pp. 353–363. Kluwer Academic, Norwell, MA.

SINHA, A. K., BOGARD, D .G. & CRAWFORD, M. E. 1991 Film-cooling effectiveness downstream of a single row of holes with variable density ratio. *Transactions of the ASME. The Journal of Turbomachinery* **113**, 442–449.

SMAGORINSKY, J. 1963 General circulation experiments with the primitive equations. *Journal of Monthly Weather Review* **91** (3), 99–164.

SMITH, A. J. & DUSSAUGE, J. 1996 Boundary layer mean-flow behavior. In *Turbulent shear layers in supersonic flows*, p. 161. AIP, New York.

SPALART, P. R. 1988 Direct simulation of a turbulent boundary layer up to $r_\theta = 1410$. *Journal of Fluid Mechanics* **187**, 61–98.

SPALART, P. R. 2000 Strategies for turbulence modeling and simulations. *International Journal of Heat and Fluid Flow* **21**, 252–263.

SPALART, P. R. & ALLMARAS, S. R. 1994 A one equation turbulence model for aerodynamic flows. *La Recherche Aerospatiale* **1**, 5–21.

SPALART, P. R. & HATMUFF, J. H. 1993 Experimental and numerical study of a turbulent boundary layer with pressure gradients. *Journal of Fluid Mechanics* **249**, 337.

SPALART, P. R., JOU, W. H., STRELETS, M. & ALLMARAS, S. R. 1997 Comments on the feasibility of les for wings, and on a hybrid rans/les approach. In *advances in DNS/LES*. Greyden Press, Columbus, OH, USA, in 1st AFOSR international conference on DNS/LES, Aug. 4-8, 1997, Ruston, LA.

SPALDING, D. B. 1961 A single formula for the law of the wall. *Journal of Applied Mechanics* pp. 455–458.

Squires, K. D. 2005 Detached eddy simulation: current status and perspectives. *Proceedings of 2005 DLES5 DES* .

Stewartson, K. 1949 Correlated compressible and incompressible boundary layers. *Proceedings of the Royal Society* **A 200**, 84–100.

Stolz, S. & Adams, N. A. 2003 Large-eddy simulation of high-reynolds-number supersonic boundayr layers using the approximate deconvolution model and a rescaling and recycling technique. *Physics of Fluids* **15** (8), 2398–2412.

Strelets, M. 2001 Detached eddy simulation of massively separated flows. *AIAA Paper* 01–0879.

Strikwerda, J. C. & Scarbnick, C. D. 1993 A domain decomposition method for incompressible viscous flow. *SIAM Journal on Scientific Computing* **14** (1), 49–67.

Subramanya, K. & Porey, P. D. 1984 Trajectory of a turbulent cross jet. *Journal of Hydraulic Research* **22** (5), 343–354.

Taylor, G. I. 1918 On the dissipation of eddies. *Aero.Res.Comm, R and M* p. 598.

Thole, K. A., Sinha, A., Bogard, D. G. & Crawford, M. E. 1992 Mean temperature measurements of jets with a crossflow for gas turbine film cooling application. p. 69. Hemisphere, New York.

Tidriri, M. D. 1995 Domain decomposition for compressible Navier-Stokes equations with different discretizations and formulations. *Journal of Computational Physics* **119** (2), 271–282.

Turkel, E. 1987 Preconditioned methods for solving the incompressible and low speed compressible equations. *Journal of Computational Physics* **72**, 277–298.

Turkel, E. 1999 Preconditioning techniques in computational fluid dynamics. *Annual Review of Fluid Mechanics* **31**, 385–416.

Turkel, E., Fiterman, A. & van Leer, B. 1994 Preconditioning and the limit to the incompressible flow equations. In *Computing the Future: Frontiers of Computational Fluid Dynamics*, pp. 215–234. ed. DA Caughey, MM Hafez, New York: Wiley.

Tyagi, M. & Acharya, S. 1999*a* Large eddy simulations of jets in crossflow: Freestream turbulence effects. In 3rd ASME/JSME Joint fluids engineering conference.

TYAGI, M. & ACHARYA, S. 1999*b* Large eddy simulations of jets in crossflow: Large scale turbulence effects. IMECE, Nashville, TN.

TYAGI, M. & ACHARYA, S. 1999*c* Large eddy simulations of rectangular jets in crossflow: Effect of hole-aspect ratio. In *Adv. in DNS/LES, proceedings of SAICDL* (ed. Sakell), pp. 431–442. Kluwer Publications.

TYAGI, M. & ACHARYA, S. 2000 Large eddy simulations of jets in crossflow: Effect of jet inclination angle. In 4th ISHMT/ASME heat and mass transfer conference, INDIA.

TYAGI, M. & ACHARYA, S. 2003 Large eddy simulation of film cooling flow from an inclined cylindrical jet. *Transactions of the ASME. The Journal of Turbomachinery* **125** (4), 734–742.

URBIN, G. & KNIGHT, D. 2001 Large-eddy simulation of a supersonic boundary layer using an unstructured grid. *AIAA Journal* **39** (7), 1288–1295.

VAN LEER, B., LEE, W. T. & ROE, P. L. 1991 Characteristic time-stepping or local preconditioning of the Euler equations. *AIAA Paper* 1991-1552.

VASILYEV, O. V., LUND, T. S. & MOIN, P. 1998 A general class of commutative filters for les in complex geometries. *Journal of Computational Physics* **146**, 82–104.

VENKATESWARAN, S. & MERKLE, C. L. 1995 Dual time stepping and preconditioning for unsteady computations. *AIAA Paper* 1995-0078.

VEREECKE, B., BAVESTRELLO, H. & DUREISSEIX, D. 2003 An extension of the feti domain decomposition method for incompressible and nearly incompressible problems. *Computer Methods in Applied Mechanics and Engineering* **192** (31), 3409–3429.

WALTERS, D. K. & LEYLEK, J. H. 1997 A systematic computational methodology applied to a three-dimensional film-cooling flowfield. *Transactions of the ASME. The Journal of Turbomachinery* **119**, 777–785.

WANG, L., TSANG, H., SIMON, T. W. & ECKERT, E. R. G. 1996 Measurements of a mean flow and eddy transport over a film cooling surface. *ASME* HTD-Vol. 327, pp. 71–79. In Proceedings 31st National Heat Transfer Conference.

WEISS, J. M. & SMITH, W. A. 1994 Preconditioning applied to variable and constand density time accurate flows on unstructured meshes. *AIAA Paper* 1994-2209.

WITTIG, S., SCHULTZ, A., GRITSCH, M. & THOLE, K. 1996 Transonic film cooling investigations: Effects of hole shapes and orientations. *ASME Paper* 96-GT-222.

XIONG, Z. 2004 Stagnation point flow and heat transfer under free-stream turbulence. PhD thesis, Deparment of Mechanical Engineering, Stanford University.

XU, S. & MARTIN, M. P. 2004 Asessment of inflow boundary conditions for compressible turbulent boundary layers. *Physics of Fluids* **16** (7), 2623–2639.

YORK, W. D. & LEYLEK, J. H. 1999 Numerical prediction of mainstream pressure gradient. effects in film cooling. *ASME Paper* 99-GT-166. IGTI, Ontario.

YUAN, L. L., STREET, R. L. & FERZIGER, J. H. 1999 Large-eddy simulations of a round jet in crossflow. *Journal of Fluid Mechanics* **379**, 71–104.

ZIEGLER, H. & WOOLER, P. T. 1973 Analysis of stratified and closely spaced jets exhausting into a cross-flow. *Tech. Rep.*. NASA CR-132297.